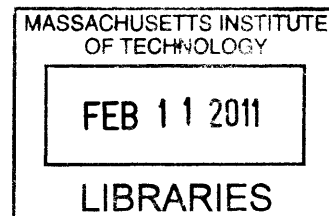


# Surface Modifications of Iron Oxide Nanoparticles for Biological Applications

by

**Numpon Insin**

B.Sc. in Chemistry  
Faculty of Science, Chulalongkorn University  
Thailand 2003



**ARCHIVES**

Submitted to the Department of Chemistry in  
Partial Fulfillment of the Requirements for the Degree of

**DOCTOR OF PHILOSOPHY**

at the

MASSACHUSETTS INSTITUTE OF TECHNOLOGY

February 2011

©2011 MASSACHUSETTS INSTITUTE OF TECHNOLOGY  
All Rights Reserved

Signature of Author \_\_\_\_\_

Department of Chemistry  
November 9, 2010

Certified by \_\_\_\_\_

Moungi G. Bawendi  
Professor of Chemistry  
Thesis Supervisor

Accepted by \_\_\_\_\_

Robert W. Field  
Chairman, Departmental Committee on Graduate Students



This doctoral thesis has been examined by a committee of the Department of Chemistry as follows:

Professor Daniel G. Nocera




Chairman

Professor Mounji G. Bawendi



Thesis Supervisor

Professor Mircea Dincă



Department of Chemistry





# **Surface Modifications of Iron Oxide Nanoparticles for Biological Applications**

by

Numpon Insin

Submitted to the Department of Chemistry on November 9, 2010 in partial fulfillment  
Of the requirements for the degree of Doctor of Philosophy in Chemistry

## **ABSTRACT**

Iron oxides magnetic nanoparticles (MPs) of high crystallinity, high magnetization, and size-monodispersity were synthesized with oleic acid as their native ligands. These hydrophobic and non-functionalized MPs have magnetic properties that are suitable for various biological applications. Surface modifications were studied for transferring these MPs into biological environments as well as transforming them into functional nanoparticles.

Certain surface modifications of MPs, such as attaching silane groups and silica coating, lead to formation of more complex structures of superparamagnetic and fluorescent silica microspheres and nanostructures. These microspheres and nanostructures comprising MPs and semiconductor quantum dots (QDs) are useful tools for biological applications such as for magnetically controlling with fluorescent tracking of particles and for bimodal imaging.

Surface modifications of MPs with hydrophobically-modified polyacrylic acid (mPAA) amphiphilic polymer and catechol-derivative surfactants resulted in hydrophilic MPs that are stable in physiological environment and small in their hydrodynamic size. These MPs are also designed to possess active functional groups that are necessary for further conjugations with proteins and molecules of interest. These hydrophilic and functional MPs are useful in biological applications such as magnetic resonance imaging and sensing applications.

Thesis Supervisor: Mounji G. Bawendi  
Title: Professor of Chemistry



*To my family and friends*



## Table of Contents

Title page.....	1
Signature page.....	3
Abstract.....	5
Dedication... ..	7
Table of contents.....	9
List of Figures.....	13
<b>Chapter 1: Introduction</b>	
1.1 Magnetic properties of Materials.....	17
1.2 Magnetic nanoparticles and superparamagnetic properties.....	19
1.3 Biological applications of magnetic nanoparticles.....	21
1.3.1 Magnetic attraction.....	21
1.3.2 Hyperthermia.....	22
1.3.3 Magnetic resonance imaging.....	22
1.4 Semiconductor quantum dots and their biological applications.....	23
1.5 Thesis Overview.....	25
1.6 References.....	26
<b>Chapter 2: Magnetic Nanoparticle: Synthesis and Characterization</b>	
2.1 Introduction.....	29
2.2 Iron oxides nanoparticles.....	29
2.2.1 Synthesis and characterization of iron oxides nanoparticles.....	30
2.2.2 Magnetic properties of iron oxides nanoparticles.....	35
2.3 Other magnetic nanoparticles.....	40
2.3.1 Manganese ferrite.....	40
2.3.2 Cobalt ferrite nanoparticles.....	42
2.3.3 Iron Platinum Alloy nanoparticles.....	44
2.4 Conclusion.....	45
2.5 References.....	46
<b>Chapter 3: Surface Modification of Iron Oxide Nanoparticles with Silanes: Formation of Magnetic and Fluorescent Silica Microspheres</b>	
3.1 Introduction.....	49
3.2 Synthesis of magnetic and fluorescent microspheres.....	50
3.2.1 Surface modification of MPs and QDs .....	51
3.2.2 Incorporation process .....	53
3.3 Physical Properties of magnetic and fluorescent microspheres.....	62
3.3.1 Fluorescence.....	62
3.3.2 Magnetic Properties.....	64
3.4 Demonstration of combined superparamagnetism and fluorescence of the MP-and QD-incorporated micropsheres.....	67
3.4.1 Demonstration using microelectromagnetic device.....	67

3.4.2 Demonstration using magnetic tips.....	72
3.5 Surface functionalization of the microspheres.....	75
3.6 Conclusion.....	78
3.7 References.....	78
3.8 Appendix	
Appendix A: Calculation of MP and QD content in microspheres from ICP-OES elemental analysis.....	82
Appendix B: Calculation of magnetic susceptibility of a microsphere used in trapping experiment.....	85

**Chapter 4: Surface Modification of Iron Oxide Nanoparticles through a Reverse Micro-emulsion Process and Preparation of QD-decorating Silica-coated Iron Oxide Nanoparticles**

4.1 Introduction.....	87
4.2 Synthesis of silica-coated iron oxides MPs through a reverse micro-emulsion process.....	88
4.3 Incorporation of QDs into the silica shell of silica-coated iron oxides MPs.....	95
4.4 Decoration of QDs onto silica-coated MPs.....	97
4.5 Increase of MP loading: Use of the agglomeration of MPs.....	101
4.6 Conclusion.....	103
4.7 References.....	104

**Chapter 5: Surface Modification of Iron Oxides Nanoparticles using Hydrophobically-Modified Acrylic Acid**

5.1 Introduction.....	107
5.2 Preparation of hydrophobically-modified polyacrylic acid.....	109
5.3 Preparation of iron oxides MPs with mPAA on their surface.....	111
5.4 Bio-conjugation of the mPAA-coated MPs.....	119
5.5 Conclusion.....	122
5.6 References.....	122

**Chapter 6: Surface Modification of Iron Oxide Nanoparticles using Catechol-derivative Surfactants**

6.1 Introduction.....	125
6.2 Surfactants with mono-catechol and polyethylene glycol.....	128
6.3 Surfactants with poly-catechol and polyethylene glycol.....	131
6.3.1 Synthesis of PCP surfactants .....	132
6.3.1.1 Monomer synthesis.....	133
6.3.1.2 Polymerization of PCP surfactants.....	137
6.3.2 Surfactant-exchanging process.....	141
6.3.3 Physical properties of the MPs with PCP surfactants.....	142
6.3.4 Conjugations of the MPs.....	149
6.3.5 Properties of the MPs in biological systems.....	155
6.4 Mono-catechol zwitterionic surfactant.....	158
6.5 Conclusion.....	163
6.6 References.....	163

6.7 Appendix C: $^1\text{H}$ NMR and IR spectra of Compounds.....	166
<b>Chapter 7 QD-Decorated Iron Oxide Nanoparticles</b>	
7.1 Introduction.....	171
7.2 QD-Conjugation of MPs with mPAA surfactants.....	172
7.3 QD-conjugation of MPs with PEG-catechol derivative surfactants.....	174
7.4 Conclusion.....	182
7.5 References.....	183
<b>Curriculum vitae</b> .....	185
<b>Acknowledgments</b> .....	189





## List of Figures

<b>Figure 1.1</b>	Arrangement of atomic dipole in materials.....	17
<b>Figure 1.2</b>	Magnetic responses of materials to magnetic field (H).....	18
<b>Figure 1.3</b>	Magnetic responses superparamagnetic materials.....	20
<b>Figure 1.4</b>	TEM images and absorption-emission spectra of CdSe/CdZnS QDs .....	24
<b>Figure 2.1</b>	Reaction scheme for the synthesis of the iron oxide MPs.....	31
<b>Figure 2.2</b>	TEM images of MPs of different sizes .....	32
<b>Figure 2.3</b>	XRD patterns of the as-synthesized MPs .....	33
<b>Figure 2.4</b>	XPS spectra for Fe 2p of the as-synthesized MPs.....	35
<b>Figure 2.5</b>	Saturation magnetization of the iron oxide MPs.....	36
<b>Figure 2.6</b>	Zero-field-cooled magnetization versus temperature of MPs.....	37
<b>Figure 2.7</b>	Photographs of the macroscopic magnetic response of the MPs.....	39
<b>Figure 2.8</b>	Schemes for preparation of manganese ferrite nanoparticles.....	41
<b>Figure 2.9</b>	TEM images of manganese ferrite nanoparticles.....	42
<b>Figure 2.10</b>	TEM image of cobalt ferrite nanoparticles.....	43
<b>Figure 2.11</b>	Saturation magnetization of the cobalt ferrite nanoparticles.....	44
<b>Figure 2.12</b>	TEM image of iron platinum alloy nanoparticles.....	45
<b>Figure 3.1</b>	Reaction scheme for the surface modification of the MPs.....	52
<b>Figure 3.2</b>	Reaction scheme for the incorporation of silica microspheres.....	53
<b>Figure 3.3</b>	Size distributions of silica microspheres.....	55
<b>Table 3.1</b>	Properties of additional surfactants in dispersion of MPs into ethanol and incorporation of MPs into silica microsphere.....	57
<b>Figure 3.4</b>	TEM images of MP-incorporating microspheres.....	58
<b>Figure 3.5</b>	TEM images of the microspheres of 50-nm in diameter.....	59
<b>Figure 3.6</b>	Images of the microspheres from STEM .....	60
<b>Figure 3.7</b>	Results from STEM line-scanning analysis.....	61
<b>Figure 3.8</b>	Graph representing the relationship between $h$ and $r_p$ of a core-shell microsphere.....	62
<b>Figure 3.9</b>	Images of the microspheres from an optical microscope.....	63
<b>Figure 3.10</b>	Magnetization versus magnetic field at 5 K of 500-nm microspheres .....	65
<b>Figure 3.11</b>	Zero-field-cooled magnetization of 500-nm microspheres.....	67
<b>Figure 3.12</b>	Images of the straight wires trapping experiment.....	69
<b>Figure 3.13</b>	Images of the ring trapping experiment.....	70
<b>Figure 3.14</b>	Images of the magnetic tip attraction experiment.....	74
<b>Figure 3.15</b>	Reaction scheme for surface functionalization of silica microspheres.....	75
<b>Figure 3.16</b>	Zeta potential of 300 nm silica microspheres.....	77
<b>Table 3.2</b>	Calculation for obtaining the loading of MPs and QDs in the microsphere....	83
<b>Table 3.3</b>	Calculation for obtaining the loading of MPs and QDs in the microsphere after adjusting the density of incorporated microspheres.....	84
<b>Figure 4.1</b>	Schematic representation of the silica-coating process.....	89
<b>Figure 4.2</b>	TEM images of the MPs before and after silica coating.....	90
<b>Figure 4.3</b>	TEM images of the silica-coated MP of different shell thickness .....	91

<b>Figure 4.4</b>	DLS Size distribution of the silica-coated MPs.....	92
<b>Figure 4.5</b>	TEM images of the MPs with incomplete silica coating.....	93
<b>Figure 4.6</b>	TEM images of the thin-shelled MPs.....	94
<b>Figure 4.7</b>	Schematic representation of the QD incorporation into silica-coated MPs.....	96
<b>Figure 4.8</b>	TEM images of the QD-incorporated silica-coated MP.....	97
<b>Figure 4.9</b>	QD decoration of the silica-coated MPs.....	98
<b>Figure 4.10</b>	TEM images of QD-decorating silica-coated MPs.....	99
<b>Figure 4.11</b>	DLS Size distribution of QD-decorating silica-coated MPs.....	99
<b>Figure 4.12</b>	Images of QD-decorating silica-coated MPs under excitation by UV,....	100
<b>Figure 4.13</b>	TEM images of the silica-coated MPs with multiple-MP cores.....	101
<b>Figure 4.14</b>	Scheme for the process of colloidal superparticles preparation .....	102
<b>Figure 4.15</b>	TEM images of the colloidal superparticles.....	103
<b>Figure 5.1</b>	The mechanism for calcium-sensing using MRI.....	108
<b>Figure 5.2</b>	Reaction scheme for synthesis of mPAA.....	109
<b>Figure 5.3</b>	Infrared transmission spectra of polyacrylic acid and mPAA.....	110
<b>Figure 5.4</b>	Schematic representation of the preparation of mPAA-coated MPs.....	112
<b>Figure 5.5</b>	TEM images of MPs before and after being coated with mPAA.....	113
<b>Figure 5.6</b>	Size determinations of mPAA-coated MPs.....	114
<b>Figure 5.7</b>	Reaction scheme for applying amino-PEG groups onto mPAA-MPs.....	116
<b>Figure 5.8</b>	TEM images of amino-functionalized mPAA-MPs .....	117
<b>Table 5.1</b>	Properties of amino-functionalized mPAA-MPs compared to commercial T2 contrast agents.....	118
<b>Figure 5.9</b>	Bio-conjugation of mPAA-coated MPs.....	119
<b>Figure 5.10</b>	Absorption spectra of the MPs conjugation with CaM and RS20.....	121
<b>Figure 6.1</b>	Molecules with observed ability to bind onto iron oxide surface.....	126
<b>Figure 6.2</b>	MPs with hydrocaffeic acid.....	127
<b>Figure 6.3</b>	General reaction schemes for synthesis of mono-catechol ligands.....	129
<b>Table 6.1</b>	Properties of some iron oxide MPs with mono-catechol ligands .....	130
<b>Figure 6.4</b>	TEM image of MPs with HCF-PEG12-OMe surfactant. ....	130
<b>Figure 6.5</b>	PCP ligand and MPs after being modified with this surfactant.....	132
<b>Figure 6.6</b>	Syntheses of the monomers for the PCP ligands.....	134
<b>Figure 6.7</b>	RAFT polymerization for the syntheses of the PCP ligands.....	138
<b>Figure 6.8</b>	Chromatogram from GPC of the PCP polymers.....	140
<b>Figure 6.9</b>	Surfactant-exchanging process.....	142
<b>Figure 6.10</b>	Size distributions of MPs with PCP ligand <b>8</b> .....	143
<b>Figure 6.11</b>	Size distributions of MPs with PCP surfactant <b>9</b> .....	145
<b>Table 6.2</b>	Properties of MPs with the PCP surfactant compared to commercial T2 contrast agents .....	146
<b>Figure 6.12</b>	Size distributions of MPs with PCP ligand <b>10</b> .....	147
<b>Figure 6.13</b>	Magnetization of the MPs before and after surfactant-exchanging process.....	148
<b>Table 6.3</b>	Magnetization of magnetic nanoparticles used as T2 contrast agent compared	

to the MPs with PCP ligands.....	149
<b>Figure 6.14</b> Conjugation of MPs with PCP 9 ligand.....	150
<b>Figure 6.15</b> Conjugation of MPs with PCP 10 ligand .....	152
<b>Figure 6.16</b> RAFT polymerization for the synthesis of the PCP ligand with azide and biotin groups as orthogonal functional groups.....	153
<b>Figure 6.17</b> Conjugation of MPs with PCP 12 ligand .....	154
<b>Figure 6.18</b> Protein non-specific binding test in serum.....	156
<b>Figure 6.19</b> Protein non-specific binding test with HeLa cells.....	157
<b>Figure 6.20</b> Synthesis of zwitterionic ligand.....	159
<b>Figure 6.21</b> TEM images of the MPs before and after being surfactant-exchanged with ZDS.....	160
<b>Figure 6.22</b> DLS hydrodynamic diameters of the MPs with ZDS .....	161
<b>Figure 6.23</b> Stability of the MPs with ZDS surfactants measured using zeta-potential analyzer and UV-Vis spectrometer.....	162
<b>Figure 7.1</b> MP and QD conjugation using EDC coupling agent.....	172
<b>Figure 7.2</b> TEM images of the MP-QD conjugation using EDC coupling agent.....	173
<b>Figure 7.3</b> MP and QD conjugation using streptavidin-biotin interaction.....	175
<b>Figure 7.4</b> TEM images of MP-QD conjugation using streptavidin-biotin interaction..	176
<b>Figure 7.5</b> TEM images of MP-QD conjugation using streptavidin-biotin interaction after purification by centrifugal filter dialysis.....	177
<b>Figure 7.6</b> MPs and QDs conjugation using maleimide-thiol coupling reaction.....	179
<b>Figure 7.7</b> TEM images of the MP-QD conjugation using maleimide-thiol coupling reaction.....	181



# Chapter 1

## Introduction

### 1.1 Magnetic properties of Materials

Every substance has its own magnetic properties. Materials can be divided into three main classes of magnetic properties: diamagnetic, paramagnetic, and ferromagnetic. The arrangements of atomic dipoles are the main causes of different magnetic properties, as shown in Figure 1.1.

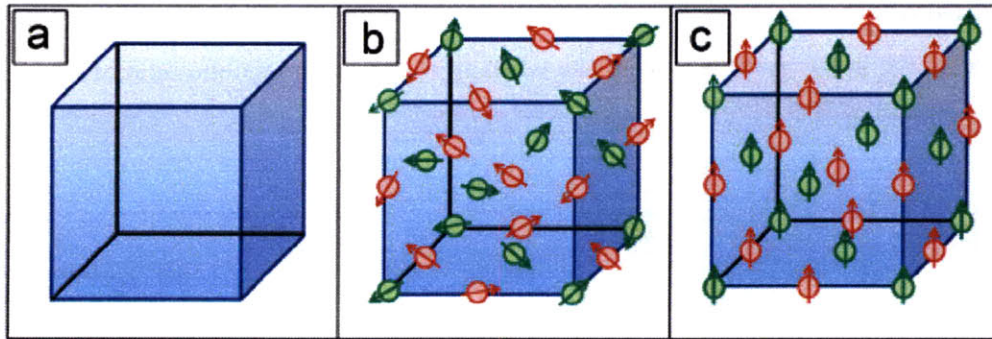


**Figure 1.1** Diagram represents the arrangement of atomic dipole in (a) diamagnetic, (b) paramagnetic and (c) ferromagnetic materials.

Diamagnetism, which is intrinsic to most materials, is dominant in materials without unpaired electrons (Figure 1.1a). Examples of diamagnetic materials are gold, water, and argon.<sup>1</sup> The second class is paramagnetic materials. These materials include atoms with unpaired electrons, but there is no coupling between these spins (Figure 1.1b). Paramagnetic materials in nature include aluminum, titanium, and oxygen.<sup>1</sup> The third class of magnetic properties is ferromagnetic materials. These materials have atoms with unpaired electrons, and all of their spins are coupled and aligned in parallel fashion (Figure 1.1c). As a result, these materials have permanent magnetic moments. Examples of ferromagnetic materials include iron and cobalt.<sup>1</sup>

The differences in magnetic response to magnetic field of these materials are significant. As shown in Figure 1.2, behaviors and degrees of response to amagnetic field of these three classes of materials are readily observed. In diamagnetic materials (Figure

1.2a), very small repulsions in response to an external magnetic field are observed. The volumetric magnetic susceptibility,  $\chi$ , of these materials falls in the range of  $-10^{-6}$  to  $-10^{-3}$ .<sup>2</sup> This repulsion force comes from the induced magnetic field from orbiting electrons of opposite direction to the applied magnetic field.<sup>1</sup> In contrast, paramagnetic materials show a small attraction response to the applied magnetic field (Figure 1.2b). This response is in the range of 10 times higher than the response of diamagnetic materials in opposite direction. Magnetic susceptibility,  $\chi$ , of these materials falls in the range of  $10^{-6}$  to  $10^{-1}$ .<sup>2</sup> For ferromagnetic materials (Figure 1.c), strong attractions to an applied magnetic field, at the range of 100 times higher than paramagnetic case, are observed. Also, there will be some permanent magnetic moment after removal of the magnetic field, as shown in the hysteresis response when applied to the magnetic field of the opposite direction.

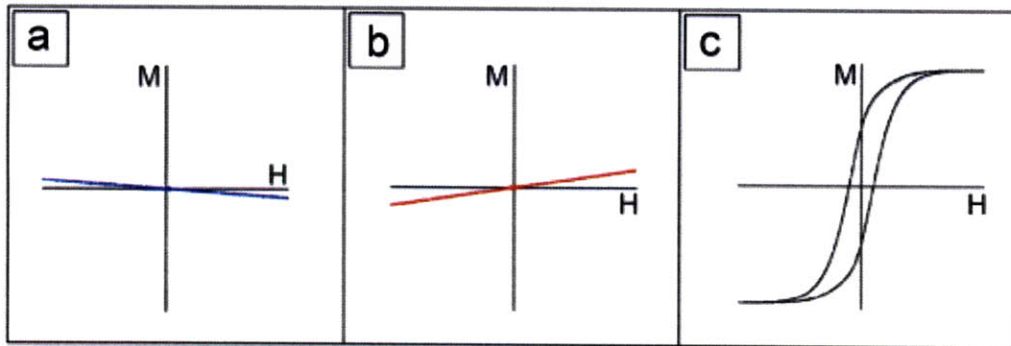


**Figure 1.2** Magnetic responses of (a) diamagnetic, (b) paramagnetic and (c) ferromagnetic materials to magnetic field (H).

There are two more special cases of ferromagnetism: ferrimagnetism and antiferromagnetism. Ferrimagnetic materials, such as in magnetite and maghemite iron oxides,<sup>3</sup> possess unpaired electrons, and these unpaired electrons are all coupled. In contrast to the case with ferromagnetism, these couplings have some anti-parallel arrangement and cause some subtraction of the overall magnetic moment. However, their magnetic responses are still high and similar to the magnetic response of ferromagnetism (Figure 1.2c). Antiferromagnetic materials, such as hematite ( $\alpha$ -Fe<sub>2</sub>O<sub>3</sub>) and

chromium,<sup>1</sup> possess atoms with unpaired electrons, and these unpaired electron are all coupled in anti-parallel arrangements, resulting in no net magnetic moment.

Conventionally, magnetic materials in general terms mean the materials with a permanent magnetic moment. For this reason, only ferromagnetic and ferrimagnetic materials are referred to as magnetic materials.

## **1.2 Magnetic nanoparticles and superparamagnetic properties**

When these ferromagnetic and ferrimagnetic materials become nanoparticles, ranging in size from a few nanometers to tens of nanometers, special magnetic behaviors are observed. Sufficiently small magnetic nanoparticles (MPs) in this size regime exist as single-domain magnets,<sup>4</sup> in which each MP has a constant magnetic moment, which can be reoriented in an applied field.

However, with a little thermal energy from a low temperature, the orientational stability of the magnetic moment in these small MPs begins to be perturbed. With this thermal energy, the magnetic moment of each MP can constantly switch its orientation and balance out. As a result, on the macroscopic scale, there is no net magnetization of the MPs observed in absence of applied magnetic fields.<sup>5</sup> Therefore, in the absence of a magnetic field, paramagnetic-like characters are observed for the MPs. The interesting character of these materials on the nanoscale is that in the presence of an applied magnetic field, the MPs are readily and strongly attracted to the magnetic field because of the reorientation of each MP. The behavior of switching between paramagnetic-like in the absence of an applied magnetic field and ferromagnetic in the presence of a magnetic field of the MPs is called superparamagnetism.<sup>2,4,5</sup> Superparamagnetic response to an external field is shown in Figure 1.3b in comparison with paramagnetic (Figure 1.3a) and ferromagnetic (Figure 1.3c) responses. Another magnetic response of the superparamagnetic material observed in Figure 1.3 is that there is no hysteresis loop in Figure 1.3b. This response indicates that after removal of an applied magnetic field, there is no net magnetization, and the MPs switch back to the paramagnetic-like behavior.<sup>5</sup>



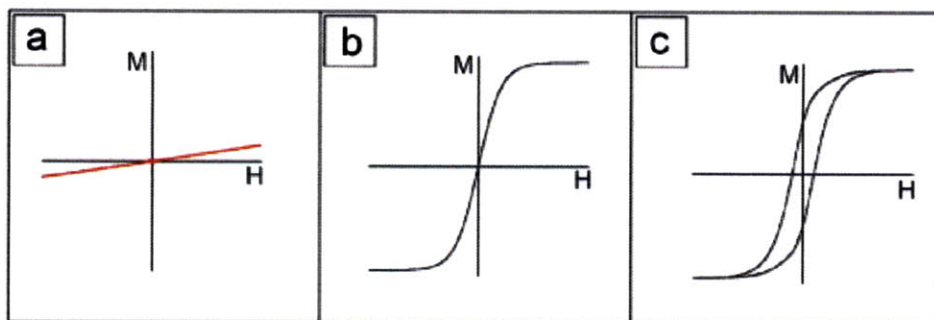


**Figure 1.3** Magnetic responses of (a) paramagnetic, (b) superparamagnetic and (c) ferromagnetic materials to an external magnetic field.

As mentioned above, this superparamagnetic character comes from the fact that a magnetic moment of each MP can be readily flipped to the opposite direction at a certain temperature so that the thermal energy is enough to overcome an energy barrier. This energy barrier, which comes from the magnetocrystalline and shape anisotropy of the materials,<sup>2</sup> is directly proportional to the volume of the particles. In large ferromagnetic particles, the change in the magnetic moment direction cannot take place as thermal energy is lower than the energy barrier. In contrast, in nanoparticles with small volumes, this energy is so small that the thermal energy from the environment can cause the rapid flipping back and forth of the magnetic moment, leading to superparamagnetism.

The temperature at which the thermal energy overcomes the energy barrier is called the blocking temperature ( $T_B$ ).<sup>2,3</sup> The blocking temperature is also identified by the temperature at which the transition from ferromagnetic at a low temperature to superparamagnetic at a high temperature takes place. As implied above,  $T_B$  increases directly proportional to the volume of the particle. Small superparamagnetic MPs with low  $T_B$  are much less susceptible to aggregation than larger ones. The  $T_B$  of MPs can be measured by the zero field-cooled experiment, in which changes of the magnetic moment of the particles at very low magnetic field from a very low temperature to a high temperature were measured. This zero field-cooled experiment is discussed in more detail in Chapters 2 and 3.



### **1.3 Biological applications of magnetic nanoparticles**

The superparamagnetic character of the magnetic nanoparticles leads to their applications in biological systems. Superparamagnetic MPs can be colloidally stable as there is no net magnetic moment and magnetic coupling between particles.<sup>5</sup> At the same time, the intrinsic ferromagnetic character of the materials leads to the high magnetic moment of these nanoparticles. These colloidal MPs are expected to generate a magnetic field and be readily attracted to an external magnetic field when applied in biological systems, resulting in various applications.

The sizes of the MPs also make them suitable for biological applications. The MPs are smaller than cells, which are normally 10-100 microns, and can possibly enter into these biological systems.<sup>2</sup> Moreover, the sizes of the MPs are in the same size range of biomolecules such as proteins (5-50 nm) and genes (2 nm wide and 10-100 nm long).<sup>2</sup> The comparable sizes of MPs and these biomolecules reduce steric hindrance for the interaction or conjugation between the MPs and these biological entities.

Because of the properties mentioned above, the MPs have been used for various biological applications.<sup>2,5-7</sup> Three main applications are discussed below.

#### **1.3.1 Magnetic attraction**

There are many biological applications that use the properties of high magnetic moment yet colloidal behavior of the superparamagnetic MPs. In these applications, MPs are in different structures including in the form of individual MPs and in the form of magnetic microspheres synthesized using incorporation of MP into microspheres of micron sizes. These MPs are conjugated to proteins and other bio-molecules, and the conjugates are directed to specific sites by means of their strong magnetic attraction to the magnetic field. The biological applications using this mechanism include magnetic separation, drug targeting, and magnetofection.<sup>2, 5, 7, 8</sup>

In magnetic separation, the bio-molecules are separated from their environment by a two-step process.<sup>2, 7, 9</sup> First, the molecules of interest are tagged by the MPs through specific interactions. Then, an external magnetic field is applied to separate out the MPs along with the molecules. This process can be useful in concentrating the samples of proteins and bio-molecules for further analysis and other uses.

Targeted drug deliveries are applications that use the MPs as drug carriers or include MPs in the drug carrier systems.<sup>9</sup> The superparamagnetic carriers loaded with drugs are then targeted to specific organs or tissues using a guide from an external magnetic field. Applying the MPs to the drug carrier systems results in more site-specific delivery of drug and reduces the side effects of certain medicines.

Magnetofection is a technique invented and named by Plank and Bergemann.<sup>8</sup> This technique is used to enhance the yield of the transfection process. This process is done by attaching nucleic acids to the MPs, and it uses an applied magnetic field to locally concentrate the MPs as well as the attached nucleic acid around the cells.

### **1.3.2 Hyperthermia**

Hyperthermia treatment is one of approaches in treating cancerous tissues. Increase of local temperature to 41°C to 46°C can stimulate the immune response to cancer in non-specific immunotherapy, and in the temperature range of 46°C up to 56°C, thermoablation takes place and tumors are destroyed.<sup>10</sup>

Heating of the local environment using superparamagnetic MPs is a well-established approach. The heating process is done by induction of superparamagnetic MPs using an alternating current (AC) magnetic field. In this mechanism, the heat comes from the relaxation of the particle moment to its equilibrium orientation (Néel relaxation) and the rotation of magnetic particles within a carrier liquid (brown relaxation).<sup>10</sup>

In the process for hyperthermia treatment of cancer, the MPs are injected into bodies and led or targeted to accumulate at the tumors. Upon application of the alternate magnetic field to the superparamagnetic MPs, heat is dissipated due to the relaxation processes mentioned above. Local heat is then enough to destroy the tumors.

### **1.3.3 Magnetic resonance imaging**

Magnetic resonance imaging (MRI) is a useful technique in the visualization of deep tissue and sensitive organs. MRI operates with the same principle as in nuclear magnetic resonance (NMR) spectroscopy. In these experiments, a magnetic field  $B_0$  is applied to excited protons in molecules of interest; in the case of MRI, the protons are mostly from water and fat in bodies. The protons will align their magnetic moment along

the  $B_0$ . For MRI, another magnetic field perpendicular to  $B_0$  is then applied to the system and the protons are resonantly excited to the excited state, or they align perpendicular to  $B_0$ . After removal of the second magnetic field, the protons relax back to the lower energy state. The relaxation is divided into two components. The moments along the  $z$  axis or along  $B_0$  relax through longitudinal relaxation or spin-lattice relaxation. The relaxation time is called T1 relaxation. The magnetic moment along the  $xy$  plane will relax as transverse relaxation, which is spin-spin relaxation or outer sphere relaxation. The relaxation time for the transverse relaxation is termed T2. The T2 relaxation comes from the loss of magnetic field homogeneity around the protons.

In the presence of superparamagnetic MPs around the protons, the magnetic field from the MPs strongly affects the homogeneity of the magnetic field around the protons. As a result, the T2 in presence of superparamagnetic MPs ( $T2^*$ ) is significantly shorter than the T2 in the absence of these MPs. Since MR images are based on signals from protons, in the presence of superparamagnetic MPs, the proton signals are fewer and darker images are obtained.

For these reasons, superparamagnetic MPs can act as T2 contrast agents to enhance the difference between protons that are around and affected by the magnetic field fluctuation from the MPs and the protons further away. Areas of the protons close to the MPs appear darker than the protons from the areas inaccessible by the MPs in the MR images.<sup>11</sup>

The abilities of the MPs to act as good contrast agents are compared by their T2 relaxivity ( $R2$ ), which is calculated from the inversion of T2 per mol of iron in the sample. The higher the  $R2$ , the shorter the T2 of the protons obtained. The MPs with high  $R2$  value are considered good T2 contrast agents.

#### **1.4 Semiconductor quantum dots and their biological applications**

Semiconductor nanocrystals or quantum dots (QDs) are used as fluorophores in this thesis. These semiconductors are so small that the valence band and conduction band are not fully formed as in the bulk semiconductors. Instead, the electron transition energy levels of these QDs consist of a series of discrete states similar to that of atoms. Absorption and emission wavelengths of the QDs can be controlled by their size. Increase

in the size of QDs results in decrease of band gap energy, and emission and absorption peaks shift to the red. As examples in Figure 1.4, CdSe/CdZnS core/shell QDs with green emission (Figure 1.4a) are smaller than the QDs with emission in red (Figure 1.4b).

In comparison to organic fluorescent dyes, QDs are better fluorophores in terms of high photostability toward photo bleaching, continuous absorption spectra, and large two-photon absorption cross-sections for two-photon microscopy. Moreover, QDs can give narrow emission bandwidths and their emissions can be tuned by controlling the size of the QDs. The properties of continuous absorption spectra and narrow and tunable emissions are shown in Figures 1.4c and d.

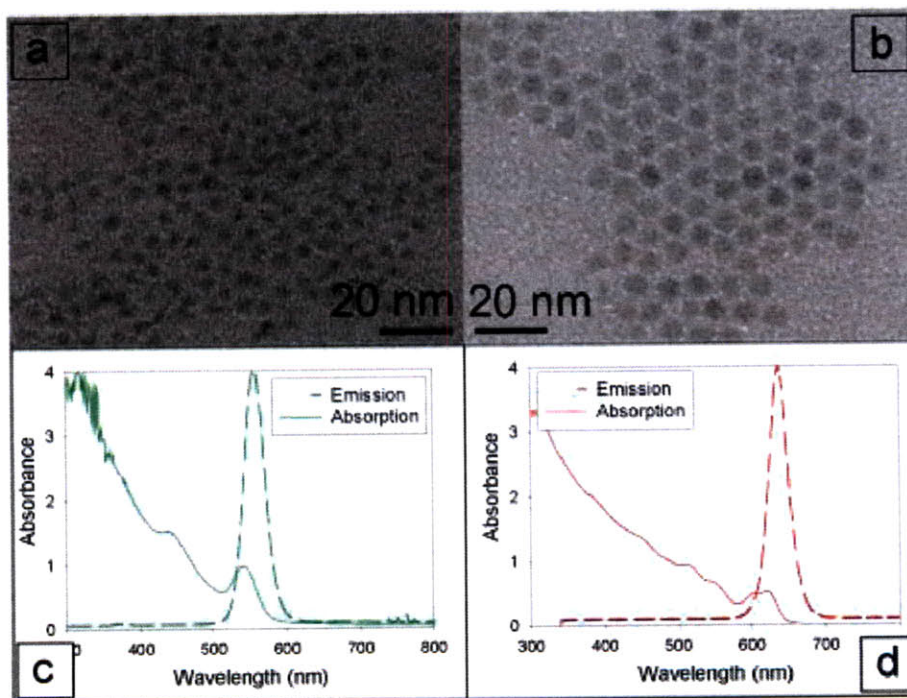


**Figure 1.4** (a-b) TEM images of CdSe/CdZnS QDs with green (a) and red (b) emission, (c-d) absorption and emission spectra of the QDs above.

The QDs used in this thesis are mainly CdSe/CdZnS core/shell QDs. These QDs were prepared by a two-step procedure developed in our group.<sup>12</sup> The CdSe cores were prepared by injection of cadmium and selenium precursors in a high temperature solution of coordinating solvents of trioctylphosphine (TOP), trioctylphosphine oxide (TOPO),

and hexadecylamide (HDA). The CdSe cores were overcoated with a CdZnS shell to ensure the photostability. In order to use these hydrophobic QDs, surface modifications of different procedures were employed. These surface modifications will be discussed in the following chapters.

QDs have been used in many applications in biological systems. These applications include multiplex imaging,<sup>13, 14</sup> cell targeting and labeling,<sup>15, 16</sup> and sensing through fluorescent resonance energy transfer (FRET).<sup>17</sup> More biological applications of the QDs are under development.

### **1.5 Thesis Overview**

In this thesis, superparamagnetic nanoparticles of iron oxides-based are the main focus. Syntheses and characterizations of the iron oxides MPs and other magnetic nanoparticles are discussed in Chapter 2. Iron oxides MPs of high crystallinity, high magnetization and narrow size distribution were synthesized with hydrophobic oleic acid as their native ligand. Surface modifications of these MPs were studied for transforming these MPs into useful materials for biological applications. The subsequent chapters discuss various procedures of surface modifications.

Chapter 3 discusses the modification of MPs with alkoxy silane groups and their incorporation into silica microspheres along with QDs. The resulted silica microspheres incorporating MPs and QDs are multi-functional materials as they are superparamagnetic, fluorescent materials with active surface for further functionalization. The demonstrations for potential applications of these microspheres are also discussed.

Chapter 4 discusses the modification of MPs using a reverse-micro-emulsion process in order to coat them with a silica shell. The silica-coated MPs are transferrable into more hydrophilic and water-based solvent systems. They are also studied as a building block for more complex nanostructures comprising MPs, QDs, and silica, which are similar in function to the microspheres in Chapter 2 but smaller in the size range.

Chapters 5 and 6 focus on surface modifications of MPs for transferring the MPs into water-based solutions. The amphiphilic polymer discussed in Chapter 5 modifies the MPs surface by forming micellar structures on the MPs. Chapter 6 discusses the application of water-soluble catechol derivatives directly onto the MPs by means of

replacing the native oleic acid ligand. The water-soluble MPs from surface modifications discussed in these chapters are small in their hydrodynamic size and possess functional groups for further conjugations.

Chapter 7 studies conjugation chemistries of the functional hydrophilic MPs from Chapters 5 and 6. One goal of these studies is to conjugate MPs with QDs through chemical bonding and aim at forming nanostructures comprising MPs and QDs. These nanostructures are proposed to be the smallest possible systems that can function as both superparamagnetic and fluorescent materials.

From these surface modifications, MPs, nanostructures, and microspheres with different functionality were obtained. These materials are suitable tools for many applications in biological systems. We hope that the advent of these materials can take part in finding some answers to prevention and treatment of diseases and better understanding some biological systems.

## 1.6 References

1. Klabunde, K. J., *Nanoscale Materials in Chemistry*. John Wiley & Sons, Inc.: 2001.
2. Pankhurst, Q. A.; Connolly, J.; Jones, S. K.; Dobson, J., Applications of magnetic nanoparticles in biomedicine. *Journal of Physics D-Applied Physics* **2003**, 36, (13), R167-R181.
3. Jun, Y. W.; Seo, J. W.; Cheon, A., Nanoscaling laws of magnetic nanoparticles and their applicabilities in biomedical sciences. *Accounts of Chemical Research* **2008**, 41, (2), 179-189.
4. Krishnan, K. M.; Pakhomov, A. B.; Bao, Y.; Blomqvist, P.; Chun, Y.; Gonzales, M.; Griffin, K.; Ji, X.; Roberts, B. K., Nanomagnetism and spin electronics: materials, microstructure and novel properties. *Journal of Materials Science* **2006**, 41, (3), 793-815.
5. Berry, C. C.; Curtis, A. S. G., Functionalisation of magnetic nanoparticles for applications in biomedicine. *Journal of Physics D-Applied Physics* **2003**, 36, (13), R198-R206.
6. Tartaj, P.; Morales, M. D.; Veintemillas-Verdaguer, S.; Gonzalez-Carreño, T.; Serna, C. J., The preparation of magnetic nanoparticles for applications in biomedicine. *Journal of Physics D-Applied Physics* **2003**, 36, (13), R182-R197.
7. Safarik, I.; Safarikova, M., Magnetic nanoparticles and biosciences. *Monatshefte Fur Chemie* **2002**, 133, (6), 737-759.

8. Scherer, F.; Anton, M.; Schillinger, U.; Henkel, J.; Bergemann, C.; Kruger, A.; Gansbacher, B.; Plank, C., Magnetofection: enhancing and targeting gene delivery by magnetic force in vitro and in vivo. *Gene Therapy* **2002**, 9, (2), 102-109.
9. Corchero, J.; Villaverde, A., Biomedical applications of distally controlled magnetic nanoparticles. *Trends in Biotechnology* **2009**, 27, (8), 468-476.
10. Mornet, S.; Vasseur, S.; Grasset, F.; Duguet, E., Magnetic nanoparticle design for medical diagnosis and therapy. *Journal of Materials Chemistry* **2004**, 14, (14), 2161-2175.
11. Weinstein, J. S.; Varallyay, C. G.; Dosa, E.; Gahramanov, S.; Hamilton, B.; Rooney, W. D.; Muldoon, L. L.; Neuwelt, E. A., Superparamagnetic iron oxide nanoparticles: diagnostic magnetic resonance imaging and potential therapeutic applications in neurooncology and central nervous system inflammatory pathologies, a review. *Journal of Cerebral Blood Flow and Metabolism* 30, (1), 15-35.
12. Fisher, B. R.; Eisler, H. J.; Stott, N. E.; Bawendi, M. G., Emission intensity dependence and single-exponential behavior in single colloidal quantum dot fluorescence lifetimes. *Journal of Physical Chemistry B* **2004**, 108, (1), 143-148.
13. Han, M. Y.; Gao, X. H.; Su, J. Z.; Nie, S., Quantum-dot-tagged microbeads for multiplexed optical coding of biomolecules. *Nature Biotechnology* **2001**, 19, (7), 631-635.
14. Chan, Y.; Zimmer, J. P.; Stroh, M.; Steckel, J. S.; Jain, R. K.; Bawendi, M. G., Incorporation of luminescent nanocrystals into monodisperse core-shell silica microspheres. *Advanced Materials* **2004**, 16, (23-24), 2092-+.
15. Liu, W.; Howarth, M.; Greytak, A. B.; Zheng, Y.; Nocera, D. G.; Ting, A. Y.; Bawendi, M. G., Compact biocompatible quantum dots functionalized for cellular imaging. *Journal of the American Chemical Society* **2008**, 130, (4), 1274-1284.
16. Howarth, M.; Liu, W. H.; Puthenveetil, S.; Zheng, Y.; Marshall, L. F.; Schmidt, M. M.; Wittrup, K. D.; Bawendi, M. G.; Ting, A. Y., Monovalent, reduced-size quantum dots for imaging receptors on living cells. *Nature Methods* **2008**, 5, (5), 397-399.
17. Snee, P. T.; Somers, R. C.; Nair, G.; Zimmer, J. P.; Bawendi, M. G.; Nocera, D. G., A ratiometric CdSe/ZnS nanocrystal pH sensor. *Journal of the American Chemical Society* **2006**, 128, (41), 13320-13321.





## **Chapter 2**

### **Magnetic Nanoparticles: Synthesis and Characterization**

#### **2.1 Introduction**

Magnetic nanoparticles (MPs) are useful in a variety of applications, and there are many procedures to prepare them based on the quality and quantity needed for each application.<sup>1,2</sup> For large quantity production, the mechanical processes<sup>3,4</sup> might be the most suitable method for preparation of MPs. However, in terms of quality, this “top-down” process for making MPs normally yields particles of large size distribution.<sup>3,4</sup> Syntheses of magnetic nanoparticles in the gas phase such as spray pyrolysis usually yield particles of irregular size distribution.<sup>5</sup>

Chemical syntheses or “bottom-up” processes in general yield MPs of higher quality, smaller size, and narrow size distribution of the MPs.<sup>1</sup> However, there are some variations in the chemical synthesis between the process in water-based solution and the one in high-boiling-point solvent. The MPs formed in water-based syntheses are usually lower in crystallinity and broader in size distribution as the nucleation and crystallization were performed at low temperature.<sup>1,6</sup> For this chapter, the procedures used for synthesizing the MPs are based on the solvothermal process, which is known for yielding MPs of high crystallinity, high magnetization, and narrow size distribution.<sup>1,7</sup> Discussion of the synthesis of iron oxides MPs and MPs of other materials occurs in the following sections.

#### **2.2 Iron oxides nanoparticles**

As mentioned in Chapter 1, iron oxides MPs are some of the most interesting magnetic nanoparticles for biological applications. One of the reasons why iron oxides are preferable is the known biocompatibility of the use of iron oxides. Iron is less harmful compared to other metals, and the mechanisms by which the body excretes the excess iron are well studied.<sup>8</sup>

Among the six known structures of iron oxides, magnetite ( $\text{Fe}_3\text{O}_4$ ) and maghemite ( $\gamma\text{-Fe}_2\text{O}_3$ ) are the more useful iron oxides for biological applications as both of them are

ferrimagnetic materials and become superparamagnetic when they are in nanoparticle forms.<sup>9</sup> Both magnetite and maghemite are similar in their crystal structures. The structure of magnetite is an inverse spinel while maghemite is a defect spinel.<sup>9</sup> Also, in term of magnetization, magnetite is a little higher in magnetization, but the fully oxidized maghemite is superior in terms of stability toward oxidization.

Maghemite and its partially reduced counterpart magnetite,  $\text{Fe}_3\text{O}_4$ , have been prepared with various methods, including solution and aerosol methods. Solution methods include coprecipitation of ferrous and ferric ion from basic solution,<sup>10</sup> the so-called “polyol process,”<sup>1</sup> and high temperature decomposition of an organometallic precursor.<sup>1</sup> An aerosol process is the rapid and high throughput production of MPs by spray pyrolysis.<sup>1</sup> The size distribution of MPs obtained from solution processes is generally more monodispersed than that obtained through an aerosol method; therefore the former methods are preferred for biological applications. Hence, this work employs a solution approach in order to prepare monodispersed iron oxides MPs.

### **2.2.1 Synthesis and characterization of iron oxides nanoparticles**

As mentioned earlier for the syntheses of magnetic nanoparticles, a method of high-temperature decomposition of organometallic precursors was used. This method was reported to yield a narrow size distribution and good crystallinity, with less aggregation of MPs than achieved with an aqueous route. Pentacarbonyliron(0) is widely used as an iron precursor in the presence of surfactants such as oleic acid or stearic acid.<sup>11, 12</sup> With this method, monodisperse MPs 3 to 25 nm in diameter can be produced.

MPs were synthesized by a two-step process modified from the literature.<sup>7, 11, 12</sup> First,  $\text{Fe}(\text{CO})_5$  was slowly heated to 275°C in dioctylether in the presence of oleic acid in an inert atmosphere, leading to the decomposition of  $\text{Fe}(\text{CO})_5$ , and nucleation and growth of low-crystallinity nanoparticles composed of iron nanoparticles. These Fe nanoparticles were readily oxidized when exposed to air. Wüstite ( $\text{FeO}$ ) and maghemite phases were usually detected when the nanoparticles at this step were taken out of the air-free condition. Next, the nanoparticles were fully oxidized using a mild oxidizing agent, trimethylamine *N*-oxide, yielding MPs. The scheme for this process is shown in Figure 2.1.

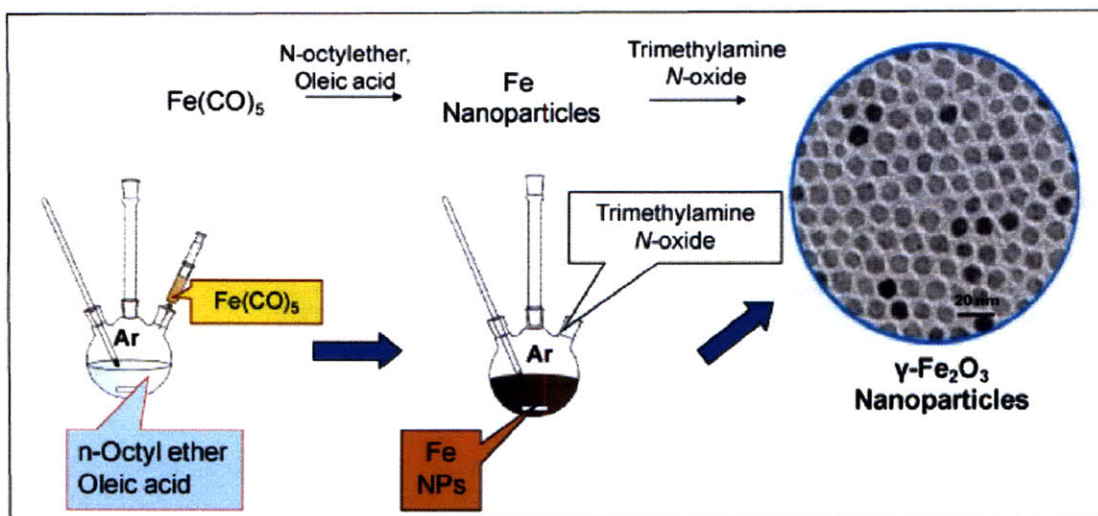


**Figure 2.1** Reaction scheme for the synthesis of the iron oxide MPs.

*Detailed experiments:*

The  $\gamma\text{-Fe}_2\text{O}_3$  or maghemite magnetic nanoparticles (MPs) were prepared using a method modified from the literature.<sup>7, 11, 12</sup> This modified process was published in print.<sup>13</sup> For example, in the synthesis of 7-nm MPs, in an inert atmosphere, 400  $\mu\text{L}$  of  $\text{Fe}(\text{CO})_5$  were injected into a solution of 2 mL of oleic acid in 20 mL of dioctyl ether at 100  $^\circ\text{C}$ . While the solution was stirred, the temperature of the reaction mixture was increased at a rate of 2  $^\circ\text{C}$  per minute to a final temperature of 275  $^\circ\text{C}$ , at which it was held constant for 1.5 hours. At this temperature, the size of the MPs can be increased by increasing the refluxing time. After the solution was cooled to room temperature, the intermediate nanoparticles were oxidized upon addition of 0.30 g of  $(\text{CH}_3)_3\text{NO}$ . The reaction mixture was heated to 130  $^\circ\text{C}$  for two hours and was then quickly heated to 275  $^\circ\text{C}$  stirred at this temperature for 15 minutes. After cooling, the MPs were separated from the reaction mixture by adding ethanol to precipitate them. After centrifuging, the supernatant, comprising excess oleic acid and octylether, was discarded; the MPs were then redispersed and kept in hexanes. The 7-nm MPs from this procedure were imaged using Transmission Electron Microscopy (TEM) as shown in Figure 2.1. All the chemicals in this process were purchased from Sigma-Aldrich and used without further purification.

The MP particle size was varied by varying the molar ratio of  $\text{Fe}(\text{CO})_5$  to oleic acid and the duration of heating at  $275\text{ }^\circ\text{C}$  prior to addition of  $(\text{CH}_3)_3\text{NO}$ . For example, when the growth time was varied, the size of the MPs could be tuned from 5-18 nm in diameter, as shown in Figure 2.2.

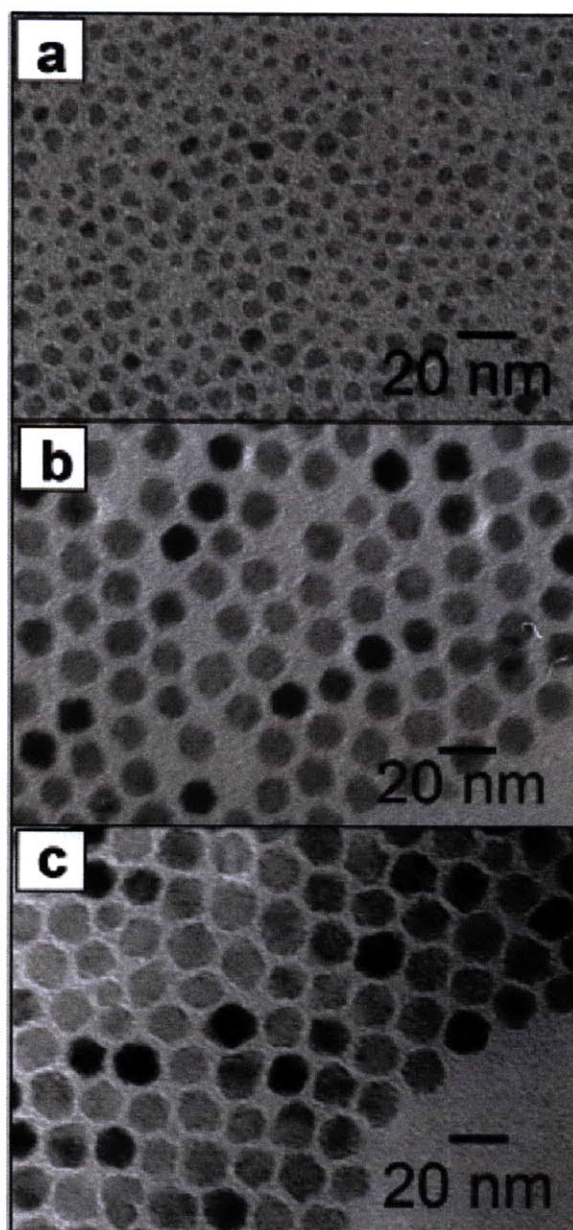


**Figure 2.2** TEM images of MPs of different sizes as controlled by reaction time (a) 60 min, (b) 120 min, (c) 180 min.

In order to identify the structure of the MPs synthesized from this process, X-ray diffraction (XRD) analysis and X-ray photoelectron spectroscopy (XPS) were employed. The XRD pattern of a sample of MPs is shown in Figure 2.3.

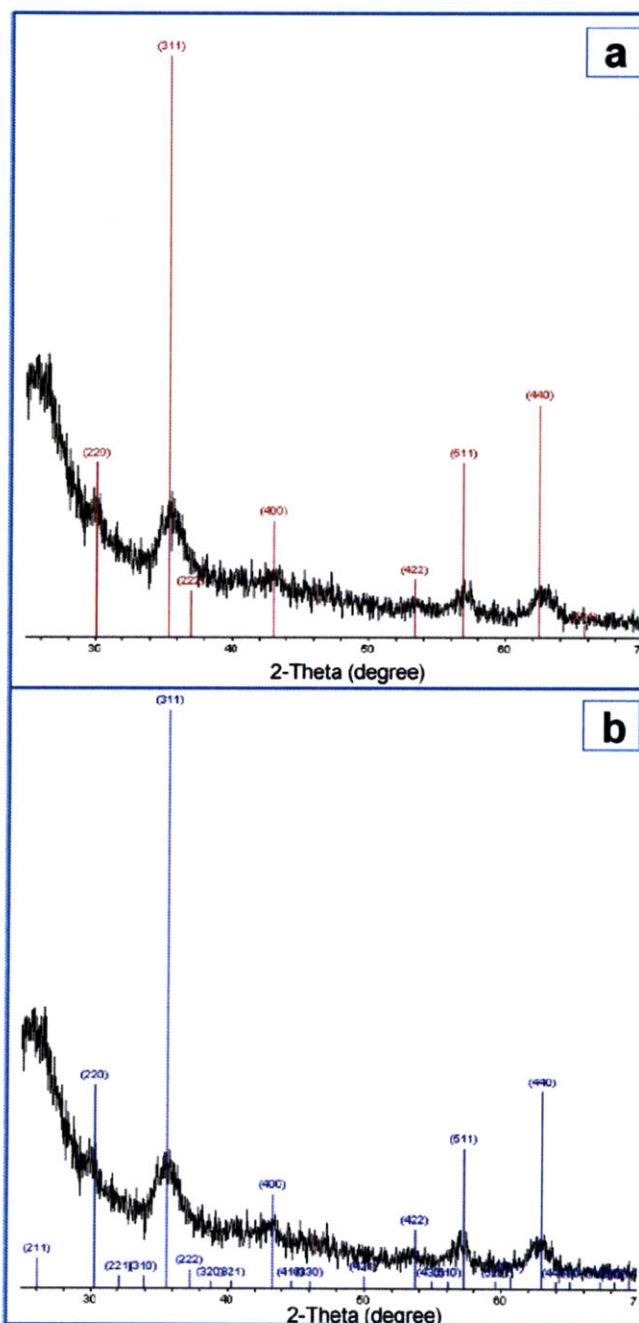


**Figure 2.3** XRD patterns of the as-synthesized MPs compared to (a) magnetite (PDF# PDF#00-019-0629) and (b) maghemite (PDF#00-039-1346).

The XRD pattern of the resulted MPs indicated that the crystalline phases of the nanoparticles are observed. As seen from the XRD pattern, most of the peaks of the MPs are closed to the patterns of both magnetite (Figure 2.3a) and maghemite (Figure 2.3b) phases. As mentioned earlier with regard to the similarity in the structures of maghemite and magnetite, the XRD patterns of maghemite and magnetite are too close to be distinguished, especially when the patterns are broad. XRD cannot exactly indentify the phase of iron oxides of these MPs. From viewing the XRD pattern, it can be concluded only that the MPs are crystalline and can be either maghemite or magnetite.

In order to indentify the phase of MPs more specifically, an X-ray photoelectron spectroscopy was used. In this technique, core electrons of atoms are excited by x-ray and simultaneously the binding energy and number of excited electrons are measured. Core electron lines of ferrous and ferric ions can be detected and distinguished from each other. In this case, the responsive core electrons are Fe 2p electrons. The XPS spectra of a representative sample of MPs are shown in Figure 2.4a in comparison with XPS spectra of standard maghemite and magnetite previously reported, as shown in Figure 2.4b.<sup>7</sup>

The binding energy of 710 eV from Fe 2p<sub>3/2</sub> and 723 eV from Fe 2p<sub>1/2</sub> observed from the XPS spectra of the MPs are close to that reported for the maghemite phase. Moreover, the shoulder between these two peaks was reported to be a characteristic feature observed in maghemite. Both the position and shape of the XPS spectra of the MPs matched better with that of maghemite than magnetite. Therefore, it can be concluded that the main phase of iron oxide synthesized using the discussed procedure is maghemite, or  $\gamma\text{-Fe}_2\text{O}_3$ .



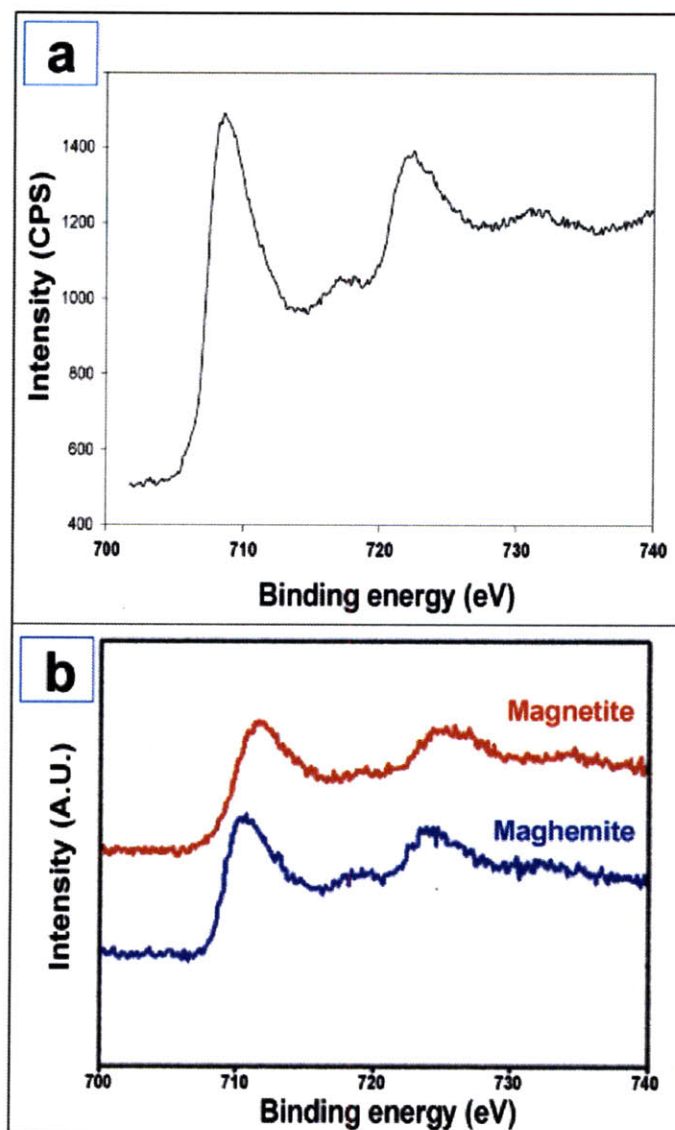


**Figure 2.4** XPS spectra for Fe 2p of the as-synthesized MPs (a) compared to previously reported XPS spectra of magnetite and maghemite.<sup>7</sup>

### 2.2.2 Magnetic properties of iron oxide nanoparticles

The magnetic properties of the MPs were studied using a superconducting quantum interference device (SQUID, Quantum Design MPMS-5S). In these measurement, MPs were dispersed in poly(laurylmethacrylate) cross-linked with ethyleneglycol dimethacrylate polymer in order to avoid dipolar coupling between MPs and facilitate the handling of samples.<sup>14</sup> There are two magnetic characters that were measured by SQUID, saturation magnetization and the blocking temperature of the MPs.

The saturation magnetization of the MPs was measured at 5K as shown by a plot of magnetization versus magnetic field in Figure 2.5. The saturation magnetization of these 7-nm MPs is  $\sim 87$  emu/g of Fe, which is lower than that reported for bulk maghemite.<sup>15</sup> The lower values in the magnetization of the nanoparticles are mainly due to size<sup>16</sup> and ligand effects<sup>17</sup> when the materials reach nanometer-size range. However, this value of saturation is on the high side when compared to MPs synthesizing with other methods.<sup>18</sup> This high value of magnetization resulted from the high crystallinity of the MPs obtained.

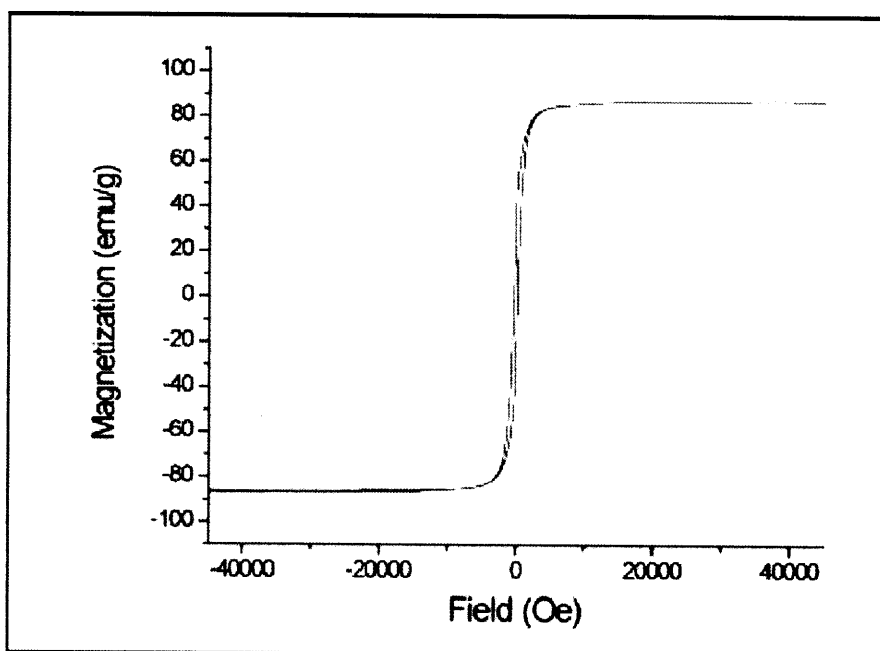


**Figure 2.5** Saturation magnetization of the iron oxide MPs.

From the shape of the hysteresis loop of the MPs in Figure 2.5, it was observed that the MPs were still ferrimagnetic at 5K. As mentioned in Chapter 1, one character of superparamagnetism is that there is no coercivity when the magnetic field is switched and hysteresis should be observed. The MPs become superparamagnetic above the blocking temperature, which depends on the size of the MPs.

The blocking temperature ( $T_B$ ) of 7-13-nm MPs can be determined by measuring the temperature-dependent magnetization in a small field after a sample is cooled down in a zero field to low temperature (as in zero-field-cooled, or ZFC, experiment). In this



experiment, the highest magnetization occurs at the  $T_B$ , at which the MP sample changes from ferromagnetic to superparamagnetic. As shown in Figure 2.6, ZFC experiments revealed that MPs of this size range are superparamagnetic at room temperature, and the blocking temperature ( $T_B$ ) increases with the size of the MPs. Moreover, if we extrapolate the data in Figure 2.6, the largest size of the MPs that can still exhibit superparamagnetism at room temperature is around 30 nm. Therefore, for most of applications in biological systems, the MPs used should be smaller than 30 nm.

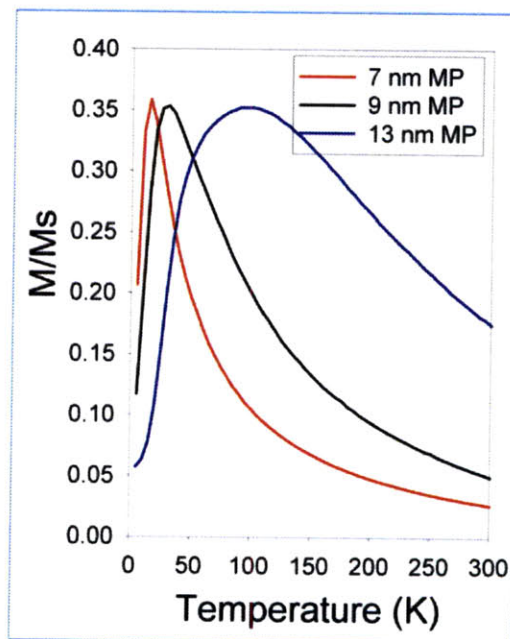


**Figure 2.6** Zero-field-cooled magnetization versus temperature measured in a 100 Oe field of MPs with different sizes.

On the macroscopic scale, the magnetic response of the MPs dispersed in hexane also exhibits superparamagnetic behavior. The demonstration of their superparamagnetism was performed using an application of a permanent magnet with strong magnetic field to the MP dispersion as shown in Figure 2.7. In the absence of an external magnetic field, MPs in their superparamagnetic states have no net magnetic moment and can freely disperse in hexane without magnetic coupling to and aggregation with each other. As shown in Figure 2.7a. When a magnet approached, the magnetic

moment of each nanoparticle was readily aligned and the MPs were readily attracted to the magnetic field as shown in Figure 2.7b. This strong attraction originates from the intrinsic ferromagnetic property of the MPs. After the magnet was removed, the MPs readily re-dispersed and behaved as if they were paramagnetic materials again.

From these syntheses and characterization of the iron oxide MPs, these MPs appear to be of high quality and superparamagnetic character. With these properties, the MPs from this procedure are suitable for various applications.

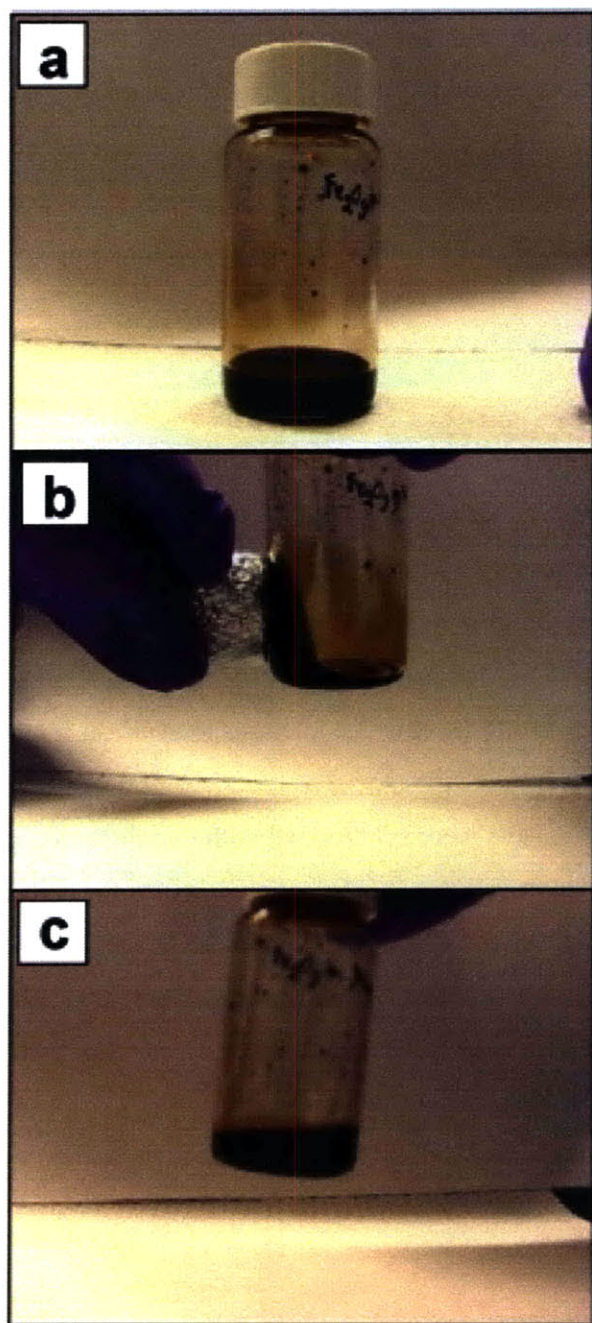


**Figure 2.7** Photographs of the macroscopic response of the MPs in presence (b) and absence (a) of external magnetic field, and (c) when the MPs re-dispersed after removal of the magnet.

## 2.3 Other magnetic nanoparticles

Other than iron oxides, other magnetic materials were synthesized and characterized. This section discusses manganese ferrite, cobalt ferrite, and iron-platinum alloy nanoparticles. The chemical and magnetic properties of these nanoparticles differ from those of iron oxides and are possibly more suitable for some applications than the iron oxide MPs.

### 2.3.1 Manganese ferrite

The interest in manganese ferrite ( $\text{MnFe}_2\text{O}_4$ , in the ideal case) nanoparticles came from the calculation made using bulk materials that these materials are some ten percent higher in their magnetization than iron oxides.<sup>19</sup> Therefore, these MPs should be stronger in magnetic attraction and higher in their T2 relaxivity. In the case of *in vivo* applications, a lower dose of MPs can be used while the same results can be obtained, which is very beneficial. For these reasons, attempts to synthesize manganese ferrite MPs were pursued.

Manganese ferrite MPs were synthesized with two different approaches modified from previously reported procedures.<sup>20, 21</sup> Reaction schemes for both approaches are shown in Figure 2.8. For the first approach, manganese ferrite MPs were prepared from decomposition of  $\text{Fe}(\text{CO})_5$  and  $\text{Mn}_2(\text{CO})_{10}$  in presence of oleic acid in octylether.<sup>20</sup> In the second approach, manganese ferrite MPs were synthesized from iron acetylacetonate ( $\text{Fe}(\text{acac})_3$ ) and manganese acetylacetonate ( $\text{Mn}(\text{acac})_2$ ) using oleic acid and oleylamine as co-surfactants in benzyl ether.<sup>21</sup> TEM images of the manganese ferrite MPs from both approaches are shown in Figure 2.9a and 2.9b.

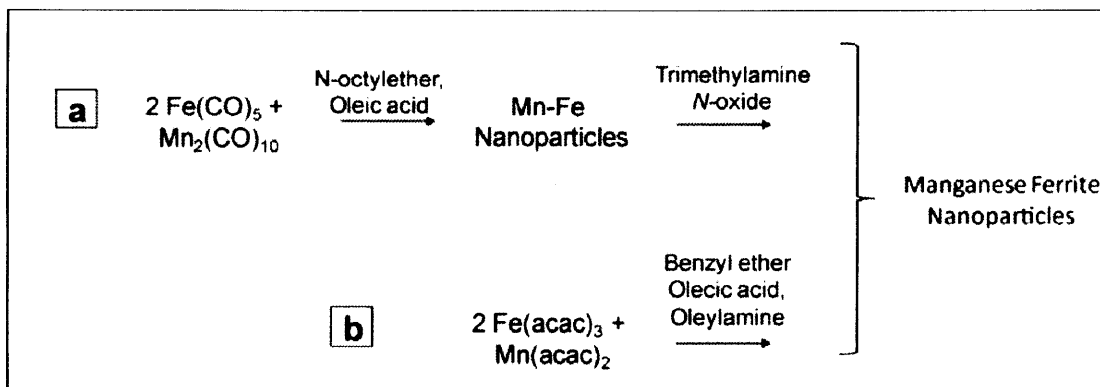


**Figure 2.8** Two reaction schemes for preparation of manganese ferrite nanoparticles.

Manganese ferrite MPs from the two approaches differ in their size distributions and chemical compositions. The TEM images indicate that controlling of the size of the MPs using the first approach is better as the resulting MPs were more monodispersed (Figure 2.9a). The chemical compositions of the MPs also differ from the ideal  $\text{MnFe}_2\text{O}_4$ . Inductively coupled plasma-optical emission spectroscopy (ICP-OES) elemental analysis indicates that the molar ratio of Mn:Fe is 1:2.6 in the MPs from the first approach and 1:4.6 in the MPs from the second approach. Moreover, from characterization using the SQUID magnetometer, the saturation magnetization of both manganese ferrite MPs is lower than expected and lower than the iron oxide MPs synthesized using the method discussed in the previous section.

The difficulty in controlling the manganese-to-iron ratio prevented this type of MPs from being useful at the moment. Reproducibility of composition ratio needs to be maintained as the magnetization depends on this factor. However, with the possibility of high magnetization, manganese ferrite MPs could find their way into biological applications.

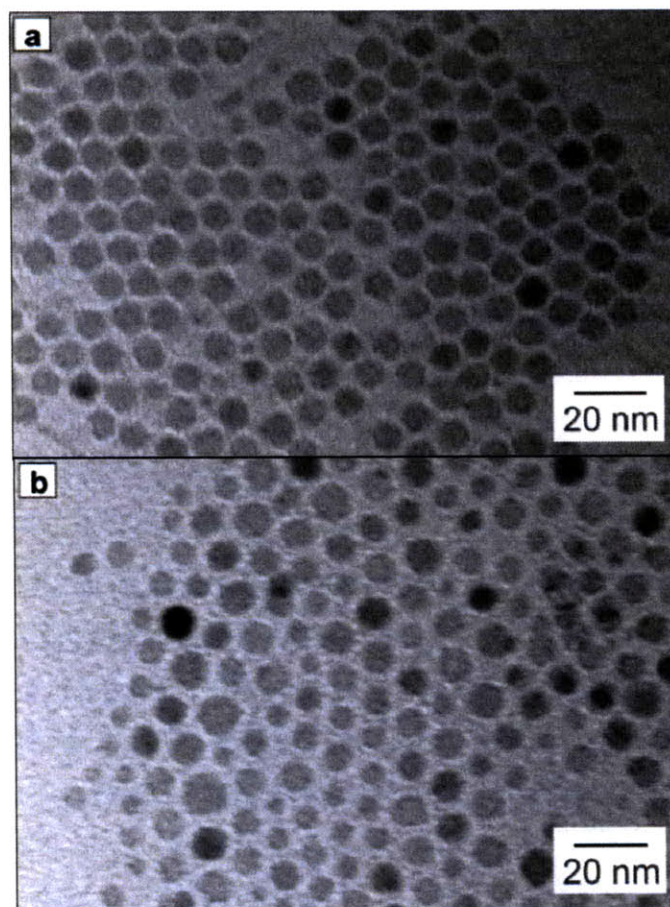


**Figure 2.9** TEM images of manganese ferrite nanoparticles of two different reactions: (a) nanoparticles from carbonyl complex precursors and (b) nanoparticles from acetylacetonate salt precursors.

### 2.3.2 Cobalt ferrite nanoparticles

Cobalt ferrite is another ferrimagnetic material that could be useful for some applications. Even though the saturation magnetization of cobalt ferrite is calculated to be lower than that of magnetite and manganese ferrite,<sup>19</sup> the high coercivity of this material can be more useful in some applications. The synthesis and magnetic character of cobalt ferrite MPs are discussed below.

Synthesis of cobalt ferrite nanoparticles was performed by the process reported previously by Sun et al.<sup>22</sup> In this process,  $\text{Co}(\text{acac})_2$  and  $\text{Fe}(\text{acac})_3$  in a 1:2 molar ratio were used as starting materials. Oleic acid and oleylamine were used as surfactants, and



benzyl ether was a solvent. TEM image of the resulted cobalt ferrite nanoparticles are shown in Figure 2.10.

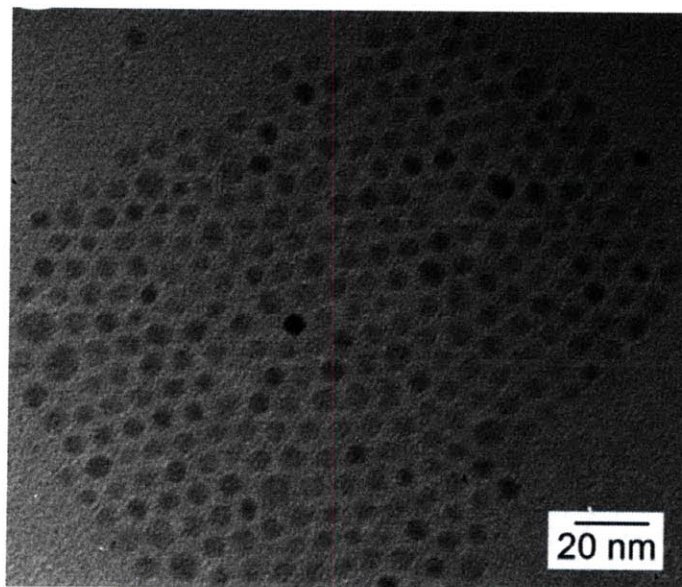


**Figure 2.10** TEM image of cobalt ferrite nanoparticles

The magnetic properties of the resulting cobalt ferrite nanoparticles were studied by using a SQUID magnetometer. Changes of magnetizations in different magnetic field of the cobalt ferrite nanoparticles at 5K are shown in comparison with those of the iron oxide MPs discussed in an earlier section in Figure 2.11. From Figure 2.11, it can be observed that the saturation magnetization of this sample of cobalt ferrite nanoparticles was some twenty percent lower than that of iron oxide MPs. More interestingly, significantly high coercivity of cobalt ferrite nanoparticles was observed from their hysteresis loop. This large hysteresis loop is due to the higher magnetocrystalline anisotropy of cobalt ferrite nanoparticles compared to iron oxide MPs. This large hysteresis loop feature of the cobalt ferrite nanoparticles can be useful when these particles are applied in such biological applications as magnetically-induced hyperthermia for cancer treatment.<sup>22</sup> In those applications, heat that dissipates from the hysteresis loss of cobalt ferrite nanoparticles is proposed to be higher than that of other MPs discussed earlier.

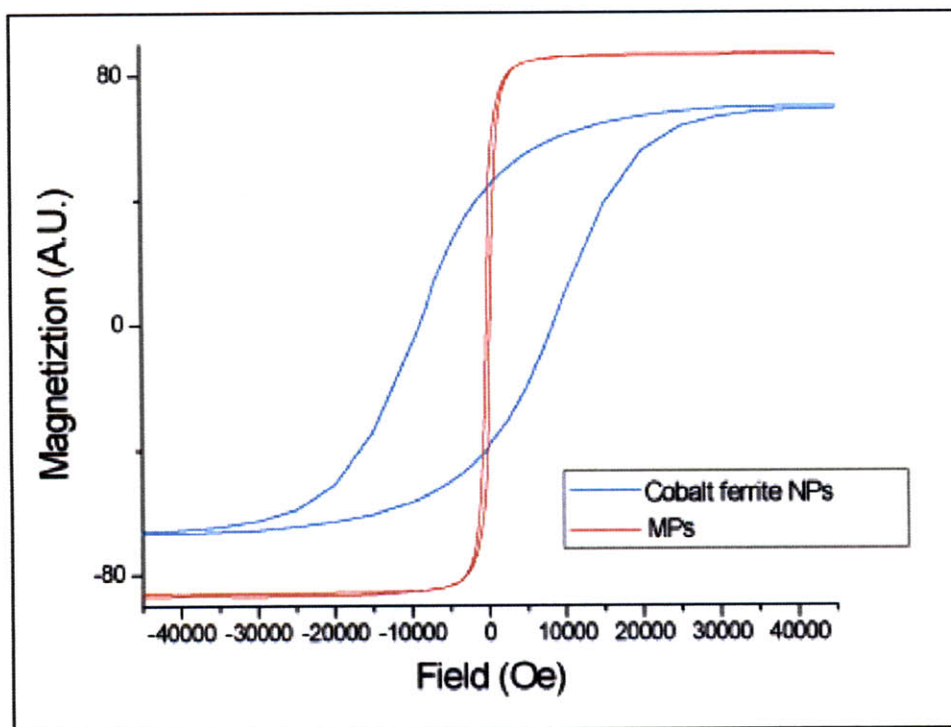


**Figure 2.11** Saturation magnetization of the cobalt ferrite nanoparticles (blue line) compared to that of iron oxide MPs (red line).

Cobalt ferrite nanoparticles synthesized using this procedure are potentially useful in some applications even though their magnetization is lower than the other ferrite MPs discussed earlier. However, certain surface modifications needed to be studied to transfer these hydrophobic cobalt ferrite nanoparticles into biological environments.

### 2.3.3 Iron Platinum Alloy Nanoparticles

Iron platinum alloy (FePt) nanoparticles are another class of magnetic materials that can be synthesized in the nanoparticle-size range. Depending on the ratio of the alloy, the magnetization of FePt nanoparticles can be high and stable.<sup>23</sup> Synthesis of FePt nanoparticles was done following the previously reported procedure by Chen et al.<sup>24</sup> In this procedure, FePt nanoparticles were synthesized using  $\text{Fe}(\text{CO})_5$  and  $\text{Pt}(\text{acac})_2$  as starting materials. The same molar ratio of oleic acid and oleylamine was used as



surfactants and benzyl ether was used as a solvent. The resulting FePt nanoparticles were imaged by TEM as shown in Figure 2.12.

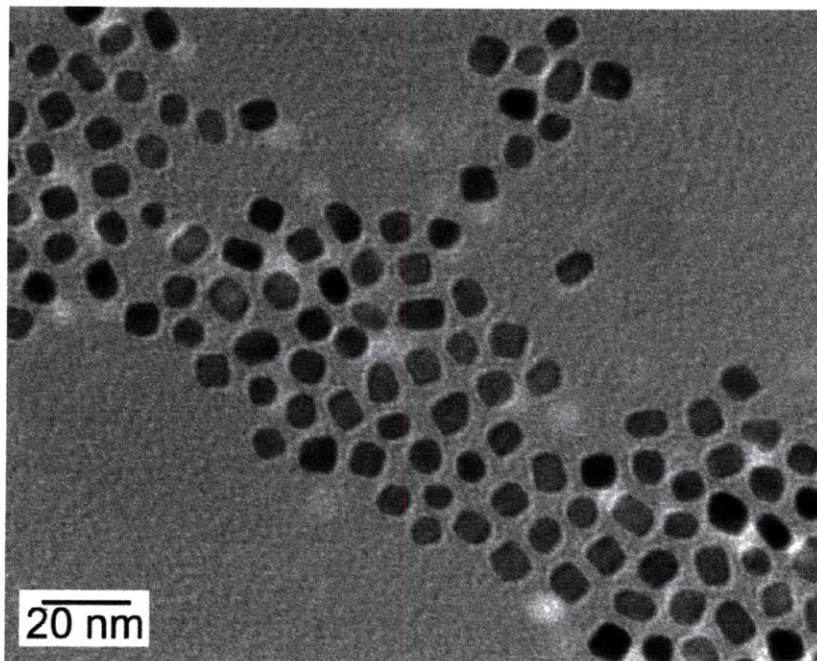


**Figure 2.12** TEM image of iron platinum alloy nanoparticles.

These FePt nanoparticles are of our interest because their surface chemistry is different of those oxides MPs discussed earlier. Platinum on their surface is likely active to different ligand systems from other MPs and could be useful for some surface modification technique. The surface modification of the FePt nanoparticles is of interest but beyond the scope of this thesis.

## **2.4 Conclusion**

This chapter discusses the syntheses of magnetic nanoparticles of different chemical composition. Each magnetic nanoparticle has its unique properties and could be suitable for different applications. However, given that this work aims at biological applications, iron oxides MPs are the most suitable as they have fewer toxicity concerns compared to cobalt and manganese ferrites. Therefore, the rest of this thesis focuses mainly on the surface modifications and reactions of the iron oxide MPs.

Iron oxide MPs of high crystallinity, high magnetization, controllable size, and narrow size distribution were synthesized using the procedure discussed earlier. These properties of the MPs are suitable and can be made as useful tools in various biological applications. However, the MPs synthesized using this method are hydrophobic as they have oleic acid as their native ligands. In order for these MPs to be transferrable into biological systems and become useful for biological applications, certain surface modifications need to be performed.

The following chapters discuss different processes of surface modifications on the MPs. Chapter 3 discusses the modification of MPs for incorporation into silica microspheres along with quantum dots (QDs) for making silica microspheres with superparamagnetic and fluorescent properties. Surface modification of MPs using a silica coating process is the main focus for Chapter 4. Chapters 5 and 6 cover the surface modifications of MPs with amphiphilic polymers and catechol derivative surfactants, respectively, in order to become water dispersible, stable in physiological environment, small in hydrodynamic size, and functional for biological applications. The last chapter discusses studies of QDs-conjugation chemistries of MPs with functionalized surfaces.

## 2.5 References

1. Tartaj, P.; Morales, M. D.; Veintemillas-Verdaguer, S.; Gonzalez-Carreno, T.; Serna, C. J., The preparation of magnetic nanoparticles for applications in biomedicine. *Journal of Physics D-Applied Physics* **2003**, 36, (13), R182-R197.
2. Willard, M. A.; Kurihara, L. K.; Carpenter, E. E.; Calvin, S.; Harris, V. G., Chemically prepared magnetic nanoparticles. *International Materials Reviews* **2004**, 49, (3-4), 125-170.
3. Alcala, M. D.; Criado, J. M.; Real, C.; Grygar, T.; Nejezchleba, M.; Subrt, J.; Petrovsky, E., Synthesis of nanocrystalline magnetite by mechanical alloying of iron and hematite. *Journal of Materials Science* **2004**, 39, (7), 2365-2370.
4. Sepelak, V.; Bergmann, I.; Feldhoff, A.; Heitjans, P.; Krumeich, F.; Menzel, D.; Litterst, F. J.; Campbell, S. J.; Becker, K. D., Nanocrystalline nickel ferrite, NiFe<sub>2</sub>O<sub>4</sub>: Mechanosynthesis, nonequilibrium cation distribution, canted spin arrangement, and magnetic behavior. *Journal of Physical Chemistry C* **2007**, 111, (13), 5026-5033.

5. Gonzalezcarreno, T.; Morales, M. P.; Gracia, M.; Serna, C. J., Preparation of Uniform Gamma-Fe<sub>2</sub>O<sub>3</sub> Particles with Nanometer-Size by Spray-Pyrolysis. *Materials Letters* **1993**, 18, (3), 151-155.
6. Sugimoto, T.; Matijevic, E., Formation of Uniform Spherical Magnetite Particles by Crystallization from Ferrous Hydroxide Gels. *Journal of Colloid and Interface Science* **1980**, 74, (1), 227-243.
7. Teng, X. W.; Yang, H., Effects of surfactants and synthetic conditions on the sizes and self-assembly of monodisperse iron oxide nanoparticles. *Journal of Materials Chemistry* **2004**, 14, (4), 774-779.
8. Gupta, A. K.; Gupta, M., Synthesis and surface engineering of iron oxide nanoparticles for biomedical applications. *Biomaterials* **2005**, 26, (18), 3995-4021.
9. Jun, Y. W.; Seo, J. W.; Cheon, A., Nanoscaling laws of magnetic nanoparticles and their applicabilities in biomedical sciences. *Accounts of Chemical Research* **2008**, 41, (2), 179-189.
10. Jeong, J. R.; Shin, S. C.; Lee, S. J.; Kim, J. D., Magnetic properties of superparamagnetic gamma-Fe<sub>2</sub>O<sub>3</sub> nanoparticles prepared by coprecipitation technique. *Journal of Magnetism and Magnetic Materials* **2005**, 286, 5-9.
11. Hyeon, T.; Lee, S. S.; Park, J.; Chung, Y.; Bin Na, H., Synthesis of highly crystalline and monodisperse maghemite nanocrystallites without a size-selection process. *Journal of the American Chemical Society* **2001**, 123, (51), 12798-12801.
12. Woo, K.; Hong, J.; Choi, S.; Lee, H. W.; Ahn, J. P.; Kim, C. S.; Lee, S. W., Easy synthesis and magnetic properties of iron oxide nanoparticles. *Chemistry of Materials* **2004**, 16, (14), 2814-2818.
13. Insin, N.; Tracy, J. B.; Lee, H.; Zimmer, J. P.; Westervelt, R. M.; Bawendi, M. G., Incorporation of iron oxide nanoparticles and quantum dots into silica microspheres. *ACS Nano* **2008**, 2, (2), 197-202.
14. Tracy, J. B.; Weiss, D. N.; Dinega, D. P.; Bawendi, M. G., Exchange biasing and magnetic properties of partially and fully oxidized colloidal cobalt nanoparticles. *Physical Review B* **2005**, 72, (6), 8.
15. Tepper, T.; Ross, C. A., Pulsed laser deposition of iron oxide films. *Journal of Applied Physics* **2002**, 91, (7), 4453-4456.
16. Berkowitz, A. E.; Schuele, W. J.; Flanders, P. J., Influence of Crystallite Size on Magnetic Properties of Acicular Gamma-Fe<sub>2</sub>O<sub>3</sub> Particles. *Journal of Applied Physics* **1968**, 39, (2), 1261-1263.

17. Berkowitz, A. E.; Lahut, J. A.; Jacobs, I. S.; Levinson, L. M.; Forester, D. W., Spin Pinning at Ferrite-Organic Interfaces. *Physical Review Letters* **1975**, *34*, (10), 594-597.
18. Na, H. B.; Song, I. C.; Hyeon, T., Inorganic Nanoparticles for MRI Contrast Agents. *Advanced Materials* **2009**, *21*, (21), 2133-2148.
19. Lee, J. H.; Huh, Y. M.; Jun, Y.; Seo, J.; Jang, J.; Song, H. T.; Kim, S.; Cho, E. J.; Yoon, H. G.; Suh, J. S.; Cheon, J., Artificially engineered magnetic nanoparticles for ultra-sensitive molecular imaging. *Nature Medicine* **2007**, *13*, (1), 95-99.
20. Kang, E.; Park, J.; Hwang, Y.; Kang, M.; Park, J. G.; Hyeon, T., Direct synthesis of highly crystalline and monodisperse manganese ferrite nanocrystals. *Journal of Physical Chemistry B* **2004**, *108*, (37), 13932-13935.
21. Zeng, H.; Rice, P. M.; Wang, S. X.; Sun, S. H., Shape-controlled synthesis and shape-induced texture of MnFe<sub>2</sub>O<sub>4</sub> nanoparticles. *Journal of the American Chemical Society* **2004**, *126*, 11458-11459.
22. Pankhurst, Q. A.; Connolly, J.; Jones, S. K.; Dobson, J., Applications of magnetic nanoparticles in biomedicine. *Journal of Physics D-Applied Physics* **2003**, *36*, (13), R167-R181.
23. Sun, S. H., Recent advances in chemical synthesis, self-assembly, and applications of FePt nanoparticles. *Advanced Materials* **2006**, *18*, (4), 393-403.
24. Chen, M.; Liu, J. P.; Sun, S. H., One-step synthesis of FePt nanoparticles with tunable size. *Journal of the American Chemical Society* **2004**, *126*, (27), 8394-8395.

## Chapter 3

### Surface Modification of Iron Oxide Nanoparticles with Silanes: Formation of Magnetic and Fluorescent Silica Microspheres\*

#### 3.1 Introduction

Iron oxide magnetic nanoparticles (MPs), which were synthesized and discussed in Chapter 2, can be very useful materials after certain surface modifications are performed. The first surface modification of these hydrophobic iron oxide MPs occurs to make the surface of the MPs suitable for reaction with silica precursors. The goal of this process of surface modifications is to make magnetic silica microspheres containing MPs and semiconducting quantum dots (QDs).

Magnetic silica microspheres gain many interest in biomedical and environmental research applications.<sup>1</sup> Applications of these magnetic microspheres include bio-separation, drug targeting, cell isolation, enzyme immobilization, protein purification, and wastewater treatment.<sup>2-4</sup> Among the various types of matrices for the magnetic microspheres, silica microspheres have superior properties in that they have high stability and biocompatibility.<sup>2, 5, 6</sup> Moreover, silica microspheres can be readily modified using commercially available silane coupling reagents, yielding microspheres of a wide range of functional groups.<sup>6</sup> For these reasons, magnetic silica microspheres have been widely synthesized by many techniques, such as layer-by-layer self-assembly,<sup>2</sup> the Stöber process,<sup>7</sup> ferrite plating,<sup>8</sup> aerosol pyrolysis,<sup>9</sup> and sonochemical deposition.<sup>10</sup>

Incorporating MPs along with chromophores enables additional applications for silica microspheres. These fluorescent and superparamagnetic microspheres can be moved with an external magnetic field while monitoring their real-time movement through their fluorescence.<sup>11, 12</sup> Fluorescent and magnetic microspheres have been previously fabricated by combining magnetic nanoparticles with organic dyes or lanthanide metal complexes.<sup>11, 12</sup> Advantages of using QD as fluorophores, as mentioned earlier in Chapter 1, are their continuous adsorption spectra, narrow emission bandwidths, and large two photon absorption cross-section.<sup>13-15</sup>

---

\*Reproduced in part with permission from *ACS Nano* 2008, 2: 197-202.

Due to the advantages of a system which combines a substantial magnetic moment and luminescence, composite silica microspheres containing both MPs and QDs have attracted great interest.<sup>5, 6, 16, 17</sup> Previous fabrication methods included the use of MPs and QDs as cores followed by the growth of a silica shell,<sup>6, 16</sup> and the inverse suspension method.<sup>5</sup> However, most samples prepared using these methods were polydisperse.<sup>5, 16</sup> Moreover, the numbers of MPs and QDs in each particle within the same sample were not uniform.<sup>5, 6, 16</sup> More recently, magnetic and fluorescent silica microspheres were prepared by using silica-coated MPs as cores, followed by layer-by-layer (LbL) assembly of polyelectrolyte and QDs onto the cores' surfaces, which were then coated with a final silica shell.<sup>17</sup> However, the size-dispersity of the particles was not characterized, and the MP content in each microsphere was limited and uncontrolled. In addition, the technique of polyelectrolyte-assisted QD assembly limited the number of QDs adsorbed onto the cores' surfaces to a monolayer. This technique also used QDs with negatively-charged surfaces prepared with an aqueous method,<sup>18</sup> which was known to yield QDs with lower crystallinity, monodispersity, and fluorescence efficiency than QDs prepared in non-aqueous coordinating solvents using the "hot-injection" technique.<sup>18, 19</sup>

Here we report the synthesis of monodispersed silica microspheres with MPs and QDs both uniformly incorporated, and we demonstrate their practical bifunctionality. Potential applications of these microspheres include monitoring drug delivery and the combination of deep-tissue MRI imaging with high-resolution confocal laser scanning microscopy.

### **3.2 Synthesis of magnetic and fluorescent microspheres**

Our approach is based on previous work in our group,<sup>13</sup> in which QDs were incorporated into silica shells grown on pre-made silica microsphere cores through a sol-gel process. This fabrication method is advantageous because it maintains the monodispersed microsphere size and QD optical properties, and it incorporates the nanoparticles uniformly into the MS shell. We have modified the shell of the microspheres to include not only QDs, but also MPs.

The synthesis of the MP- and QD-incorporated-silica microspheres is divided into two steps. The first step is surface modification of MPs and QDs to functionalize them with methoxysilane groups and make them dispersible into ethanol to render them compatible with the silica-shell-growing process. In the second step, MPs and QDs with silane-coupling active surfaces are incorporated simultaneously with growth of the silica shells on microspheres. Details of each step are discussed in the following sections.

### **3.2.1 Surface modification of MPs and QDs**

Surface modification of the nanoparticles is the most important step in the process of making superparamagnetic and fluorescent microspheres. QDs and MPs must be highly soluble in ethanol and also possess accessible alkoxy silane groups, which polymerize with tetraethoxysilane (TEOS) to form the shell onto silica microspheres. The surface modification scheme of the MPs is shown in Figure 3.1. Surface modification of the QDs with triocylphosphine oxide (TOPO) on their surface was done following the same scheme. In this process, the native hydrophobic surfactants of MPs and QDs were replaced with two new surfactants, 3-aminopropyl-trimethoxysilane (APS) and 5-amino-1-pentanol (AP). APS gave the required alkoxy silane group while AP transferred the nanoparticles into ethanol.

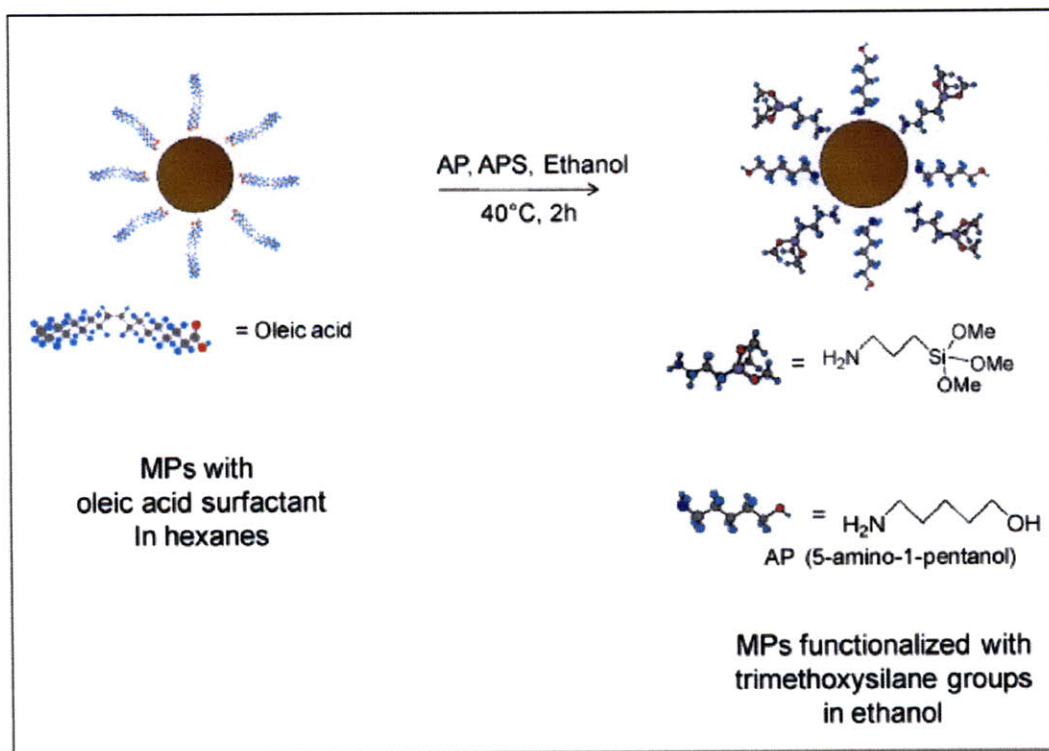


**Figure 3.1** Reaction scheme for the surface modification of the MPs.

*Detailed experiments: Preparation of MP and QD stock solutions in ethanol*

CdSe/ZnS and CdSe/CdZnS core/shell QDs were prepared in a two-step synthesis, similar to our previous work. MPs were synthesized from high temperature decomposition of ironpentacarbonyl in presence of oleic acid as discussed in Chapter 2.

The QD stock solution in ethanol was prepared using a previously reported technique. In a typical procedure, as-synthesized QDs were precipitated twice with a methanol/butanol mixture to remove their native trioctylphosphine oxide (TOPO) caps, and were dried under vacuum. Next, 26 mg of dried QDs were mixed with 195 mg of anhydrous ethanol, 29 mg of 3-aminopropyltrimethoxysilane (APS), and 54 mg of 5-amino-1-pentanol (AP). The mixture was then heated to 40 °C for about 1 h, leading to the formation of a clear solution of QDs.

The MP stock solution in ethanol was prepared by two slightly different procedures. The first procedure was the same as the preparation of QD solution mentioned above, with three times more AP added. The second procedure, more delicate but yielding higher MP content, the MP stock solution in ethanol was prepared using



addition of 12-hydroxydodecanoic acid, sonication, and syringe filtration. For example, the MPs kept in hexanes were precipitated using ethanol to remove their native oleic acid caps, and were then dried under vacuum. Then, 47 mg of dried MPs, 95 mg of 12-hydroxydodecanoic acid, and 1.49 g of ethanol were sonicated for 1 h, yielding a clear solution of MPs. 418 mg of AP and 772 mg of APS were then added to the MP solution, and the mixture was heated to 40 °C for 1 h to ensure cap exchange with AP and APS. The mixture was then filtered through a 20- $\mu\text{m}$  syringe filter, leading to a clear solution of MPs.

### 3.2.2 Incorporation process

After MPs and QDs were surface modified and have suitable surface for silane coupling reaction, the MP and QD incorporation process was done at the same time as growing of silica shell. The scheme for MP and QD incorporation process are shown in Figure 3.2. In this process, the alkoxy silane groups on the nanoparticle surfaces and tetraethoxysilane silica precursor were hydrolyzed upon addition of ammonium hydroxide and water. Then, the silanol groups from both sources are co-condensation resulting in the incorporation of the nanoparticle inside the silica matrix of the newly grown shell. After this sol-gel process was completed, silica microspheres incorporating MPs and QDs were obtained.

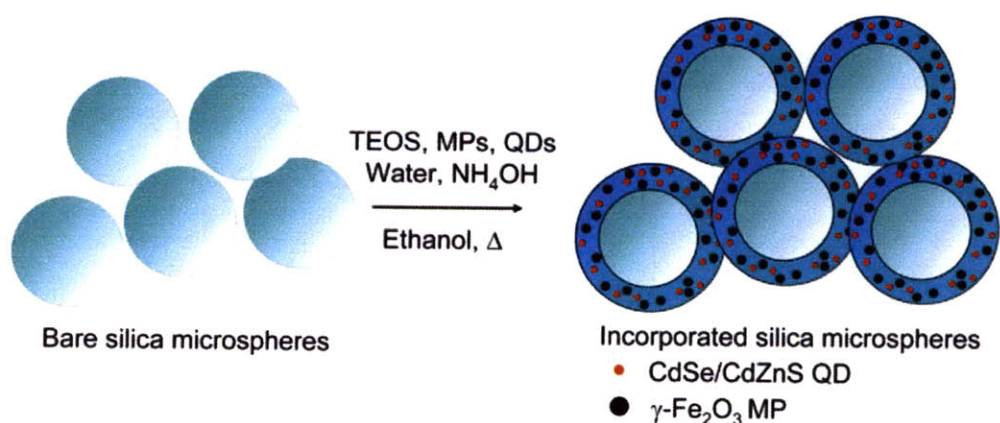


**Figure 3.2** Reaction scheme for the incorporation of silica microspheres.

*Detailed Experiment: Incorporation of QDs and MPs into silica microspheres*

The procedure for incorporating MPs and QDs together into silica microspheres was adapted from Chan et al. In a typical procedure, 30 mg bare silica microspheres and 16 mg of hydroxypropyl cellulose (HPC) were added to 10 mL of ethanol, and this mixture was sonicated for ten minutes. 50-500  $\mu$ L of MP solution and 10  $\mu$ L of QD solution were added into the reaction mixture while vigorously stirring, followed by the addition of 50  $\mu$ L of H<sub>2</sub>O, 50  $\mu$ L of NH<sub>4</sub>OH, and 0.15 mL TEOS. The mixture was stirred in an oil bath at 75 °C for four hours. The silica(core)/silica-MPs-QDs(shell) microspheres were then purified by performing five cycles of centrifuging, discarding the supernatant, and re-dispersing the microspheres in ethanol. The reaction scheme for this process is shown in Figure 3.2.

The resulted microspheres were then characterized using both scanning electron microscopy (SEM) and transmission electron microscopy (TEM) as shown in Figure 3.3. SEM and TEM images show that the morphology of the core microspheres (Figures 3.3a,b) did not change upon the addition of QD- and MP-doped shells (Figures 3.3c,d), but rougher surfaces were observed. The increase in roughness of the microspheres' surface might result in changes in biocompatibility and toxicity of the resulted microspheres compared to the bare ones, which need to be studied before utilizing these microspheres in biological applications. Size distributions (Figures 3.3e,f) measured from TEM images indicated that the incorporation process did not significantly affect the size dispersity of the microspheres. Moreover, the increase in average size of the overcoated microspheres confirmed that the core/shell structure was formed.

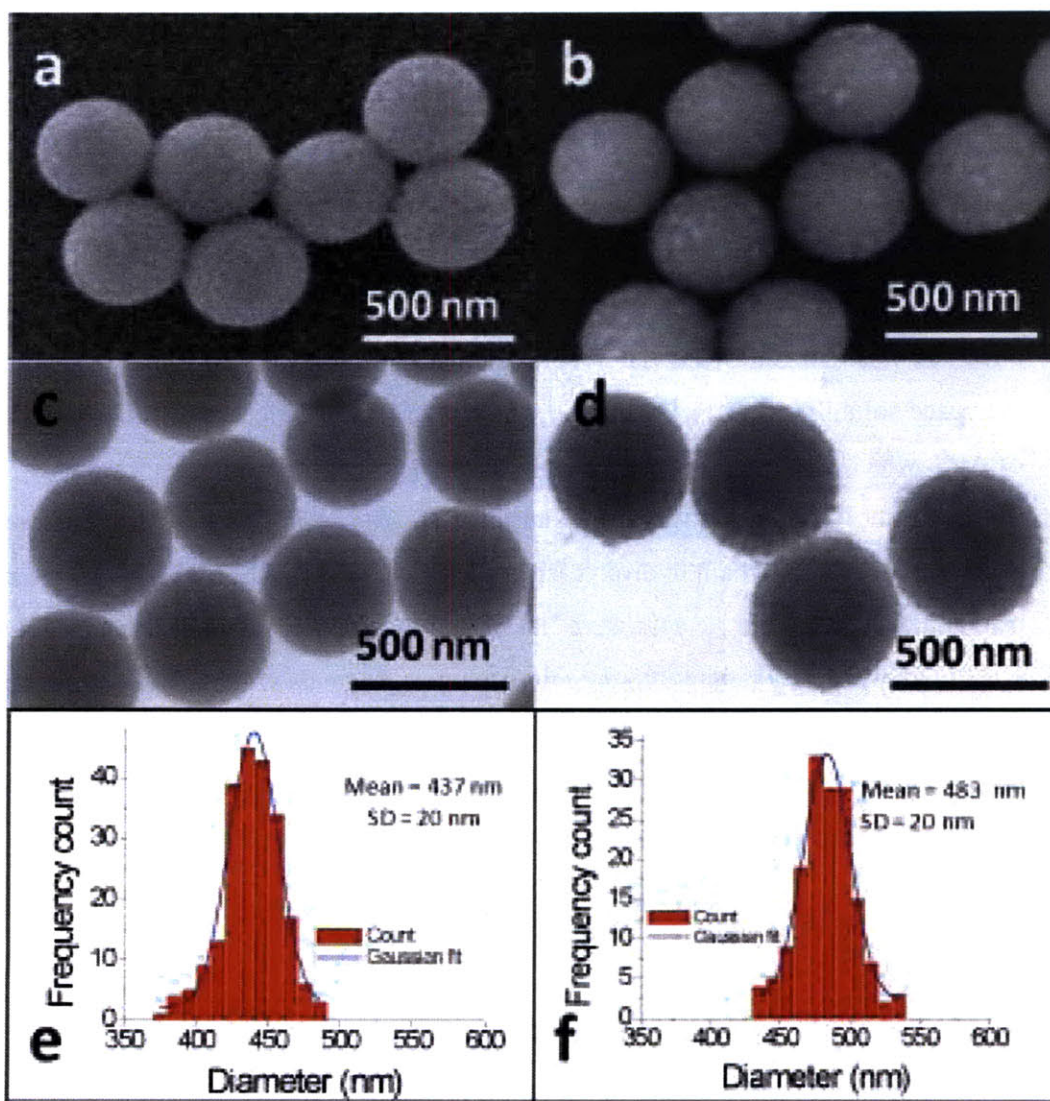


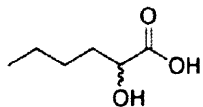
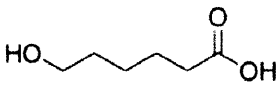
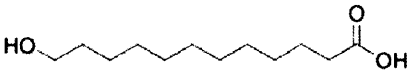

**Figure 3.3** Size distributions of (b-d) 500 nm silica microsphere (Polysciences,  $500 \pm 70$  nm) before incorporation showings (b) SEM image, (c) TEM image, (d) size distribution analysis, and (e-g) 500 nm silica microspheres after incorporation of QDs and MPs (7-nm MP, 12000 MPs per microsphere) showing (e) SEM image (f) TEM image and (g) size distribution analysis.

As noted earlier, the crucial step for incorporating MPs into silica microspheres was the preparation of MP stock solution in ethanol. The MPs' native surfactant, oleic acid or stearic acid, was displaced by 5-amino-1-pentanol (AP) and 3-aminopropyl-trimethoxysilane (APS) in order for the MPs to become ethanol-soluble and

polymerizable with TEOS, respectively. Addition of a small amount of 12-hydroxy-dodecanoic acid (HAD, structure shown in Table 3.1) helped increase the number of MPs incorporated into the microspheres. For instance, in the incorporation of 7-nm MPs into 500-nm microspheres, the MP content was as high as 13000 MPs per microsphere when HDA was added to the MP solution. When no HDDA was added, however, the highest MP content achievable before the aggregation of MPs outside the microspheres was observed was four times less. The improved incorporation was most likely due to the increased solubility of MPs in ethanol, which could reduce the rate of self-condensation of APS, which was probably the reason for MP aggregation outside microspheres.

Other ligand systems that are similar in structure to HDA were also explored. Some shorter carbon chain hydroxycarboxylic acids, such as DL-alpha-hydroxycaproic acid and 6-hydroxycaproic acid were less effective in dispersing MPs into ethanol and yielded a lower MP loading into the microspheres. Ligands with different functional group such as 12-amino-1-dodecanol were also investigated but HDA gave better result in terms of MP dispersibility and loading. Structures and properties of these ligands are shown in Table 3.1.

**Table 3.1** Properties of additional surfactants in dispersion of MPs into ethanol and incorporation of MPs into silica microsphere (MS).

Structure of surfactants	Solubility of MPs in ethanol	Loading of MPs per MS (as calculated from magnetization)
 DL- $\alpha$ -hydroxycaproic acid	Fair	Less than 1000 MPs/MS
 6-hydroxycaproic acid	Good	1500 MPs/MS
 12-hydroxydodecanoic acid (HDA)	Very good	13000 MPs/MS
 12-amino-1-dodecanol (AD)	Fair	Less than 1000 MPs/MS

The numbers of QDs and MPs incorporated in each microsphere were determined by elemental analysis using inductively coupled plasma–optical emission spectroscopy (ICP-OES) performed by Galbraith Laboratories, Inc. For 500-nm microspheres, QDs accounted for  $1.1 \pm 0.3$  % of the total volume, or  $2.0 \pm 1.2$  % of the shell volume, which corresponds to  $4600 \pm 1400$  QDs per microsphere. The highest percent volume of MPs was  $3.9 \pm 1.1$  % of the total volume, or  $7.3 \pm 4.1$  % of the shell. This amount corresponds to  $13000 \pm 3700$  MPs per 500-nm microsphere. Details for this calculation of MP and QD loading in the silica microspheres with the data from ICP are shown in Appendix A.

Microspheres of smaller sizes were also studied to find the limitation of this process. Microspheres of 300 nm and 100 nm in diameter were prepared using the same process. The resulting microspheres were shown in Figure 3.4. The incorporation processed successfully but the loading of the MPs per microsphere decrease significantly. In 300-nm MS, the loading of MPs is 450 MPs/MS, while in the case of 100-nm MS, the loading of the MPs is as low as 45 MPs/MS.



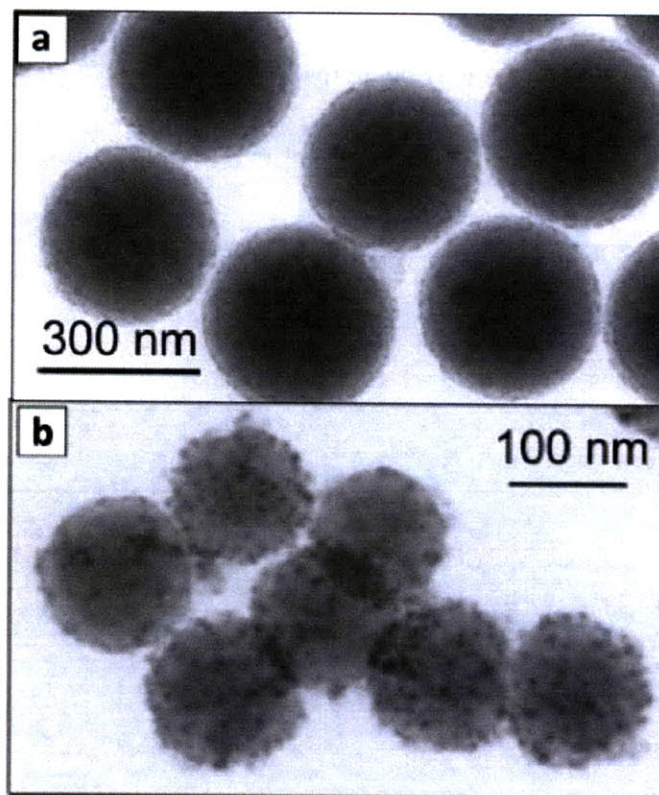


**Figure 3.4** TEM images of MP-incorporating MS with starting MS diameter of (a) 300 nm MS and (b) 100 nm.

For even smaller silica microspheres, such as the 50-nm microspheres as shown in Figure 3.5a, the incorporation process was not successful. Large active surface area of the microspheres of this size range caused a tendency to form cross-linked microspheres as shown in Figure 3.5b when the same equivalent of TEOS silica precursor was used. Several approaches for decrease the cross-linking and overgrowth of silica shells such as decrease the quantity of TEOS, decrease the reaction temperature, and reduce reaction time resulted in microspheres with very low loading such as shown in Figure 3.5c. For this reason, MP and QD-incorporated microspheres of lower than 100 nm in diameter are not obtainable using this process.

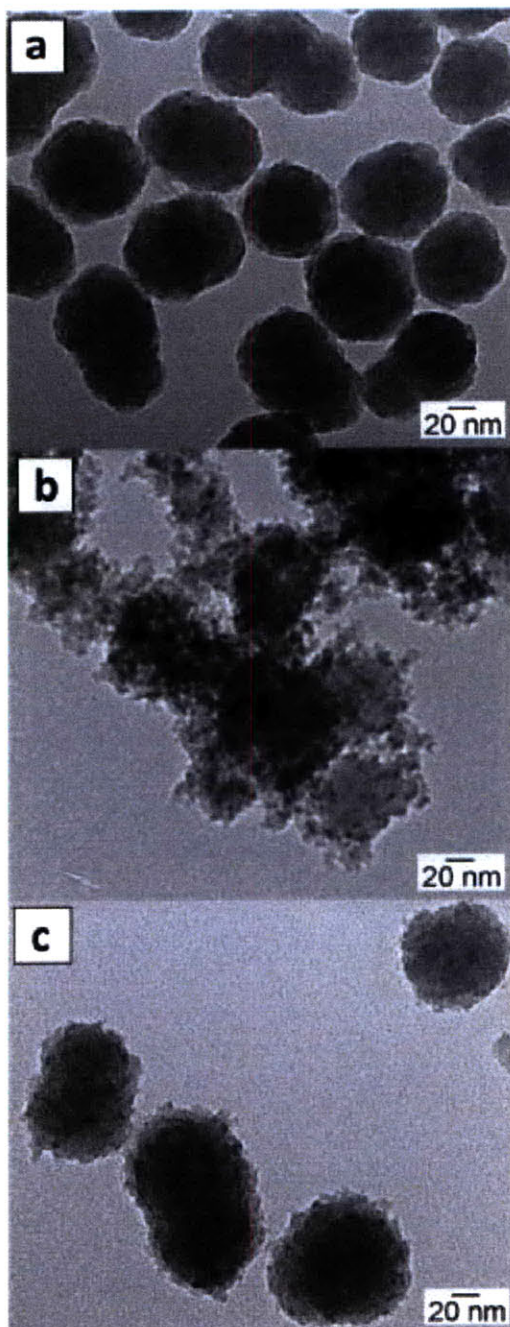


**Figure 3.5** TEM images of the microspheres of 50-nm in diameter (a) before the reaction, and (b-c) after the MP incorporation process in overgrowth condition of the silica shell (b), and few MP loading condition (c).

The distribution of iron was observed using scanning transmission electron microscopy (STEM) equipped with an energy-dispersive X-ray analyzer, as shown in Figure 3.6. Uniform distribution of iron signals among many microspheres was observed. Moreover, this plot of iron (red spots) and silicon atoms (white spots), identified the shell as the area of dense distribution of iron atoms. This observation, combined with data from a line scanning across a single microsphere as shown in Figure 3.7, indicated a shell thickness of  $55 \pm 10$  nm.

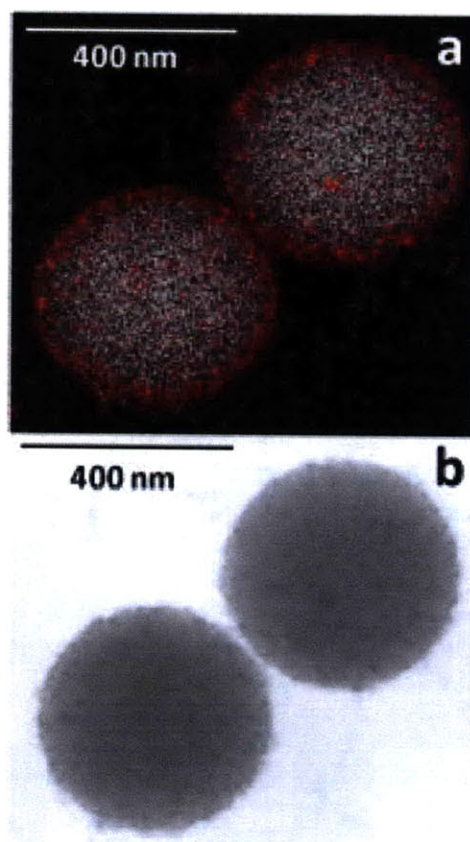


**Figure 3.6** Images of the microspheres from STEM (a) distribution map of silicon (white spots) and iron (red spots) and (b) transmission image of microspheres shown in (a).



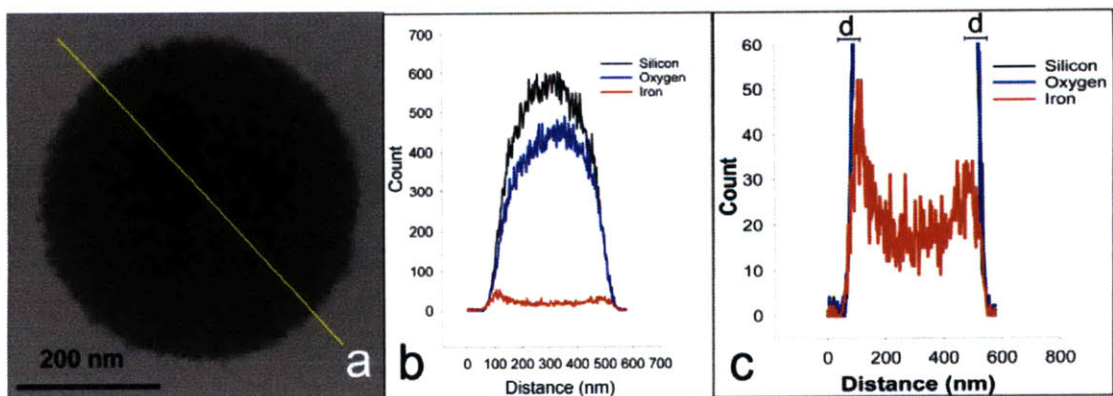


**Figure 3.7** Results from STEM line-scanning analysis (a) position of line scanning across the microspheres; (b) graph presenting signal of silicon (black line), oxygen (blue line) and iron (red line) along the line in (a); (c) same graph as (b) but enlarged to emphasize the shape of the iron signal (d represents the shell thickness).

*Detailed Characterization:* TEM images of the microspheres were obtained with a JEOL 200CX electron microscope operated at 200 kV. SEM images were obtained using a FEI/Philips XL30 field-emission gun-environmental scanning electron microscope (FEG-ESEM) at an acceleration voltage of 20 kV. Elemental mapping and line-scanning were done using a VG HB603 scanning transmission electron microscope operating at 250 kV equipped with a Link Systems energy-dispersive X-ray analyzer.

#### ***Detailed calculation of the thickness of the microspheres***

In a given core-shell microsphere of inner radius  $r_i$  and outer radius  $r_o$ , the intensity of the signal from atoms in the shell is proportional to the depth of the shell ( $h$ ) under the point where the signal is collected (Figure 3.8b). We assign  $r_p$  as the radius of this core-shell microsphere that is perpendicular to  $h$ . The relation between  $h$  and  $r_p$  can be formulated by considering these following two cases.

We plot a graph between  $h$  and  $r_p$  of a microsphere with known inner and outer radii and determine the shell thickness from the plot. For example, we plot a graph of  $h$  and  $r_p$  of a microsphere with inner radius of 200 nm and outer radius of 250 nm. One can

observe the shell thickness ( $t$ ) as a distance from outermost position of the microsphere to the position of highest  $h$  as shown in figure 3.8a.

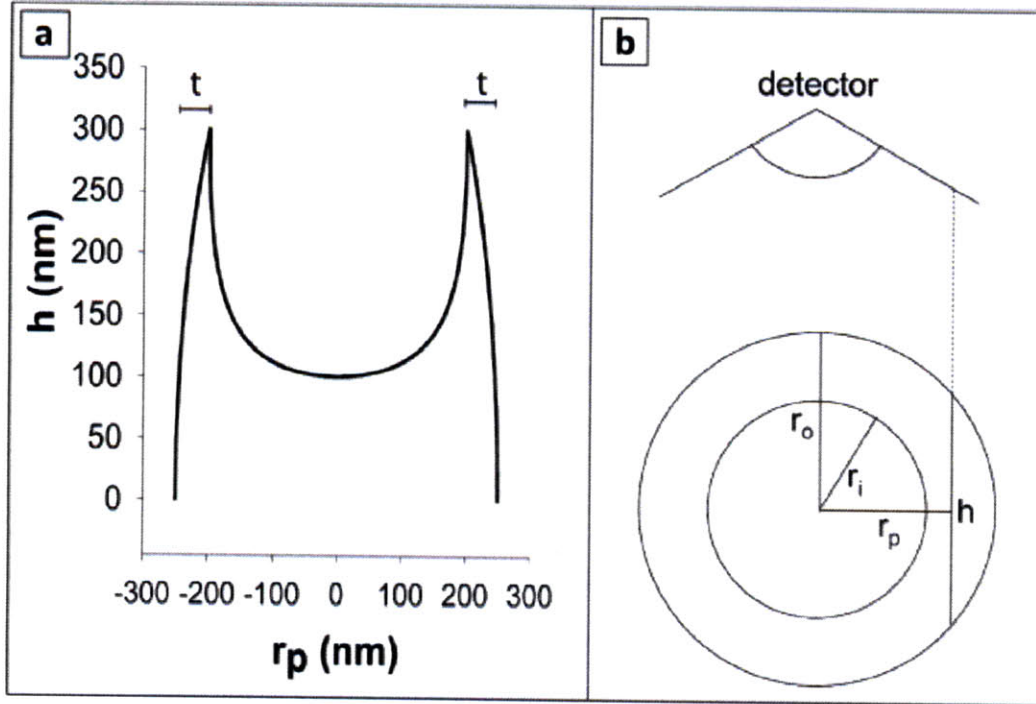


**Figure 3.8** (a) Graph representing the relationship between  $h$  and  $r_p$  of a core-shell microsphere (shown in b) with inner ( $r_i$ ) and outer radii ( $r_o$ ) of 200 and 250 nm, respectively ( $t$  denoted the shell thickness).

As MPs are incorporated into the shell of the microspheres, the signal of iron from the MPs represents the signal from the shell. The iron signal from a line scan across a microsphere (red line in Figure 3.7c) is consistent with that in Figure 3.8a. Therefore, the shell thickness is defined as the distance from the outermost position of the microsphere to the position of the highest signal of iron (distance  $d$  in Figure 3.7c). The shell thickness was therefore  $55 \pm 10$  nm.

### 3.3 Physical Properties of magnetic and fluorescent microspheres

#### 3.3.1 Fluorescence

In order to observe the distribution of QDs in microspheres, an optical microscope was used to visualize the QDs using their fluorescent signals. Fluorescence microscopy

showed that the microspheres were suitably bright for imaging applications. In addition, every microsphere exhibited QD fluorescence of similar intensities, implying that the QDs were incorporated and distributed uniformly as seen in Figures 3.9a and b.

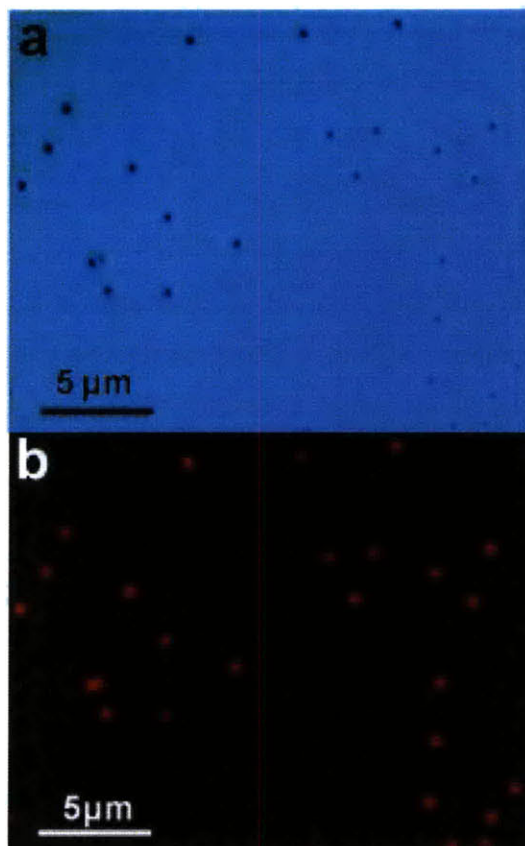


**Figure 3.9** Images of the microspheres from an optical microscope (a) transmission image and (b) fluorescent image of the same position.

Fluorescent images of the microspheres were obtained using a Nikon Eclipse ME600 epifluorescence optical microscope equipped with a Nikon DXM1200 digital camera. In order to obtain a monolayer of microspheres for light microscope imaging, we prepared samples by spin coating the microspheres dispersed in ethanol onto glass microscope slides.

### 3.3.2 Magnetic Properties

The magnetic properties of these microspheres were measured using a SQUID magnetometer (Quantum Design MPMS-5S). Figure 3.10 shows the magnetization versus magnetic field at 5 K for three different microsphere samples. From the shapes of the hysteresis loops, it can be inferred that microspheres containing both MPs and QDs were ferromagnetic at 5 K (green and black lines in Figure 3.9), while the microspheres with only QDs incorporated were diamagnetic (pink line). Moreover, the value of the saturation magnetization ( $M_S$ ) of each sample was measured and used to estimate the amount of  $\gamma\text{-Fe}_2\text{O}_3$  in each sample based on the known  $M_S$  of bulk  $\gamma\text{-Fe}_2\text{O}_3$  ( $3.9 \times 10^5 \text{ Am}^{-1}$ ).<sup>20</sup> The number of incorporated MPs per microsphere was estimated using the diameter of the microspheres and MPs measured from TEM images, the mass of the sample, and the assumption that MPs were uniformly incorporated and did not significantly alter the density of bulk  $\text{SiO}_2$ . Accordingly, 500-nm microspheres with 7-nm MPs incorporated exhibited an  $M_S$  of 5.35 emu/g and thus contained  $11000 \pm 3100$  MPs per microsphere. This number of MPs is 20% lower than indicated by ICP-OES elemental analysis. The higher number is probably more reliable, because size<sup>21</sup> and ligand effects<sup>22</sup> cause  $M_S$  of MPs to be lower than that of bulk maghemite.

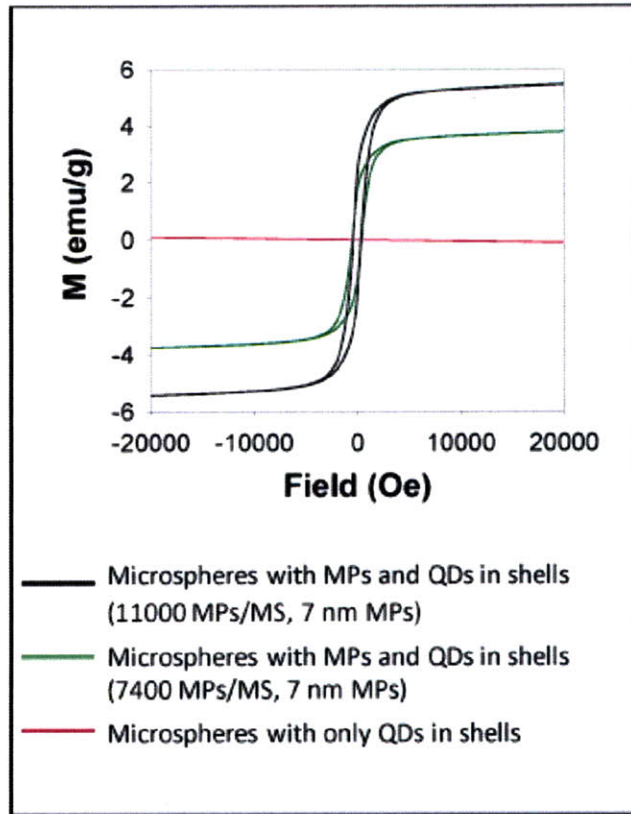


**Figure 3.10** Magnetization versus magnetic field at 5 K of 500-nm microspheres with different MP loadings.

*Detail for the calculation of MP content in microspheres from saturation magnetization measurement*

The saturation magnetization of bulk maghemite is  $3.9 \times 10^5 \text{ Am}^{-1}$ . We used the diameters of the microspheres and MPs measured from TEM images, and measured the mass of the sample before the saturation magnetization measurement.

As an example, 500-nm microspheres incorporated with 7-nm MPs exhibit an  $M_S$  of 5.35 emu/g.

For the number of MPs, we calculated that there were  $7.7 \times 10^{16}$  MP particles in a gram of the sample by calculating the  $M_S$  of one MP and the  $M_S$  of a gram of sample.  $M_S$  for one MP was calculated from the volume of a MP and the  $M_S$  of  $\gamma\text{-Fe}_2\text{O}_3$  ( $7500 \mu_B$ ).  $M_S$  of a gram of sample from the SQUID measurement was

$$5.77 \times 10^{20} \mu_B.$$



For the number of microspheres, we used the mass of microspheres (0.938 g in a gram of sample), and the mass of one microsphere ( $1.34 \times 10^{-13}$  g) which was calculated using the silica and QD content from calculated from elemental analysis in Appendix A and the MP content from above. We calculated that there were  $7.0 \times 10^{12}$  microspheres in a gram of the sample.

Therefore, we obtained the number of MPs per microsphere as 11000 MPs per microsphere. Using the same method to obtain errors as in Appendix A, in conjunction with accounting for the error from the SQUID measurement, number of MPs per microsphere was obtained as  $11000 \pm 3100$ .

The number of MPs per microspheres obtained by this method is in agreement with the value obtained by elemental analysis, within error.

In Figure 3.11,  $T_B$  corresponds to the maximum in the zero field cooled magnetization curves measured in a small field (100 Oe). As the MP concentration increases, the dipolar interaction between MPs becomes stronger, which causes  $T_B$  to increase and the magnetization at low temperature to decrease. At high temperature, the temperature-dependent magnetization curves for samples of different concentrations converge, when thermal energy has overcome interparticle dipolar coupling. As a reference in which dipolar coupling was negligible,<sup>23</sup> we prepared a sample of MPs dispersed in poly(laurylmethacrylate) cross-linked with ethyleneglycol dimethacrylate.<sup>24</sup> As shown in Figure 3.10, MPs dispersed in polymer have a blocking temperature of 30 K (red line) while the magnetic microspheres have  $T_B$  of 45-50 K (green and black lines). The increase in  $T_B$  indicates that the packing density of the MPs in the microspheres was higher than that of the MPs dispersed in polymer.<sup>23</sup> However, when compared to vacuum-dried MPs, whose  $T_B$  is 70 K (the blue line), the MPs in the microspheres had a lower  $T_B$ , which indicates that the packing density of the MPs in microspheres was still not as high as that of the dried powder MPs.

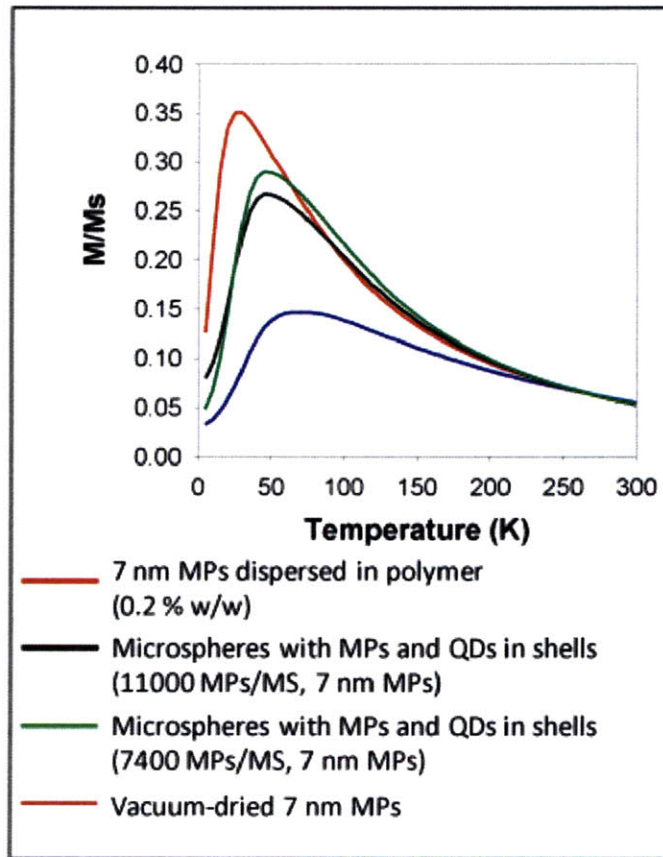


**Figure 3.11** Zero field cooled magnetization versus temperature measured in a 100 Oe field of 500-nm microspheres with different MP loadings.

### 3.4 Demonstration of combined superparamagnetism and fluorescence of the MP- and QD-incorporated microspheres.

#### 3.4.1 Demonstration using microelectromagnetic device

*(This work is done in collaboration with Hakho Lee, Westervelt Research Group, Department of Physics, Harvard University)*

To demonstrate the combined magnetic/fluorescence characteristics of the microsphere, we have performed the magnetic manipulation of the microspheres in fluid. Microelectromagnets, which are lithographically-patterned conducting wires, were used to control the motion of microspheres.<sup>25</sup> Local magnetic fields generated by microelectromagnets interact with MPs in the microspheres, which pulls the microspheres toward the maximum in the field magnitude. Two types of microelectromagnets, an array of wires (Figure 3.12) and a ring trap (Figure 3.13), were

prepared for this demonstration. The manipulation process can be easily monitored in real-time by observing the emission from QDs in the microspheres.

When an external magnetic field  $\mathbf{B}$  is generated by microelectromagnets, the microspheres assume induced magnetic moments  $\mathbf{m} = \chi V \mathbf{B} / \mu_0$ , where  $\chi$  and  $V$  are the magnetic susceptibility and the volume of the microspheres, respectively, and  $\mu_0$  is the permeability of vacuum. Subsequent interactions between  $\mathbf{B}$  and  $\mathbf{m}$  pull the microspheres towards the maximum in the magnetic field magnitude where the microspheres are trapped. The trapping potential energy of microspheres is  $U = -\frac{1}{2} \mathbf{m} \cdot \mathbf{B} = -\frac{1}{2} \chi V B^2 / \mu_0$ , and microspheres remain trapped provided  $|U| > k_B T$ , where  $k_B$  is the Boltzmann constant and  $T$  is the temperature. This condition sets the criterion on the minimum magnetic field magnitude  $B_m = (2\mu_0 k_B T / \chi V)^{1/2}$  required for trapping at given temperature. The microspheres used in this experiment have  $\chi = 0.53$  (see Appendix B) and  $V = 5.9 \times 10^7 \text{ nm}^3$ , which gives  $B_m = 6 \text{ G}$  at  $T = 300 \text{ K}$ . Using microelectromagnets, magnetic fields  $> 10 \text{ G}$  can be easily generated, ensuring the stable trapping of microspheres in fluids.



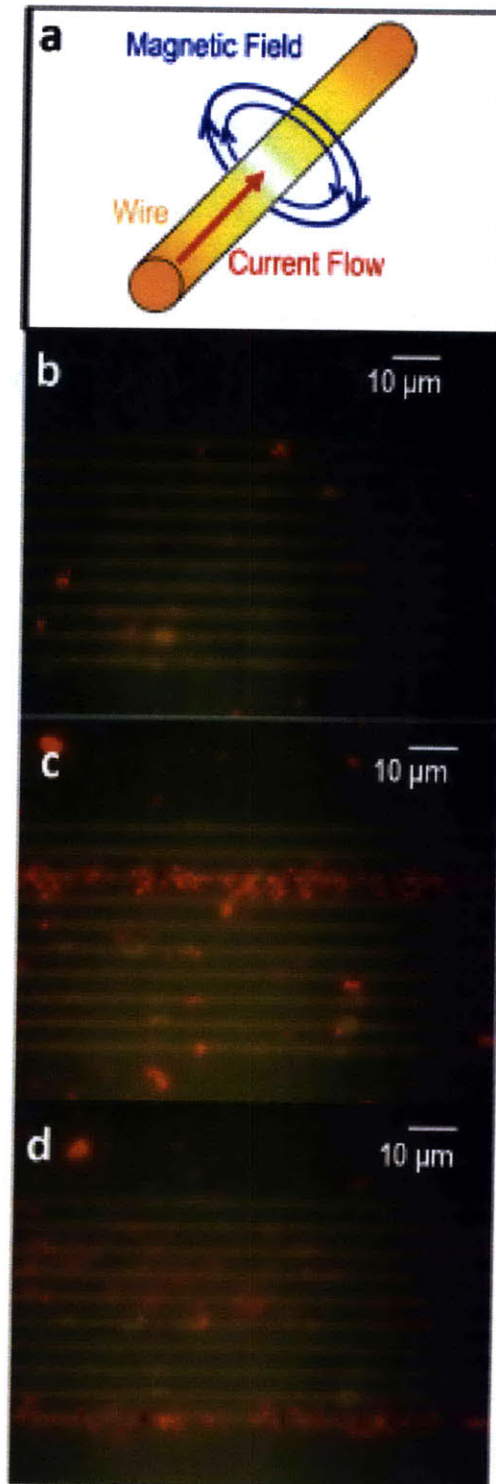


**Figure 3.12** Images of the straight wires trapping experiment (a) the current flow and magnetic field from the wires (b) no current in wires (c) third wire from the top turned on (d) bottom wire turned on.

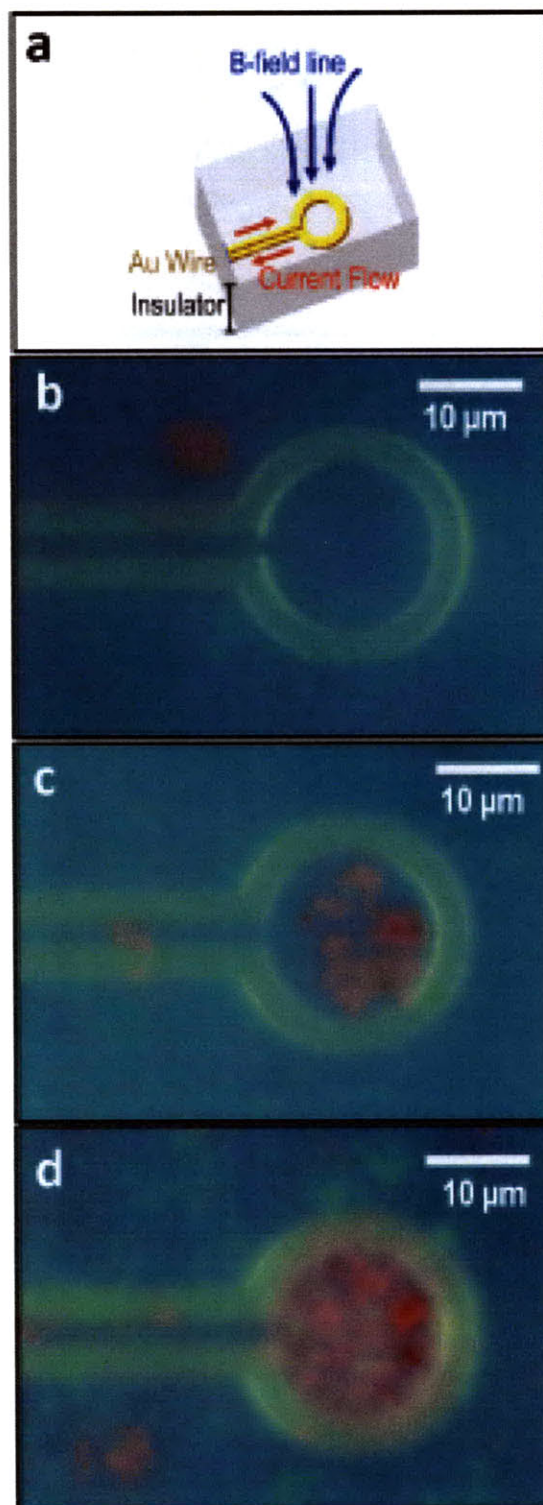


**Figure 3.13** Images of the ring trapping experiment (a) the current flow and magnetic field from the ring (b) no current (c) after the ring current was turned on for one minute (d) after the ring current was turned on for six minutes.

For straight wires, the maximum magnetic field is located around the current-carrying wire (Figure 3.12a). Before turning the current on, the red-emitting microspheres floated randomly over an array of wires (Figure 3.12b). After the third wire from the top was activated, the microspheres were immediately attracted to the third wire (Figure 3.12c). After the third wire was turned off, the bottom wire was switched on (Figure 3.12d). Additional microspheres were attracted to the bottom wire, and the cloud of microspheres shown between the third and sixth (from the top) wires, which had been trapped on the third wire, were later trapped on the bottom wire. This experiment demonstrated that the microspheres were responsive to small magnetic field gradients, because the microspheres which were on the third bar were moved to the bottom bar from more than 50  $\mu\text{m}$  away.

In experiments using a ring trap, we used two different types of microspheres, green-emitting microspheres without MPs incorporated, and red-emitting microspheres with MPs incorporated. (The green-emitting microspheres were in relatively low concentration, and they are difficult to discern against the background in this experiment.) In this device, the magnetic field maximum was in the middle of the ring, as shown in Figure 3.13a. When there was no current, both green and red microspheres floated freely over the device (Figure 3.13b). One minute after turning on the ring current, red-emitting microspheres were attracted to the middle of the ring (Figure 3.13c), more were attracted after longer on-times (Figure 3.13d). The green-emitting microspheres, in contrast, still floated randomly.

*Detailed Experiment for the Demonstration of trapping of the microspheres with external magnetic fields*

The manipulations of the microspheres using external magnetic fields were performed using microelectromagnets. The fabrication process of the microelectromagnets is previously reported. Two types of devices used in this work were arrays of Au wires (Figure 3.12a) and an Au wire patterned into a ring (Figure 3.13a). The maximum current used in these experiment was 0.09 A, corresponding to magnetic field of  $\sim 67$  G in the Au straight wire trap, and  $\sim 42$  G in the middle of the ring trap. In

these trapping experiments, we used microspheres dispersed in water instead of ethanol to avoid rapid evaporation of the solvent. The microspheres were transferred from the ethanol medium to a water medium by two cycles of centrifugation and redispersion into water.

The microspheres incorporating MPs and QDs were demonstrated to be trapped by microelectromagnetic devices which high local magnetic field can be generated. In the next section, less complicated systems for generating external magnetic field such as permanent magnetic tips are demonstrated as another approach for controlling the microspheres.

### **3.4.2 Demonstration using magnetic tips**

*(This work is done in collaboration with Barbara Muller, Dahan Research Group, Ecole Normale Supérieure, France)*

One of the potential biological applications of these microspheres is that they can be attached to molecules or proteins of interest and magnetically controlled while the movement of the particles is visualized using their fluorescence. In addition to the controlled movement of the microspheres using complex microelectromagnetic devices in the previous section, a simpler magnetic control set-up such as the use of permanent magnetic tips to attract microspheres can be utilized. One specific biological research project that could use this set-up is the study of protein localization in an asymmetric cell-division process.

Asymmetric cell division is an important process in cell differentiation such as in neurogenesis.<sup>26</sup> In this process, progenitor mother cells are polarized and experience localization of different proteins in each pole before asymmetric cell division. After cell division, one daughter cell will leave the division cycle and differentiate finally into a neuron while the other daughter remains in the cell division cycle. This process is an important step for the genesis of neural systems. However, many proteins that may participate in this process are not yet fully studied. Our collaborator has some interest in using the MP- and QD-incorporating microspheres for magnetic controlling localization of these proteins and fluorescent visualizing the location of the proteins simultaneously.

Proteins of interest are proposed to be chemically attached to the microspheres, followed by magnetic localization and fluorescent visualization. We propose that conducting this experiment will give us a better understanding of the neural system.

The initial experiment to prove this concept of magnetically controlling the localization of the microspheres with real-time visualization was demonstrated in a model system of a droplet of water in oil as shown in Figure 3.14a. Fluorescent images from an optical microscope of this demonstration appear in Figures 3.14b-d. Attraction of the microspheres to the approaching permanent magnetic tips was clearly observed in Figure 3.13d. The results of this experiment suggest that the proposed localization of proteins attached to the microspheres can probably be achieved.

However, in real cell experiments, the size of the microspheres is likely to impede the attraction and localization of the microspheres to a magnetic tip. The microspheres of 500-nm-diameter as in this experiment are likely too large to move through the cytoskeleton in the cytoplasm of cells. The microspheres of smaller than 100-nm-diameter with sufficient magnetization are proposed to be the maximum size for achieving controlled movement inside cells. As mentioned in earlier sections, the microspheres with diameters smaller than 100 nm created with this reaction scheme lack high-enough quality and sufficient MP loading, so new nanostructures comprising MPs and QDs are needed for use in this experiment. These new types of nanostructures are discussed in Chapters 4 and 5.

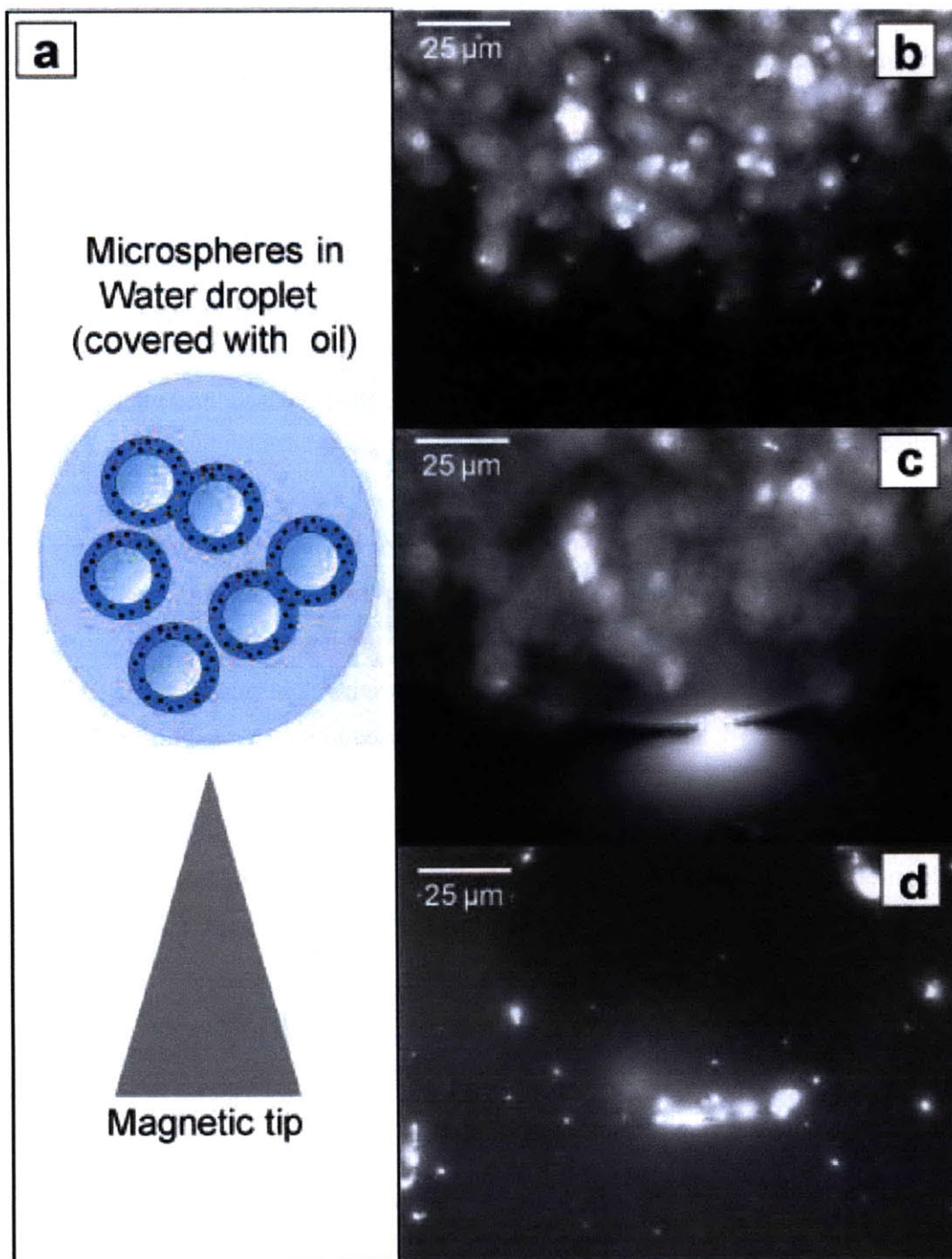


**Figure 3.14** Images of the magnetic tip attraction experiment: (a) diagram of the experiment set-up, fluorescent images of microspheres (b) in water droplet without magnetic field, (c) when magnetic approaches, and (d) 30 seconds after magnetic tip approaches.



In conclusion, by incorporating MPs and QDs into the silica shells of the pre-made microspheres, we have developed a new type of silica microsphere with tight size distribution and both magnetic and fluorescent properties. We have also demonstrated the bifunctionality of the microspheres by manipulating them using external magnetic fields with real-time fluorescence monitoring. These microspheres have potential for biomedical applications as a probe that responds to magnetic field gradients and simultaneously luminesces. For many applications in biological systems, surface modification of the microspheres is needed both for applying functional groups for conjugation and for reducing protein non-specific binding. This surface functionalization of the silica microspheres is discussed in Section 3.5.

### 3.5 Surface functionalization of the microspheres

In order to use the microspheres by conjugating them with other molecules, the functional groups have to be applied onto surfaces of the microspheres. The surface modification of the microspheres can be done by using silane-coupling chemistry to attach different functional groups to the MP surfaces. Moreover, for some biological applications, the microspheres must have low protein-non-specific binding because in a biological system, a high concentration of protein could affect the size and stability of the microspheres. In order to reduce the protein-non-specific binding of the microspheres, a polyethylene glycol (PEG) chain, which is known for having low protein-non-specific binding, can be attached onto surfaces of the MPs. Examples of these surface modifications of the microspheres are shown in the reaction scheme in Figure 3.15.

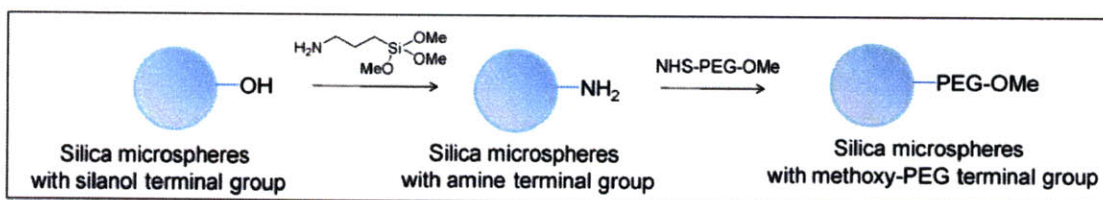


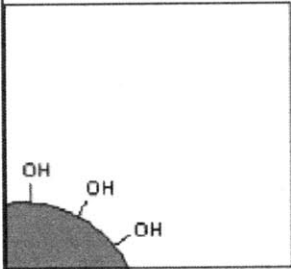
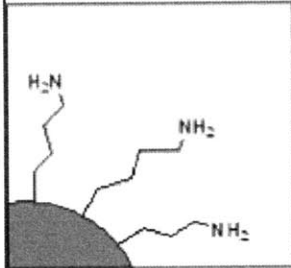
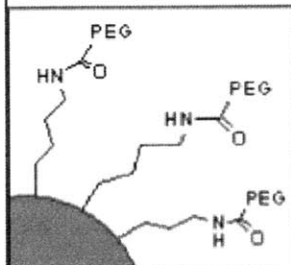
**Figure 3.15** Reaction scheme for surface functionalization of silica microspheres.

Surface modification of the silica microspheres in order to attach functional groups such as amino groups can be done in a one-step reaction as shown in the first reaction in Figure 3.15. Amino-functionalized silica microspheres can be prepared from the silane-coupling reaction between native silica microspheres with silanol groups on their surfaces and a silane-coupling reagent such as APS (3-aminopropyltrimethoxysilane, Sigma-Aldrich). This reaction was done in ethanol at 40 °C for 1 hour with ammonium hydroxide and water as catalysts. This reaction scheme can also be used for functionalization using other silane-coupling agents such 3-mercaptopropyltrimethoxy-silane for attaching thiol groups to the microspheres.

PEGylated microspheres can then be prepared from the amino-functionalized microspheres as shown in the second reaction in Figure 3.15. The PEGylation step was done using an amide-coupling reaction between the amino groups on the microspheres and the *N*-Hydroxysuccinimide (NHS) ester group on mPEG-NHS (5 KDa Molecular weight, Creative PEGWorks). This coupling reaction was done in a PBS solution at room temperature for 6 hours. The resulting PEGylated microspheres are then dispersible and stable in PBS solutions.

The changes in the surface of the microspheres during these surface modifications processes can be tracked by analyzing the changes in their surface charges. A zeta-potential analyzer was employed to measure the charges of the microspheres in the form of zeta potential. The zeta potentials of the microspheres in a diluted PBS solution before and after surface modification processes are shown in Figure 3.16.



Functional groups on the microsphere surface	Zeta Potential (mV)
	-32.17
	+3.70
	-5.24

**Figure 3.16** Zeta potentials of 300-nm silica microspheres of different surface modifications.

The zeta potentials of the microspheres revealed the success of the surface-modification reaction used in Figure 3.15 because the changes of the zeta potential correspond to the functional groups applied to the microsphere surfaces. The silica microspheres with only native silanol groups are highly negatively charged because they have zeta potentials of less than -30mV. After being functionalized with amino groups, the microspheres turned their zeta potentials into the positive range, corresponding to the positive charges of the protonated amino groups in the PBS solution. Then, the slightly negative charges on the surface of the MPs were observed in PEGylated microspheres due to the PEG and some excess native silanol groups.

The surface modification discussed in this section suggests that the microspheres can change their surface properties and charges, which can be useful for some biological experiments. Moreover, a variety of functional groups can be attached to the surfaces of silica microspheres with a one-step reaction for each group. Microspheres with available functional groups are important for biological applications because they can be conjugated with proteins and molecules of interest such as the experiment discussed in Section 3.4.2, which required the conjugation of proteins with the microspheres.

### **3.6 Conclusion**

The surface modification of iron oxide MPs with silane groups discussed in this chapter can lead to the formation of silica microspheres containing MPs and QDs. These superparamagnetic and fluorescent silica microspheres show high potential for being a useful tool for various biological applications as demonstrated in the magnetically controlled and real-time fluorescence-visualization experiments. Moreover, the surface of the silica microspheres can be readily changed and functionalized with various functional groups. This is the first production of nanostructures that combine sufficient superparamagnetism, fluorescence, and functional surfaces for biological applications in the same particles.

The size limitation of the MP and QD-incorporated silica microspheres that they cannot be synthesized in a smaller-than-100-nm range can hinder them from being used in some biological applications. The applications that require microspheres of diameters under 100 nm, such as the experiment in magnetically-controlled movement of the microspheres inside cells mentioned in Section 3.4.2, require nanostructures of different designs. Chapters 4 and 7 discuss smaller nanostructures comprising iron oxide MPs and semiconductor QDs as candidates for those applications requiring smaller superparamagnetic and fluorescent particles.

### **3.7 References**

1. Pankhurst, Q. A.; Connolly, J.; Jones, S. K.; Dobson, J., Applications of magnetic nanoparticles in biomedicine. *Journal of Physics D-Applied Physics* **2003**, 36, (13), R167-R181.

2. Zhu, Y. H.; Da, H.; Yang, X. L.; Hu, Y., Preparation and characterization of core-shell monodispersed magnetic silica microspheres. *Colloids and Surfaces a-Physicochemical and Engineering Aspects* **2003**, 231, (1-3), 123-129.
3. Yang, C. L.; Guan, Y. P.; Xing, J. M.; Liu, J. G.; Shan, G. B.; An, Z. T.; Liu, H. Z., Preparation of magnetic polystyrene microspheres with a narrow size distribution. *Aiche Journal* **2005**, 51, (7), 2011-2015.
4. Tanyolac, D.; Ozdural, A. R., Preparation of low-cost magnetic nitrocellulose microbeads. *Reactive & Functional Polymers* **2000**, 45, (3), 235-242.
5. Muller-Schulte, D.; Schmitz-Rode, T.; Borm, P., Ultra-fast synthesis of magnetic and luminescent silica beads for versatile bioanalytical applications. *Journal of Magnetism and Magnetic Materials* **2005**, 293, (1), 135-143.
6. Yi, D. K.; Selvan, S. T.; Lee, S. S.; Papaefthymiou, G. C.; Kundaliya, D.; Ying, J. Y., Silica-coated nanocomposites of magnetic nanoparticles and quantum dots. *Journal of the American Chemical Society* **2005**, 127, (14), 4990-4991.
7. Claesson, E. M.; Philipse, A. P., Monodisperse magnetizable composite silica spheres with tunable dipolar interactions. *Langmuir* **2005**, 21, (21), 9412-9419.
8. Zhang, M. J.; Itoh, T.; Abe, M., Ultrasonic visualization of still and flowing waters using contrast agents of magnetite-encapsulated porous silica microspheres. *Japanese Journal of Applied Physics Part 1-Regular Papers Short Notes & Review Papers* **1997**, 36, (1A), 243-246.
9. Tartaj, P.; Gonzalez-Carreno, T.; Bomati-Miguel, O.; Serna, C. J.; Bonville, P., Magnetic behavior of superparamagnetic Fe nanocrystals confined inside submicron-sized spherical silica particles. *Physical Review B* **2004**, 69, (9).
10. Ramesh, S.; Prozorov, R.; Gedanken, A., Ultrasound driven deposition and reactivity of nanophasic amorphous iron clusters with surface silanols of submicrospherical silica. *Chemistry of Materials* **1997**, 9, (12), 2996-3004.
11. Yoon, T. J.; Kim, J. S.; Kim, B. G.; Yu, K. N.; Cho, M. H.; Lee, J. K., Multifunctional nanoparticles possessing a "magnetic motor effect" for drug or gene delivery. *Angewandte Chemie-International Edition* **2005**, 44, (7), 1068-1071.
12. Qiu, G. M.; Xu, Y. Y.; Zhu, B. K.; Oiu, G. L., Novel, fluorescent, magnetic, polysaccharide-based microsphere for orientation, tracing, and anticoagulation: Preparation and characterization. *Biomacromolecules* **2005**, 6, (2), 1041-1047.
13. Chan, Y.; Zimmer, J. P.; Stroh, M.; Steckel, J. S.; Jain, R. K.; Bawendi, M. G., Incorporation of luminescent nanocrystals into monodisperse core-shell silica microspheres. *Advanced Materials* **2004**, 16, (23-24), 2092-2097.

14. Hong, X.; Li, J.; Wang, M. J.; Xu, J. J.; Guo, W.; Li, J. H.; Bai, Y. B.; Li, T. J., Fabrication of magnetic luminescent nanocomposites by a layer-by-layer self-assembly approach. *Chemistry of Materials* **2004**, 16, (21), 4022-4027.
15. Fu, A. H.; Gu, W. W.; Larabell, C.; Alivisatos, A. P., Semiconductor nanocrystals for biological imaging. *Current Opinion in Neurobiology* **2005**, 15, (5), 568-575.
16. Kim, J.; Lee, J. E.; Lee, J.; Yu, J. H.; Kim, B. C.; An, K.; Hwang, Y.; Shin, C. H.; Park, J. G.; Hyeon, T., Magnetic fluorescent delivery vehicle using uniform mesoporous silica spheres embedded with monodisperse magnetic and semiconductor nanocrystals. *Journal of the American Chemical Society* **2006**, 128, (3), 688-689.
17. Salgueirino-Maceira, V.; Correa-Duarte, M. A.; Spasova, M.; Liz-Marzan, L. M.; Farle, M., Composite silica spheres with magnetic and luminescent functionalities. *Advanced Functional Materials* **2006**, 16, (4), 509-514.
18. Gaponik, N.; Radtchenko, I. L.; Sukhorukov, G. B.; Rogach, A. L., Luminescent polymer microcapsules addressable by a magnetic field. *Langmuir* **2004**, 20, (4), 1449-1452.
19. Smith, A. M.; Ruan, G.; Rhyner, M. N.; Nie, S. M., Engineering luminescent quantum dots for In vivo molecular and cellular imaging. *Annals of Biomedical Engineering* **2006**, 34, (1), 3-14.
20. Tepper, T.; Ross, C. A., Pulsed laser deposition of iron oxide films. *Journal of Applied Physics* **2002**, 91, (7), 4453-4456.
21. Berkowitz, A. E.; Schuele, W. J.; Flanders, P. J., Influence of crystallite size on the magnetic properties of acicular gamma-Fe<sub>2</sub>O<sub>3</sub> particles. *Journal of Applied Physics* **1968**, 39, (2), 1261-1263.
22. Berkowitz, A. E.; Lahut, J. A.; Jacobs, I. S.; Levinson, L. M.; Forester, D. W., Spin Pinning at Ferrite-Organic Interfaces. *Physical Review Letters* **1975**, 34, (10), 594-597.
23. Frankamp, B. L.; Boal, A. K.; Tuominen, M. T.; Rotello, V. M., Direct control of the magnetic interaction between iron oxide nanoparticles through dendrimer-mediated self-assembly. *Journal of the American Chemical Society* **2005**, 127, (27), 9731-9735.
24. Tracy, J. B.; Weiss, D. N.; Dinega, D. P.; Bawendi, M. G., Exchange biasing and magnetic properties of partially and fully oxidized colloidal cobalt nanoparticles. *Physical Review B* **2005**, 72, (6).
25. Lee, C. S.; Lee, H.; Westervelt, R. M., Microelectromagnets for the control of magnetic nanoparticles. *Applied Physics Letters* **2001**, 79, (20), 3308-3310.

26. Wodarz, A.; Huttner, W. B., Asymmetric cell division during neurogenesis in *Drosophila* and vertebrates. *Mechanisms of Development* **2003**, *120*, (11), 1297-1309.
27. *CRC Handbook of Chemistry and Physics*. 86th ed.; CRC Press LLC: Boca Raton, FL, 2005-2006.
28. Leatherdale, C. A.; Woo, W. K.; Mikulec, F. V.; Bawendi, M. G., On the absorption cross section of CdSe nanocrystal quantum dots. *Journal of Physical Chemistry B* **2002**, *106*, (31), 7619-7622.
29. Shoemaker, D. P., *Experiments in Physical Chemistry*. McGraw-Hill: Boston, 1996.

### 3.8 Appendix

#### **Appendix A: Calculation of MP and QD content in microspheres from ICP-OES elemental analysis**

We used a density of  $1.96 \text{ g/cm}^3$  for silica microspheres, (Polysciences, Inc., data sheet). Densities of CdSe, CdS, and ZnS used were  $5.66$ ,  $4.82$  and  $4.1 \text{ g/cm}^3$ , respectively.<sup>27</sup> The density of maghemite used was  $4.88 \text{ g/cm}^3$ .<sup>27</sup> Sizes of microspheres, QDs, and MPs were obtained from TEM negatives scanned with a digital scanner and analyzed with ImageJ. We assumed that MPs and QDs were uniformly incorporated and did not significantly alter the density of the microspheres from that of the bare microspheres.

As an example, for which we detail our analysis, 500-nm microspheres incorporating 7-nm MPs and 6-nm QDs had an elemental composition of 39.6 % w/w silicon, 5.54 % w/w iron, 0.85 % w/w cadmium, 0.55 % w/w zinc by ICP-OES.

In Table 3.2, we summarize the calculation we used for obtaining the number of MPs and QDs per microsphere, percent volume of MPs and QDs in microspheres, and percent volume of MPs and QDs in the shell.

**Table 3.2** Calculation for obtaining the loading of MPs and QDs in the microsphere assuming that the density of the final, loaded microspheres is the same as that for the initial, bare microsphere

	Microsphere	MP	QD
% of total mass (calculated from ICP-OES)	84.7 <sup>a</sup>	7.92	2.24 <sup>b</sup>
Radius (nm) (from TEM images)	242 ± 10	3.5 ± 0.3	3.2 ± 0.3
Mass of each particles (g)	1.16 × 10 <sup>-13</sup>	8.8 × 10 <sup>-19</sup>	6.9 × 10 <sup>-19</sup>
Number of particles in 100 g of sample	7.30 × 10 <sup>14</sup>	9.0 × 10 <sup>18</sup>	3.24 × 10 <sup>18</sup>
Number of nanoparticles per microsphere	-	12000	4400
Percent volume of nanoparticles per microsphere	-	3.6	1.1
Percent volume of nanoparticles in the shell	-	6.75	1.9

<sup>a</sup> This number is the weight percent of silica in the sample. The percentages in this row add up to less than 100 due to the presence of residual organics.

<sup>b</sup> The total mass of QDs was based on the composition of CdSe/Cd<sub>0.04</sub>Zn<sub>0.96</sub>S. The molar ratio of Cd/Zn in QDs' alloyed shells was calculated using the radii of core-shell QDs measured from TEM images (3.2 ± 0.3 nm) and core (2.6 ± 0.2 nm) from absorption at 350 nm<sup>28</sup> combined with data of Cd and Zn content from ICP-OES.

In order to verify the assumption that the density of microspheres loaded with MPs and QDs does not significantly change from that of the initial microspheres, we calculated the density of the loaded microspheres by accounting for the mass of MP and QD incorporated. As a result, the density of loaded microspheres is now 2.27 g/cm<sup>3</sup>, a 16% increase from that of the bare microspheres.

When using this corrected density, the analysis is adjusted as shown in Table 1.3.

**Table 3.3.** Calculation for obtaining the loading of MPs and QDs in the microsphere after the density of incorporated microspheres has been adjusted.

Particles	Microsphere	MP	QD
% of total mass (calculated from ICP-OES)	94.87 <sup>a</sup>	7.92	2.24
Radius (nm) (from TEM images)	242 ± 10	3.5 ± 0.3	3.2 ± 0.3
Mass of each particles (g)	1.34 × 10 <sup>-13</sup>	8.8 × 10 <sup>-19</sup>	6.9 × 10 <sup>-19</sup>
Number of particles in 100 g of sample	7.07 × 10 <sup>14</sup>	9.0 × 10 <sup>18</sup>	3.24 × 10 <sup>18</sup>
Number of nanoparticles per microsphere	-	13000 ± 3700 <sup>b</sup>	4600 ± 1400 <sup>b</sup>
Persent volume of nanoparticles in the microsphere	-	3.9 ± 1.1 <sup>b</sup>	1.1 ± 0.3 <sup>b</sup>
Percent volume of nanoparticles in the shell	-	7.3 ± 4.1 <sup>b</sup>	2.0 ± 1.2 <sup>b</sup>

<sup>a</sup> This number here is the weight percent of combined silica, QDs, and MPs. This percentage is less than 100 due to the presence of residual organics.

<sup>b</sup> The error was calculated using propagation of random errors.<sup>29</sup> The major contributions to the total error in the loading of QDs and MPs in microspheres comes from the standard deviation of the radii of microspheres, MPs, and QDs, and the thickness of the microsphere shell.



## Appendix B: Calculation of magnetic susceptibility of a microsphere used in trapping experiment

The magnetic susceptibility of a microsphere in small magnetic fields is

$$\chi = \mu_0 \frac{n\mu_p^2}{3k_B T},$$

where  $\mu_0$  is the permeability of vacuum,  $n$  is the number density of the MPs in a microsphere,  $\mu_p$  is the saturation magnetic moment of a MP,  $k_B$  is the Boltzmann constant, and  $T$  is the temperature. The microspheres used in the experiment have a diameter of 483 nm and contain 204 MPs, which gives a number density for the MPs of  $n = 3.46 \times 10^{21} / \text{m}^3$ .

The diameter of MPs in the microsphere is 18 nm. Assuming that the MPs are spherical and have the magnetization  $4.0 \times 10^5 \text{ A/m}^2$  as in the bulk, we calculated the saturation magnetic moment of a MP,  $\mu_p$ , as  $1.2 \times 10^{-18} \text{ A}\cdot\text{m}$ .

Therefore at  $T = 300 \text{ K}$ , the magnetic susceptibility of a microsphere is 0.53.



## **Chapter 4**

### **Surface Modification of Iron Oxide Nanoparticles through a Reverse Micro-emulsion Process and Preparation of QD-decorating Silica-coated Iron Oxide Nanoparticles**

#### **4.1 Introduction**

In order to prepare water-dispersible and colloidally stable iron oxide nanoparticles, coating the MPs with silica is one of available choice. Coating of the MPs with silica also has the advantage that the silica surface can be functionalized readily with the available silane coupling reagents.<sup>1</sup> Moreover, silica surfaces are also known for biocompatibility because they can be transferred into biological systems without significant toxicity.<sup>1-3</sup>

As indicated by the modified silica coating process in Chapter 3, the silica coating process in one phase usually requires the surface of the materials to be hydrophilic, and the surface should have a silanol group to react with the silane precursors. Also, the silica coating tends to face a limitation in that the reaction can overreact, and the overgrowth of silica could occur in the form of cross-linked particles, as was observed in the case of silica coating on small silica microspheres (Figure 3.5b). For these reasons, the one-phase solution process cannot make the silica coating nicely on MPs with a hydrophobic nature.

This chapter discusses a silica coating using a reverse micro-emulsion process. This process is a good choice for coating materials of a small size and hydrophobic surface such as the MPs with a native oleic acid surfactant. In such cases, the more complex nanostructures of QD-decorated silica-coated MPs are synthesized using the silica-coated MPs from this process. These multifunctional nanostructures are studied because they can be used as smaller versions of the silica microspheres incorporating MPs and QDs, as discussed in Chapter 3.

## **4.2 Synthesis of silica-coated iron oxides MPs through a reverse micro-emulsion process**

The micro-emulsion process used in this chapter is adopted and modified from the previously reported process for coating CdSe QDs and iron oxide MPs.<sup>3-5</sup> This process is also known to apply to other types of nanoparticles with hydrophobic surfaces. The procedure and reaction scheme for the coating of silica onto iron oxide MPs are shown in Figure 4.1.

The silica coating process using the reverse micro-emulsion process started with the formation of micelles when the Igepal CO-520 surfactant was dissolved and stirred into cyclohexane. The micelles formed in this step because the hydrophilic heads of the surfactant molecules would point away from the rest of the hydrophobic solution. Then the hydrophobic MPs were added into the reaction mixture, and the MPs tended to attract Igepal CO-520 molecules, which have a higher polarity to attract the MPs. After that, water and ammonium hydroxide solution were added to the stirring mixture. The reverse micelles, which give the name to this process, were formed in this step because the water phase stayed inside the hydrophilic head of the Igepal CO-520. The reaction occurred in the micelles of the water phase inside the hydrophobic solvent, which are the opposite of regular micelles. The silica shells started to form when the silica precursor, tetraethoxysilane (TEOS), was added into the reaction mixture. Hydrolysis of TEOS and condensation of the silanol group took place at the interface between the water phase and cyclohexane phase where the MPs were attracted. After these reactions, the MPs were finally included in the silica shell.

The silica-coated MPs were separated out from the reaction mixture after the addition of ethanol. Ethanol can dissolve the Igepal CO-520 well, so upon addition of ethanol, the micelles were broken and the silica-coated MPs could be separated out by centrifugation. The silica-coated MPs can be re-dispersed back into ethanol or a water-based solution. The TEM images of the resulted silica-coated MPs are shown in Figure 4.2.

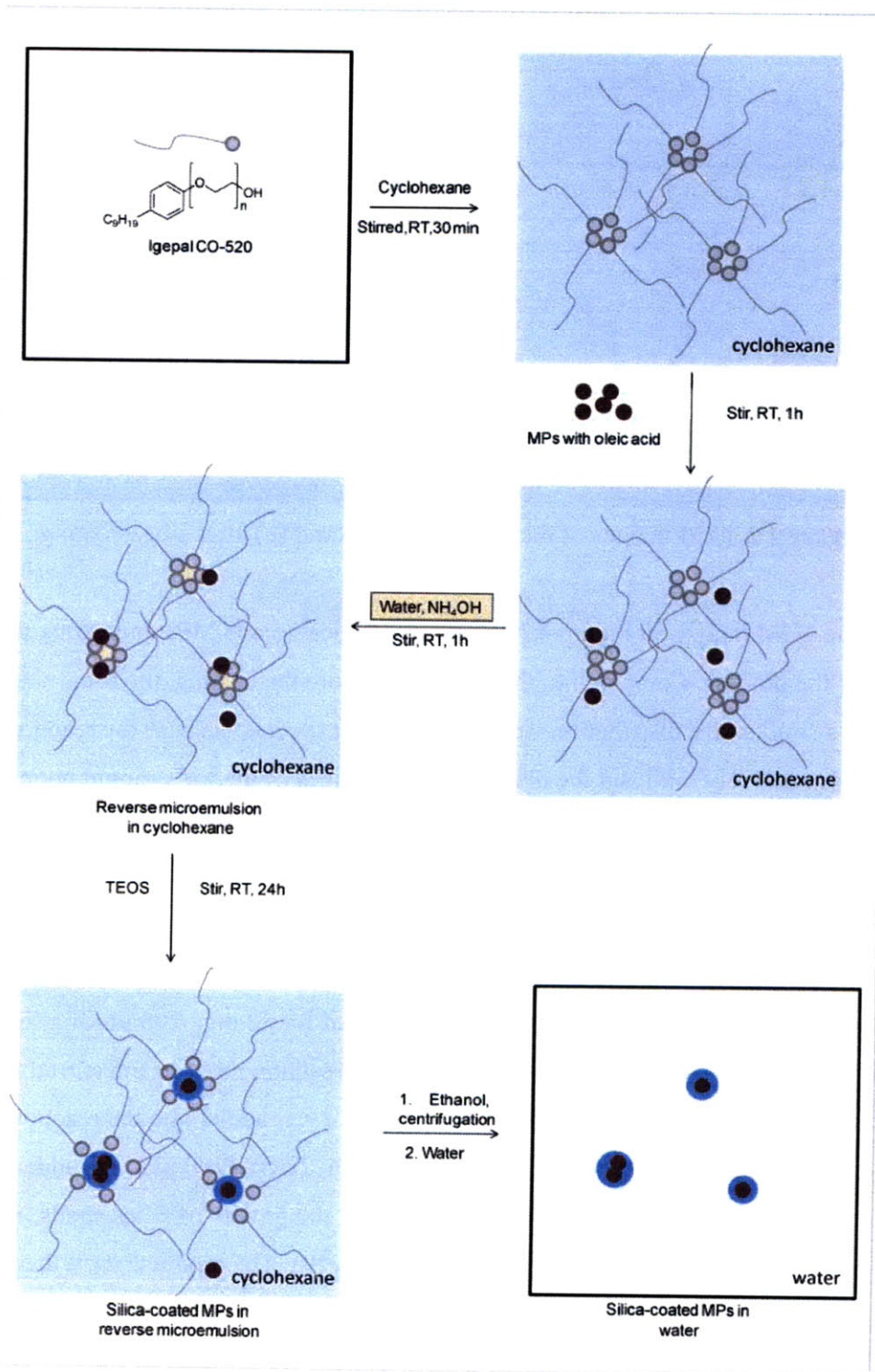


**Figure 4.1** Schematic representation of the silica-coating process.

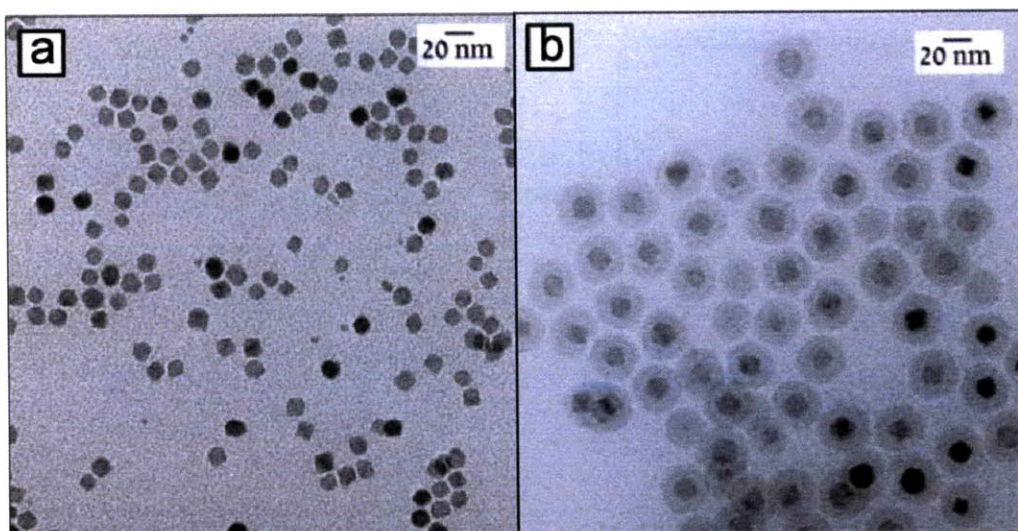


**Figure 4.2** TEM images of the MPs (a) before and (b) after silica coating.

The TEM images in Figure 4.2 show nicely silica-coated MPs, indicating the success of the process. Compared to the MP cores before the coating, the same size of the cores and a similar size distribution were observed as expected because the reaction condition is relatively mild and the dissolution or changes of the MPs should not occur. This observation implies that the magnetic properties of the MPs would also be intact.

***Experimental Details:***

For silica-coated MPs with 15-nm shell thickness: Igepal CO-520 (1.6 g, 3.75 mmol) was dissolved in 21 mL cyclohexane and stirred for 30 min. 200  $\mu$ L of a solution of 7 mg/mL of MPs in cyclohexane was added in the reaction mixture and stirred for 1h. Then, ammonium hydroxide solution (29.4 %, 100  $\mu$ L) was added into the reaction mixture and stirred for another 1h. After stirring for 1h, TEOS (100  $\mu$ L) was added into the reaction mixture and stirred for another 24h. After the growth of silica shells, 80 mL of ethanol were added to precipitate the silica-coated MPs. The products were then re-dispersed and kept in ethanol for further use.

The thickness of the silica shell can be controlled by adjusting the amount of the MP cores added to the reaction mixture. The more MPs cores, the thinner the shell of the silica coating. Also, to some extent, the amount of the TEOS added can alter the shell



thickness, but control of the overgrowth of silica must be kept in mind. When too much TEOS is added to the reaction mixture, the overgrowth of the silica shell could take place, and a cross-linked silica network of MPs is observed. Figure 4.3 depicts the controllable shell thickness of the silica coating using this method.

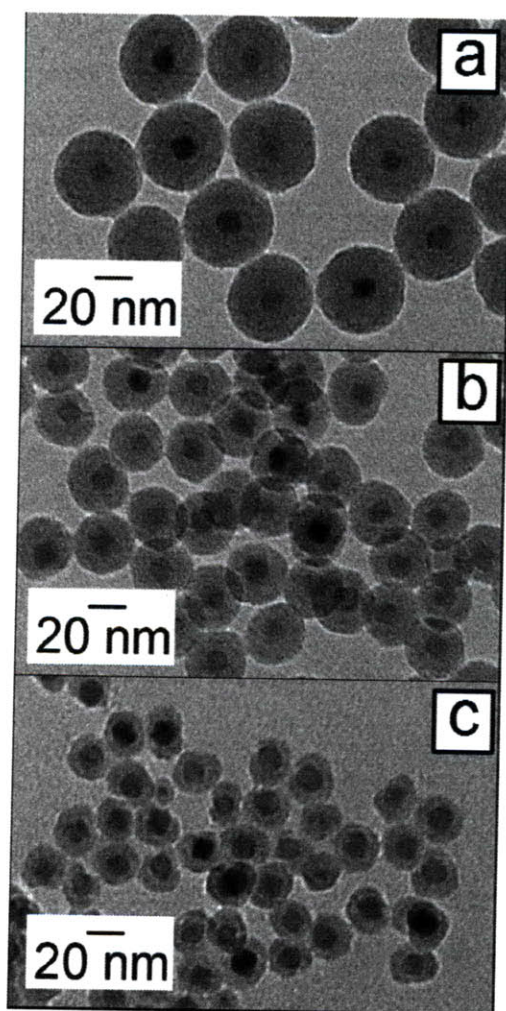


**Figure 4.3** TEM images of the silica-coated MP of different shell thickness (a, b, and c show 20-, 15- and 10-nm shell thicknesses, respectively).

These MPs were then transferred into a water-based solution. The transfer process was done by first centrifuging to precipitate the silica-coated MPs out of ethanol using a high-speed centrifuge. Then DI water was added to re-disperse the silica-coated MPs. A sonicator can be employed in this step to facilitate the re-dispersion. The precipitation

and re-dispersion were repeated a few more times to confirm that the ethanol was removed. Then the silica-coated MPs could be transferred into buffer solutions of interest.

In a water-based solution, the hydrodynamic size of these silica-coated MPs can then be analyzed using a dynamic light scattering (DLS) instrument. The size distribution of the silica-coated MPs with 20-nm shell thickness is shown in Figure 4.4. The result from the DLS showed that the hydrodynamic size is some 10 nm larger than that measured by TEM, indicating that there might be some adsorbed layers of water on the surface of the silica-coated MPs in a colloidal form.

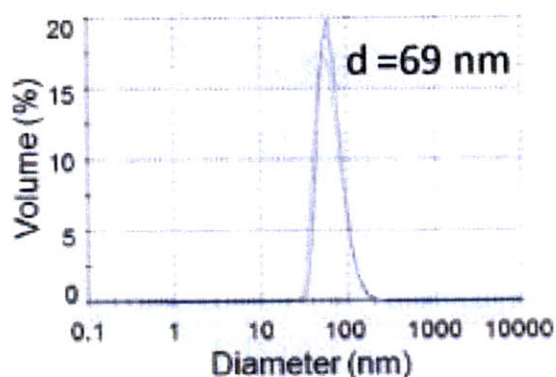


**Figure 4.4** Size distribution of the silica-coated MPs with silica shell of 20-nm thickness measured using a DLS instrument.

Another interesting property of the MPs for biological applications is the T2 relaxivity. The T2 relaxivity (R2) of the silica-coated MPs with a 20-nm silica shell is  $41 \text{ mM}^{-1} \text{ sec}^{-1}$ . This value of relaxivity indicates that this type of nanostructure can be useful as a T2 contrast agent in MRI studies. However, the value of the relaxivity is lower than what usually expected from MPs of 9-10 nm cores. One of the reasons for this low value of R2 is that the MPs are too thick and make the water molecules around the MPs too far away to be affected by the magnetic field from the MP cores.

Formation of MPs with thinner silica shells has been attempted in order to solve the problem of a thick shell causing the reduction in relaxivity. However, in this study and these reaction conditions, the thinnest silica shell that is achievable is 10 nm, as shown in Figure 4.3c. Synthesis of MPs with an even thinner shell of silica was studied



by significantly increasing the MP concentration and minimizing the quantity of TEOS added. However, it was found that the MPs with silica shell thinner than 10 nm tend to experience an incomplete shell around the MP core. The incomplete silica shells were observed by TEM as shown in Figure 4.5.

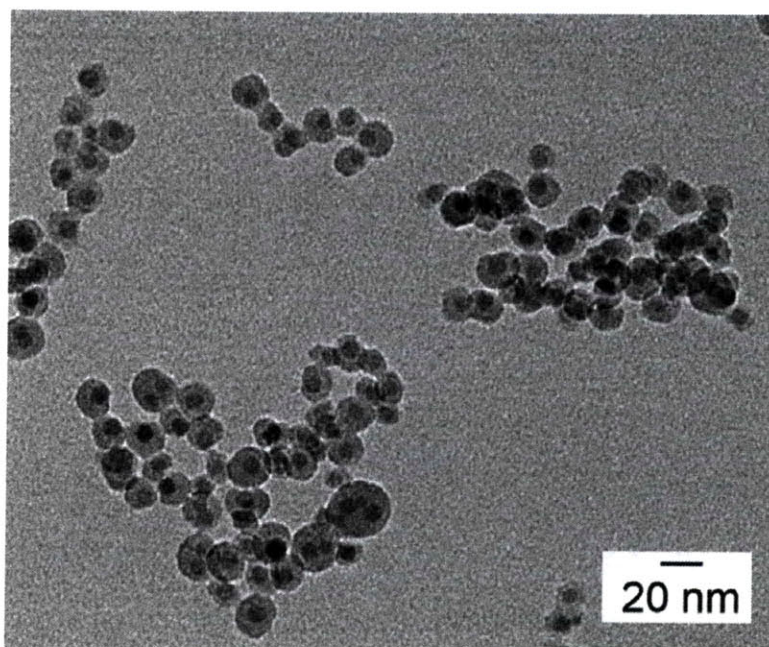


**Figure 4.5** TEM image of the MPs with incomplete silica coating.

The silica-coated MPs with incomplete coating as shown in Figure 4.5 indicate the lower limit of silica shell thickness using this method for silica coating. The thinnest silica shell for MPs is around 10 nm thick. Also, this incomplete coating can imply a mechanism for the micro-emulsion process, in which the coating starts from one side of the MP before it propagates to other sides because MPs with one-sided coatings were observed in this TEM image.

Another phenomenon was observed for silica-coated MPs with thin shells in a water-based solution of pH above 9. The silica shell can be dissolved and etched away at this pH after stirring and sonicating. The dissolution of the silica shell can be tracked by the TEM as shown in Figure 4.6.

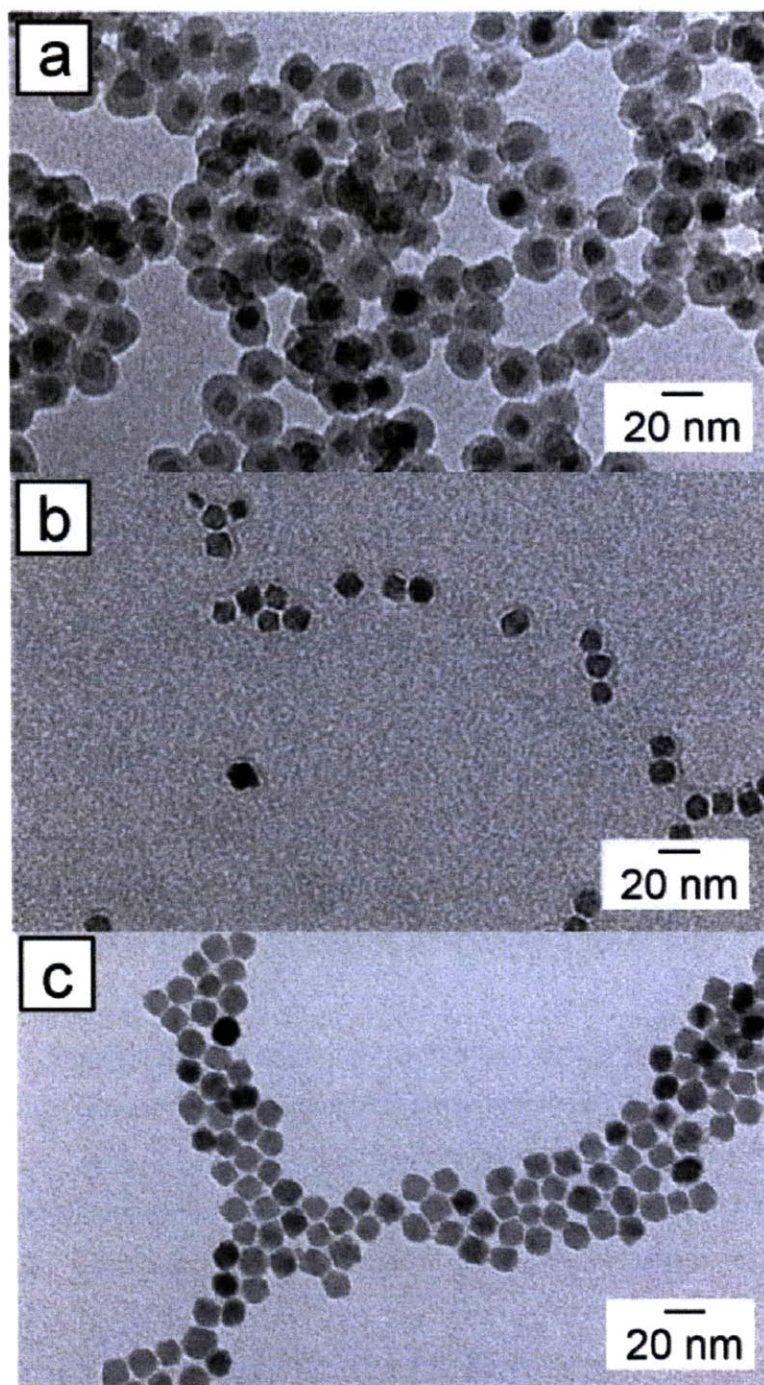


**Figure 4.6** TEM images of the thin-shelled MPs after exposed to basic solution (pH 9) at (a) 5 min, (b) 30 min, and (c) 1 h under sonication.

The dissolution of the silica shell took place at a relatively fast rate. Within 30 minutes after exposure to the basic solution, the silica shells had almost disappeared, as

shown in Figure 4.6b; in 1 hour the silica shells were completely dissolved, as shown in Figure 4.6c. This phenomenon is likely due to the loose and highly porous nature of the thin silica coating. This is one of the properties that must be considered when the thin silica-coated MPs are used.

However, the MPs with completely dissolved silica coatings show some significant properties in that they are dispersible in water-based solutions and stay colloiddally stable for an extended period. Further study of these MPs might be useful because their surfaces have been changed from hydrophobic (from their oleic acid surfactant) to hydrophilic without any added surfactants. Their hydrophilicity likely occurs due to the intrinsic properties of the iron oxide MPs, which indicates that the MPs are not coated with any surfactants at this point. The MPs at this state might be useful because their surfaces can be readily treated with any surfactants and can be manipulated easily.

The following sections discuss the use of the silica-coated MPs to prepared bi-functional nanoparticles, as proposed in the previous chapter. We propose that the nanostructures form by using the silica-coated MPs as a core and coating them with another silica shell that contains QDs. Two approaches to the formation of these nanostructures are discussed. In Section 4.3, QDs are *in situ* incorporated into a growing second silica shell, while in Section 4.4, QDs are attracted onto the silica-coated MPs before the growth of the second thin silica shell.

### **4.3 Incorporation of QDs into the silica shell of silica-coated iron oxides MPs**

In this section, the creation of a nanostructure comprising MPs, QDs, and silica is the main focus. The goal for preparing this type of nanostructure came from the previous section, which mentions an interest in having nanostructures of MPs and QDs smaller than 100 nm for biological applications. Based on the procedure used in Chapter 3 for incorporating QDs onto preformed silica microspheres, the silica-coated MPs could be used as the cores for this process. The resulting nanostructures can be smaller than 100 nm in diameter yet still comprise the needed MPs, QDs and silica compositions. The reaction scheme for preparation of these nanostructures is shown in Figure 4.7.



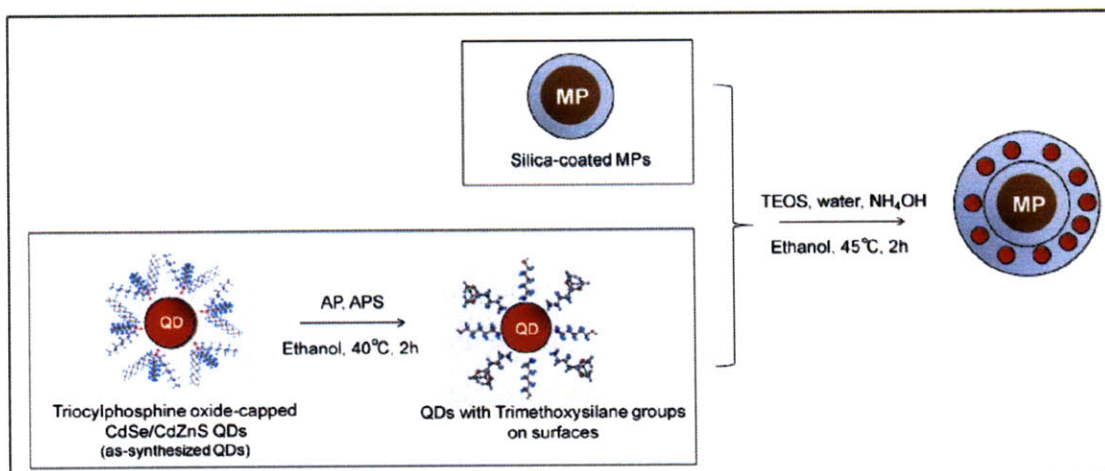


**Figure 4.7** Schematic representation of the QD incorporation into silica-coated MPs.

The process of incorporating QDs into the silica second shell is similar to the process discussed in Chapter 3. In this process, as shown in Figure 4.7, the two components were prepared separately. The silica-coated MPs were prepared using the reverse micro-emulsion process discussed earlier. The QDs were prepared to have trimethoxysilane groups on their surfaces and be dispersible in ethanol through a surfactant-exchanging process at 40°C for 2 hours as described in detail in Chapter 3 using a procedure previously reported.<sup>6,7</sup> After both components were prepared and dispersed in ethanol, the TEOS and ammonium hydroxide solution were added to start the silica growing process on the silica-coated MPs. The QDs were simultaneously included in the newly grown shell because their active methoxysilane groups can readily react with the silica precursor. After the reaction proceeded for 2 hours at 45°C, the process was stopped and the resulted nanostructures were separated from the reaction mixture using a centrifuge. The resulting QD-incorporated silica-coated MPs were re-dispersed and stored in ethanol. The TEM images of these nanostructures are shown in Figure 4.8.

The TEM images revealed that the combined nanostructures of QD-incorporated silica-coated MPs were obtainable using this process. As shown in Figure 4.8, the QDs inside the silica shell as well as the MP core at the center are clearly observed. The nanostructure was formed as proposed, and this is the first time that nanostructures of less

than 100-nm diameter comprising MPs, QDs, and silica were prepared. However, some degree of aggregation of these nanostructures can also be observed, as Figure 4.8a shows. This aggregation is due to the difficulty in controlling the silica shell growth on small particles because the small particles have a more active surface area and out-of-control cross-linking can take place.

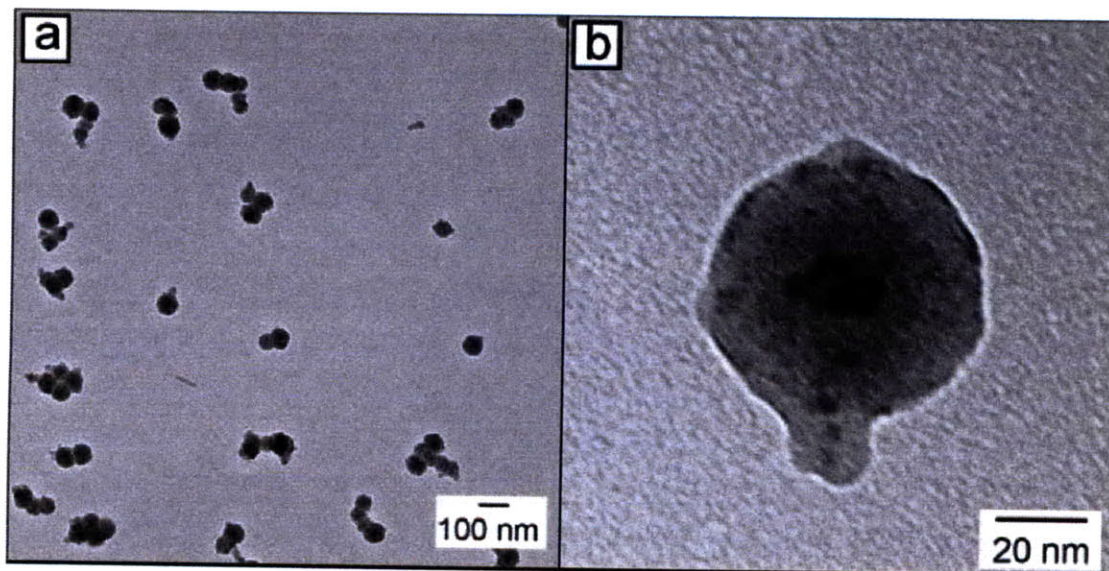


**Figure 4.8** TEM images showing the size distribution (a) and (b) close-up view of the resulting QD-incorporated silica-coated MP.

Although these QD-incorporated silica-coated MPs could be used in some biological applications, the aggregation problem might prevent them from being useful. An improved method for forming similar nanostructures is discussed in the following section.

#### **4.4 Decoration of QDs onto silica-coated MPs**

The aggregation problem that was observed in the previous section can be avoided by separating the incorporation of QDs from the growing of silica shells. This method was recently developed in our group and used for the decorating with the QDs of preformed silica microspheres.<sup>8</sup> The scheme for this process is shown in Figure 4.9.

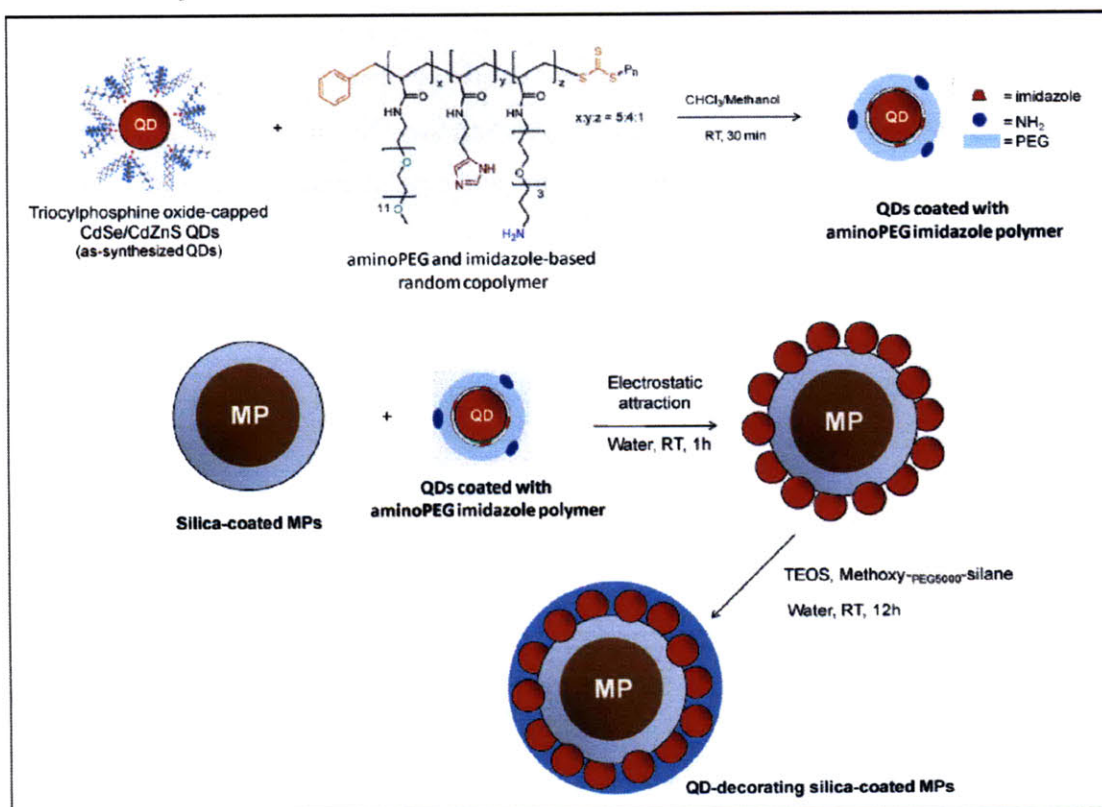


**Figure 4.9** Schematic representation of the QD decoration of the silica-coated MPs.

The success of this process comes from the ability of the QDs with amino-functionalized polyimidazole PEG polymer<sup>9</sup> as shown in the scheme to be electrostatically attracted to the silica-coated MP surfaces. In this process, the QDs were first added to the dispersion of silica-coated MPs in water. The positively charged QDs were attracted to the negative silica surfaces of the silica-coated MPs. Then a thin silica shell and PEG were coated onto the surface of the nanostructure to render the construction stable and to stabilize the nanostructure in water, respectively. After this process, the resulting nanostructures were purified by being precipitated out of the reaction mixture using a high-speed centrifuge, having excess QDs and some excess precursors discarded, and having the nanostructures re-dispersed in water. The TEM images of these QD-decorating silica-coated MPs are shown in Figure 4.10 and their hydrodynamic size distribution using DLS is shown in Figure 4.11.



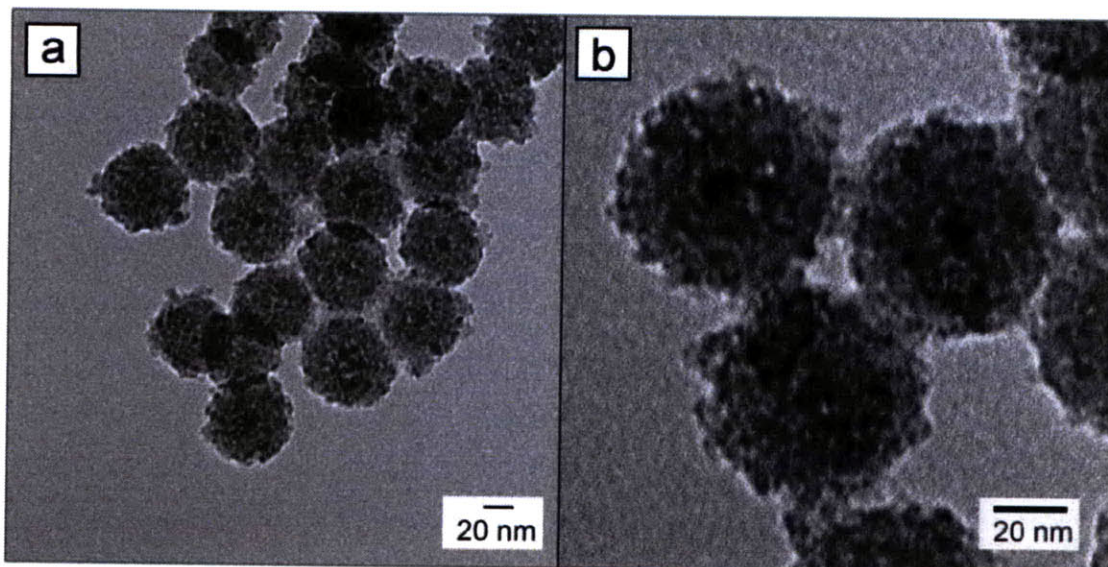


**Figure 4.10** TEM images of QD-decorating silica-coated MPs

The TEM images in Figure 4.10 revealed that the proposed structure of QD-decorating silica-coated MPs is obtainable using this procedure. Figure 4.10b clearly shows the QDs attached to the silica-coated MPs. The size of the QD-decorating silica-coated MPs shown by TEM is around 60-65 nm in diameters. Compared to the TEM images from the previous section, this process yielded particles with less extra silica coating extruding from the silica shells.

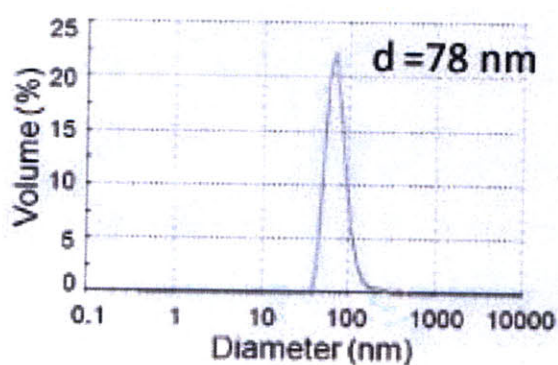


**Figure 4.11** Size distribution of QD-decorating silica-coated MPs (with 20-nm-thick silica shell) using DLS measurement.

According to DLS analysis, the QD-decorating silica-coated MPs average 78 nm in diameter. The diameter of these MPs increases from the size of the silica-coated MP core in Figure 4.3 by 10 nm, indicating that the second layer comprising QDs, a thin silica layer, and PEG is around 5nm thick. Also, no aggregation is observed in this sample in water, which indicates that these MPs are superior to nanostructures formed using the previous procedure. In the previous procedure in Section 4.3, the samples are so aggregated that signals from DLS showed random signals indicating large particles.

The demonstrations of the combined magnetic and fluorescent character of these QD-decorating silica-coated MPs are shown in Figure 4.12. The MPs are well-dispersed in water, and when they are precipitated down by centrifugation, the precipitate can be attracted and manipulated by a strong magnet as shown in Figure 4.12b. In both states, the fluorescence of the particles can be observed under UV light. These demonstrations could not be achieved unless both magnetic and fluorescent properties were combined and present in the same particle as these nanostructures.

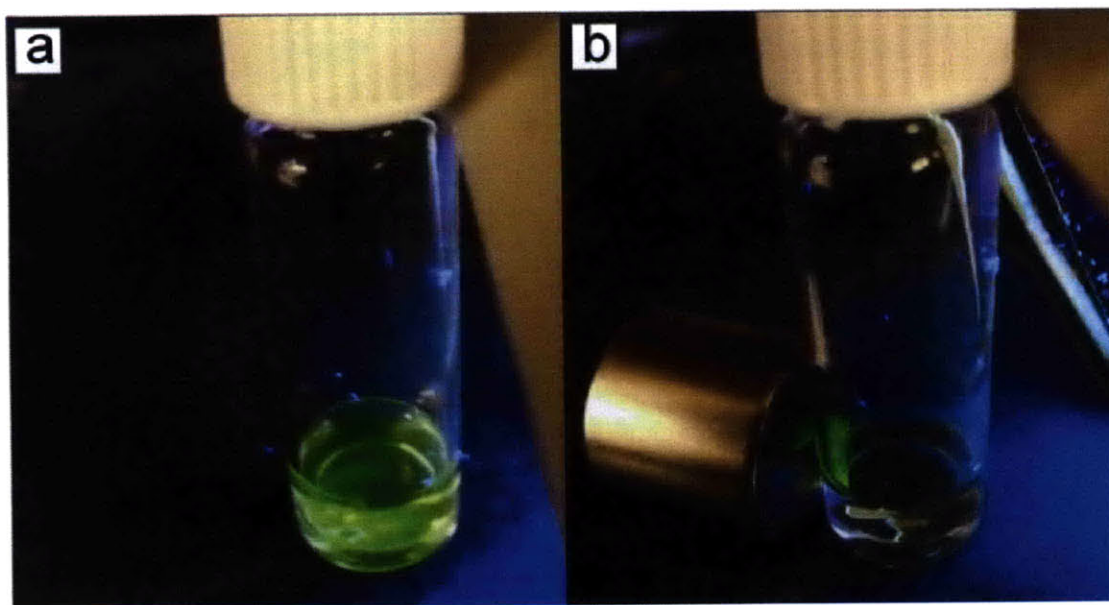


**Figure 4.12** Images of the QD-decorating silica-coated MPs under excitation by UV (a) in colloidal state without external magnetic field and (b) in pellet forms under magnetic field.



However, the magnetic properties of these silica-coated MPs with single MPs as cores are still too low to be attracted and manipulated individually in their colloidal state. The problem is that the loading of the MPs inside this structure is too low, resulting in nanostructures of low magnetization. The next section discusses possible procedures by which to increase the loading of the MPs inside these silica-coated nanostructures.

#### 4.5 Increase of MP loading: Use of the agglomeration of MPs

In order for the MPs and QD structures to increase in their magnetization, the amount of loaded MPs has to be increased. One approach to increasing the amount of the MPs in the reverse micro-emulsion process was performed by the addition of a small quantity of ethanol into the reaction mixture. Ethanol can dissolve all components in the reverse micro-emulsion process including the water phase, cyclohexane phase, and the Igepal CO-520, leading to some changes in the micelles size and structure. With these changes of the micelles, the silica-coated nanoparticles with more than one MP were obtained. Figure 4.13 shows TEM images of these nanoparticles.

The loading of MPs in the silica-coated nanoparticles increased as observed in Figures 4.13b and c. However, the distribution of the MPs in each particle is not uniform. Improvement on this issue must occur before these nanoparticles can be useful.

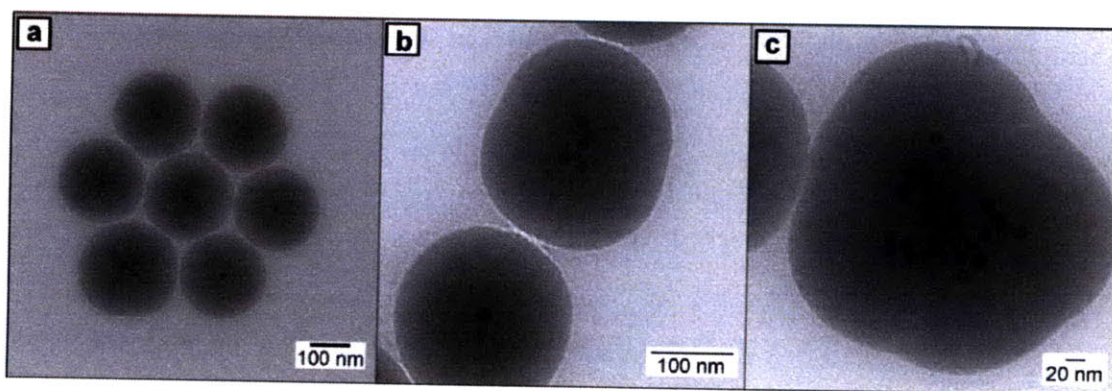


**Figure 4.13** TEM images of the silica-coated MPs with ethanol added during the reverse micro-emulsion, leading to formation of cores of multiple MPs and showing the size distribution (a) and multiple-MP cores.

Colloidal superparticles<sup>10</sup> of MPs are another candidate for use as the cores for silica coating. The superparticles can be formed by a controlled changing of the hydrophilicity of the solvents of the MPs in presence of a surfactant such as dodecyltrimethylammonium bromide (DTAB).<sup>10, 11</sup> This surfactant can transfer hydrophobic MPs into the water phase by forming the micelles of the MPs. Then, upon addition of another solvent, ethylene glycol, DTAB is dissolved into a new solvent system and the micelles are ruptured. After the micellar structures disappear, the MPs become aggregated in the water phase. In this reaction condition at a high temperature, the aggregations are relatively uniform, resulting in so-called superparticles. The scheme for preparation of these particles is shown in Figure 4.14 and the structures of these superparticles are imaged using TEM as shown in Figure 4.15.

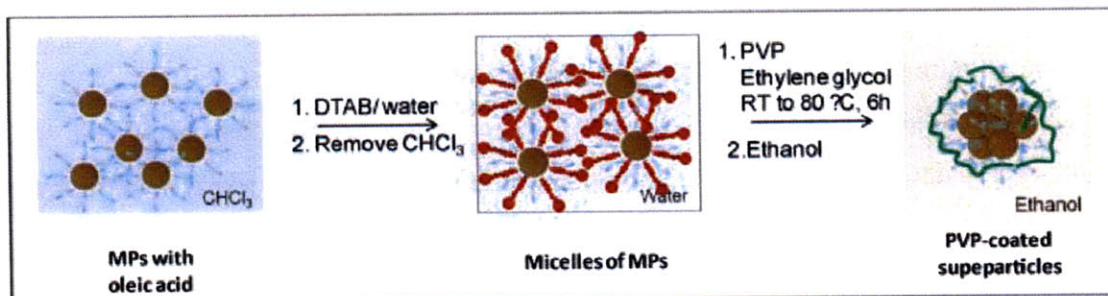


**Figure 4.14** Scheme for the process of colloidal superparticle preparation.



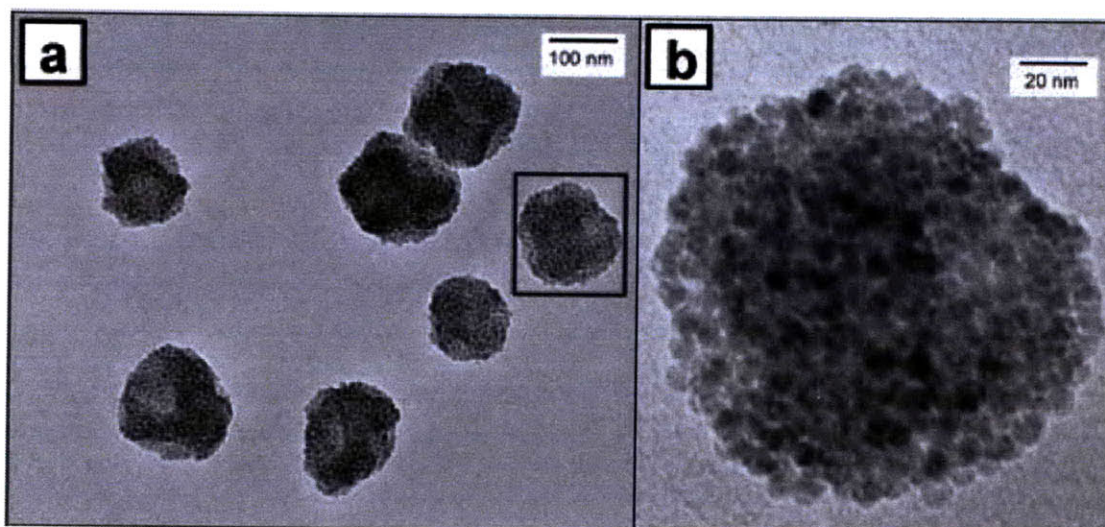


**Figure 4.15** TEM images of the colloidal superparticles show (a) size distribution and (b) the superlattice of the MPs inside the superparticles.

These superparticles can be potentially used as cores for the micro-emulsion process as they have hydrophobic surfaces that are compatible with the silica-coating process. The nanoparticles using these superparticles are proposed to have strong magnetization and could be useful in biological applications such as the experiments involving magnetically controlled movement of proteins mentioned in Chapter 3.

#### **4.6 Conclusion**

This chapter discusses the process of making silica-coated MPs through reverse-micro-emulsion. The thickness of silica can be controlled in the range of 10-25 nm. The thinnest shell that can obtain using this process is around 10 nm before incomplete coatings were observed.

The silica-coated MPs can be decorated with QDs, and the nanostructures of these QD-decorating silica-coated MPs are the smallest reported systems that are composed of MPs, QDs, and silica together in uniform distribution. These nanostructures can be useful for biological applications that require superparamagnetic and fluorescent silica-based nanostructures smaller than the microsphere systems discussed in Chapter 3. Chapter 7 discusses nanostructures comprising only MPs and QDs and aiming at formation of superparamagnetic and fluorescent systems of even smaller sizes.

#### 4.7 References

1. Zhu, Y. H.; Da, H.; Yang, X. L.; Hu, Y., Preparation and characterization of core-shell monodispersed magnetic silica microspheres. *Colloids and Surfaces a-Physicochemical and Engineering Aspects* **2003**, 231, (1-3), 123-129.
2. Muller-Schulte, D.; Schmitz-Rode, T.; Borm, P., Ultra-fast synthesis of magnetic and luminescent silica beads for versatile bioanalytical applications. *Journal of Magnetism and Magnetic Materials* **2005**, 293, (1), 135-143.
3. Yi, D. K.; Selvan, S. T.; Lee, S. S.; Papaefthymiou, G. C.; Kundaliya, D.; Ying, J. Y., Silica-coated nanocomposites of magnetic nanoparticles and quantum dots. *Journal of the American Chemical Society* **2005**, 127, (14), 4990-4991.
4. Selvan, S. T.; Tan, T. T.; Ying, J. Y., Robust, non-cytotoxic, silica-coated CdSe quantum dots with efficient photoluminescence. *Advanced Materials* **2005**, 17, (13), 1620-1625.
5. Yi, D. K.; Lee, S. S.; Papaefthymiou, G. C.; Ying, J. Y., Nanoparticle architectures templated by SiO<sub>2</sub>/Fe<sub>2</sub>O<sub>3</sub> nanocomposites. *Chemistry of Materials* **2006**, 18, (3), 614-619.
6. Chan, Y.; Zimmer, J. P.; Stroh, M.; Steckel, J. S.; Jain, R. K.; Bawendi, M. G., Incorporation of luminescent nanocrystals into monodisperse core-shell silica microspheres. *Advanced Materials* **2004**, 16, (23-24), 2092-2097.
7. Insin, N.; Tracy, J. B.; Lee, H.; Zimmer, J. P.; Westervelt, R. M.; Bawendi, M. G., Incorporation of iron oxide nanoparticles and quantum dots into silica microspheres. *ACS Nano* **2008**, 2, (2), 197-202.
8. Popovic Z, L. W., Chauhan V. P, Lee J, Wong C, Greytak AB, Insin N, Nocera DG, Fukumura D, Jain RK and Bawendi MG, A Nanoparticle Size Series for In Vivo Fluorescence Imaging. *Angewandte Chemie International Edition* **2010**, 49, (46), 8649-8652.
9. Liu, W. H.; Greytak, A. B.; Lee, J.; Wong, C. R.; Park, J.; Marshall, L. F.; Jiang, W.; Curtin, P. N.; Ting, A. Y.; Nocera, D. G.; Fukumura, D.; Jain, R. K.; Bawendi, M. G., Compact Biocompatible Quantum Dots via RAFT-Mediated Synthesis of Imidazole-Based Random Copolymer Ligand. *Journal of the American Chemical Society* **2010**, 132, (2), 472-483.
10. Zhuang, J. Q.; Wu, H. M.; Yang, Y. G.; Cao, Y. C., Controlling colloidal superparticle growth through solvophobic interactions. *Angewandte Chemie-International Edition* **2008**, 47, (12), 2208-2212.

11. Zhuang, J. Q.; Wu, H. M.; Yang, Y. A.; Cao, Y. C., Supercrystalline colloidal particles from artificial atoms. *Journal of the American Chemical Society* **2007**, *129*, 14166-14167.



## **Chapter 5**

### **Surface Modification of Iron Oxide Nanoparticles using Hydrophobically-modified Acrylic Acid**

#### **5.1 Introduction**

As mentioned in Chapter 1, iron oxide MPs are useful in various biological systems. For these applications, the MPs have to be at least dispersible in water-based solutions and stable in physiological environments. The better-quality MPs are also high in T2 relaxivity to be better MRI contrast agents. The improvements in the properties of iron oxide MPs include making the particles stable in water, small in hydrodynamic size, and in possession of available functional groups for further conjugations to molecules and proteins of interest.

One of our motivations for synthesizing iron oxide MPs of very small size is their potential application in MRI sensing. The goal of this project is to use magnetic resonance imaging (MRI) to probe calcium ions in the nervous system on a cellular scale. The mechanism of calcium-sensing is based on changes in MR images when agglomeration of a T2 contrast agent, such as MP, takes place.<sup>1-3</sup> This MP agglomeration mechanism employs the formation of complex of the protein calmodulin (CaM) and the peptide RS20 in the presence of calcium ions.<sup>3-5</sup> For this project, MPs need to be modified to become stable in water in physiological environment, have a hydrodynamic size of less than 15 nm in diameter, and have a functional group that can be covalently attached to CaM and RS20 molecules. The schematic representation of this calcium-sensing mechanism is shown in Figure 5.1.

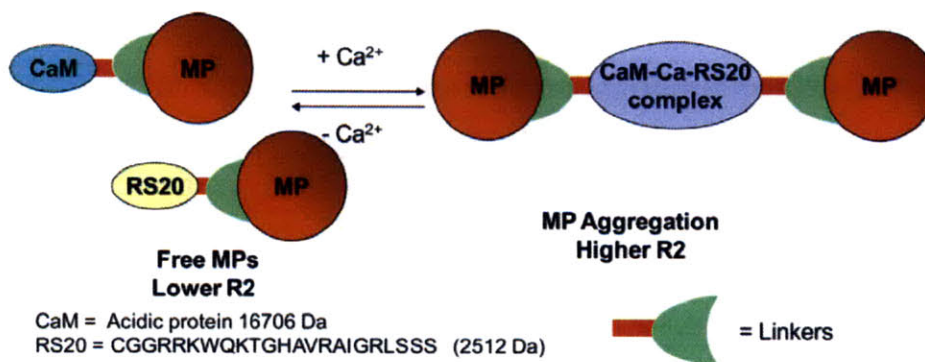


**Figure 5.1** The mechanism for calcium-sensing using MRI.

For these proposed properties, the MP surfaces have to be modified. Two main groups of surfactants have been used for transferring hydrophobic MPs into water-based solutions. The first type of these surfactants is amphiphilic molecules that can lead to formation of micelles around the MP particles. The second type, which will be discussed in more detail in Chapter 6, is the hydrophilic surfactants that can replace the native oleic acid on MP surfaces and directly bind to the MPs to make them hydrophilic. This chapter focuses mainly on the surfactants of the first type.

Amphiphilic molecules that have been used as MP surfactants include phospholipids and amphiphilic polymers.<sup>6-8</sup> The advantage of these types of surfactant is that the process for transferring MPs into water does not interfere with the native oleic acid surfactants, leading to the observation that the magnetization of the MPs could stay intact. The surfactants of these types tend to yield MPs with higher magnetization compared to the surfactants that interact directly with the MP surfaces.

The surfactant that is the main topic in this chapter is the hydrophobically-modified polyacrylic acid (mPAA).<sup>8</sup> The choice of an mPAA for use in dispersing MPs into water arises for two main reasons. First, the polyacrylic acid is cheap compared to phospholipids, and the synthesis of hydrophobically-modified polyacrylic acid can be done in a one-step reaction. Second, the molecular weight of the mPAA is low and would make the hydrophilic MPs of small hydrodynamic size. The following sections discuss mPAA preparation and the process of transferring the MPs into water.



## 5.2 Preparation of hydrophobically-modified polyacrylic acid

Hydrophobically-modified polyacrylic acid (mPAA) was synthesized using a modified process previously reported.<sup>7, 8</sup> In this process, the polyacrylic acid of ~2000 Da molecular weight formed an amide bond with octylamine using EDC (1-ethyl-3-(3-dimethylaminopropyl)carbodiimide) as an activating agent. The ratio between the carboxylic groups of the precursor and the octylamide groups was maintained between 7:3 and 6:4 in order to obtain co-polymers that could serve as good amphiphilic surfactants for the MPs. The reaction scheme and the structure of mPAA are shown in Figure 5.2.

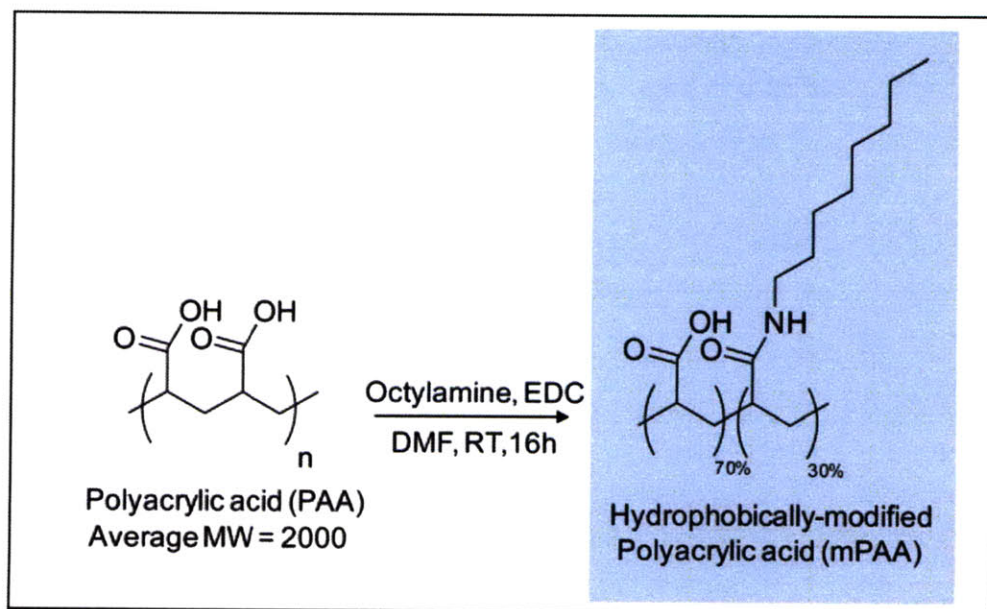


**Figure 5.2** Reaction scheme for synthesis of mPAA.

IR absorption spectra were used to track the progress of the reaction. The mPAA has an additional carbonyl peak from the amide bond at wave number  $1683\text{ cm}^{-1}$  in comparison to polyacrylic acid, which absorbs only one carbonyl peak at  $1732\text{ cm}^{-1}$  as shown in Figure 5.3.

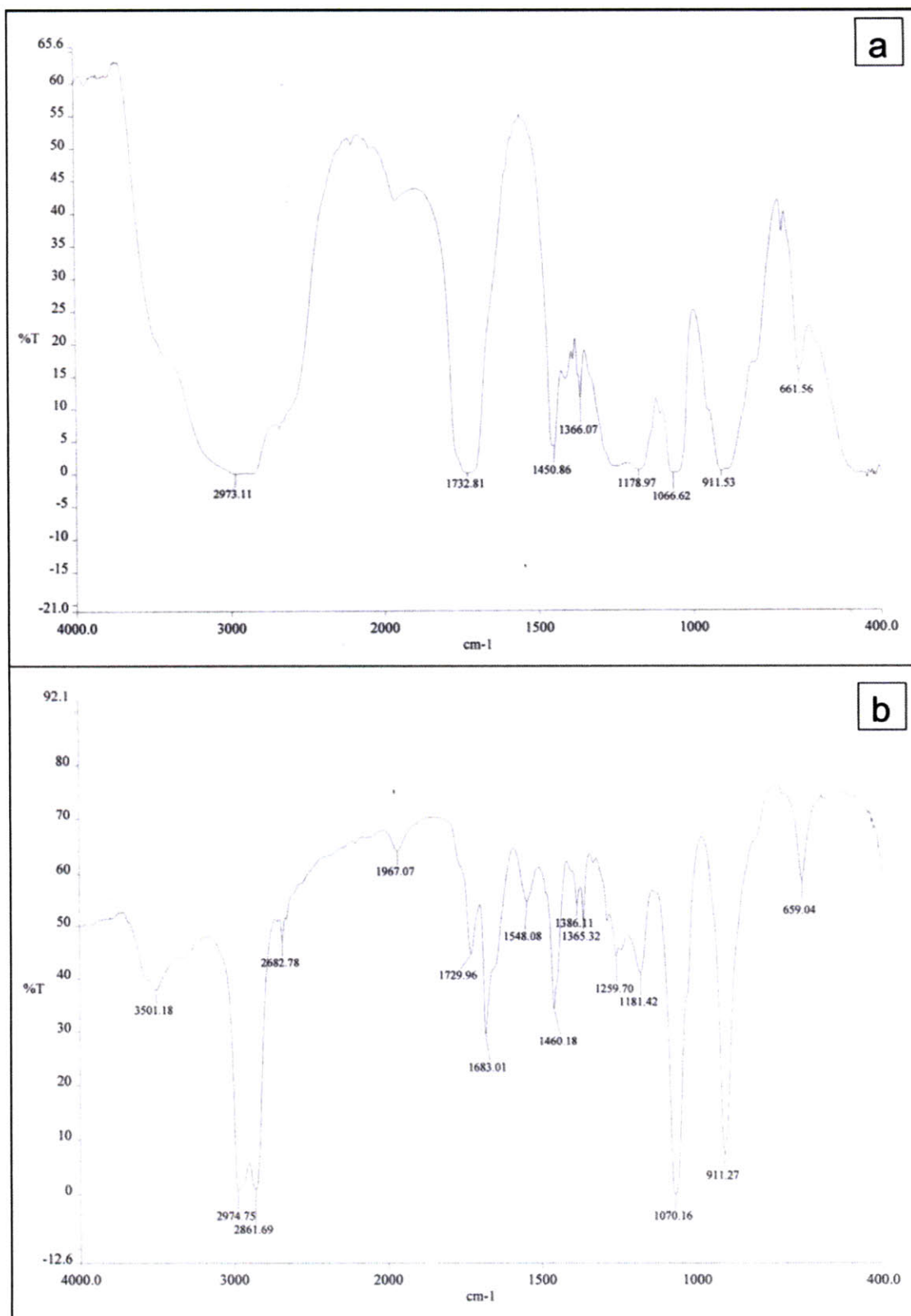


**Figure 5.3** Infrared transmission spectra of a) polyacrylic acid and b) mPAA.

After the mPAA surfactant was prepared, the next important step was the formation of the mPAA-MPs micelles. This step is critical because the micellar structures have to be formed in order for the MPs to be transferrable into water. The details of the formation of micellar MP-mPAAs are discussed in the following section.

*Experimental Details:*

Hydrophobically-modified polyacrylic acid (mPAA) synthesis: Polyacrylic acid (1800 Da molecular weight, 1 g) was dissolved in dimethylformamide (DMF, 10 mL). n-Octylamine (0.72g) were added into the solution. The reaction mixture was stirred for 15 minutes before EDC (1.06 g) was added. The reaction mixture was stirred at room temperature for 16h. DMF was then removed under reduced pressure before the 2 mL of water was added to precipitate out the mPAA. The precipitate was washed three more times with water. The mPAA were then re-dissolved into 4 mL of ethylacetate and the solution was then added 2 mL of water and 1 g of tetramethylammonium hydroxide and stirred for 2h. The reaction mixture was then added 4 mL of 1.3 M hydrochloric acid to re-precipitate the mPAA and the supernatant were removed. The purified mPAA were then dissolved and kept in ethylacetate. Before the use of the mPAA, tetramethylammonium hydroxide in methanol was added into the mPAA solution to adjust the pH of the mPAA to pH 8-9 before undergoing the surface modification process.

### **5.3 Preparation of iron oxides MPs with mPAA on their surfaces**

The critical step for applying the mPAA surfactant to MPs is the micelle-forming step. Because the mPAA possesses many carboxylic groups, the direct binding of the carboxylic to the MPs could also take place competitively with the micelle formation. The scheme for transferring MPs into a water-based solution is shown in Figure 5.4.

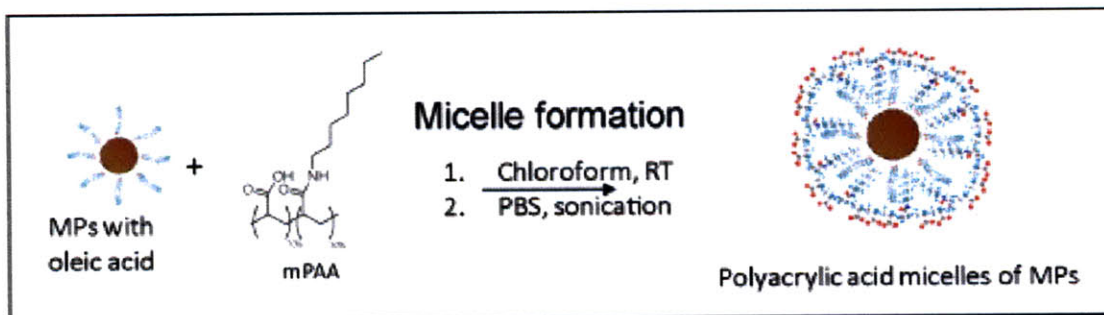


**Figure 5.4** Schematic representation of the preparation of mPAA-coated MPs.

As shown in the scheme, the MPs with oleic acid were first mixed with mPAA in chloroform. This procedure includes two critical steps. First, as mentioned in the previous section about the synthesis of mPAA, the final mPAAs must be in deprotonated form by adjustment of the final product to pH 9. These mPAAs, of which carboxylic acid groups are mostly in the carboxylated form, are hydrophilic and did not bind to the MPs. The second critical step is the micelle formation. In this step, the original solvent, chloroform, was slowly removed under reduced pressure. After thin films of mPAA-MPs were obtained, the PBS solution was then added into the reaction mixture dropwise during sonication. This critical step was performed in order to ensure that the micelles could be formed. Any abrupt change in concentration or dilution of the sample to a very low concentration can lead to the aggregation of the MPs.

After being transferred into the PBS solution, the mPAA-MPs were characterized using TEM, gel filtration chromatography, and dynamic light scattering. The results from these analyses are shown in Figures 5.5, 5.6a, and 5.6b, respectively.



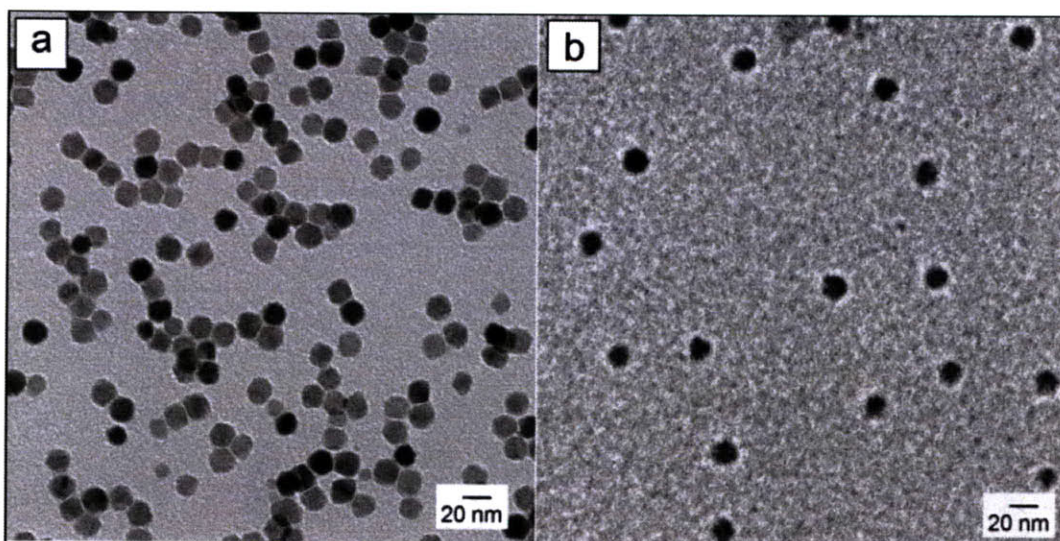


**Figure 5.5** TEM images of MPs (a) before and (b) after being coated with mPAA.

The TEM images in Figure 5.5 indicate that the mPAA-MPs in the PBS solution were well dispersed because there was no aggregation observed in the TEM images. After being transferred into the PBS solution (Figure 5.5b), the MP cores retain the same size as the MP cores before the micelles-formation process (Figure 5.5a). The similarity in size before and after the surface modification process indicates that this process is minimally destructive to the MPs. This finding is foreseeable because the surface modification of MPs using the micelle formation process does not involve replacing the native oleic acid surfactant, but instead coats the MPs with another amphiphilic polymer. The stability of the cores that are shown in TEM images suggests that the magnetization of the MPs and T2 relaxivity remain high, which will be discussed later.

Using the gel filtration chromatogram in Figure 5.6a, the hydrodynamic diameter of the resulting mPAA-MPs was calculated to be 10.5 nm in diameter. This hydrodynamic size was determined by fitting the retention time of the MPs into the calibration curve formed using four protein standards of different sizes (from largest to smallest proteins: thyroglobulin 18.8 nm, alcohol dehydrogenase 10.1 nm, ovalbumin 6.12 nm, and lysozyme 3.86 nm). The GFC was performed using Superose 6 (Amersham) as the stationary phase and the PBS solution as the mobile phase. The majority of the mPAA-MPs fell in the range of the standard curve and correspond to 10.5 nm in diameter. However, there are some small signals of aggregation observed at the

very beginning of the chromatogram. This experiment indicates that the water-dispersible MPs with hydrodynamic diameter less than 15 nm can be obtained using this mPAA-MP system.

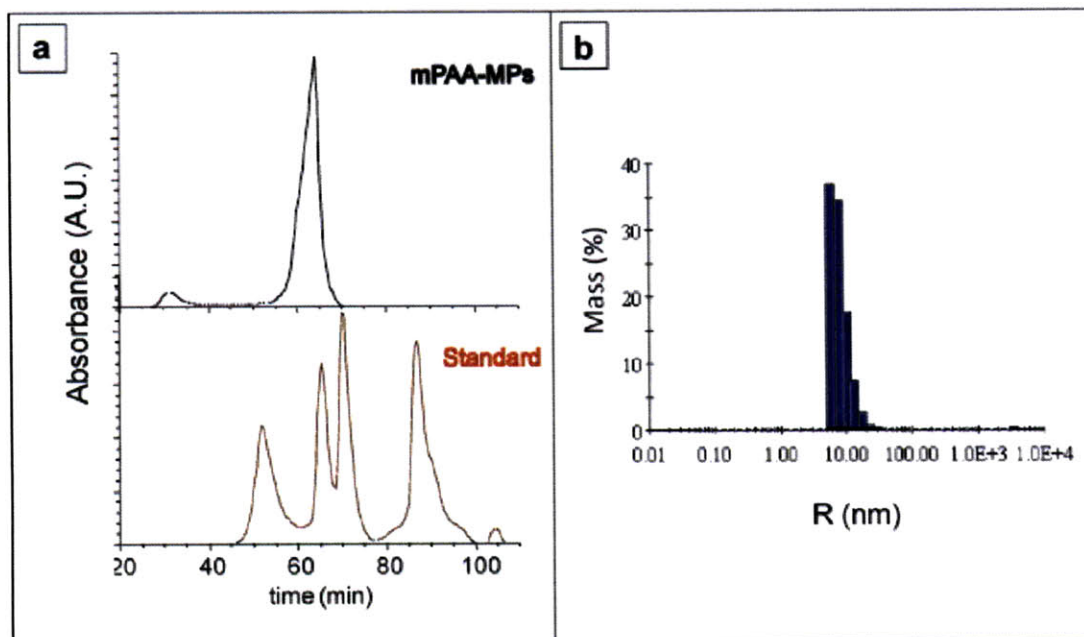


**Figure 5.6** Size determinations of mPAA-coated MPs using (a) gel filtration chromatography and (b) DLS measurements.

The hydrodynamic size indicated by using the GFC chromatography is based on the assumption that no physical or chemical interaction occurs between the carbohydrate-based stationary phase in the column and the nanoparticles other than size exclusion. However, that ideal situation might not be reached, and it is likely that the interaction between the MPs and the standard proteins to the stationary phase is significantly different. Therefore, there is some error in the size of the MPs determined using this method.

Another conventional method for determining the hydrodynamic size is dynamic light scattering (DLS) analysis. The size distribution of the mPAA-MPs obtained using this instrument is shown in Figure 5.6b. In the DLS analysis, the mPAA-MPs are mostly 8.6 nm in radius with a small signal (0.1 mass%) of large aggregated particles at 3500 nm. The size distribution from the DLS is somewhat different from that in the GFC

analysis, but it follows the same trend in that most of the particles are small and non-aggregated with a small population of aggregated particles.

The size distribution analysis of the mPAA-MPs indicates that the resulting MPs have a small hydrodynamic size compared to those in commercial superparamagnetic nanoparticles with dextran and phospholipid coating.<sup>9</sup> In addition, the stability of the mPAA-MPs is significantly higher because they are stable in the PBS solution for extended periods as long as six months without changes in their size. Given these properties, the mPAA-MPs are suitable for many experiments and especially for MRI sensing, which requires MPs of small size and high stability.

Functionalization of the mPAA-MPs is another aspect that needs to be considered. In order for the MPs to be used, the surfaces of the MPs have to be active for functionalization without changing the size and their stability after conjugation with new molecules. In this mPAA system, the carboxylic groups on the surface of the MPs can act as active functional groups, but the functionalization has to be limited because the solubility of the MPs can be reduced and the aggregations are observed when large ratios of carboxylic groups are converted. Moreover, in many cases, the carboxylic group is not compatible with the available functional groups in the proteins or molecules of interest.

The other functional group that is widely used for conjugation is the amine group. In many cases, the amino group is more compatible than the carboxylic group in some specific conjugations. In order to introduce an amino group into the mPAA-MPs without losing the MPs' stability in water with the decrease in carboxylic groups, a polyethylene glycol (PEG) chain was employed to help maintain stability. As mentioned in Chapter 3, PEG is known to be hydrophilic and can maintain the stability of nanoparticles in water-based solutions. Another reason for including a PEG chain in the amino-functionalization process is that the PEG chain can increase the space between the MPs and the amino group, leading to less steric hindrance for the conjugation with the amino group at the end of the PEG chain.

The mPAA-MPs can be functionalized to have an amino group available for conjugation with other molecules of interests. Here we introduce the amino group onto the mPAA surface by means of an EDC coupling reaction between the carboxylic groups of mPAA-MPs and diamino-PEG as shown in the scheme in Figure 5.7



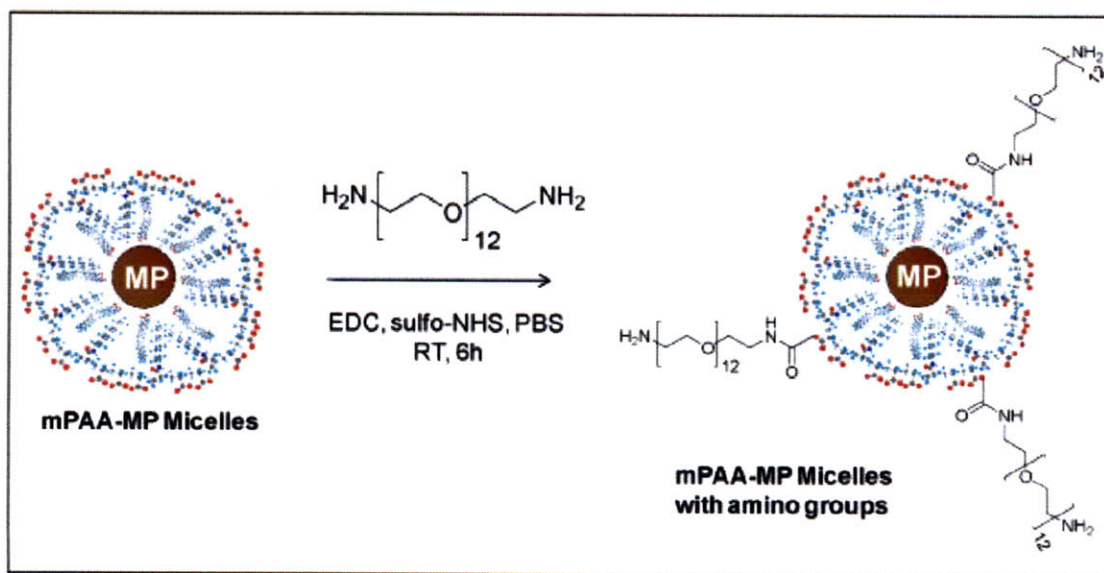


**Figure 5.7** Reaction scheme for applying amino-PEG groups onto mPAA-MPs.

The reaction for introducing amino groups onto mPAA-MPs surfaces proceeded at room temperature in the PBS solution for 6 hours. The large excess (20× equivalent) of diaminoPEG (600 Da molecular weight) was added to the reaction mixture in order to prevent cross-linking between the MPs. The EDC and sulfo-NHS were added to facilitate amide bond formation between the carboxylic group of the mPAA and amino group on one end of the diaminoPEG, leaving the amino group at the other end as an available functional group. Six hours after reaction, the excess diaminoPEG and other by-products were removed from the reaction mixture by means of thorough dialysis using a centrifugal filter with a 50 KDa molecular weight cut-off membrane. The resulting amino-functionalized mPAA-MPs were kept in a PBS solution for further use.

The resulting amino-functionalized mPAA-MPs were tested to verify the availability of the amino group by being reacting with fluorescamine. The fluorescent product detected from the reaction of the MPs with fluorescamine indicates that this conjugation procedure can yield mPAA-MPs with available amino groups for further conjugations.

Size distributions of the MPs after they were functionalized with diaminoPEG were analyzed by TEM (Figure 5.8b) and DLS (Figure 5.8c). The TEM images show that the amino-functionalized mPAA-MPs are similar to the mPAA-MPs before the



functionalization with diaminoPEG in that the size distribution of MP cores still does not change from that of the MP cores before the mPAA coating and amino-functionalization (Figure 5.8a). Also, there is no aggregation and excess PEG and by-product molecules observed in the TEM images in Figure 5.8b. This finding indicates that the functionalization process has little or no effect on the MP cores and the stability of the mPAA-MPs.

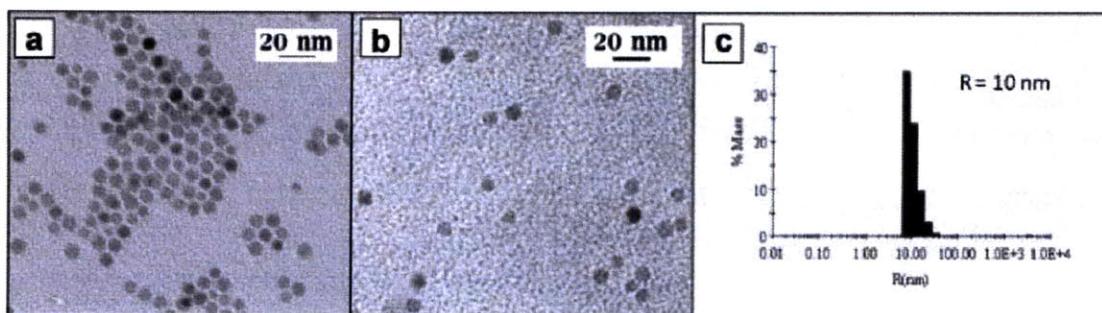


**Figure 5.8** (a,b) TEM images of amino-functionalized mPAA-MPs (b) compared to that of the MPs before being coated with mPAA (a); and (c) size distributions of the mPAA measured using a DLS instrument.

Size distribution of the amino-functionalized mPAA-MPs was also determined by DLS analysis. The size distribution of the MPs is shown in Figure 5.8c. The DLS analysis showed that the hydrodynamic size of the mPAA-MPs after being functionalized with diaminoPEG was a few nanometers larger than that of the original mPAA-MPs. The increase in the size is likely due to the attachment of a long PEG chain onto the MP surfaces. The DLS also showed no observable aggregation of the MPs even after the functionalization. This result suggests a high stability of the mPAA-MPs, implying that they are suitable for applications that require small MPs with high stability.

Another property of the MPs that is important for biological applications is their high T2 relaxivity for being a good T2 contrast agent. The relaxivity of amino-functionalized mPAA-MPs was measured and compared to the relaxivity of other commercial T2 and a currently used contrast agent as displayed in Table 5.1.<sup>9</sup>

**Table 5.1** Properties of amino-functionalized mPAA-MPs compared to commercial T2 contrast agents.<sup>9</sup>

Name	Core Materials	Surface	Diameter of Core (nm)	Hydrodynamic Diameter (nm)	R2 (mM <sup>-1</sup> s <sup>-1</sup> )
Ferumoxides (Feridex)	Fe <sub>3</sub> O <sub>4</sub> , γ-Fe <sub>2</sub> O <sub>3</sub>	Dextran	4.96	160	120
Ferucarbotran (Resovist)	Fe <sub>3</sub> O <sub>4</sub>	Carboxy-dextran	4	60	186
Ferumoxtran (Combidex)	Fe <sub>3</sub> O <sub>4</sub>	Dextran	5.85	35	65
Amino-mPAA-MPs	γ-Fe <sub>2</sub> O <sub>3</sub>	mPAA, aminoPEG	7	20	260

Compared to currently used and commercial available T2 contrast agents, the mPAA-MPs are superior in that they are smaller in hydrodynamic size and much higher in T2 relaxivity. The smaller size of the MPs compared to other systems comes from the nature of the mPAAs: they are more compact and smaller in molecular weight than the dextran coatings. The rise in T2 relaxivity originates from the high magnetization of the MP cores because they are synthesized using a solvothermal process, leading to higher crystallinity and higher magnetization than those MP cores synthesized in low-temperature aqueous systems. Moreover, as mentioned earlier, because the surface modification process has minimal effects on the MP cores, the magnetization of the MP is likely to remain high. In addition, the mPAA-MPs are functional as they contain both carboxylic groups and amino groups for further conjugations.

The mPAA-MPs with small size, high T2 relaxivity, and availability of functional groups on the surface are suitable for biological applications. As mentioned in the first section of this chapter, one of the applications for these MPs is use in MRI calcium-sensing. The next section discusses the conjugation of the mPAA-MPs with the protein for calcium-sensing.

#### 5.4 Bio-conjugation of the mPAA coated MPs

(This work is done in collaboration with Tatjana Atanasijevic, Jasanoff Group, Department of Nuclear Engineering, MIT)

Conjugation of the mPAA-MPs to proteins of interest is one of the critical steps in making use of the resulting MPs. This section focuses on the proteins calmodulin (CaM) and peptide RS20 in order to reach the goal of using mPAA-MPs as a contrast agent for MRI sensing. However, the technique and conjugation scheme used here can be readily applied to other systems.

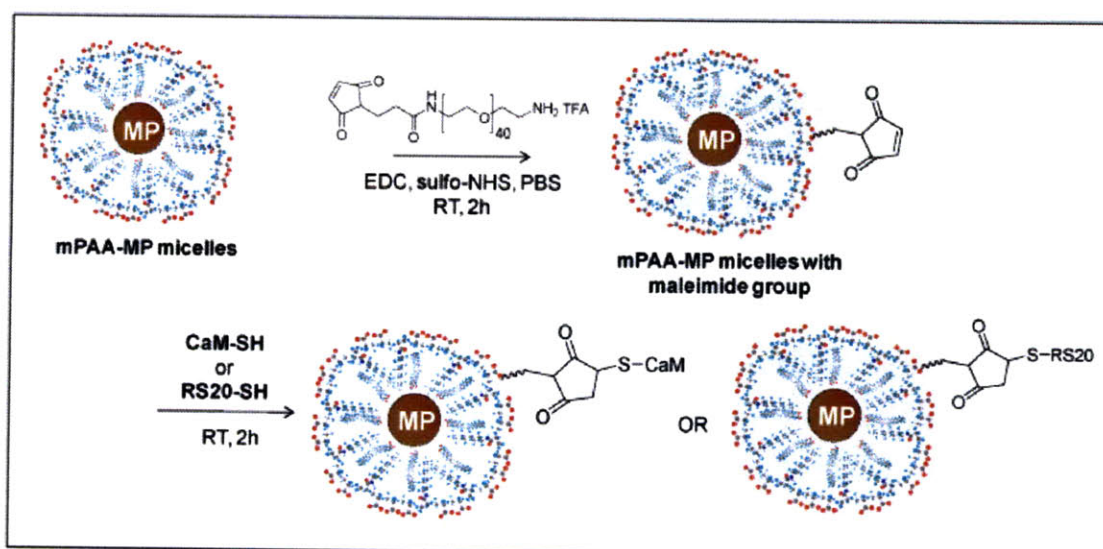


**Figure 5.9** Schematic representation of the bio-conjugation of mPAA-coated MPs.

The reaction scheme for the conjugation of the mPAA-MPs to calmodulin and peptide RS20 is shown in Figure 5.9. The conjugation is based on the use of a cross-linker molecule, maleimide-PEG-NH<sub>2</sub> (Creative PEGWorks, Inc, 2000 Da molecular weight), which forms an amide bonding with the carboxylic group and leaving the maleimide group for further conjugations with the MPs. The amide bonds between carboxylic groups of the mPAA and amino groups of the cross-linker molecule were formed in the presence of EDC and sulfo-NHS. The CaM and RS20 are chemically-modified to possess available thiol groups. The coupling between maleimide and thiol groups leads to the conjugation of the MPs with CaM and RS20. The reaction mixtures

were then purified by means of centrifugal dialysis. The control groups for this conjugation were performed without addition of the cross-linker molecules in order to illustrate the non-specific binding of the biomolecules to the mPAA-MPs.

The protein conjugations to the MPs were monitored by using a UV-visible spectroscope. For the conjugates, both bio-molecules (CaM and RS20) have strong absorption at around 280 nm and show their absorption features in addition to the MP absorption spectra. The absorption spectra of the MP-biomolecule conjugates are shown in Figure 5.10.

The absorption spectra of the MP-CaM conjugate in Figure 5.10a suggest that the conjugation between the MPs and CaM using this reaction scheme was successful because the strong absorption feature of CaM was observed to be significantly higher than that for the control group. However, when comparisons were made between the absorption spectra of mPAA-MPs and that of the control mixture of mPAA-MPs and CaM, non-specific binding of CaM to the MPs was clearly observed.

In the case of the MP-RS20 conjugate, the non-specific binding of RS20 to the MPs is more severe, as the absorption feature of the RS20 was nearly equally observed in the conjugate and in the control mixture. The increase in non-specific binding of RS20 compared to that of CaM probably arises from the highly positively-charged nature of the RS20, as can be seen from its peptide sequences in Figure 5.1.

The conjugates of MP-CaM and MP-RS20 cannot function in the MRI calcium-sensing experiment because they did not agglomerate and form MP clusters in the presence of calcium as proposed. The loss of sensing activity probably arises from the fact that the non-specific binding of the CaM and RS20 to the MPs blocks the active sites of CaM and RS20 because the conjugating sites of the MP are no longer controllable. The modification to reduce the non-specific binding must be done before the mPAA-MP system can be useful in this type of experiments.

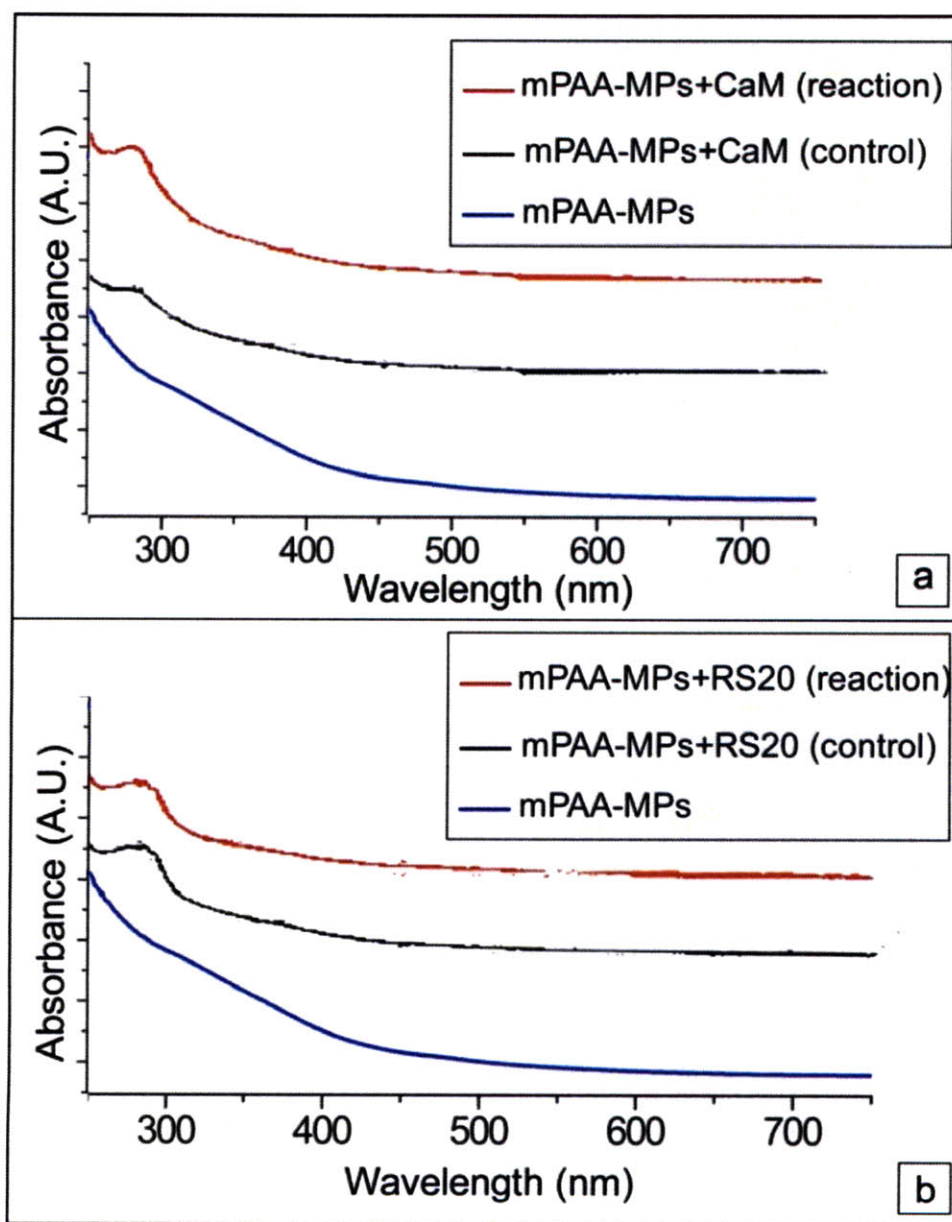


**Figure 5.10** Absorption spectra of the MPs conjugation with a) camodulin and b) RS20 peptide.

This bio-conjugation study suggests that the mPAA-MPs are not suitable for biological experiments involving high concentrations of proteins. The highly negatively charged surfaces of the mPAA-MPs are probably the main reason for their proneness to protein-non-specific binding. Reducing the negative charge while maintaining the stability of the MPs could be the solution for the mPAA-MP systems with low non-



specific binding. However, the development of other surface modifications for MPs discussed in the next chapter may create other candidates for application in biological systems.

## 5.5 Conclusion

Surface modification of MPs using hydrophobically-modified polyacrylic acid (mPAA) yields MPs that are transferrable into, and stable in, water-based solutions. The mPAA-MPs are superior to the commercial and currently used T2 contrast agents in that they are small and have very high T2 relaxivity. The stability of the mPAA-MPs in water-based solutions is also significantly high in terms of long-term storage and further surface modifications.

The limitation of these mPAA-MPs systems is that their stability in water is based on the negative charges on their surfaces. Therefore, the mPAA-MPs are not stable at low pH and tend to aggregate at pH lower than 5. Also, the highly negatively charged surfaces lead to protein and biomolecule non-specific binding. Making surface modifications to reduce the charge while maintaining the stability and the hydrodynamic size is one possible approach to improve the mPAA-MPs systems. However, there are also possible approaches for making MPs with small hydrodynamic size, high stability and minimal protein non-specific binding, which are discussed in Chapter 6.

## 5.6 References

1. Berret, J. F.; Schonbeck, N.; Gazeau, F.; El Kharrat, D.; Sandre, O.; Vacher, A.; Airiau, M., Controlled clustering of superparamagnetic nanoparticles using block copolymers: Design of new contrast agents for magnetic resonance imaging. *Journal of the American Chemical Society* **2006**, 128, (5), 1755-1761.
2. Atanasijevic, T.; Shusteff, M.; Fam, P.; Jasanoff, A., Calcium-sensitive MRI contrast agents based on superparamagnetic iron oxide nanoparticles and calmodulin. *Proceedings of the National Academy of Sciences of the United States of America* **2006**, 103, (40), 14707-14712.
3. Atanasijevic, T.; Jasanoff, A., Preparation of iron oxide-based calcium sensors for MRI. *Nature Protocols* **2007**, 2, (10), 2582-2589.



4. Miyawaki, A.; Llopis, J.; Heim, R.; McCaffery, J. M.; Adams, J. A.; Ikura, M.; Tsien, R. Y., Fluorescent indicators for Ca<sup>2+</sup> based on green fluorescent proteins and calmodulin. *Nature* **1997**, 388, (6645), 882-887.
5. Ozawa, T.; Sasaki, K.; Umezawa, Y., Metal ion selectivity for formation of the calmodulin-metal-target peptide ternary complex studied by surface plasmon resonance spectroscopy. *Biochimica Et Biophysica Acta-Protein Structure and Molecular Enzymology* **1999**, 1434, (2), 211-220.
6. Nitin, N.; LaConte, L. E. W.; Zurkiya, O.; Hu, X.; Bao, G., Functionalization and peptide-based delivery of magnetic nanoparticles as an intracellular MRI contrast agent. *Journal of Biological Inorganic Chemistry* **2004**, 9, (6), 706-712.
7. Snee, P. T.; Somers, R. C.; Nair, G.; Zimmer, J. P.; Bawendi, M. G.; Nocera, D. G., A ratiometric CdSe/ZnS nanocrystal pH sensor. *Journal of the American Chemical Society* **2006**, 128, (41), 13320-13321.
8. Wu, X. Y.; Liu, H. J.; Liu, J. Q.; Haley, K. N.; Treadway, J. A.; Larson, J. P.; Ge, N. F.; Peale, F.; Bruchez, M. P., Immunofluorescent labeling of cancer marker Her2 and other cellular targets with semiconductor quantum dots. *Nature Biotechnology* **2003**, 21, (1), 41-46.
9. Na, H. B.; Song, I. C.; Hyeon, T., Inorganic Nanoparticles for MRI Contrast Agents. *Advanced Materials* **2009**, 21, (21), 2133-2148.



## Chapter 6

### Surface Modification of Iron Oxide Nanoparticles using Catechol-derivative Surfactants

#### 6.1 Introduction

As mentioned earlier, it is very useful for biological applications to have iron oxide MPs with high magnetization, high T2 relaxivity, high stability in water and physiological environment. The MPs with these properties can be even more interesting when they have the ability to be functionalized with molecules and proteins of interest. Moreover, for a longer circulation time *in vivo* and faster response in MRI-sensing applications,<sup>1</sup> the MPs also have the smallest possible hydrodynamic sizes. However, all of these properties are not readily satisfied in commercially available and currently used MPs systems.

Chapter 5 discusses one approach to making MPs with a high magnetic moment, high T2 relaxivity, high stability, available functionality, and small size. However, one of the main drawbacks of the mPAA systems for stabilizing and functionalizing the MPs is the highly negative charges on the surface of the final MPs, which make their surfaces prone to protein non-specific binding.

Moreover, the MPs with mPAA on their surface are stabilized using the nature of oil-in-water micelles. These micelles are very sensitive to the changes in the solvent and concentration. Once formed and stabilized in water, the MPs are very difficult to transfer or mix into other solvents, even into a high-polarity solvent such as methanol or DMF. With subtle changes in the polarity of the solvent, the micelles of the MPs can be ruptured; then the hydrophobic MP cores lose their colloidal stability and become aggregated.

To move away from using the mPAA and other micellar approaches to make water-stable MPs, we are interested in direct surfactant-exchanging approaches. We can change the polarity and functionality of the MPs by replacing the native oleic acid ligand on as-synthesized MPs with new surfactants with an equal or stronger ability to bind to the MP surfaces, as described in Chapter 3. Previous studies show that many surfactants have a high ability to attach and stabilize on iron oxide MP surfaces both found in nature

and rendered using chemical approaches.<sup>2-5</sup> The structures of some of these surfactants are shown in Figure 6.1.

As indicated in Figure 6.1, the potential functional groups that bind firmly to the iron oxide MPs are mostly carboxylic and catechol groups. Another observation is that some of these surfactants have multiple binding groups in their molecules, leading to the ability of the surfactant to form chelation on the MP surfaces. It is also reported that the catechol group tends to bind strongly to iron, due to the stability of the five-member ring of the resulting complex.<sup>2</sup> After review of the results from the literature<sup>2-5</sup> and some of our initial experiments, the catechol group was chosen to serve as the binding group for our new types of surfactants.

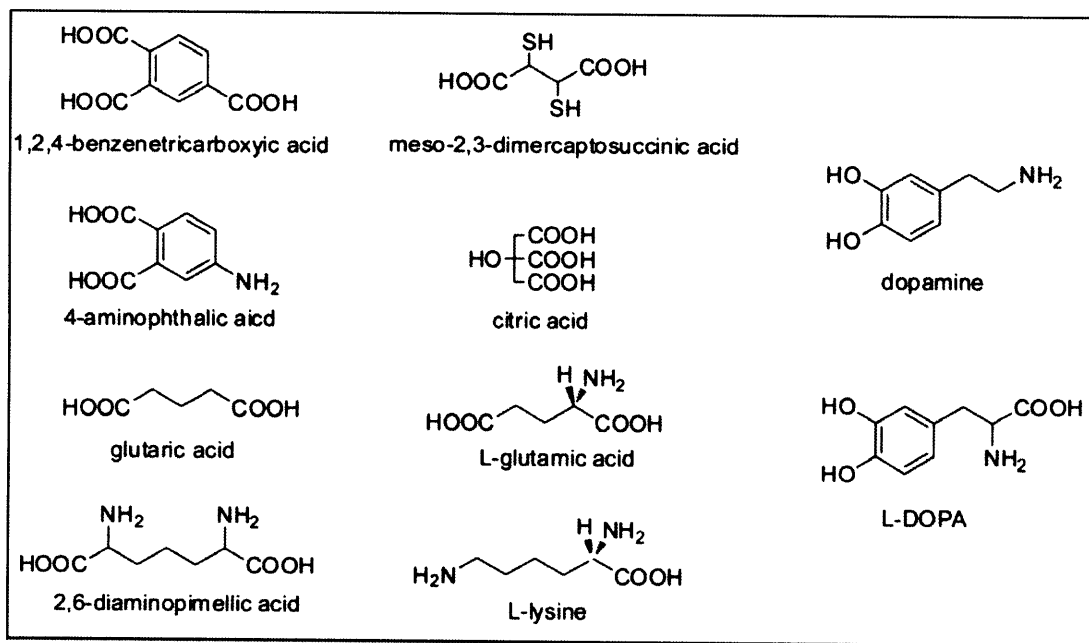


**Figure 6.1** Molecules with observed ability to bind onto iron oxide surface.

Our initial experiment to explore the ability and stability of the catechol-derivative surfactants was done using the commercially available carboxylic derivative of the catechol, hydrocaffeic acid (HCF, structure shown in Figure 6.2a) as a new surfactant. The HCF surfactant exchanging was processed at 75 °C in methanol for replacing the native oleic acid with HCF (Figure 6.2b). The TEM images showed that the MPs with HCF on their surface (Figure 6.2d) did not show any feature suggesting any aggregations

when compared to the MPs with the native oleic acid (Figure 6.2c.) Moreover, the DLS measurement (Figure 6.2e) showed a reasonably small hydrodynamic size of these new MPs.

These results are promising as the MPs can be then transferred into the water phase without any aggregation observed in DLS and TEM images. The resulting MPs suggest that the catechol group can replace the carboxylic group and can be stabilized on the surface of the MPs.

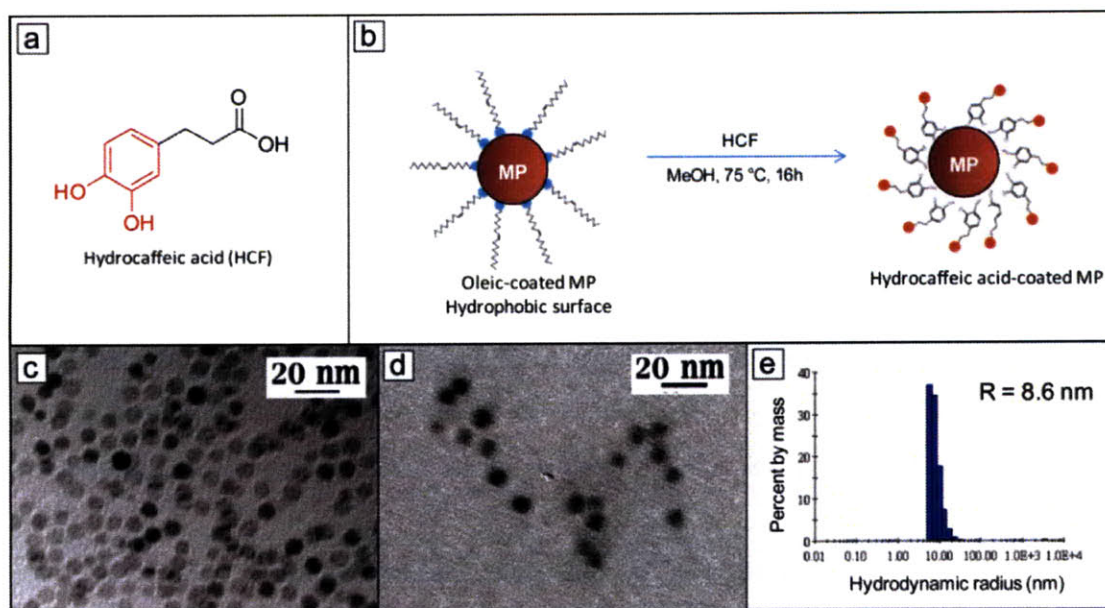


**Figure 6.2** (a) Structure of hydrocaffeic acid; (b) surfactant-exchanging process for applying HCF; (c,d) TEM images of the MPs (c) before and (d) after replacing their surfactant with HCF; and (e) size distribution of the MPs with HCF surfactant measured by DLS.

The problem that hindered HCF from being useful is its lack of functionality because the carboxylic groups are needed to keep the MPs stable in water, inhibiting the functionalization using the carboxylic group. Moreover, as discussed in Chapter 5, the highly negatively charged MPs and the MPs with mPAA, as well as the MPs with this HCF surfactant, have a strong tendency to bind to proteins nonspecifically, which prevents them from being used in biological systems.

Given these initial observations, we continue utilizing the catechol groups as the MP-binding group in our new surfactants. The problem that needs to be solved is that we have to design and modify our new surfactant to keep the non-specific protein-binding as low as possible. We chose to include polyethylene glycol (PEG) and zwitterions in our surfactants to serve this purpose.

## **6.2 Surfactants with mono-catechol and polyethylene glycol**

*(This work is done in collaboration with Dr. Jongnam Park)*

Polyethylene glycol (PEG) groups are known to be hydrophilic and have low protein non-specific binding.<sup>6</sup> PEG was previously studied and has been used with nanoparticles both as a hydrophilic part of transferring nanoparticles to the water phase and as a low-biofouling coating.<sup>6</sup>

PEG has been used with iron oxide MPs.<sup>4,7</sup> The resulting MPs coated with PEG usually show significant stability in water-based media. However, some of these PEG-MPs are very large due to the high molecular weight of the PEG used. Moreover, in some of these works, the surfactants that were coated on MP surfaces, such as dextran and phospholipid, are already considered large molecules even before being attached to PEG molecules.<sup>7</sup>

Our surfactants were designed to combine a catechol group with a PEG group, using catechol as a binding group for the MPs and PEG as hydrophilic group rendering the MPs water-dispersible. The molecular weights of PEG were chosen to be just enough to keep the MPs stable in water-based solutions in order to synthesize the MPs with the smallest hydrodynamic size. The amino group is also included in the design in order for the resulting MPs to have functional groups available for further conjugation with molecules of interests.

The surfactant of similar design was reported earlier and used for iron oxide MPs.<sup>4,8</sup> However, the reported MPs with mono-catechol with PEG were synthesized in a one-pot synthesis, resulting in surfactants of badly characterized.<sup>8</sup> We aim to improve the synthesis process of these MPs by dividing the process into two steps: first synthesizing and characterizing the surfactants and then applying the new surfactants through a surfactant-exchanging process.



Our mono-catechol with PEG was synthesized as shown in the scheme in Figure 6.3. The synthesis is based on forming the amide bond between hydrocaffeic acid (HCF) and amino-PEG. To activate the carboxylic group, 1-Ethyl-3-(3-dimethylaminopropyl)carbodiimide (EDC) is used. This overnight reaction was done in DMF at room temperature. The crude products were purified using a silica gel column with dichloromethane (DCM) and methanol as eluents.

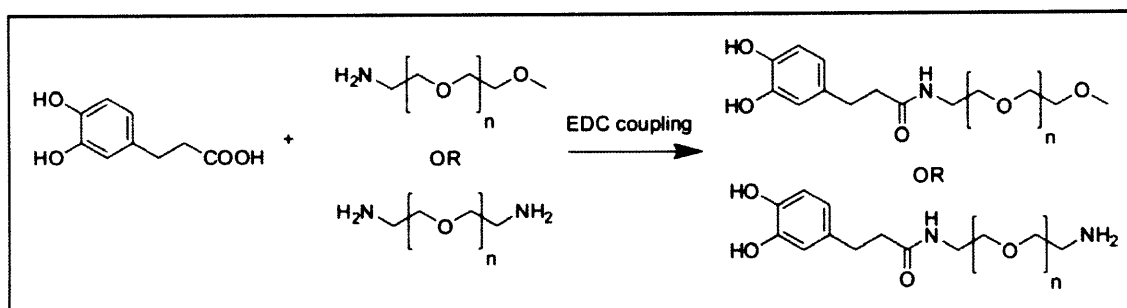


**Figure 6.3** General reaction schemes for synthesis of mono-catechol ligands.

The HCF-PEG surfactants were then applied to the oleic-acid MPs. The surfactant-exchanging process was done in methanol at 75 °C for 16 hours in order to replace the native oleic acid surfactant with an excess amount of HCF-PEG surfactants. After the surfactant-exchanging process, the MPs were precipitated by adding butanol and hexane into the methanol-based mixture. Oleic acid and excess HCF-PEG were then discarded along with the supernatant. The precipitated MPs were briefly dried under a vacuum and transferred into Phosphate Buffer Saline (PBS) solution and purified using dialysis through centrifugal filters with a 50-KDa molecular weight cut-off membrane to get rid of excess HCF-PEG. The surfactant-exchanging process is later improved to achieve a higher yield of the MPs transferred into PBS and will be discussed in Section 6.3.2.

As mentioned earlier, we intended to use PEG with the lowest molecular weight that could keep the MPs stable in water-based solutions in order to obtain the smallest hydrodynamic size of the resulting MPs. The observations of the MPs with these HCF-PEG surfactants of different PEG molecular weights appear in Table 6.1. The

hydrodynamic diameters of the MPs were measured using dynamic light scattering (DLS) analysis (Malvern instrument).

**Table 6.1** Properties of some iron oxides MPs with mono-catechol ligands.

Ligands	MW of PEG (g/mol)	Appearance in PBS	Hydrodynamic Diameter (nm)
HCF-PEG3-OMe	150	Aggregate	
HCF-PEG12-OMe	600	Dispersible	22 nm
HCF-PEG16-OMe	800	Dispersible	23 nm
HCF-PEG40-OMe	2000	Dispersible	30 nm
HCF-PEG3-NH <sub>2</sub>	150	Aggregate	
HCF-PEG8-NH <sub>2</sub>	400	Aggregate	
HCF-PEG18-NH <sub>2</sub>	900	Partially dispersed	50 nm

Table 6.1 illustrates the direct relation between the molecular weight of PEG used and the hydrodynamic diameter of the MPs. The larger the molecular weight of PEG, the larger the hydrodynamic size of the MPs. In the case of methoxy-PEG, the smallest PEG that can keep MPs dispersible into PBS is 600 g/mol, leading to the MPs of 22 nm in hydrodynamic diameter. The TEM images of these MPs are shown in Figure 6.4.

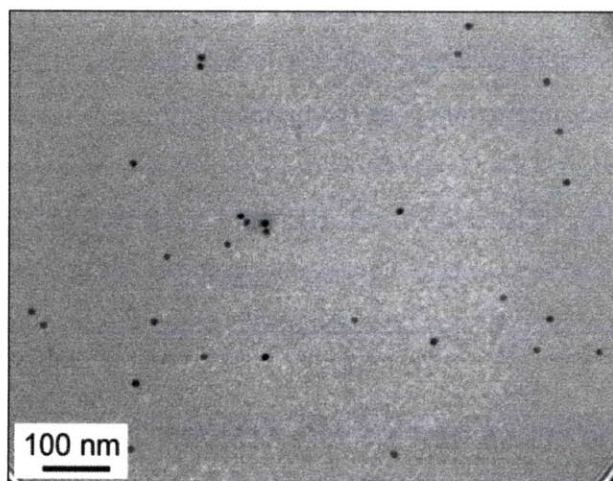


**Figure 6.4** TEM image of MPs with HCF-PEG12-OMe surfactants from PBS solution.

The TEM image in Figure 6.4 shows that the MPs with this HCF-PEG-OMe are well dispersed in the water-based solution, and there is no appearance of aggregation as we expected from their appearance in solution and from the DLS measurement. These results indicate that the mono-catechol PEG surfactant can be utilized for making small and water-stable MPs.

However, HCF with amino-PEG, which we intended to use for functionalization of the MPs after they are transferred into water, turned out to have some problems. As Table 6.1 shows, the MPs required larger amino-PEG to be dispersible into PBS, and the MPs with HCF-PEG-NH<sub>2</sub> appeared to be prone to aggregations. These results probably occur because of the ability of the amino group to bind to MP surfaces and can lead to cross-linking between MP particles. The HCF-PEG-NH<sub>2</sub> surfactants can be used only with PEG of high molecular weight, or, for purposes of functionalization, the HCF-PEG-NH<sub>2</sub> can be functionalized with molecules of interests before the surface-exchanging process, which reduces the aggregations.

As shown in Figure 6.1, surfactants with more than one group binding to the MP surfaces tend to be more strongly stabilized on the MP surfaces due to the chelating effect. The mono-catechol PEG can be improved in term of their stability on the MP surfaces by designing new types of surfactant molecules that have more than one catechol groups on the same molecule. The next section focuses on this poly-catechol surfactant.

### **6.3 Surfactants with poly-catechol and polyethylene glycol**

In the experiments in Sections 6.1 and 6.2, the catechol group has shown a significant ability to bind strongly to the iron oxide MP surfaces, and PEG molecules have seemed hydrophilic and able to bring the MPs into a water-based solution. This section discusses surfactants with more than one catechol group because they are proposed to chelate to the MP surfaces and bind to MP surfaces stably. The PEG molecules are also included in this new type of surfactant to render water-dispersibility and reduce protein non-specific binding when the new MPs are used in biological systems. The schematic design of these new poly-catechol PEG polymer (PCP) surfactants is shown in Figure 6.5.

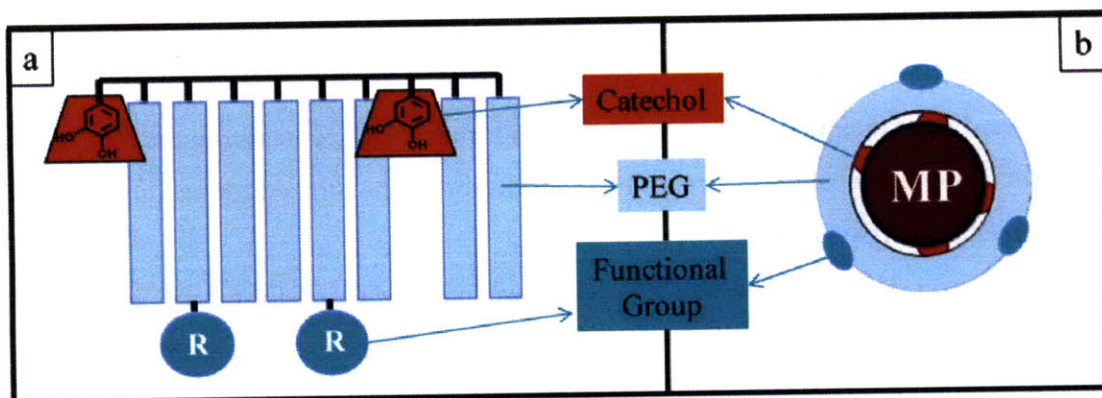


**Figure 6.5** Schematic representation of a) the designed PCP ligand and b) MPs after being modified with this surfactant.

The designed PCP surfactants are random co-polymers of the catechol-derivative monomer and the PEG monomer; the functional group can be included in the designed PCP surfactants by attaching them at the end of the PEG chain as shown in Figure 6.5a. After these surfactants are applied to the MP surfaces, we propose that the catechol groups bind to the MP in chelating fashion, leaving the PEG and available functional groups on the outermost part of the MP surfaces. The proposed structure of these MPs with PCP surfactant is shown in Figure 6.5b.

The process to obtain the MPs with this new surfactant is separated into two parts. First, PCP surfactants are synthesized using Reversible Addition-Fragmentation chain Transfer (RAFT) polymerization. Then the surfactant-exchanging process is performed in order to replace the native oleic acid surfactant with these new PCP surfactants. The details of these processes are discussed in Sections 6.3.1 and 6.3.2 below.

### 6.3.1 Synthesis of PCP surfactants

PCP surfactants are synthesized using the RAFT polymerization because this process can give controlled polymerization. The polymers synthesized using the RAFT polymerization process are found to have low polydispersity. Also, RAFT polymerization allows predetermination of the molar mass of the polymer and allows the production of complex architectures such as block copolymers.<sup>9</sup> These characters of RAFT polymerization suit our needs for synthesizing the PCP surfactant.

The synthesis of PCP surfactants is divided into two parts. First, a monomer with catechol group and a monomer with PEG entities were separately synthesized. Then, the monomers of interest were polymerized using the RAFT polymerization. Sections 6.3.1.1 and 6.3.1.2 discuss the details of both processes.

#### **6.3.1.1 Monomer synthesis**

Monomers that are needed for the polymerization contain acrylate or acrylamide groups for the addition polymerization in the following step. The schemes for monomer synthesis reactions are shown in Figure 6.7. The catechol monomer (Compound 1) is synthesized by amide bond formation through nucleophilic acyl substitution of acryloyl chloride by dopamine. The methoxyPEG monomer (Compound 2) is formed by ester bond formation between acrylic acid and methoxyPEG using N, N'-dicyclohexylcarbodiimide (DCC) as an activating agent. The other two functional PEG monomers (Compounds 3 and 4) are synthesized using similar reactions. The experimental details are described below.

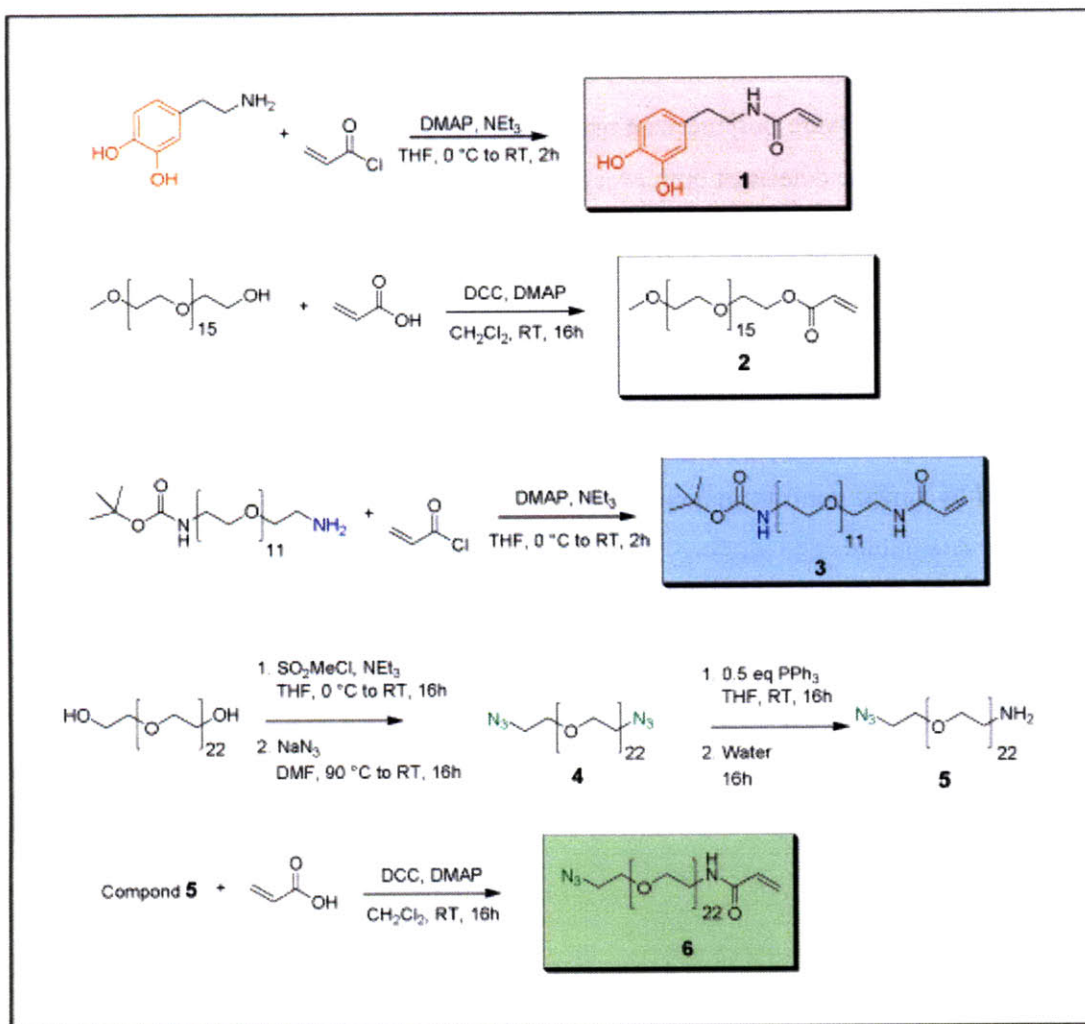


**Figure 6.6** Reaction schemes for synthesis of the monomers for the PCP ligands.

**Experimental Details:**

**Materials and Instrumentation:** All the chemicals were purchased from Sigma-Aldrich and used without further purification except those indicated differently. The solvents are all spectroscopic grade. In thin layer chromatography (TLC), all compounds were visualized by iodine staining, amine-bearing compounds were stained by a ninhydrin solution, and vinyl groups on acrylate-derivative compounds were visualized by  $\text{KMnO}_4$  staining. All the purification steps using flash column chromatography were performed on a Teledyne Isco CombiFlash Companion.  $^1\text{H-NMR}$  spectra were obtained from a Bruker AVANCE-400 NMR Spectrometer. FT-IR spectra were recorded on Perkin-Elmer Model 2000 FT-IR spectrophotometer.



**Compound 1.** Dopamine hydrochloride (1 g, 5.29 mmol), 4-dimethylamino-pyridine (DMAP, 65 mg, 0.53 mmol), and acryloyl chloride (0.48 g, 5.29 mmol) were dissolved into 50 mL dried tetrahydrofuran (THF). The reaction mixture was stirred and cooled down to 4 °C before triethylamine (0.17 g, 1.71 mmol) was added dropwise. The reaction was monitored by TLC and was completed in 1h. The precipitated by-products were then filtered out. THF was removed under reduced pressure. The reaction mixture was then re-dissolved again into ethylacetate (25 mL) and was left for 30 min in ice-bath to precipitate more of by-products. After filtered out to separate the precipitated by-products, ethylacetate was removed *in vacuo*. The crude product was purified using silica gel flash column chromatography (DCM/methanol gradient 100:0 to 5:1, v/v) and yields a colorless oil product (0.4 g, 37% yield).

**Compound 2.** MethoxyPEG (2 g, 2.67 mmol, average MW 750 g/mol), DMAP (36 mg, 0.29 mmol), and acrylic acid (0.21 g, 2.9 mmol) were dissolved in 100 mL dichloromethane (DCM). The solution were cooled down to 4 °C in an ice bath and then added a 10 mL solution of N, N'-dicyclohexyl-carbodiimide (DCC, 0.6 g, 2.9 mmol) in DCM dropwise. The reaction mixture were stirred at room temperature for 16h. Precipitates were removed by filtration and the solvent was evaporated using rotary evaporator. Ethylacetate (50 mL) was added for further precipitating of the by-products, and the filtration-evaporation steps were then repeated once more. The crude product was purified using silica column (DCM/methanol gradient 100:0 to 5:1, v/v) and yields a colorless oil product (1.07 g, 50% yield).

**Compound 3.** O-(2-Aminoethyl)-O'-[2-(Boc-amino)ethyl]decaethylene glycol (1 g, 1.55 mmol) and acryloyl chloride (0.842 g, 9.30 mmol) were transferred into 50 mL dried THF. The reaction mixture was cooled down to 4 °C before triethylamine (0.17 g, 1.71 mmol) was added dropwise. The reaction was monitored by TLC and was completed in 1 h. The precipitated by-products were then filtered out. THF were removed under reduced pressure. The reaction mixture was then re-dissolved again into ethylacetate (25 mL) and was left for 30 min in ice-bath to precipitate more of by-products. After filtered out to separate the precipitated by-products, ethylacetate was removed *in vacuo*. The crude product was purified using silica gel flash column

chromatography (DCM/methanol gradient 98:2 to 9:1, v/v) and yields a colorless oil product (0.7 g, 65% yield).

**Compound 4.** The synthesis of Compound 4 was modified from previously reported procedure.<sup>10</sup> PEG (43.75 g, 43.75 mmol) and methanesulfonylchloride (11.53 g, 100.5 mmol) were dissolved in 220 mL dry tetrahydrofuran (THF). The reaction mixture was then cooled to 4 °C in an ice bath and then added 15 mL of triethylamine dropwise. The reaction mixture was stirred at room temperature for 12h. The precipitates of by-products were filtered out and the THF was removed *in vacuo*. 300 mL of N, N'-dimethylformamide (DMF) was added to the dried product. Sodium azide (7.75 g, 120 mmol) was added to the reaction mixture and then the reaction mixture was heated under reflux setup at 90°C for 12h. The excess of sodium azide was filtered out and then DMF was removed *in vacuo*. The product was re-dissolved in 100 mL DCM and the leftover sodium azide was removed by extraction using 20 mL 2M sodium chloride solution. The water phase was then back-extracted with 150 mL chloroform. The combined solution of DCM and chloroform fractions was removed the solvents *in vacuo*. The product was clear yellow oil (38 g, 80% yield) and used without further purification.

**Compound 5.** The synthesis of Compound 5 was modified from previously reported procedure.<sup>10</sup> Compound 4 (38 g, 35 mmol) was dissolved in 200 mL of THF. Triphenylphosphine (9.21 g, 35 mmol) in 50 mL THF was added into the reaction mixture dropwise under nitrogen atmosphere. The reaction mixture was stirred at RT for 16h, and then added 2 mL of deionized water and stirred for another 16h at room temperature. THF was then removed using rotary evaporator and the crude product was dissolved in 150 mL methanol. The methanol solution was washed with hexanes in order to remove by-products and methanol was then removed *in vacuo*. The crude product was purified using silica column (DCM/methanol gradient 100:0 to 5:1, v/v) and yields a slightly yellow oil product. The percent yield was not calculated as the column has been done in separated multiple times due to the large amount of the crude product.

**Compound 6.** Compound 5 (3.24 g, 3.07 mmol), DMAP, (83 mg, 0.67 mmol), and acrylic acid (0.49 g, 6.76 mmol) were dissolved in 100 mL dichloromethane (DCM). The solution was cooled down to 4 °C in an ice bath and then added a 10 mL solution of DCC (1.27 g, 6.14 mmol) in DCM dropwise. The reaction mixture was stirred at room

temperature for 16h. Precipitates of by-products were removed by filtration and the solvent was evaporated using rotary evaporator. Ethylacetate (50 mL) was added for further precipitating of the by-products, and the filtration-evaporation steps were then repeated once more. The crude product was purified using silica column (DCM/methanol gradient 100:0 to 5:1, v/v) and yields a slightly yellow oil product (1.8 g, 53% yield).

### 6.3.1.2 Polymerization of PCP surfactants

The polymerization of the monomers from the previous section was performed using the RAFT polymerization. The schemes for syntheses of PCP surfactants are shown in Figure 6.7.

The PCP surfactants that were mainly used and discussed here are the PCPs with only methoxyPEG (Compound 8), with methoxyPEG and aminoPEG (Compound 9) and with azidePEG (Compound 10). The main interest in Compound 8 came from the fact that this PCP is the most inert PCP as it lacks any functional group and could be a good model for studying the properties of the PCP in term of stability of the surfactant without interference from the functional groups. The Compounds 9 and 10 are of interest as they bear available functional groups for further conjugation to other molecules such as dyes and proteins. In the case of Compound 9, the PCP not only consists of an aminoPEG monomer, but must also include the methoxyPEG monomer in the polymer. The PCP that comprised only aminoPEG and catechol monomers gave poor ability to transfer the MPs into water-based solution and was not useful. The poor water dispersibility of the MPs with these entirely amino-PEG PCPs is most likely due to the ability to bind to the MP surfaces of the amino group itself, which leads to the cross-linking between MPs and the poor dispersibility of the MPs. In contrast, Compound 10, which is composed entirely of azidePEG and catechol monomers, has the ability to transfer MPs into a water-based solution similar to Compound 8.

The PCP surfactants were prepared by radical addition polymerization using azobisisobutyronitrile(AIBN) as a radical initiator. The RAFT reagent (Compound 7) was synthesized by Wenhao Liu using a previously reported procedure.<sup>11</sup> The reaction was performed under air-free conditions in DMF. The experimental details are described below.

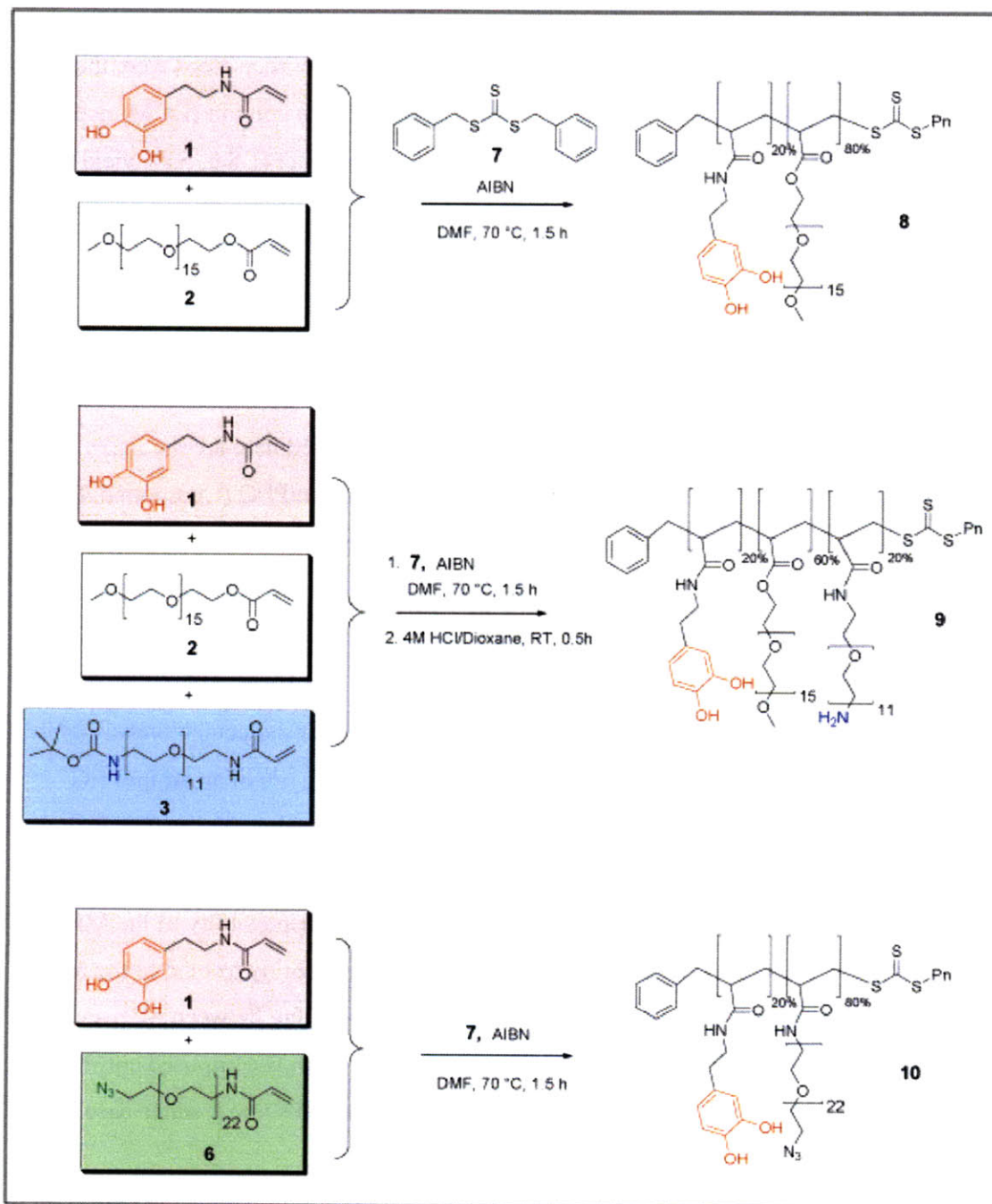


**Figure 6.7** Reaction schemes for RAFT polymerization for the synthesis of the PCP ligands.

### ***Experimental Details:***

**Materials and Instrumentation:** All the materials and instrument were as described in Section 6.3.1.1. The molecular weights of the PCP surfactants were determined in DMF solutions on an Agilent 1100 series HPLC/GPC system with three PLgel columns (103, 104, 105 Å) in series using narrow polystyrene standard.

**Compound 8.** Monomer 1 (4.5 mg, 0.02 mmol) and Monomer 2 (73 mg, 0.09 mmol) were dried under vacuum and dissolved in dried DMF (30 µL) in a 1 mL glass ampule. RAFT agent (Compound 7, 1.44 mg, 5 µmol) and AIBN (0.8 mg, 5 µmol) were added into the reaction mixture. The reaction mixture was then degassed through three cycles of freeze-pump-thaw process. The ampule was sealed with flame under vacuum, and the reaction mixture was then incubated in 70 °C oil bath for 2h. The PCP Compound 8 was then used without purification.

**Compound 9.** Monomer 1 (6.2 mg, 0.03 mmol), Monomer 2 (75 mg, 0.09 mmol), and Monomer 3 (17 mg, 0.03 mmol) were dried under vacuum and dissolved in dried DMF (30 µL) in a 1 mL glass ampule. RAFT agent (Compound 7, 1.96 mg, 6.8 µmol) and AIBN (1.1 mg, 6.8 µmol) were added into the reaction mixture. The reaction mixture was then degassed through three cycles of freeze-pump-thaw process. The ampule was sealed with flame under vacuum, and the reaction mixture was then incubated in 70 °C oil bath for 2 h. The reaction mixture was added 4M hydrochloric acid in dioxane (0.5 mL) at RT for 1h in order to remove the *t*-Butyloxycarbonyl (Boc) protecting group. Dioxane was removed under vacuum. The pH of final PCP product was adjusted to pH 6-7 using 1 M sodium hydroxide in methanol. The PCP surfactant was then used without further purification.

**Compound 10.** Monomer 1 (6.21 mg, 0.03 mmol) and Monomer 6 (133 mg, 0.12 mmol) were dried under vacuum and dissolved in dried DMF (30 µL) in a 1 mL glass ampule. RAFT agent (Compound 7, 1.96 mg, 6.8 µmol) and AIBN (1.1 mg, 6.8 µmol) were added into the reaction mixture. The reaction mixture was then degassed through three cycles of freeze-pump-thaw process. The ampule was sealed with flame under vacuum, and the reaction mixture was then incubated in 70 °C oil bath for 2 h. The PCP Compound 10 was then used without purification.

The molecular weights and size-dispersity of the PCP surfactants were determined using gel permeation chromatograph (GPC) with a refractive index detector. The typical GPC traces of the PCP polymers are shown in Figure 6.8. The GPC chromatogram shows that the molecular weights of a typical PCP polymer using the same equivalents of RAFT and AIBN are in the range of 17-25 KDa. As Figure 6.8 shows, the trend of molecular weight is in the following order: Compound 10 > Compound 8 > Compound 9. The trend has a direct relation to the molecular weight or the PEG chain of the monomers used in each polymer, which are Monomer 6 > Monomer 2 > Monomer 3. Another calculation obtained from the GPC trace is that the polydispersity indexes (PDIs) of these PCP polymers falls in the range of 1.1-1.3, which is considered a narrow size distribution. This observation indicates that the RAFT agent functioned properly in these reaction conditions.

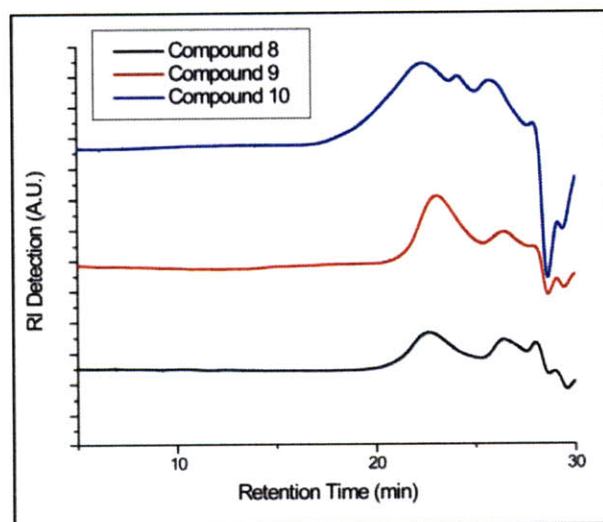


**Figure 6.8** Chromatogram from Gel Permeation Chromatography column of the PCP polymer.

Using the molecular weight of the PCP polymers, which range from 17-25 KDa, the number of monomers, functional groups and catechol binding groups per polymer molecule can be calculated. As an example, Compound 9 of 17 KDa has a molecular weight composed of 26 monomer units, 5 of which are catechol monomer units, and 5 of



which are animoPEG monomer units. Using the calculation, the proposed structure of PCP surfactants (Figure 6.5) can be achieved, which leads to the possibility for the surfactant to bind to MP surfaces in a chelating fashion.

The PCP polymers were obtained using the RAFT polymerization discussed above. The surfactant-exchanging process, the other equally important step for obtaining the MPs with PCP surfactants, is discussed in the next section.

### **6.3.2 Surfactant-exchanging process**

The surfactant-exchanging process is one of the important steps in obtaining a good quality of the MPs with PCP surfactant. The aggregations of MPs in water-based solution can be observed when the surfactant-exchanging process is not completed.

As discussed in Section 6.1, the common process for the surfactant exchange was performed in a one-step reaction. In this one-step process, the solvent that was chosen to be the medium cannot disperse both hydrophobic MPs and hydrophilic surfactants at the same time. For example, methanol, which is used as a medium for the one-step surfactant-exchanging process, cannot disperse the oleic acid-coated MPs at the beginning of the process. Instead, the MPs started to be dispersed in methanol after the exchanging proceeded for some time and the MPs had enough new hydrophilic surfactant on their surfaces. This problem can lead to the aggregation of the MPs in water because the MPs were already aggregated at the beginning, and re-dispersing every MP could be too difficult.

Another problem with the one-step surfactant exchanging process is that the native oleic acid is easily re-bound to the MP surface. Since the surfactant exchanging process is based on equilibrium, the new surfactants were replaced by adding an excess amount of the new surfactants to drive the equilibrium toward the MPs with mainly new surfactants on their surfaces. The drawbacks of this process are that the new surfactants are usually too valuable to use in great excess and in some cases the new surfactant is more bulky and less accessible than the oleic acid, so it cannot replace the oleic acid efficiently.

The two-step surfactant-exchanging process was used in order to solve the previous problem with the one-step process. The scheme for this process is shown in Figure 6.9.

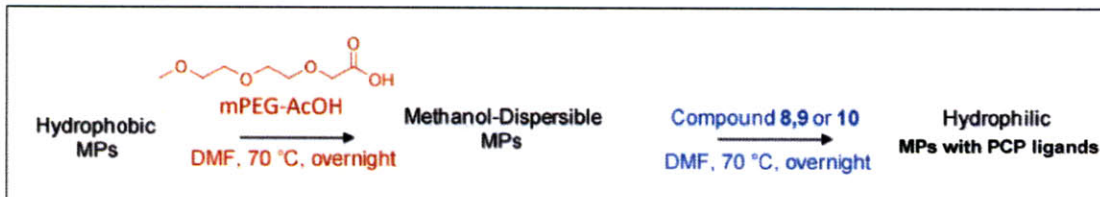


**Figure 6.9** Schematic representation of the surfactant-exchanging process.

This two-step surfactant-exchanging process employs a new intermediate surfactant, mPEG-acetic acid (mPEG-AcOH). This new surfactant is cheap and commercially available, so it can be added in great excess compared to the native oleic acid. Also, it is small in terms of molecular weight and can gain access to MP surfaces more readily than bulky molecules. In addition, the hydrophilicity of this surfactant is intermediate and can readily disperse the MPs with oleic acid. Due to these properties, we chose the mPEG-AcOH for use as an intermediate surfactant.

### 6.3.3 Physical properties of the MPs with PCP surfactants

After the surfactant-exchanging process, the resulting MPs with PCP surfactants were characterized using various methods, including TEM and DLS for size distribution, magnetization, and T2 relaxation.

MPs with Compound 8 are first characterized because they are free of other functional groups that can interfere with the size distribution. As the TEM images and the DLS data show (Figure 6.10), the MPs with PCP 8 are well-dispersed. The TEM images of the MPs before (Figure 6.10a) and after applying new surfactant (Figure 6.10b) are similar in term of size distribution and no appearance of aggregation. Also, the sizes of the MP cores in both cases are similar, indicating that this PCP surfactant did not etch away the iron oxide materials, a phenomenon some previous work suggested might occur when using catechol-derivative as a surfactant.<sup>2</sup>

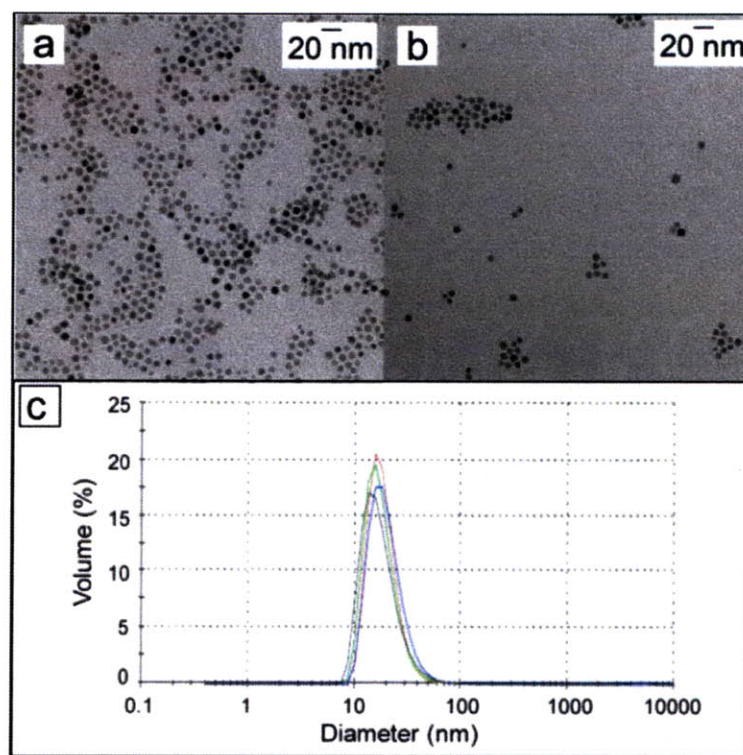


**Figure 6.10** Size distributions of MPs with PCP ligand **8** using TEM (b) compared to MPs with oleic acid ligands of the same MP cores (a) and using DLS (c).

The size distribution from DLS measurement (Figure 6.10c) showed results in agreement with the observation from TEM images. The DLS also indicated that there is no observable aggregation as there is no other signal or long, large tail in the size distribution curve. In addition to the TEM images, the hydrodynamic size from the DLS analysis showed that the MPs with this surfactant are 18 nm in hydrodynamic diameter, which is relatively small considering the size of the PEG chain used in this PCP.

The results from both TEM and DLS measurement are very promising because they indicate success in applying these new PCP surfactants to the MP surfaces and stabilizing the MPs in a water-based solution. The next challenge is to incorporate functional groups onto the MP surfaces in order to make them useful for further conjugation with other molecules. This challenge comes from the fact that many functional groups can interact with the MP surfaces. With the hindrance from the large

PEG chain, the strong binding ability of the catechol group and the chelating fashion of the surfactant, attaching functional groups onto the MPs could be achieved.

The amino-functionalized PCP Compound 9 is the first PCP with a functional group that was applied to MP surfaces because the amino group is one of the most common and widely used functional groups for conjugation. After the surfactant-exchanging process, the resulted MPs were well dispersed into PBS and show similar appearances, as in the case of MPs with Compound 8, such as they can be easily filtered through a 200-nm filter membrane (HT Tuffryn Membrane, Acrodics, Inc.). The MPs were then characterized using TEM and DLS analysis as Figure 6.11 shows.

From the TEM images and the DLS data (Figure 6.11), the MPs with PCP 9 are dispersible into PBS with some small degree of aggregation. TEM images of the MPs with the new surfactant (Figure 6.11a) show some appearance of aggregation as is seen as an irregular stacking of the MPs on the TEM grid. Also, the size distribution from DLS measurement (Figure 6.11b) shows that the MPs with this surfactant are significantly larger in hydrodynamic size (32 nm in diameter) than that with PCP 8, and aggregation tails are observed from the size distribution curve.

This aggregation character of the PCP 9 is foreseeable because this surfactant contained an amino group. The amino group is known for its ability to bind to MP surfaces, so the aggregation due to the cross-linking between MP particles would be possible. However, the degree of aggregation is low enough and the MPs are still stable in PBS and still useful in the systems when MPs in water-based with amino group are needed without the demand for ultra-small nanoparticles. The hydrodynamic radii of the MPs with amino-PCP are still comparable and smaller than many commercially used T2 contrast agents as shown in Table 6.2.<sup>12</sup>

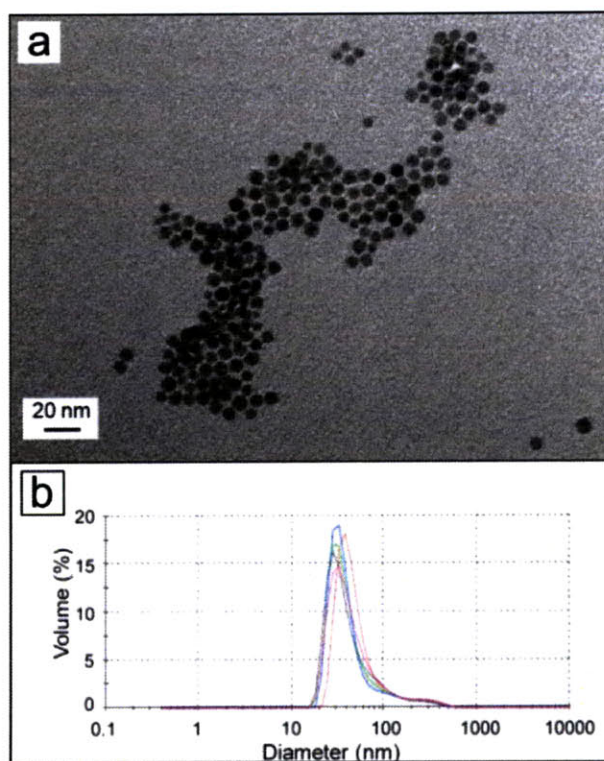


**Figure 6.11** Size distributions of MPs with PCP surfactant **9** using TEM (a) and DLS (b), respectively.

Table 6.2 not only shows the size of the MPs with PCP surfactant, but also compares the T2 relaxivity (R2), which is of interest in MPs for biological applications as a T2 contrast agent. As Table 6.2 shows, compared to a commercial T2 contrast agent, the MPs with PCP surfactant show superior properties in many aspects. First, in the case of MPs with PCP8, the size of the particles is much smaller than the commercial contrast agents. The size of the partially aggregated MPs-PCP 9 is also comparable to the smallest contrast agent from the table, ferumoxtran. Also, the relaxivities of the MPs with both PCP surfactants are on the high side and comparable to those commercial contrast agents. These comparisons indicate that these new MPs are potentially useful.



**Table 6.2** Properties of MPs with the PCP surfactant compared to commercial T2 contrast agents<sup>12</sup>

Name	Core Materials	Surface	Diameter of Core (nm)	Hydrodynamic Diameter (nm)	R2 (mM <sup>-1</sup> s <sup>-1</sup> )
Ferumoxides (Feridex)	Fe <sub>3</sub> O <sub>4</sub> , γ-Fe <sub>2</sub> O <sub>3</sub>	Dextran	4.96	160	120
Ferucarbotran (Resovist)	Fe <sub>3</sub> O <sub>4</sub>	Carboxy-dextran	4	60	186
Ferumoxtran (Combidex)	Fe <sub>3</sub> O <sub>4</sub>	Dextran	5.85	35	65
MPs with PCP 8	γ-Fe <sub>2</sub> O <sub>3</sub>	Compound 8	7	18	135
MPs with PCP 9	γ-Fe <sub>2</sub> O <sub>3</sub>	Compound 9	7	32	195

In order to obtain the MPs with functional groups for future conjugation while minimizing the aggregation, MPs with Compound 10 were studied as proposed to substitute for the amino group in the case that aggregation is not compromised. The azide group in this PCP 10 can be used for conjugation with a terminal alkyne through click chemistry, which is discussed in Section 6.3.4. The MPs with PCP 10 are well dispersed into PBS after surfactant-exchanging process and give an appearance similar to those of MPs with PCP 8 and 9. The MPs were then characterized using TEM and DLS analysis as shown in Figure 6.12.

As the TEM images and the DLS data show (see Figure 6.12), the MPs with PCP 8 are well dispersed. TEM images of the MPs with the new surfactant (Figure 6.12a) show no appearance of aggregation. Size distribution from DLS measurement (Figure 6.12b) shows that the MPs with this surfactant are small in hydrodynamic size (22-nm-diameter) with little sign of large particles that could be eventually filtered out. The smaller size of MPs compared to the PCP 9 is likely from the fact that the azide group does not have the ability to bind to the MP surfaces as an amino group and the cross-linking did not take place in this case. However, the size of the MPs with PCP 10 is observably larger than the size of the MPs with PCP 8, which is 18 nm in diameter. One



of the reasons for the larger hydrodynamic size of the MPs-PCP10 is that the PEG chain that was used in PCP10 (PEG22) is larger than that used in PCP8 (PEG16). The PEG molecules used in both cases were limited by the commercial source of the starting materials. The azide-functionalized MPs with smaller size could be obtained when smaller azide-PEG monomers were synthesized from different starting materials and used in the PCP instead of the currently used Monomer 6.

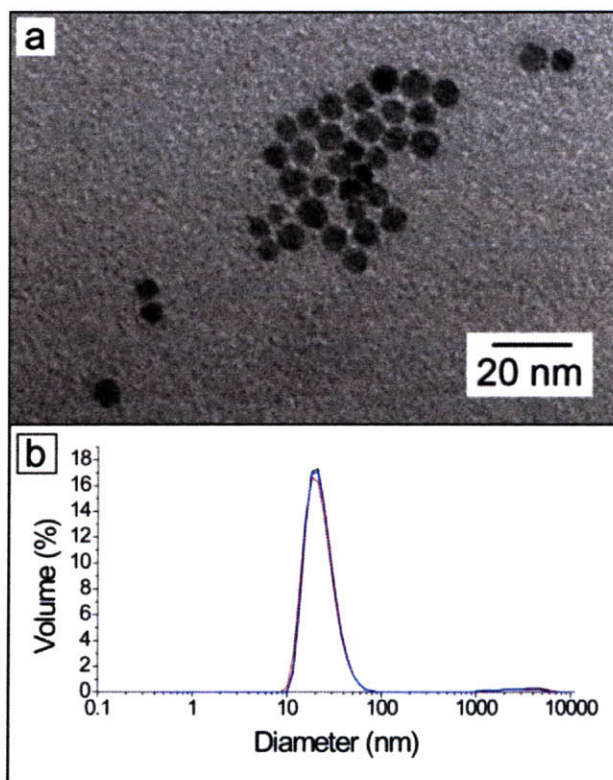


**Figure 6.12** Size distributions of MPs with PCP ligand **10** using TEM (a) and DLS (b), respectively.

Magnetization, another magnetic property of the MPs with PCP surfactants, was also studied. This measurement is different from R2 measurement, which is affected by many factors including the magnetization of the MPs, size of the MP cores, and hydrodynamic size of the MPs-PCPs. Magnetization can provide more information on the intrinsic magnetic property of the MP cores. The magnetizations of the MPs were studied

during each step of the surfactant-exchanging process with PCP surfactants using the SQUID magnetometer as discussed in Chapter 1; the results are shown in Figure 6.13.

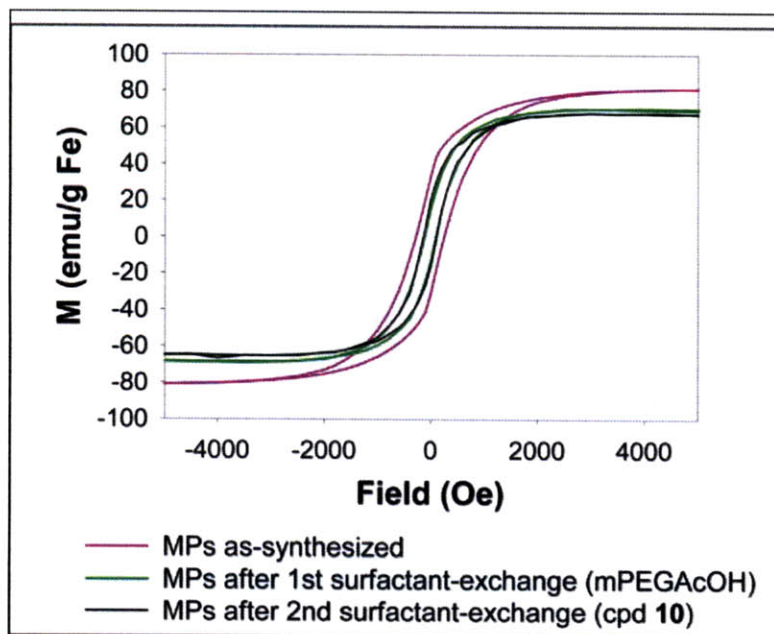


**Figure 6.13** Magnetization of the MPs before and after surfactant-exchanging process.

The magnetization of the MPs in different stages of the surfactant-exchanging process shows a total 22% decrease in their magnetization compared to that of the MPs with the native oleic acid surfactant. The significant decrease was observed during the first step in the surfactant-exchanging process, where the native oleic acid surfactant was replaced by the mPEG-AcOH surfactant. This phenomenon can be explained in two ways. First, the dissolution of the MPs and release of  $\text{Fe}^{3+}$  can cause the decrease in magnetization of the MPs. However, this situation might not be the main reason for this decreased magnetization because there is no significant decrease in the size of the MPs observed in TEM images of the MPs before and after the surfactant-exchanging process (such as those shown in Figure 6.10). Second, the decrease in magnetization could come from the surface-canting effect.<sup>13</sup> In this effect, the decrease of the magnetization comes from the increase in the thickness of the disorder surface layer. The new surfactant could

increase the thickness of this surface layer and result in the decrease in the magnetization of the MPs.

Even though some decrease appears in the magnetization of the MPs with PCP surfactants, when the magnetization of these MPs is compared to that of other T2 contrast agents, these MPs still have a comparable magnetization as shown in Table 6.3. With the exception of the FeNP case, in which the stability relative to oxidation in physiological environments was highly possible for long-term uses, our MPs are still high in their magnetization. From this table and the relaxivity in Table 6.2, the MPs with new PCP surfactants have shown to have satisfying magnetic properties as contrast agents and are potentially useful.<sup>12</sup> The next section discusses other aspects of these MPs, their functionality and their availability for conjugations.

**Table 6.3** Magnetization of magnetic nanoparticles used as T2 contrast agent compared to the MPs with PCP ligands.<sup>12</sup>

Name	Core Materials	Surface	Diameter of Core (nm)	Magnetization (emu/g Fe)
Ferumoxides (Feridex)	Fe <sub>3</sub> O <sub>4</sub> , γ-Fe <sub>2</sub> O <sub>3</sub>	Dextran	4.96	45
Ferumoxtran (Combidex)	Fe <sub>3</sub> O <sub>4</sub>	Dextran	5.85	61
CLIO-Tat	Fe <sub>3</sub> O <sub>4</sub>	Dextarn	5	60
FeNP	α-Fe	PEG	10	70
MPs with PCP <b>10</b>	γ-Fe <sub>2</sub> O <sub>3</sub>	Compound <b>10</b>	7	63

#### 6.3.4 Conjugations of the MPs

As mentioned in Section 6.3, one of the goals for using these PCP surfactants for the MPs is that the design of PCP surfactants can include the available functional group on MP surfaces. After discussion in previous sections that the other properties including stability in water, and high T2 relaxivity of the MPs with PCP surfactants are satisfied, this section focuses on the functionality of the MPs. The functionality of the MPs was

tested by conjugating them with dyes through different chemistries depending on the functional group on the MPs. The reason for using dye molecules for studying the conjugation is that the fluorescence from the dye can be easily detected and used to verify the success of conjugations.

The first conjugation chemistry was explored with the MPs with an amino-functional group. The MPs with PCP 9 were conjugated with 5-carboxy-X-rhodamine *N*-succinimidyl ester (ROX-NHS) in PBS solution as in the scheme shown in Figure 6.14a. After thorough purification using dialysis through a centrifugal filter with a cut-off molecular weight of 50 KDa, the excess dye molecules were filtered through the membrane and discarded. The resulting MPs-ROX dye conjugate was then analyzed using UV-Vis absorption and emission spectrophotometers. The absorption and fluorescence spectra of the conjugate appear in Figures 6.14b and c, respectively.

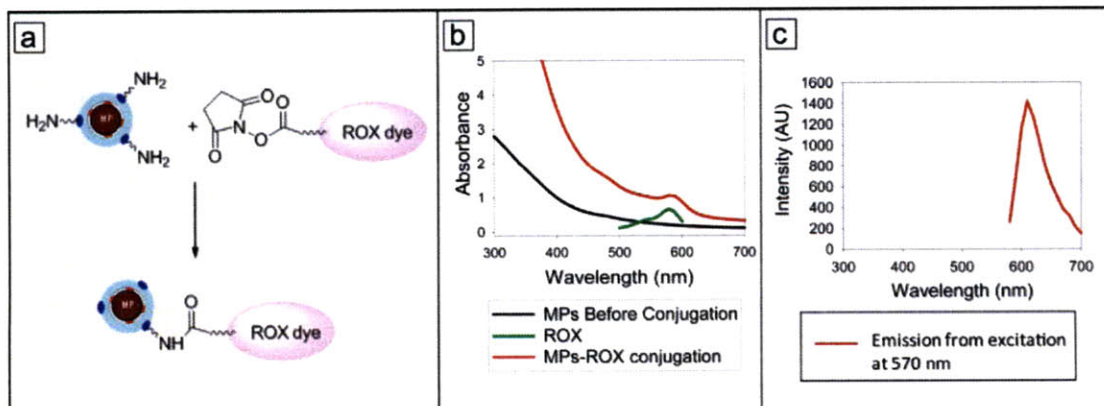


**Figure 6.14** Conjugation of MPs with PCP 9 ligand (a) the reaction scheme, (b) UV-Vis absorption and (c) fluorescence spectra of the rhodamine-MP-conjugate.

The absorption and fluorescence spectra of the products reveal that the conjugation between the amino-functionalized MPs and the ROX-NHS successfully took place. The absorption spectra in Figure 6.14b show that the absorption of the conjugate shows significant absorption features of the dye molecules, as well as the detected dye fluorescence in Figure 6.14c. This observation indicates that the amino groups on the MP surfaces are still available for conjugation even though, as discussed in previous section, there were hints that the amino group can bind directly to the MP surfaces. However,

from the calculation using the absorption coefficient of the dye and the MPs, the degree of conjugations is still low, as it was calculated to have ~4 dye molecules per MP or ~4 active amino groups per MP for this conjugation condition. These results suggest that the MPs with the amino group using PCP 9 as a surfactant could be useful to some extent in the system that needed water-stable MPs with functional amino group but did not require an ultra-small hydrodynamic size.

The other functional group that was explored is the azide group. The azide group is known and used for conjugation with a terminal alkyne group through the cycloaddition reaction or click chemistry. This reaction processed in the presence of copper(I) as a catalyst for the reaction and yielded 1,2,3-triazole as the product. The scheme for this reaction is shown in Figure 6.15a. For the conjugation of the MPs with PCP 10, the alkyne-functionalized Alexa Fluor 488 dye was used to conjugate with the MPs. After a thorough purification using dialysis through a centrifugal filter to filter out the excess dye, the resulting MPs-Alexa Fluor 488 dye conjugate was analyzed using UV-Vis absorption and emission spectrophotometers. The absorption and fluorescence spectra of the conjugate are shown in Figure 6.15b and c, respectively.

The absorption and emission spectra of the resulting MPs indicate that the conjugation between dye and the MPs proceeded successfully. The absorption spectra show the absorption feature of the dye clearly. The emission spectra show the dye fluorescence. These spectra are clearly different from the control experiment, where no copper catalyst was added. Given the absorption spectra, the quantity of the dye attached to the MPs can be calculated using the absorption coefficient of the dye. It was calculated to have ~8 dye molecules per MP for this particular condition of the reaction. With these results, the MPs with PCP 10 showed the high functionality and could be useful for further conjugation with other molecules of interest.



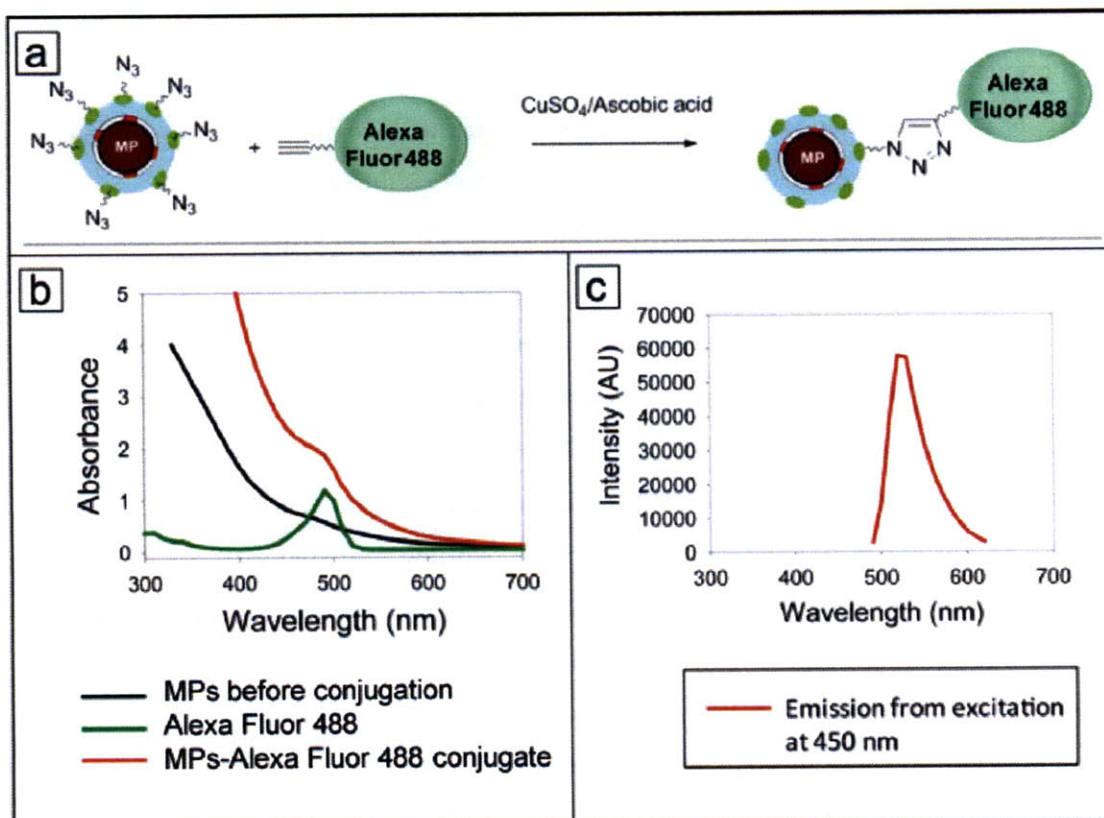


**Figure 6.15** Conjugation of MPs with PCP 10 ligand (a) the reaction scheme, (b) UV-Vis absorption and (c) fluorescence spectra of the Alexa Fluor 488-MP-conjugate.

Another feature of the design of the PCP surfactants is that more than one functional group can be incorporated into the polymer at the same time in a controllable ratio. However, the orthogonal functional groups that were chosen to be put in the same polymer had to be compatible with the total reaction scheme of each functional group. For example, Monomers 3 and 6 could not be put into the same polymer to create the PCP with both azide and amino functional groups. The fact that prevented the use of this polymer is that the reaction of the amine monomer 3 went through a highly acidic condition for the Boc-group de-protecting, and the azide monomer 6 cannot survive that condition. In order to demonstrate this orthogonal feature of this PCP surfactant, the other functional group was used. The biotinylated-PEG monomer (Compound 11) in Figure 6.16, which was synthesized by Jongnam Park using the published procedure,<sup>11</sup> was



chosen as another functional group that could be put into the same polymer as azide monomer (Compound 6). The reaction scheme for this bi-functional group PCP is shown in Figure 6.16.

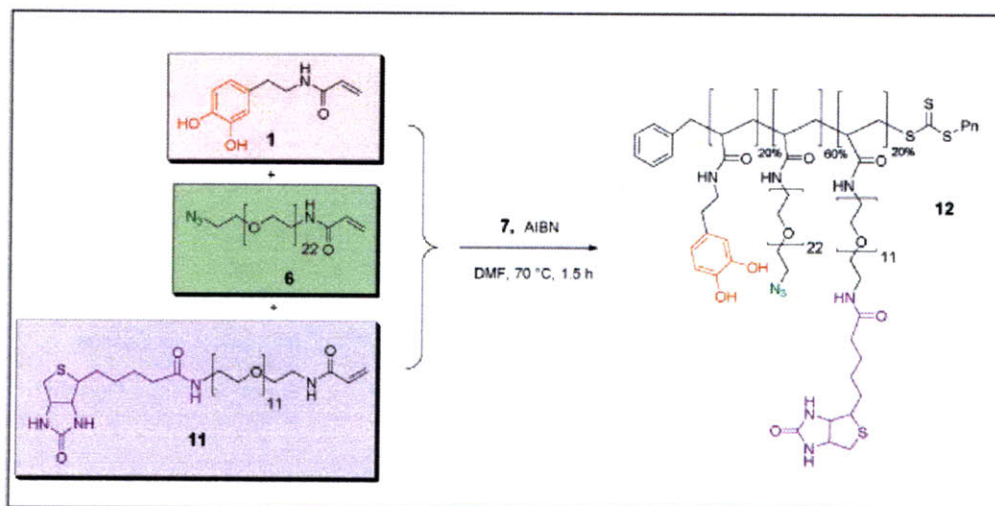


**Figure 6.16** Reaction scheme for RAFT polymerization for the synthesis of the PCP ligand with azide and biotin groups as orthogonal functional groups.

The surfactant-exchanging process and transferring of the MPs into water are the same as the procedures for other PCP surfactants. After the MPs with this PCP 12 were transferred into water, the experiment to prove that the MPs with two active orthogonal functional groups can be achieved by means of the PCP surfactant was performed by conjugation with two different dyes. The conjugation scheme for these MPs with two functional groups is shown in Figure 6.17a.

The conjugation was divided in two steps. First, the conjugation between the azide group and the alkyne-functionalized Alexa Fluor 488 dye was done through click chemistry as previously discussed. Then, after purification and filtering out of excess dye and catalyst, the MPs were incubated with streptavidin that attached with Alexa Fluor 647 dye. The strong biotin-streptavidin interaction led the conjugation of the MPs to the second dye applied. After incubation, the reaction mixture was purified using dialysis through centrifugal filters with a 100 KDa molecular weight cut-off membrane in order to get rid of the excess streptavidin-dye molecules. The purified MPs were then analyzed by

a UV-Vis spectrophotometer and the absorption and emission spectra of the resulting MPs are shown in Figures 6.17b and c, respectively.

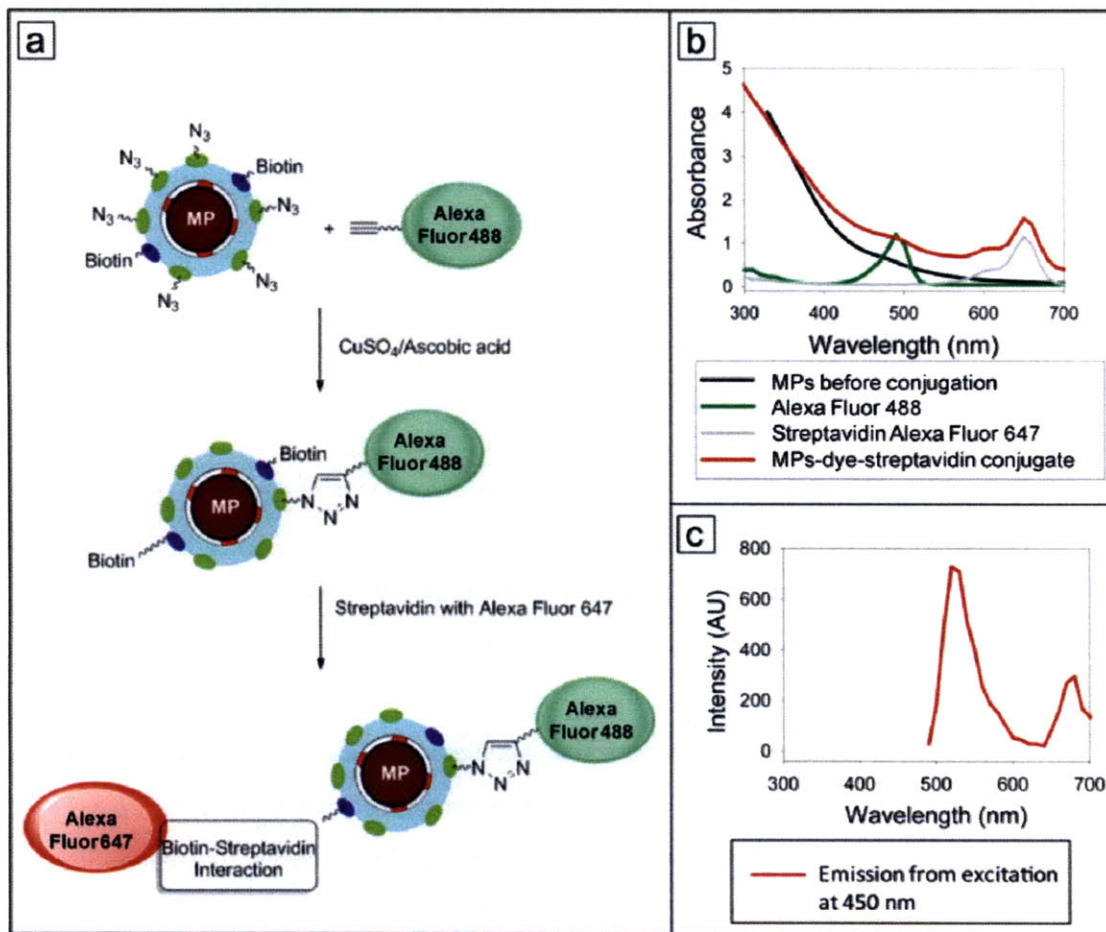


**Figure 6.17** Conjugation of MPs with PCP 12 ligand: (a) the reaction scheme, (b) UV-Vis absorption and (c) fluorescence spectra of the dye-streptavidin-MP-conjugate.

The absorption and emission spectra of the conjugate reveal that the conjugation with both through click chemistry and streptavidin-biotin interaction succeeded. The absorption spectra show absorption features of both Alexa Fluor 488 and Alexa Fluor 647, and the emission spectra also showed emission from both dyes. In this particular experiment, ~5 Alexa Fluor 488 and ~8 Alexa Fluor 647 were attached to one of the MPs. This experiment successfully demonstrated the feature of these PCP surfactants in

that they have the ability to include more than one functional group in the same polymer and eventually in the MPs.

The resulting products from the conjugation chemistry demonstrate not only that the MPs have available functional groups for conjugation to other molecules of interest, but also that the resulting MPs-dye conjugates can be useful materials. The MPs conjugated with dye are considered bi-functional materials as they have both superparamagnetic and fluorescent properties. These materials can be useful in the applications that required both superparamagnetism and fluorescence in the same particles, such as in the bimodal imaging applications.

Fluorescent dyes that were conjugated to MPs are also useful for the experiment in the next section where the properties of the MPs in biological systems are discussed. In the experiment for studying the interaction between proteins and cells and the MPs, dyes that were conjugated to the MPs are essential tools for detecting and visualizing the MPs. These experiments were a first demonstration of the use of the MP-dye conjugates.

### **6.3.5 Properties of the MPs in biological systems**

In order for the MPs to be useful in biological applications, the behavior of the MPs has to be compatible with an environment that is rich in various proteins, peptides, and other biomolecules. One of the problems with many nanoparticles when transferred into biological systems is the non-specific binding of protein, which can lead to changes in their properties. In the case of MPs with PCP surfactants, even though PEG is known for low non-specific binding, the whole construction including the catechol groups, the functional groups, and the MPs must be proved to have little or no non-specific binding to the proteins.

To demonstrate the low non-specific binding to the proteins of the MPs with PCP, two experiments have been performed. The first one is the serum-binding study using a HPLC-GFC column to track the changes in the size of the MPs before and after incubation with fetal bovine serum (FBS). The second experiment is the cell non-specific binding test using the optical microscope to visualize the stickiness of the MPs to cells after incubation.

For the first experiment, the serum-binding test was performed by incubating the MPs in the 100% serum and monitoring the changes in their size using the gel filtration chromatography (GFC) column in an HPLC system with a fluorescence detector. The MPs that were used in this experiment were the MPs with azide-PCP (Compound 10) conjugated with Alexa Fluor 488 for the fluorescent detector. The MPs were incubated in the 100% FBS for 4h at 37 °C, and the control sample was the MPs incubated just in PBS under the same conditions. In the GFC column, the separation was done by size-exclusion chromatography. The particles or molecules of larger size eluted from the column before the molecules of smaller size. Therefore, if changes in size occur, the retention time of nanoparticles will change. The chromatograms for the MPs-Alexa Fluor 488 before and after incubation with FBS are shown in Figure 6.18.

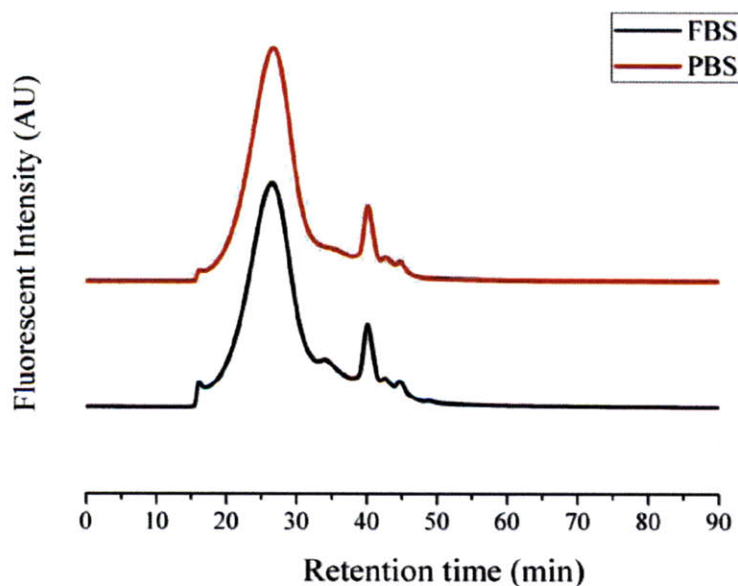


**Figure 6.18** Chromatograms of the MPs with Alexa Fluor 488 after incubation (a) with and (b) without FBS for protein non-specific binding test.

Using the GFC chromatograms in Figure 6.18, we observed no change in the retention time of the MPs. The retention of the main peak of the MPs stayed at the same position as the controlled MPs. This observation indicates that there is no significant evidence that the MPs have been attached non-specifically to proteins of various types in



the FBS. This observation implies that the MPs have low non-specific binding with proteins in serum and can be potentially useful *in vivo*.

The second non-specific binding experiment is the cell non-specific binding test. In this experiment, HeLa cells were incubated with the MPs with Alexa Fluor 488 for 15 min at 4 °C and washed thoroughly to get rid of the non-sticky MPs. Then the cells were imaged under the excitation to visualize the Alexa Fluor 488 that came from the MPs conjugates that were stuck to the cells. The images of these cells along with the cells without exposure to the MPs conjugate as a controlled experiment are shown in Figure 6.19.

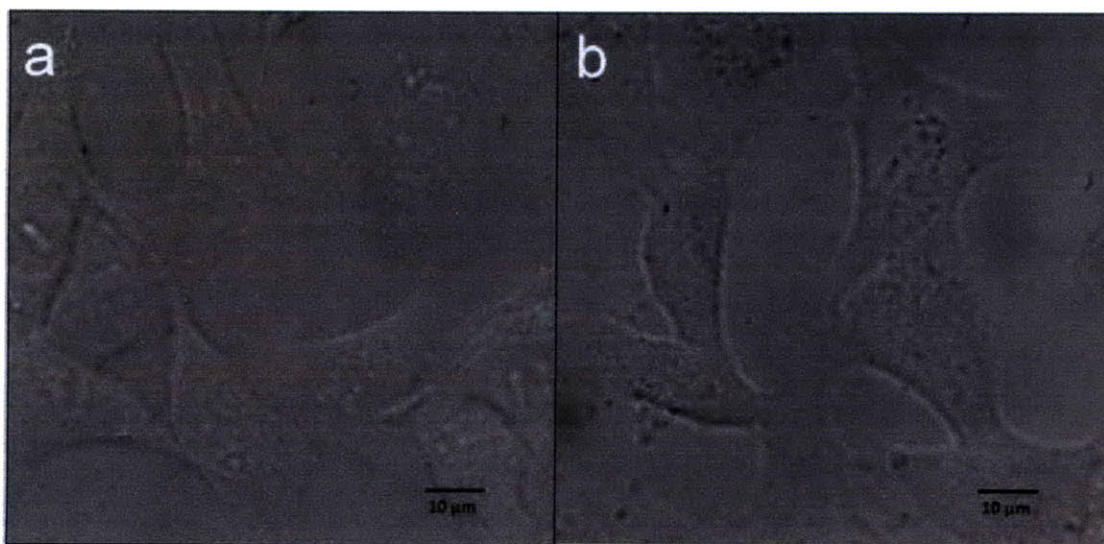


**Figure 6.19** Fluorescent and differential interference contrast (DIC) merged images of HeLa cells (a) without and (b) with incubation with MPs-Alexa Fluor 488 (*This experiment was done in collaboration with Jungmin Lee, Bawendi Group*)

After incubation of the MPs with HeLa cells, no significant different fluorescent signal was observed when compared to the cells without exposure to MPs. Both of them showed very little fluorescent signal. This observation indicates the low non-specific binding to the cell of the MPs and implies that the MPs could be used for cell imaging applications as well.

In conclusion, poly-catechol PEG polymer (PCP) shows many superior properties in stabilizing and transferring the MPs into water-based solution. The MPs with PCP surfactant are relatively small compared to the commercially used T2 contrast agents; are water-stable; and have high T2 relaxivity, high magnetization, and functionality. Also, the MPs show very low non-specific binding to the proteins in serum and to the cells.

The next section discusses the other catechol-based surfactant. This surfactant is based on using a zwitterionic entity to make the MPs water-dispersible. The goal for this surfactant is to keep the MPs with very small hydrodynamic size, stable, and low in protein non-specific binding.

#### **6.4 Mono-catechol zwitterionic surfactant**

*(This work was done in collaboration with He Wei, Bawendi Group)*

Sections 6.2 and 6.3 describe the inclusion of the PEG molecules in the surfactant structure to make MPs hydrophilic and transferrable into water. Also, the PEG has been shown to have low non-specific binding to protein and can be used in biological applications. The drawback of using PEG as a surfactant for the MPs is that the PEG has to be large in molecular weight. For example, in our study, the minimum PEG chain that was found to stabilize the MPs is the PEG with 12 units of ethylene glycol. The larger the PEG molecular weight, the larger the hydrodynamic size of the resulting MPs. Therefore, there is a lower limit for the size of the MPs that we would get from a PEG-derivative at ~18 nm in diameter in our study.

This section includes zwitterions in the surfactant structure, replacing the PEG molecule. Zwitterions are very hydrophilic in nature, and they are found to be very low biofouling.<sup>14</sup> Materials with zwitterionic surfaces were found to be low in their protein non-specific binding.<sup>15</sup> These properties make PEG of interest in nanoparticle coating applications. Therefore, the zwitterions that have similar properties should be applicable for coating nanoparticles as well. The advantage over PEG is that the zwitterions could be very small molecules, so they could potentially make MPs of very small hydrodynamic size. Given these properties of the zwitterions, the new surfactant with catechol and zwitterion was prepared, as discussed in this section. The scheme for synthesis of the zwitterionic catechol surfactant is shown in Figure 6.20.



The reactions for synthesis of the zwitterionic surfactant are synthesized using a two-step reaction. First, dopamine was sulfonated upon the ring-opening reaction with 1,3-propane sultone in ethanol at 50 °C for 18h. Dopamine sulfonate (DS, Compound 13) was the first intermediate catechol derivative product that can also act as a non-permanent zwitterionic surfactant since the protonation-deprotonation reactions of the secondary amine are dependent on pH. The DS was then methylated after reacting with iodomethane in DMF at 50 °C for 5h, and the resulted zwitterionic dopamine sulfonate (ZDS, Compound 14) was obtained. Quaternary amine and sulfonate groups of ZDS stabilize the zwitterionic character of this surfactant over a wide pH range.

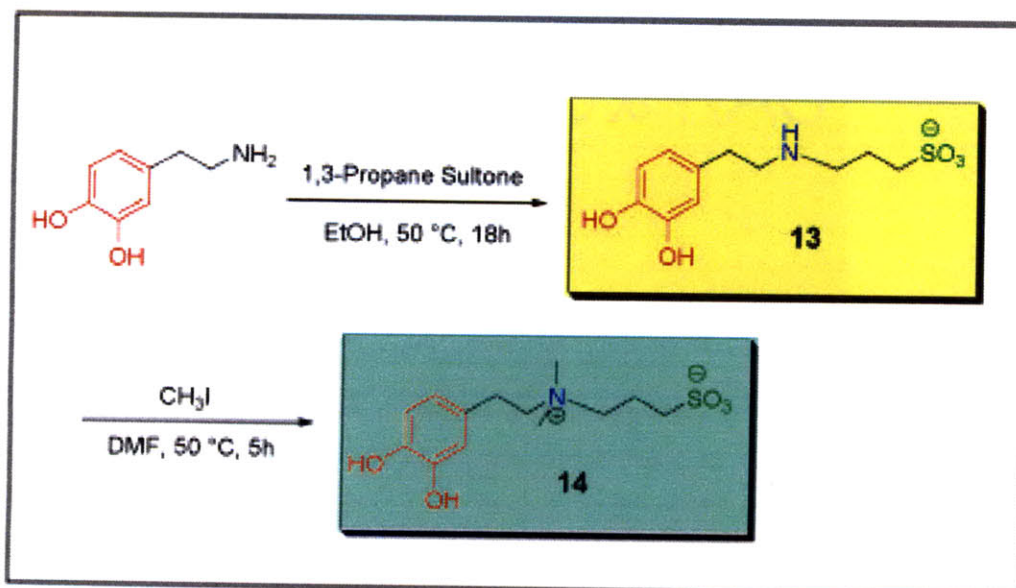


**Figure 6.20** Reaction scheme for synthesis of zwitterionic ligand.

The surfactant-exchanging process for the DS and ZDS proceeds in two steps, similar to the procedure for PCP as mentioned in Section 6.3.2. The difference between the surfactant-exchanging process of these surfactants and PCP surfactants is that the solubility of ZDS in DMF is lower and the solvent system for the second step was changed from DMF to a water/DMF solution. After being surfactant-exchanged, MPs with ZDS surfactant were then purified, and their properties were studied in the following ways.

Size distribution of the MPs with ZDS surfactants was imaged using TEM as shown in Figure 6.21. The TEM images show that the MP cores after surfactant-exchanging process with ZDS (Figure 6.21b) are similar in their size distribution to the MP cores with native oleic acid (Figure 6.21a). This observation of remaining in their MP cores size indicates that this surfactant has minimal destructive effects on the MP cores. Also, from the TEM image of ZDS-MPs, well-dispersed MPs were observed in the water-based solution and there was no aggregation of MPs. This observation suggests a high stability of the ZDS-MPs.

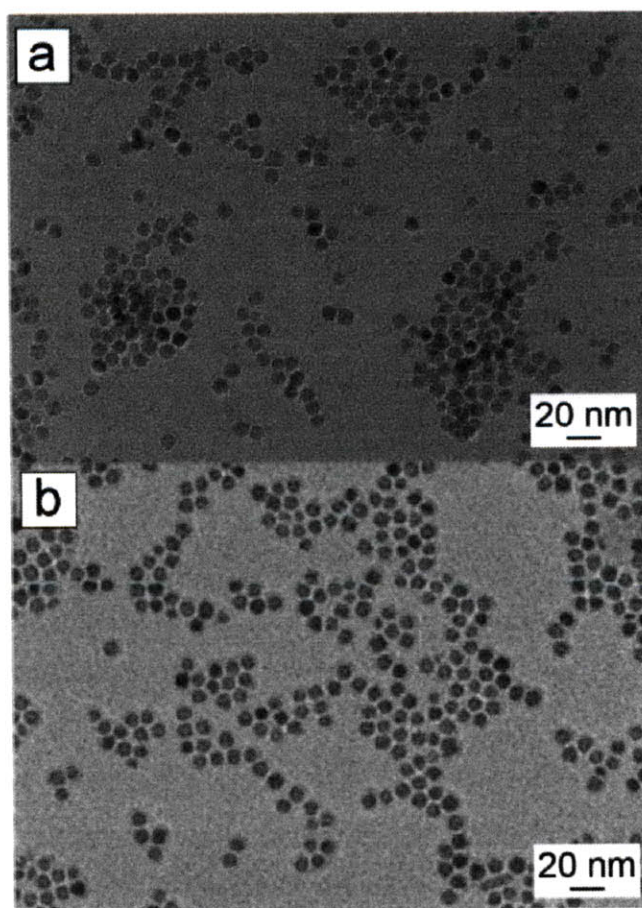


**Figure 6.21** TEM images of the MPs before (a) and after (b) being surfactant-exchanged with the zwitterionic ligand.

Size distribution of the resulted ZDS-MPs was also determined by using a dynamic light scattering analyzer. Hydrodynamic size distributions of the ZDS-MPs from

DLS are shown in Figure 6.22. The data shown in Figure 6.22a suggests that average hydrodynamic diameter of the ZDS-MPs is around 10 nm and stays at this size range in pH 6-9 with narrow size distribution similar to the curve measured at pH 7.5, as shown in Figure 6.22b. These DLS measurements demonstrate that the ZDS-MPs have excellent colloidal stability over the pH range of 6 to 9, which is within the range for physiological environments for biological applications and reaction conditions for many conjugation chemistries.

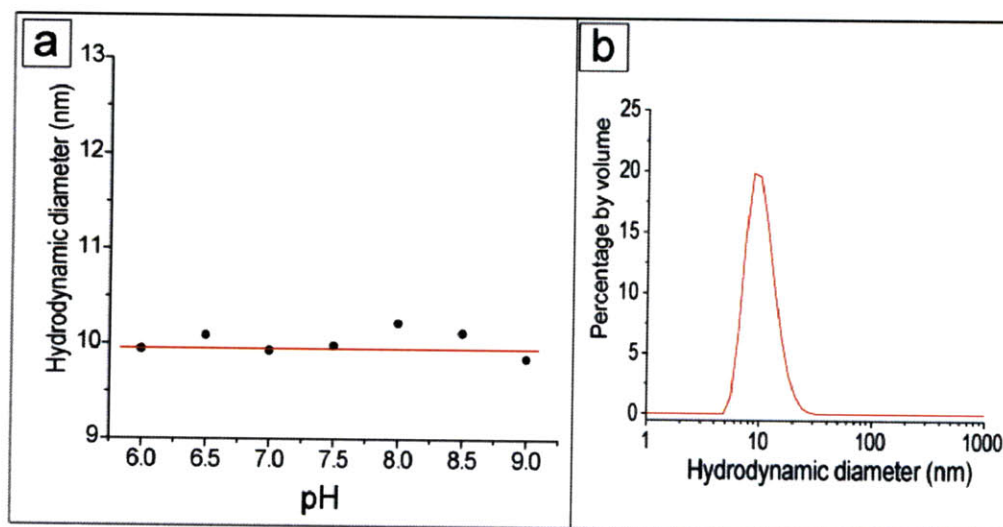


**Figure 6.22** DLS Hydrodynamic diameters of the MPs with ZDS surfactant at different pHs (a) and size distribution of the MPs at pH 7.5 (b).

Comparing the size of MP cores from TEM images and the hydrodynamic size of the ZDS-MPs reveals that the ZDS surfactant gives a very thin coating on the MP surfaces. The MPs with MP cores of ~8 nm in diameter were ~10 nm in their hydrodynamic size, indicating that only ~1 nm increase occurred in the radius when ZDS was used as a surfactant. The ZDS-MPs are significantly smaller than MPs with other catechol-derivative surfactants discussed earlier.

The zwitterionic stability of the ZDS-MPs was then studied by measuring the zeta potential over the range of pH 6-9 using a zeta potential analyzer (Malvern Instrument) as shown in Figure 6.23a. The zeta potential of the ZDS-MPs is ~-23 mV and stable over this pH range. Compared to the zeta potential of the DS-MPs, in which the secondary



amines are not permanently charged, the abrupt change in zeta potential was observed at  $\sim$ pH 7.5 (red curve in Figure 6.23a). This abrupt change in zeta potential is most likely from the deprotonation of the secondary amine in DS above pH 7.5. The DS loses its zwitterionic nature and could lead to protein non-specific binding if utilized in biological environments. In contrast, the ZDS is stable in its zwitterionic character over this pH range and could be useful for biological applications because low protein non-specific binding would be expected.

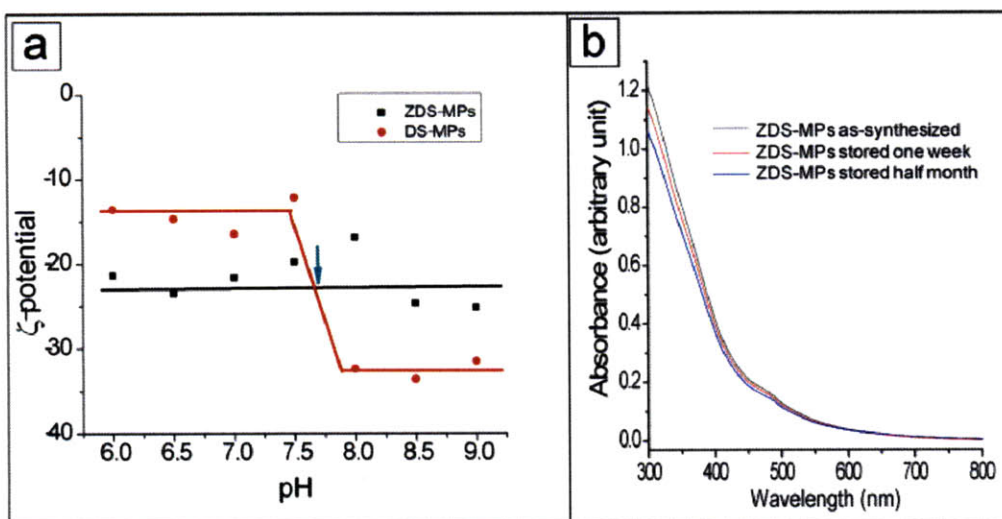


**Figure 6.23** Stability of the MPs with ZDS surfactants measured using (a) zeta-potential in different pH compared to the DS surfactant (the blue arrow indicates where the protonation and deprotonation of the DS surfactant occurred) and (b) UV-Vis spectra of ZDS-MPs with the increase in storage time.

Stability over time of the ZDS-MPs was also studied by tracking their absorption spectra over extended periods as shown in Figure 6.23b. Absorption spectra of ZDS-MPs showed some small decrease (less than 10%) in the absorbance after the ZDS-MPs were stored in PBS solution for a half-month period. Using this result, the limitation on the storage time was observed and suggested that the ZDS-MPs should be used quickly after being prepared rather than kept for a long time.

The decrease in absorbance was likely due to aggregation of ZDS-MPs, leading to their precipitation out of PBS solutions. This observation suggested that mono-catechol

group of ZDS is not enough to stabilize the surfactant on the MPs for longer storage time. Use of zwitterionic surfactants with poly-catechol groups similar to that discussed in Section 6.3 is proposed to increase stability of surfactants on the MPs.

In order to use and conjugate molecules of interest to the ZDS-MPs, another surface modification is needed for attaching functional groups onto the MPs. Functionalization of these MPs can be done by adding co-surfactants that have an available functional group. One molecule that is currently used as co-surfactants is thiol-PEG-catechol, which is similar in its structure to the monocatechol-PEG derivative discussed in Section 6.3 but uses a shorter chain of PEG.

## 6.5 Conclusion

Catechol derivatives of different structures are used and studied as surfactants for iron oxide MPs. Among these surfactants that have been studied, polycatechol polyethylene (PCP) and zwitterionic catechol hold the most interest as they have properties superior to those of other surfactants. The MPs with PCP surfactants are superior in term of their stability from the chelating effect of polycatechol and controllable quantity of functional groups from the co-polymer chains. The MPs with zwitterionic catechol are superior in term of the small size of the MPs obtained.

The MPs with high stability in water-based solutions, small hydrodynamic size, and low protein non-specific binding are ready to be useful tools in biological applications. Moreover, MPs with available functional groups such as the MPs with PCP surfactants can also serve as building blocks for even more complex structures. In Chapter 7, various conjugation techniques for these functional MPs are discussed, aiming at a formation of bi-functional nanostructures comprising MPs and semiconductor QDs.

## 6.6 References

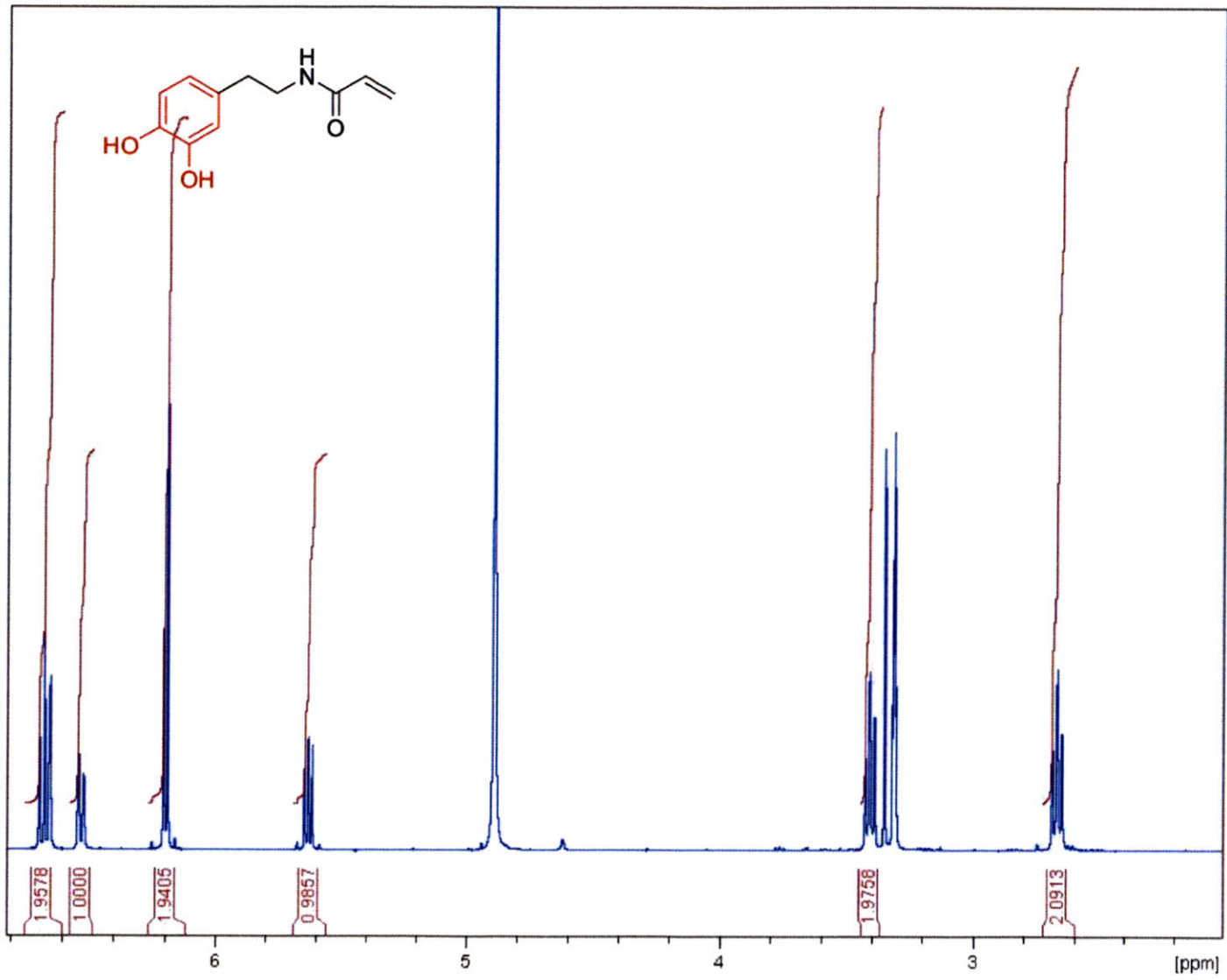
1. Atanasijevic, T.; Shusteff, M.; Fam, P.; Jasanoff, A., Calcium-sensitive MRI contrast agents based on superparamagnetic iron oxide nanoparticles and calmodulin. *Proceedings of the National Academy of Sciences of the United States of America* **2006**, 103, (40), 14707-14712.

2. Shultz, M. D.; Reveles, J. U.; Khanna, S. N.; Carpenter, E. E., Reactive nature of dopamine as a surface functionalization agent in iron oxide nanoparticles. *Journal of the American Chemical Society* **2007**, 129, (9), 2482-2487.
3. Xu, C. J.; Xu, K. M.; Gu, H. W.; Zheng, R. K.; Liu, H.; Zhang, X. X.; Guo, Z. H.; Xu, B., Dopamine as a robust anchor to immobilize functional molecules on the iron oxide shell of magnetic nanoparticles. *Journal of the American Chemical Society* **2004**, 126, (32), 9938-9939.
4. Wang, L.; Yang, Z. M.; Gao, J. H.; Xu, K. M.; Gu, H. W.; Zhang, B.; Zhang, X. X.; Xu, B., A biocompatible method of decorporation: Bisphosphonate-modified magnetite nanoparticles to remove uranyl ions from blood. *Journal of the American Chemical Society* **2006**, 128, (41), 13358-13359.
5. Lee, J. H.; Huh, Y. M.; Jun, Y.; Seo, J.; Jang, J.; Song, H. T.; Kim, S.; Cho, E. J.; Yoon, H. G.; Suh, J. S.; Cheon, J., Artificially engineered magnetic nanoparticles for ultra-sensitive molecular imaging. *Nature Medicine* **2007**, 13, (1), 95-99.
6. Liu, W.; Howarth, M.; Greytak, A. B.; Zheng, Y.; Nocera, D. G.; Ting, A. Y.; Bawendi, M. G., Compact biocompatible quantum dots functionalized for cellular imaging. *Journal of the American Chemical Society* **2008**, 130, (4), 1274-1284.
7. Nitin, N.; LaConte, L. E. W.; Zurkiya, O.; Hu, X.; Bao, G., Functionalization and peptide-based delivery of magnetic nanoparticles as an intracellular MRI contrast agent. *Journal of Biological Inorganic Chemistry* **2004**, 9, (6), 706-712.
8. Xie, J.; Xu, C.; Kohler, N.; Hou, Y.; Sun, S., Controlled PEGylation of monodisperse Fe<sub>3</sub>O<sub>4</sub> nanoparticles for reduced non-specific uptake by macrophage cells. *Advanced Materials* **2007**, 19, 3163-3166.
9. Chiefari, J.; Chong, Y. K.; Ercole, F.; Krstina, J.; Jeffery, J.; Le, T. P. T.; Mayadunne, R. T. A.; Meijs, G. F.; Moad, C. L.; Moad, G.; Rizzardo, E.; Thang, S. H., Living free-radical polymerization by reversible addition-fragmentation chain transfer: The RAFT process. *Macromolecules* **1998**, 31, (16), 5559-5562.
10. Susumu, K.; Uyeda, H. T.; Medintz, I. L.; Pons, T.; Delehanty, J. B.; Mattoussi, H., Enhancing the stability and biological functionalities of quantum dots via compact multifunctional ligands. *Journal of the American Chemical Society* **2007**, 129, 13987-13996.
11. Liu, W. H.; Greytak, A. B.; Lee, J.; Wong, C. R.; Park, J.; Marshall, L. F.; Jiang, W.; Curtin, P. N.; Ting, A. Y.; Nocera, D. G.; Fukumura, D.; Jain, R. K.; Bawendi, M. G., Compact Biocompatible Quantum Dots via RAFT-Mediated Synthesis of Imidazole-Based Random Copolymer Ligand. *Journal of the American Chemical Society* **2010**, 132, (2), 472-483.

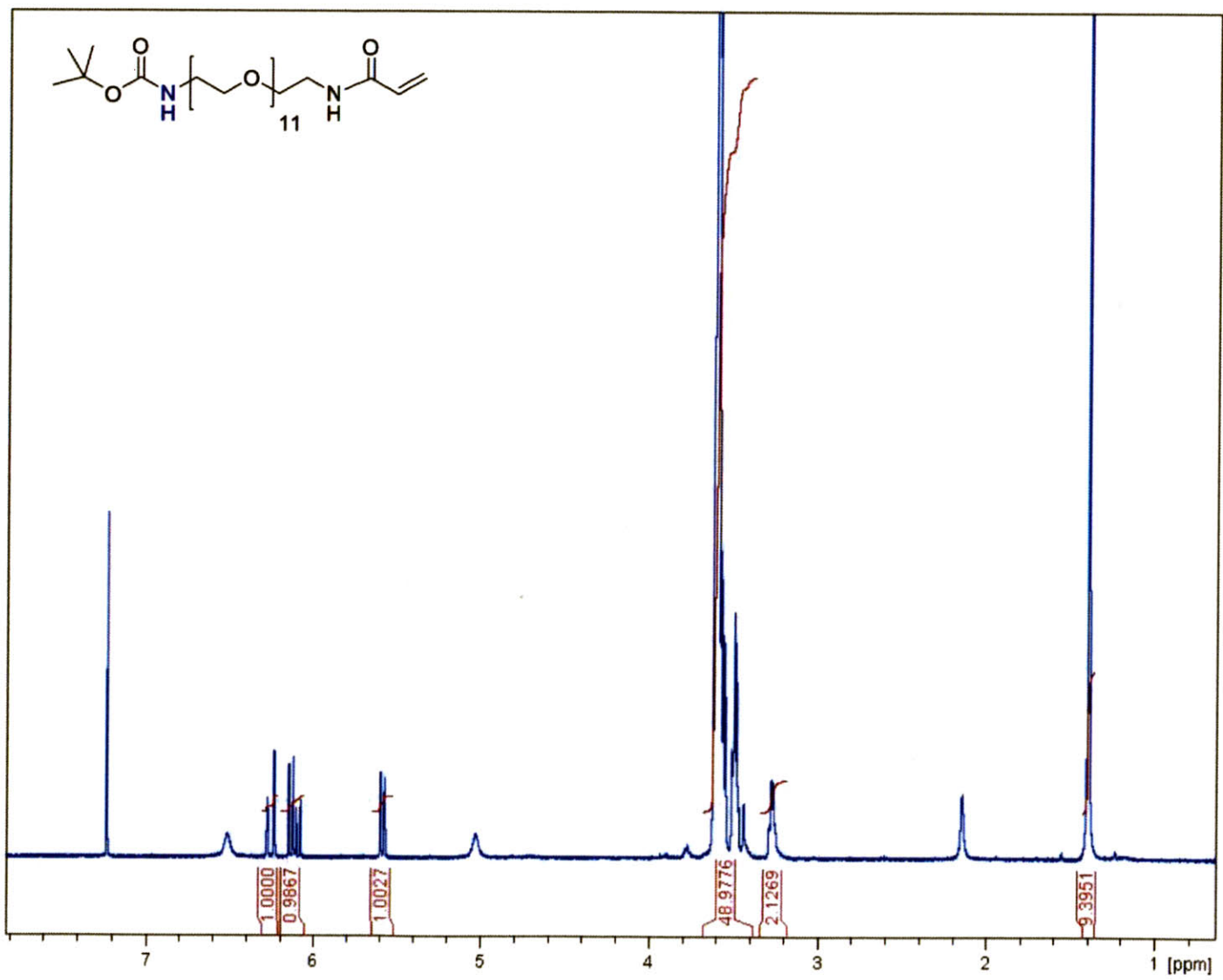


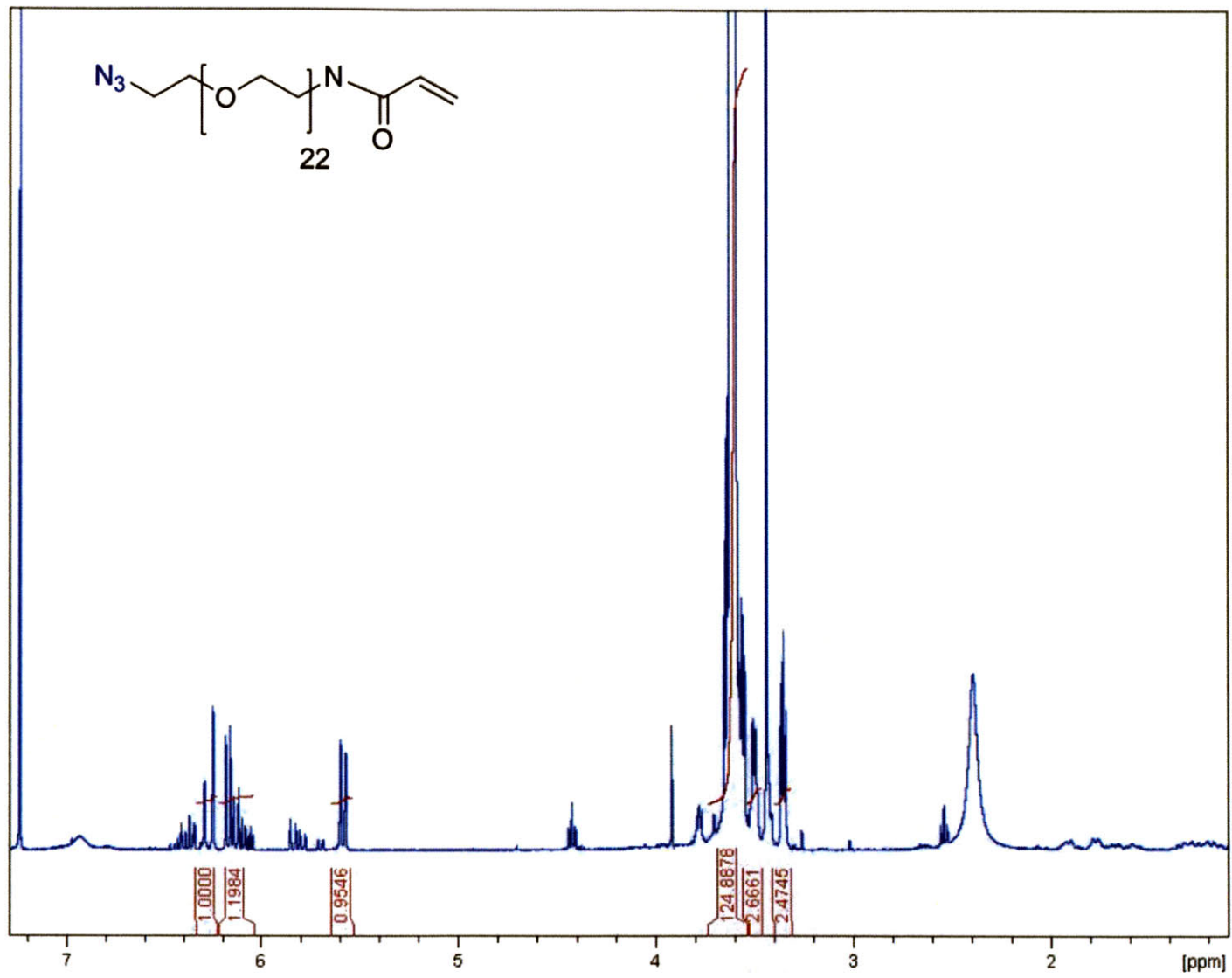
12. Na, H. B.; Song, I. C.; Hyeon, T., Inorganic Nanoparticles for MRI Contrast Agents. *Advanced Materials* **2009**, 21, (21), 2133-2148.
13. Morales, M. P.; Veintemillas-Verdaguer, S.; Montero, M. I.; Serna, C. J.; Roig, A.; Casas, L.; Martinez, B.; Sandiumenge, F., Surface and internal spin canting in gamma-Fe<sub>2</sub>O<sub>3</sub> nanoparticles. *Chemistry of Materials* **1999**, 11, (11), 3058-3064.
14. Brault, N. D.; Gao, C. L.; Xue, H.; Piliarik, M.; Homola, J.; Jiang, S. Y.; Yu, Q. M., Ultra-low fouling and functionalizable zwitterionic coatings grafted onto SiO<sub>2</sub> via a biomimetic adhesive group for sensing and detection in complex media. *Biosensors & Bioelectronics* 25, (10), 2276-2282.
15. Vaisocherova, H.; Zhang, Z.; Yang, W.; Cao, Z. Q.; Cheng, G.; Taylor, A. D.; Piliarik, M.; Homola, J.; Jiang, S. Y., Functionalizable surface platform with reduced nonspecific protein adsorption from full blood plasma-Material selection and protein immobilization optimization. *Biosensors & Bioelectronics* **2009**, 24, (7), 1924-1930.

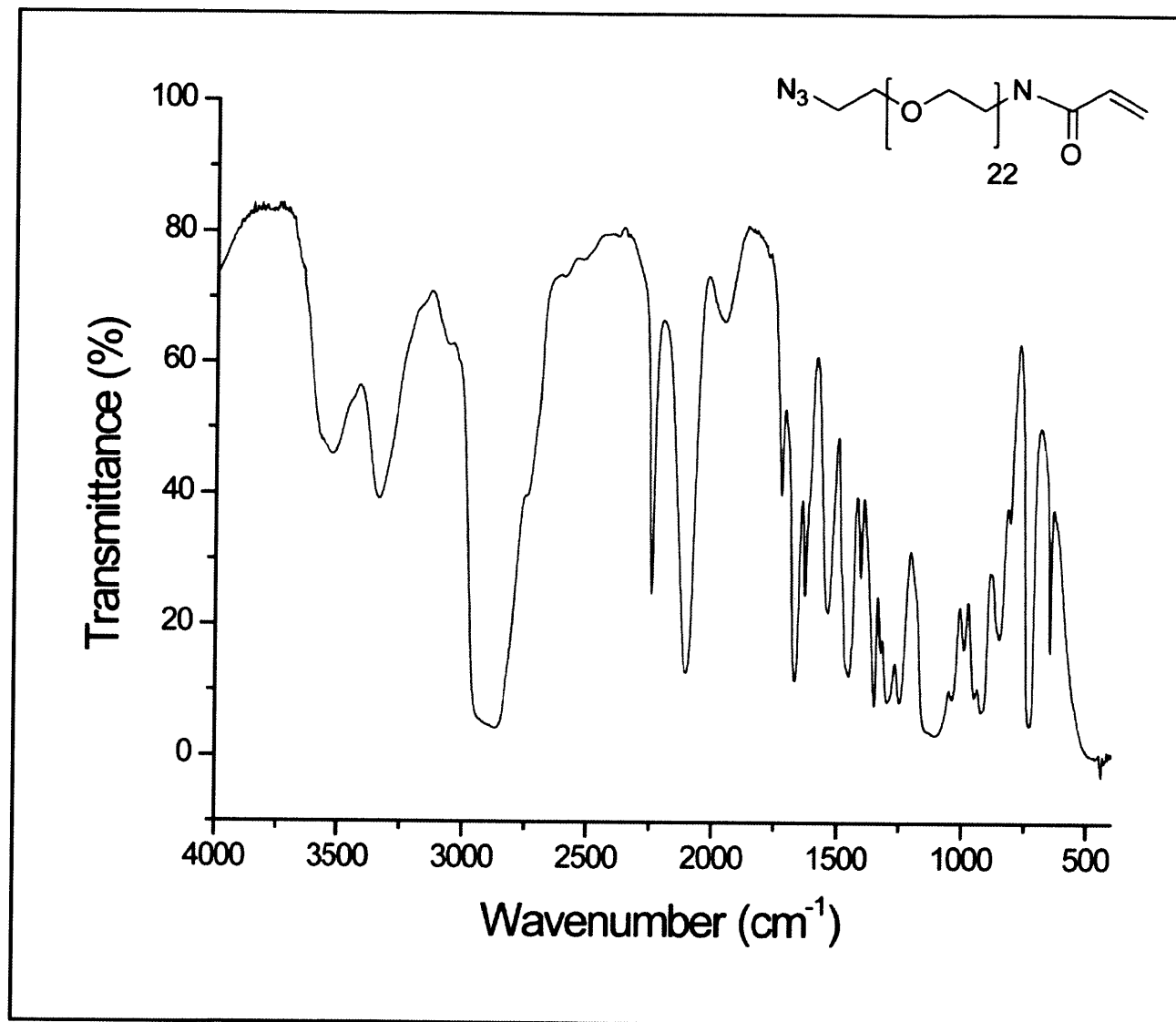
6.7 Appendix C: <sup>1</sup>H NMR and IR Spectra of Compounds













## Chapter 7

### QD-Decorated Iron Oxide Nanoparticles

#### 7.1 Introduction

Chapters 3 and 4 discuss the reasons for interest in nanostructures that combine superparamagnetic nanoparticles and quantum dots. This chapter discusses approaches to synthesizing the smallest possible clusters of MPs and QDs. Preparation of these nanostructures aims to make a new tool for MRI-fluorescent bimodal imaging and to study the conjugations of the water-dispersible MPs with different surface modification methods.

The nanostructures of MPs and QDs have been synthesized and studied recently.<sup>1-6</sup> In these works, the direct growth of QDs on MP surfaces can lead to clustering of the MPs and QDs.<sup>3-5</sup> However, the nanostructures from these direct attachment syntheses suffer from quenching of the fluorescence of the QDs and very low quantum yield of the QD observed.<sup>3,6</sup> Moreover, the direct growth of the QDs on MP surfaces tends to yield nanostructures of irregular shape and uncontrollable ratio of MPs to QDs.<sup>3,5,6</sup> In addition, difficulties in transferring these nanostructures into water-based solutions for biological applications are foreseeable as the surface chemistries of MPs and QDs are different. Therefore, it is difficult to find the surface modification systems that are compatible with both materials at the same time.

This chapter explores formations of QD-MP nanoparticles that are based on the MPs and QDs that are water-soluble with available functional groups. We propose that these nanostructures will inherit the properties of stability in water-based solutions and availability of functional groups from their QD and MP starting materials. Moreover, with these conjugations, the MPs and QDs do not directly attach to each other's surfaces and quenching of the QDs should be less than that from the direct growth of QD on the MP systems.

This chapter proposes the use of MPs from different surface modifications (as mentioned in Chapters 5 and 6) as cores to decorate with QDs with different functional

groups. Sections 7.2 and 7.3 focus on the mPAA-MPs from Chapter 5 and the MPs with catechol-derivative surfactants from Chapter 6, respectively.

## 7.2 QD-Conjugation of MPs with mPAA surfactants

MPs with mPAA, which were discussed in Chapter 5, are observed to be highly stable in water-based solutions. Also, carboxylic groups on their surfaces are found to be reactive to conjugation with other molecules through amide bonding. After the conjugation of mPAA-MPs with other molecules, their properties of the former remain satisfactory because their hydrodynamic size, magnetization, and stability stay similar to those of the mPAA-MPs before conjugation. Given this observation, the mPAA-MPs appear to be good candidates for forming the proposed QD-decorated MPs nanostructures.

The conjugation reaction of the mPAA-MPs to QDs is shown in the scheme in Figure 7.1. In this conjugation, mPAA-MPs synthesized using the procedure in Chapter 5 are conjugated with QDs functionalized with DHLA-PEG-amine ligands synthesized using the procedure previously reported from our group.<sup>7</sup> Carboxylic groups on mPAA-MP surfaces were activated using EDC before reacting with the amino groups on QD surfaces. The ratio of MPs to QDs were controlled to be 1:30 in order to obtain the proposed QD-decorated MPs nanostructures without cross-linking between the MPs due to the multivalency of both MPs and QDs.

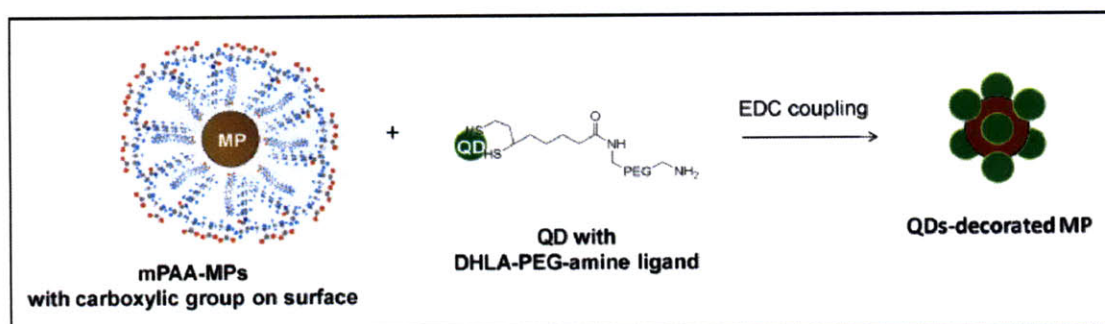


**Figure 7.1** Reaction scheme for MP and QD conjugation using EDC coupling agent.

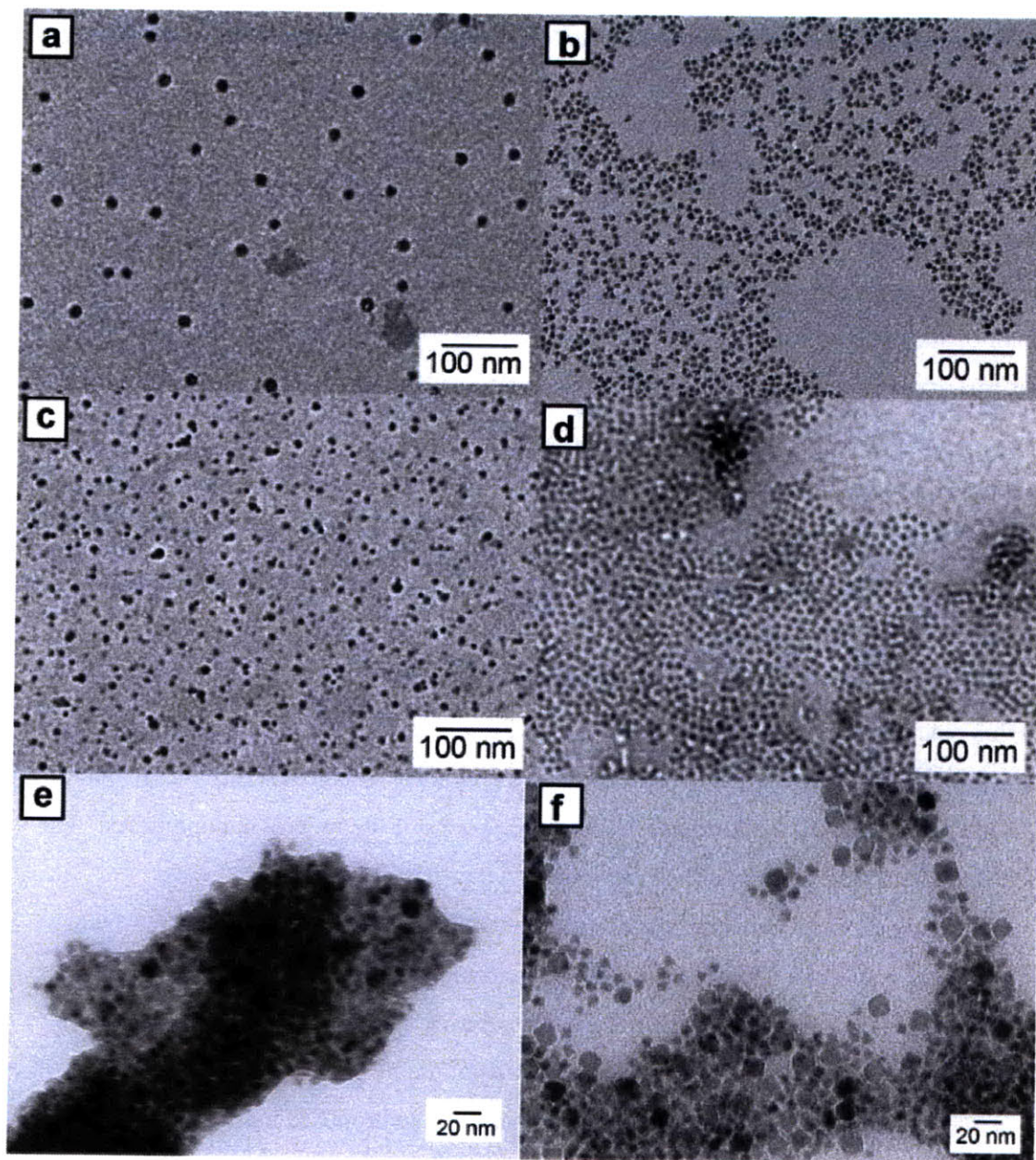


**Figure 7.2** TEM images of the MP-QD conjugation using EDC coupling agent: (a) mPAA-MPs, (b) amino-PEG-DHLA QDs, (c) control mixture of MPs and QDs with EDC, and (d-f) products from EDC coupling reaction with different magnifications.



The reaction between the mPAA-MPs and the QD-DHLA-PEG-NH<sub>2</sub> was monitored using TEM as shown in Figure 7.2. Well-dispersed MPs (Figure 7.2a) and QDs (Figure 7.2b) were observed before the reaction. The mixture of MPs and QDs before the activation of the carboxylic group using the EDC is shown in Figure 7.2c, in which the well-dispersed MPs and QDs are observed. The mixture of MPs and QDs shows a minimal non-specific attraction that could be expected from the attraction between the opposite charges of the negatively-charged MPs and the amino-functionalized QDs. This observation suggested that there is not enough force for the electrostatic attraction and other physical interactions between the MPs and QDs.

Aggregations of the MPs and QDs were observed when the EDC and sulfo-NHS were added to the reaction mixture. The clusters of MPs and QDs were observed in Figures 7.2d-f. The aggregation of the MPs and QDs indicates that reaction between the two nanoparticles is too violent and out of control because large aggregations and extended cross-linking networks of nanoparticles were observed.

The other reason why the large aggregations of the MPs and QDs were observed in this reaction scheme is that the EDC reagent can neutralize the mPAA and cause the aggregations of the MPs. This observation was previously reported when a large quantity of the EDC was used to activate the carboxylic groups of the mPAA-nanoparticles.<sup>8</sup> The neutralized nanoparticles lost their stability in water-based solutions and were precipitated out. One of the approaches to prevent the nanoparticles with mPAA from aggregating is to use a different coupling reagent such as PEG-modified EDC.<sup>8</sup>

Given the instability of the mPAA-MPs during conjugation using the reaction scheme mentioned above, the mPAA-MPs were not the most suitable systems for constructing the QD-decorated MPs nanostructures. We proposed using MPs with higher stability toward the conjugation reactions such as MPs with PEG on their surface and substituting them for the mPAA-MPs systems. The conjugation of QDs to the MPs with PEG-catechol derivative surfactants is discussed in Section 7.3.

### **7.3 QD-conjugation of MPs with PEG-catechol derivative surfactants**

MPs with polycatechol polyethylene glycol polymer (PCP, in Chapter 6) are better candidates for the construction of the QD-decorated MPs nanostructure as they are

more stable toward changes in surface charges than the mPAA-MP system. The PCP-MPs are dispersible into water-based solution because of the hydrophilicity of the PEG chain. Therefore, changes in the charge of the MP surfaces during the conjugation process will not have strong effects on the stability of the PCP-MP systems.

The conjugation of the MPs and QDs is based on the available functional groups of the PCP surfactants. The first group of interest is biotin because its interaction with streptavidin is very strong and could be a good candidate for the conjugation of QDs and MPs. The biotinylated-PCP-MPs and streptavidin-QDs should be readily attracting to each other, and the conjugation of the MPs and QDs should readily form after the incubation of the two nanoparticles. The reaction scheme for this conjugation is shown in Figure 7.3.

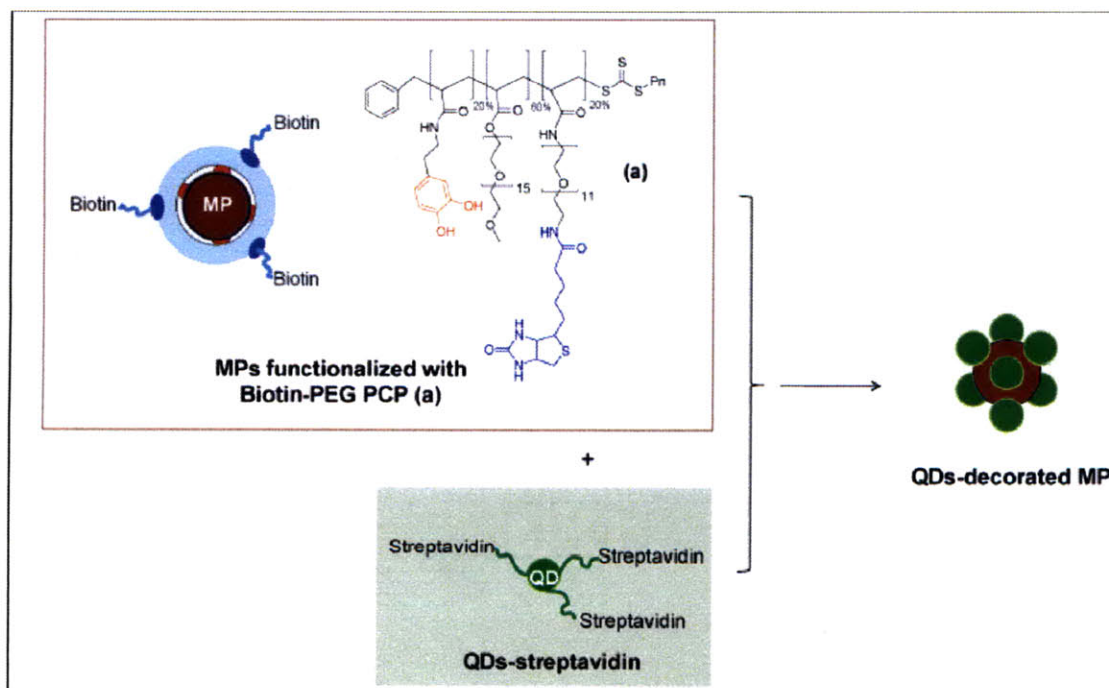


**Figure 7.3** Reaction scheme for MP and QD conjugation using streptavidin-biotin interaction.

MPs with biotinylated-PCP were prepared similar to the previously discussed procedure in Section 6.3.1. The biotinylated-PCP (Compound a, Figure 7.3) was synthesized by polymerization of three monomers: catechol monomer, methoxyPEG

monomer, and biotinylated-PEG monomer (Compounds 1, 2, and 11, respectively, in Chapter 6). After the surfactant-exchanging and purification processes, the biotin-PCP-MPs were ready for the conjugation. The TEM image of the MPs with biotin groups on their surface is shown in Figure 7.4a.

QDs with streptavidin on their surfaces were purchased from Invitrogen and used without further purification. The TEM image of these streptavidin-QDs is shown in Figure 7.4b. The TEM image shows the irregular shapes and broad size distributions observed in this commercial sample.

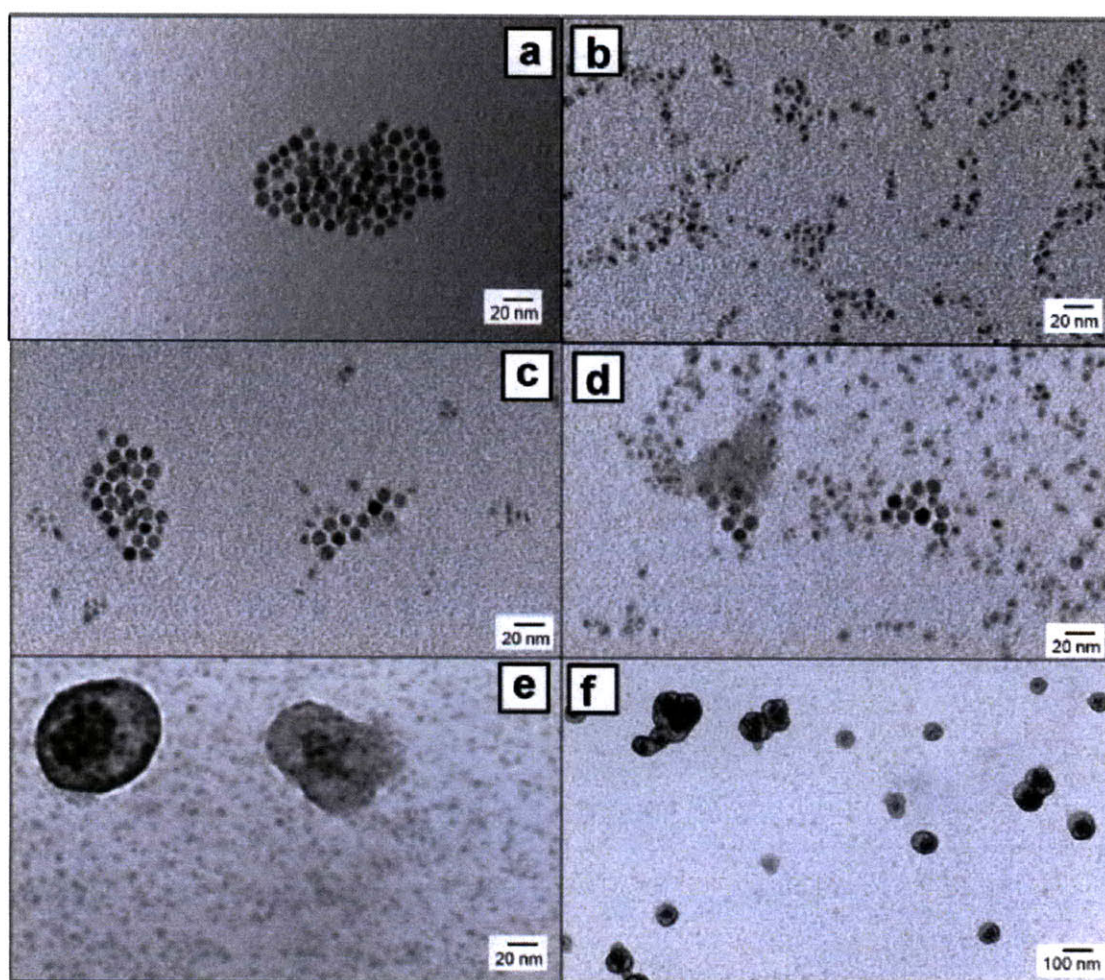


**Figure 7.4** TEM images of the MP-QD conjugation using streptavidin-biotin interaction: (a) biotin MPs, (b) streptavidin QDs, (c-f) reaction mixture with QD:MP molar ratio of (c) 1:1, (d) 30:1 and (e-f) 100:1 with different magnifications.



Three different molar ratios of biotin-MPs to streptavidin-QDs (QD:MP of 1:1, 30:1 and 100:1) were prepared and monitored in order to find the proper ratio for the formation of the proposed QD-decorated MPs nanostructures. The TEM images of these conjugation reactions are shown in Figures 7.4c-f.

The TEM images of the reaction mixtures from different ratios of QD per MP, suggest that the most suitable ratio of QD to MP is 100:1 as the formation of clusters were observed from the reaction mixture using this ratio as shown in Figures 7.4e and 7.4f. The reaction mixtures from the QD:MP ratio of 1:1 (Figure 7.4c) and 30:1 (Figure 7.4d) show some conjugation of QDs to MPs, but there is no cluster or regular pattern of the aggregation observed. In the reaction mixture with the QD:MP of 100:1, the clusters that were observed range from 40 nm to 100 nm in diameter, which falls in the size range of the proposed QD-decorated MPs nanostructures.

The reaction mixture of the QD:MP of 100:1 was then further purified using centrifugal filter dialysis with 100 KDa molecular weight cut-off membrane to get rid of the excess streptavidin-QDs. The purified clusters were then imaged using TEM as shown in Figure 7.5.

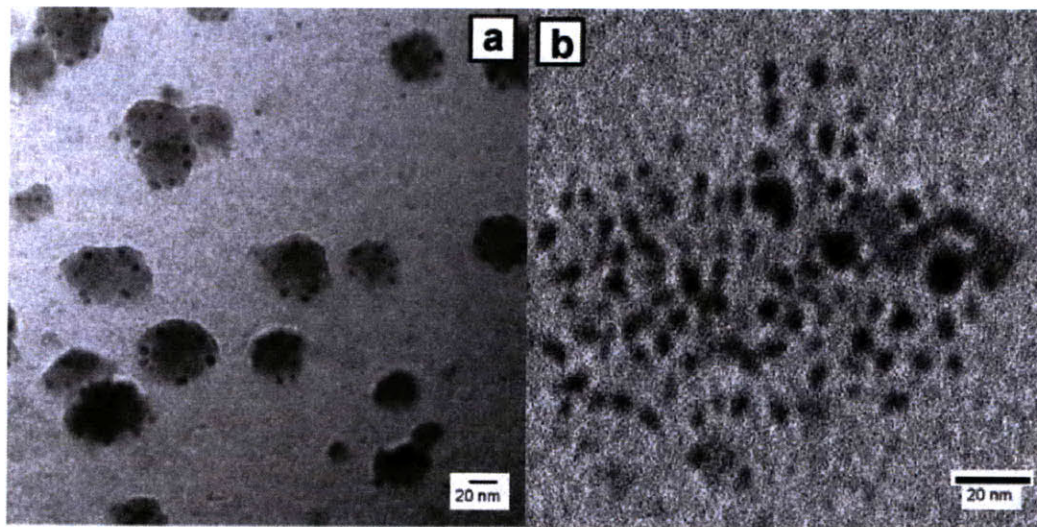


**Figure 7.5** TEM images of the MP-QD conjugation using streptavidin-biotin interaction after purification by centrifugal filter dialysis.

The purified clusters of MP and QD conjugates were found to have narrower size distribution of 40 to 60 nm in diameter (Figure 7.5a) because the larger particles were likely precipitated out after centrifugation. The TEM images reveal that most parts of the clusters are of organic compound origin as the transmission images showed the grey areas of organic compound feature. This observation is likely due to the fact that the clusters contain mostly streptavidin and the coating polymers. However, in some of the clusters, the conjugates of MPs and QDs were observed as in Figure 7.5b. The cross-linking of the MPs was observed because more than one MP was found in the same cluster.

The TEM images in Figure 7.5 suggest that the conjugation of MPs and QDs was obtained using this reaction condition. However, the sizes of the conjugates are larger than expected because the nanostructures consist of mostly the streptavidin and the polymer coating. Also, the large size of the conjugates resulted from the cross-linked nanoparticles as multiple MPs were observed in the same cluster. The control of cross-linking between the nanostructures is difficult as the commercial streptavidin was not well characterized and the multivalency of both MPs and QDs tended to cause the cross-linking structures. One approach to reducing cross-linking is using an even greater excess of the QDs over the MPs, but this approach is too costly to apply in the synthesis. The synthesis of our own streptavidin-QD using the conjugation of streptavidin with the surfactant synthesized in our group is under investigation and could be potentially used for the improved the construction of the QD-decorated MPs.

In order to reach the goal of obtaining the smallest possible nanostructure of QD-decorated MPs, a new conjugation scheme was proposed and explored. This conjugation scheme moved away from using the streptavidin-biotin interaction. The proposed conjugation employed the coupling reaction of maleimide and thiol groups as shown in Figure 7.6.

The conjugation of the MPs and QDs using this scheme is based on the highly efficient coupling reaction between maleimide and thiol groups. The thiol group was chosen to be functionalized onto MP surfaces while maleimide was attached to the QD surfaces. The reason behind this selection is that thiol groups have a high tendency to re-attach to QD surfaces, possibly causing cross-linking and loss of available thiol groups on

the proposed thiol-QDs. Therefore, thiol-MPs and maleimide-QDs were separately synthesized as starting materials for this construction.

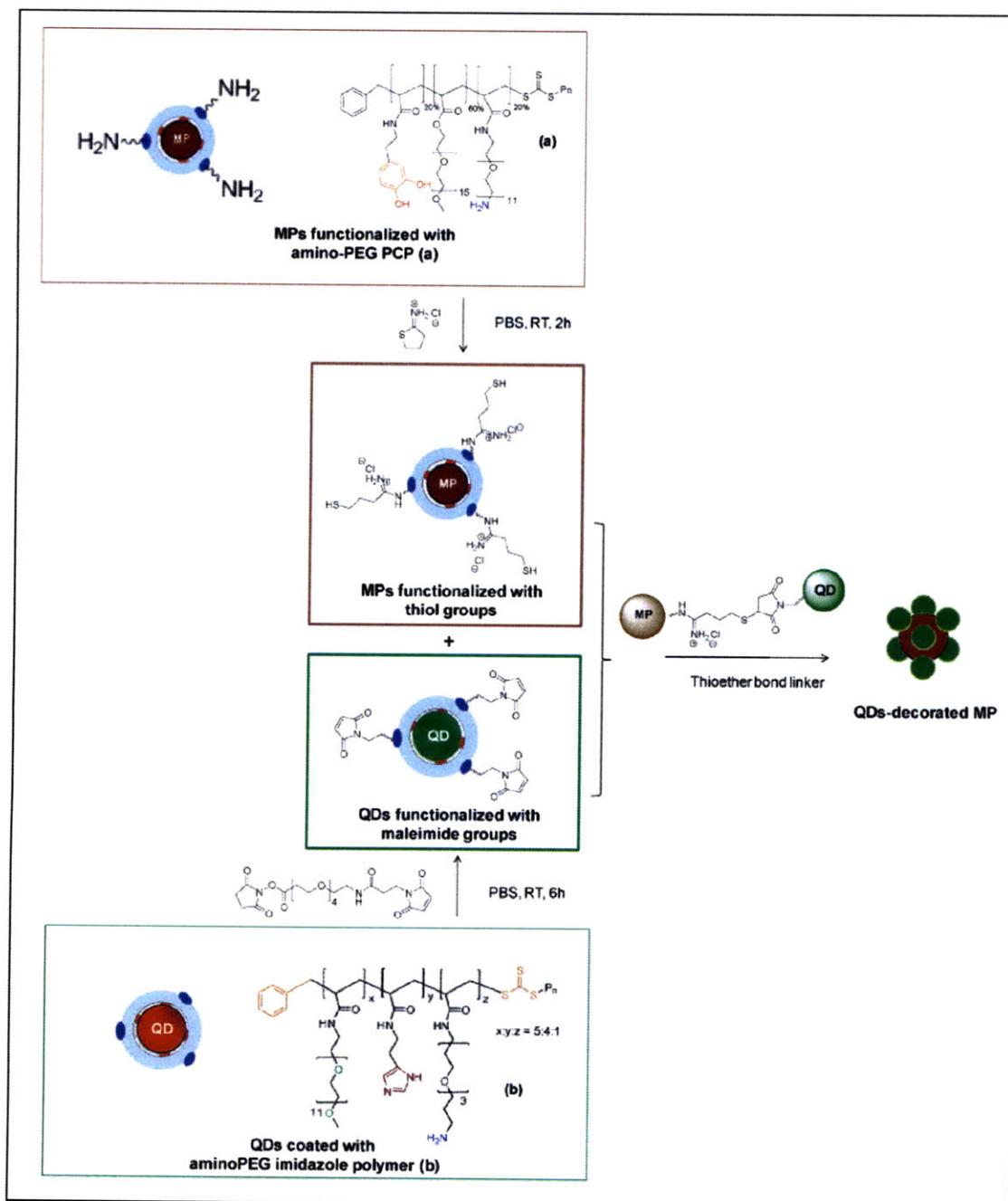


**Figure 7.6** Reaction scheme for MPs and QDs conjugation using maleimide-thiol coupling reaction.

The MPs functionalized with a thiol group were prepared from amino-functionalized MPs as shown in the reaction scheme in Figure 7.6. Amino-functionalized PCP (Compound 9 in Chapter 6) was first applied to the surfaces of the MPs using the procedure in Chapter 6. Figure 7.7b shows a TEM image of these amino-functionalized MPs. The amino groups were then converted into thiol groups using an excess quantity of Traut's reagent (2-Iminothiolane hydrochloride, Sigma-Aldrich). This converting reaction was done at room temperature in PBS solution for 2 hours right before the use of thiol-MPs in order to prevent the oxidation of the thiol groups. The reaction mixture was then purified by means of dialysis using centrifugal filter with a 50 KDa molecular weight cut-off membrane and the resulting thiol-MPs was ready for conjugation with maleimide-QDs.

The QDs functionalized with maleimide groups were synthesized from amino-functionalized QDs with aminoPEG polyimidazole polymer (Figure 7.6, structure b) as their surfactant. Preparations of the surfactant and the amino-functionalized QDs were recently reported from our group.<sup>9</sup> A TEM image of these amino-functionalized QDs is shown in Figure 7.7a. The amino groups were then converted into maleimide groups using an excess quantity of SM(PEG)<sub>4</sub> cross-linker (succinimidyl-([N-maleimido-propionamido]-tetraethyleneglycol) ester, Pierce). This converting reaction was done at room temperature in PBS solution for 6 hours right before the use of maleimide-QDs in order to prevent the decomposition of the maleimide group. The reaction mixture was purified by centrifugal dialysis through a 30 KDa molecular weight cut-off filter and the resulted maleimide-QDs are ready for conjugation with thiol-MPs.

The conjugation reaction between the thiol-MPs and maleimide-QDs was performed at room temperature in PBS solution for 6 hours. The coupling between maleimide and thiol groups led to the formation of the thioether bond and resulted in the conjugation of MPs and QDs. The conjugation using this reaction scheme was monitored by TEM as shown in Figure 7.7.



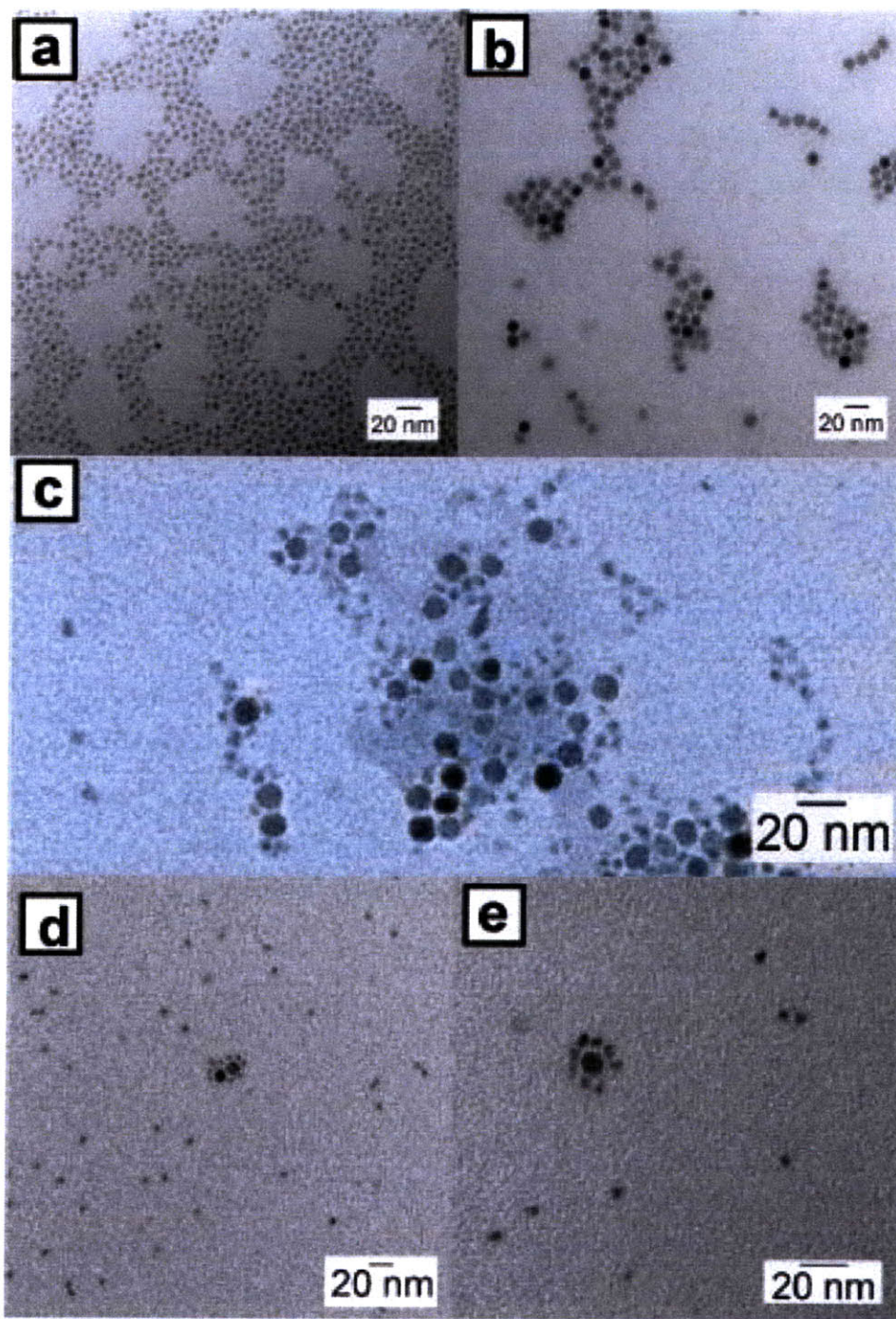


**Figure 7.7** TEM images of the MP-QD conjugation using the maleimide-thiol coupling reaction: (a) amino-functionalized QDs, (b) amino-functionalized MPs, (c-e) reaction mixture of different regions and magnifications.

The TEM images of the reaction mixture of the coupling reaction between the thiol-MPs and maleimide-QDs (Figures 7.7c-e) suggest that the conjugation of the MPs and QDs was obtainable because the attachment of the MPs and QDs were observed. However, the attachments of QDs and MPs were mostly in random fashion, and some cross-linking of the MPs and QDs was observed as shown in Figure 7.7c. The proposed nanostructures of QD-decorated MPs were observed in some places of this TEM sample as shown in Figures 7.7d and e.

The limitation for this conjugation is that the concentrations of the thiol and maleimide groups are very low, leading to a low rate of reaction. The thiol and maleimide groups are known to be unstable for long periods in water as they can be oxidized and hydrolyzed, respectively. The thiol-MPs and maleimide-QDs could become unreactive before the completion of the reaction. For this reason, the low yield of MP-QD conjugation was observed.

The proposed nanostructures of QD-decorated MPs are still not primary products from the conjugation, and they are not separable from the reaction mixture. However, this study is the first demonstration that the complex nanostructures of QD-decorated MPs can be obtained. The improvement and optimization on the conjugation need to be performed in order to obtain a significant quantity of the MP-QD nanostructures for biological applications.

#### **7.4 Conclusion**

The conjugation reactions between MPs and QDs of different functional groups were studied with the aim of constructing complex nanostructures of QD-decorated MPs. These conjugation methods suggested some features of the proposed nanostructures, but the products appeared in small quantities and were not separable from the reaction mixtures. However, this is the first observation of direct conjugation between water-dispersible MPs and QDs to result in formation of nanostructures that are readily dispersible into water-based solutions. These conjugation reactions cannot be done without the MPs of high water-stability and availability of reactive functional groups studied and discussed in earlier chapters.



Beyond studying the formation of the complex bi-functional nanostructures, it is also useful to study the conjugation techniques for the MPs with different surface modifications and functional groups. The conjugation schemes in these studies can be applied for the conjugation of the MPs to other molecules of interest. Since the steric hindrance for the conjugation with smaller molecules will decrease compared to the conjugation with relatively bulky nanoparticles, the yield of the conjugation should be significantly higher and some useful conjugates could be obtained.

Nanostructures of QD-decorated MPs of better quality in terms of narrower size distribution, higher reaction yields, and more compact size can be obtained using some developments. The first development is to synthesize of monovalent nanoparticles, or nanoparticles with only one functional group per nanoparticle. We propose that these monovalent nanoparticles will decrease the cross-linking problems when they are utilized as building blocks for the nanostructures. Also, it is helpful for development of other functional groups with higher stability and more reactivity toward the conjugation to overcome the low yield of the conjugation due to low concentration of the functional groups. These developments are currently the aim of ongoing research projects. With these improvements, the QD-decorated MPs nanostructures could be synthesized with better quality and could be a useful tool for biological imaging applications.

## 7.5 References

1. Zhang, Y.; Wang, S. N.; Ma, S.; Guan, J. J.; Li, D.; Zhang, X. D.; Zhang, Z. D., Self-assembly multifunctional nanocomposites with Fe<sub>3</sub>O<sub>4</sub> magnetic core and CdSe/ZnS quantum dots shell. *Journal of Biomedical Materials Research Part A* **2008**, 85A, (3), 840-846.
2. Ang, C. Y.; Giam, L.; Chan, Z. M.; Lin, A. W. H.; Gu, H.; Devlin, E.; Papoefthymiou, G. C.; Selvan, S. T.; Ying, J. Y., Facile Synthesis of Fe<sub>2</sub>O<sub>3</sub> Nanocrystals without Fe(CO)<sub>5</sub> Precursor and One-Pot Synthesis of Highly Fluorescent Fe<sub>2</sub>O<sub>3</sub>-CdSe Nanocomposites. *Advanced Materials* **2009**, 21, (8), 869-873.
3. McDaniel, H.; Shim, M., Size and Growth Rate Dependent Structural Diversification of Fe<sub>3</sub>O<sub>4</sub>/CdS Anisotropic Nanocrystal Heterostructures. *Acs Nano* **2009**, 3, (2), 434-440.
4. Gao, J. H.; Zhang, B.; Gao, Y.; Pan, Y.; Zhang, X. X.; Xu, B., Fluorescent magnetic nanocrystals by sequential addition of reagents in a one-pot reaction: A simple

preparation for multifunctional nanostructures. *Journal of the American Chemical Society* **2007**, 129, 11928-11935.

5. Kwon, K. W.; Lee, B. H.; Shim, M., Structural evolution in metal oxide/semiconductor colloidal nanocrystal heterostructures. *Chemistry of Materials* **2006**, 18, (26), 6357-6363.

6. Tao, K.; Zhou, H. R.; Don, H. J.; Xing, B.; Li, W. W.; Sun, K., Direct Deposition of Fluorescent Emission-Tunable CdSe on Magnetite Nanocrystals. *Journal of Physical Chemistry C* **2009**, 113, (20), 8762-8766.

7. Liu, W.; Howarth, M.; Greytak, A. B.; Zheng, Y.; Nocera, D. G.; Ting, A. Y.; Bawendi, M. G., Compact biocompatible quantum dots functionalized for cellular imaging. *Journal of the American Chemical Society* **2008**, 130, (4), 1274-1284.

8. Shen, H. Y.; Jawaid, A. M.; Snee, P. T., Poly(ethylene glycol) Carbodiimide Coupling Reagents for the Biological and Chemical Functionalization of Water-Soluble Nanoparticles. *Acs Nano* **2009**, 3, (4), 915-923.

9. Liu, W. H.; Greytak, A. B.; Lee, J.; Wong, C. R.; Park, J.; Marshall, L. F.; Jiang, W.; Curtin, P. N.; Ting, A. Y.; Nocera, D. G.; Fukumura, D.; Jain, R. K.; Bawendi, M. G., Compact Biocompatible Quantum Dots via RAFT-Mediated Synthesis of Imidazole-Based Random Copolymer Ligand. *Journal of the American Chemical Society* **2010**, 132, (2), 472-483.

## Numpon Insin

Massachusetts Institute of Technology  
550 Memorial Drive, APT#13E-4,  
Cambridge, MA, 02139 USA

Phone: (1-617)-225-1600  
Cell Phone: (1-617)-955-4503  
Email: ninsin@mit.edu

### Education:

#### **Massachusetts Institute of Technology**

*Cambridge, MA*

Ph.D. Candidate in Chemistry (Inorganic Chemistry)

Thesis title: Surface Modifications of Iron Oxides Nanoparticles for Biological Applications

Advisor: Professor Mounji G. Bawendi

#### **Chulalongkorn University**

*Bangkok, Thailand*

Bachelor of Science (1<sup>st</sup> Class Honours) in Chemistry, May 2003

Senior Thesis: Catalysis of Grease Cracking Process using ZSM-5/Al-MCM-41 composite

Thesis Advisor: Dr. Aticha Chaisuwan

### Work and Research Experience:

#### **Research Assistant, Bawendi Research Group, MIT**

*September 2004 – Present*

*Cambridge, MA*

*Advisor: Professor Mounji G. Bawendi*

Design, synthesize, and characterize of inorganic materials nanoparticles of various types including ferromagnetic materials and semiconductor/Utilize colloidal inorganic nanoparticles in biological sensing and imaging using fluorescent microscopy and magnetic resonance imaging.

#### **Department of Chemistry, Chulalongkorn University**

*June 2002 – May 2003*

*Bangkok, Thailand*

*Advisor: Dr. Aticha Chaisuwan*

Synthesize and characterize of ZSM-5/Al-MCM-41 composite materials and study their catalytic activities in the cracking process of grease.

#### **Summer Internship, Johnson & Johnson (Thailand) Ltd.**

*March 2002 – June 2002*

*Bangkok, Thailand*

Prepare and characterize new consumer products in the research and development division.

### Awards and Honors:

Anandamahidol Science Scholarship, one annual awarded in Thailand (2004-2009).

Best poster presentation award for senior projects in physical science, Faculty of Science, Chulalongkorn University (2003).

Scholarship from the Development and Promotion of Science and Technology talents project (DPST), Institute for the Promotion of Teaching Science and Technology, Thailand (2002-2003).

### **Refereed Publications:**

McKee T.D.; Grandi, P.; Mok, W.; Alexandrakis, G.; Insin, N.; Zimmer, J.P.; Bawendi, M.G.; Boucher, Y.; Breakefield, X.O. and Jain, R.K. Degradation of Fibrillar Collagen in a Human Melanoma Xenograft Improves the Efficacy of an Oncolytic Herpes Simplex Virus Vector. *Cancer Research* **2006**, 66: 2509-2513.

Insin, N.; Tracy, J.B.; Lee, H.; Zimmer, J.P.; Westervelt, R.M. and Bawendi, M.G. Incorporation of Iron Oxide Nanoparticles and Quantum Dots into Silica Microspheres. *ACS Nano* **2008**, 2: 197-202.

Stylianopoulos, T; Poh, M. Z.; Insin, N.; Bawendi, M.G.; Fukumura, D.; Munn, L.L. and Jain, R.K. Diffusion of Particles in the Extracellular Matrix: the Effect of Repulsive Electrostatic Interactions. *Biophysical Journal*, **2010**, 99: 1342-1349.

Popović, Z.; Liu, W.; Chauhan, V.P.; Lee, J.; Wong, C.; Greytak, A.B.; Insin, N.; Nocera, D.G.; Fukumura, D.; Jain, R.K. and Bawendi, M.G. Nanoparticle size series for *in vivo* imaging. *Angewandte Chemie International Edition*, **2010**, 49: 8649-8652.

Insin, N.; Park, J.; Liu, W.; Lee, J.; Popovic, Z.; and Bawendi, M.G. Surface Stabilization and Functionalization of Iron Oxide Nanoparticles with Copolymer Synthesized by RAFT polymerization, *in preparation*

Wei, H.\*; Insin, N\*; Lee, J; and Bawendi, M. G. Ultrasmall and Ultrastable Zwitterion-Coated Compact Iron Oxide Nanoparticles for Cellular Imaging, *in preparation*

### **Contributed Presentation:**

Insin, N.; Tracy, J.B.; Lee, H.; Zimmer, J.P.; Westervelt, R.M. and Bawendi, M.G. Incorporation of Magnetic Nanoparticles and Quantum Dots into Silica Microspheres. (Poster), *MRS Spring Meeting 2005*, Boston, MA

Insin, N.; Tracy, J.B.; Lee, H.; Zimmer, J.P.; Westervelt, R.M. and Bawendi, M.G. Incorporation of Magnetic Nanoparticles and Quantum Dots into Silica Microspheres. (Oral), *the 234th ACS National Meeting, 2007*, Boston, MA

Insin, N.; Tracy, J.B.; Lee, H.; Zimmer, J.P.; Westervelt, R.M. and Bawendi, M.G. Silica Microspheres and Silica Nanoparticles Containing Magnetic Nanoparticles and Semiconductor Quantum Dots. (Oral), *the 7th International Conference on Scientific and Clinical Applications of Magnetic Carriers, 2008*, Vancouver, BC

Insin, N.; Park, J.; Liu, W.; Popovic, Z.; and Bawendi, M.G. Surface Stabilization and Functionalization of Iron Oxide Nanoparticles with Copolymer Synthesized by RAFT polymerization. (Oral), *the 238th ACS National Meeting, 2009*, Washington, DC

Insin, N.; Park, J.; Liu, W.; Popovic, Z.; and Bawendi, M.G. Superparamagnetic and Fluorescent Nanoparticles Containing Iron Oxide Nanoparticles and Semiconductor Quantum Dots. (Poster), *MRS Spring Meeting 2010*, San Francisco, CA

**Patents:**

Chan, Y.; Zimmer, J.P.; Insin, N.; Tracy, J.B.; and Bawendi, M.G. Microspheres Including Nanoparticles. Patent Cooperation Treaty (PCT) Application Number US0525593, filed July 20, 2005.

Liu, W.; Allen, P.; Insin, N.; and Bawendi, M. G. Copolymer-Associated Nanomaterial. U.S. Application Number 12/857,430, filed August 16, 2010

**Professional Membership:**

American Chemical Society  
Materials Research Society





## Acknowledgments

Six years at MIT gave me plenty of invaluable experiences. It was difficult for a student from Sakon Nakhon, a small city northeast of Bangkok, Thailand, to adapt and go through the PhD program in the Department of Chemistry at MIT. A new culture, difficulty in communications, MIT classes and examinations, and development of research skills could have been more difficult and unbearable obstacles without the assistance, suggestions, and support from people whom I would like to thank in the last pages of this thesis.

First of all, I would like to thank Professor Mounji G. Bawendi, my thesis advisor, who gave suggestions and guided me through my six years of study here at MIT. His kindness, patience, and attention to me and my work are some of the most important factors for this achievement. His hospitality, ability, and knowledge create a role model for me when I become an advisor.

I also would like to thank Professor Daniel Nocera, the chairman of my thesis committee and my first year academic advisor. His advice at the beginning of my study in a foreign country was valuable and had a strong influence on my decisions about research and classes. He also always gave good suggestions and other perspectives on my research work when we met annually.

I would like to thank Professor Mircea Dincă, another member of my thesis committee. I am grateful for his suggestions, understanding, and prompt responses. I also would like to thank all inorganic chemistry professors who taught me in my first year including Professors Christopher C. Cummins, Stephen J. Lippard, Richard R. Schrock, and Greg Fu; Dr. Joseph Sadighi; and Dr. Peter Muller. Their knowledge and teaching style will influence and lead me to be a better chemistry teacher in the near future.

Because my work is interdisciplinary and very collaborative, I would not have been able to complete all these efforts without very helpful collaborators. I would like to thank Professor Alan P. Jasanoff, Dr. Tatjana Atanasijevic, and Dr. Elisenda Rodriguez from MIT's Department of Nuclear Engineering for the T2 relaxivity measurement for my samples and the collaborative MRI sensing project. As for the microelectromagnetic device and the demonstration of magnetic manipulation with real-time fluorescent imaging of microspheres, these experiments were done in collaboration with Professor Robert M. Westervelt and Dr. Hakho Lee from the Department of Physics at Harvard. The demonstration and ongoing research projects using magnetic control and fluorescent visualization of proteins for studying asymmetric cell division in neural systems were collaborative work with Professor Maxime Dahan, Dr. Barbara Muller, and Dr. Mathieu Coppey from the Ecole Normale Supérieure, France. I also would like to thank two groups of collaborators who were not mentioned in this thesis. These collaborations involved the uses of surface functionalized QDs and fluorescent microspheres in different biological systems. The first group is Professor John Frangioni and Dr. Hak Soo Choi from Beth Israel Deaconess Medical Center, the second group is Professor Rakash Jain and Ming-Zher Poh from Massachusetts General Hospital. Other than assistance with research and useful discussions that I obtained from these collaborators, the experience of dealing with co-workers in a professional fashion was also an invaluable skill that I have developed.

I would like to thank the staff from MIT's Chemistry Department, especially Li Miao and Susan Brighton. Li Miao, the assistant of my advisor, always promptly helped me with many more things than I asked for. My research and study would not have gone as smoothly without her help and her moral support. I will always remember the times when I talked to her every week while I was waiting to meet with my advisor. Susan Brighton, the Graduate Administrator of the Chemistry Department, is another person to whom I am grateful for her assistance and support during my study here.

My research would not have been successful without the tools and staff from various facilities around MIT. I would like to thank to Debby Pheasant from the Biophysical Instrumentation Facility for the DLS analysis instrument. I would like to thank Dr. Tony Garratt-Reed from the Center for Materials Science and Engineering for the scanning transmission electron microscope, Libby Shaw for XPS analysis, and Mike Frongillo and Dr. Yong Zhang for training me to use TEM. I also would like to thank Dr. David Bray and staffs from the Department of Chemistry Instrumentation Facility for training me to use NMR and IR spectrometers.

I would like to acknowledge Dr. Elizabeth Fox from MIT's Writing and Communication Center for spending time editing this thesis.

I am very grateful that I have had a chance to become a member of Bawendi research group and have worked, trained, discussed, and studied with many knowledgeable and kind people in our group. First of all, I would like to thank Professor Joe Tracy and Dr. John Zimmer, who were my mentors when I first joined the group. I learned and improved my research skills significantly during my first and second years, when they were still senior students. Without Joe and John, I might not have successfully passed my second and third year examinations. Beyond helping me inside the lab, Joe and John also advised and helped me through cultural and language obstacles during my early years. Other senior people during my first year included Professors Preston Snee and Yinthai Chan and Dr. Jonathan Steckel also took part in teaching me lots of research skills, correcting my mistakes, and preventing me from making mistakes and running risks.

Many people came into the group at the same time with me or later, and I would like to thank them for very helpful discussions that led to lots of knowledge, ideas, and new skills. Dr. Wenhao Liu is a good friend and gave lots of help in the RAFT polymerizations and organic synthesis in general. Dr. Jongnam Park and He Wei worked closely with me on the iron oxide nanoparticle projects. Dr. Binil Kandapallil, Dr. Zoran Popovic, Dr. Andrew Greytak, Dr. Cliff Wong, Juwell Wu, Hee-Sun Han, Jungmin Lee, and Jose Cordero worked on biologically related projects and always gave valuable suggestions and comments to improve my experiments. Dr. Gautham Nair and Dr. August Dorn were always helpful when I asked about math and physics problems. The rest of my former and current group members always supported me and gave me feedback when I gave presentations in group meeting or when I prepared for talks and oral examinations.

I would like to acknowledge friends from the Inorganic Chemistry Division. Dr. Rebecca Somers and Dr. Emily Nytko-Lutz, upper-class students from the Nocera group, were very helpful when I prepared for my oral examinations. Dr. Jia-Min Chin, Dr. Simone Friedle, and Dr. Kathy Lovejoy, my classmates, helped me as we studied together during our first year.

I would like to thank my Thai friends from TSMIT, especially Gift, Ae, Jane, Naan, Nok, Lek, Mon, Peng, Ob, Puk, Puye, and Oy for our friendship and making me feel as if I was at home here. My years at MIT would have been more stressful and boring without them.

I am thankful to my teachers from Anuban Sakon Nakhon and Sakonraj Wittayanukul in my hometown for imparting their knowledge and shaping my personality. I would like to acknowledge all my professors from Chulalongkorn University for giving deep and broad knowledge in Chemistry and Science. For my research skills, I would like especially to thank Dr. Aticha Chaisuwan, my first research advisor, for her advice and suggestions on both my studies and my future career.

I am also thankful to my friends from schools and university. They were very supportive throughout my studies. The idea of hanging out and having parties with them after I am done with my study and return to Thailand stimulated me to work harder.

Most importantly, moral support from my family, especially my father, mother, sister and Ple, was an integral part of my success. I would like to thank them for always believing in me as well as cheering me up when I am down. I hope my late father perceives this achievement and is happy as I and the rest of our family are.

Finally, I am very grateful that I was chosen to receive a scholarship from the Anandamahidol Foundation, which was founded by our King Rama IX. This scholarship made it possible for me to attend MIT and finish my PhD. My gratitude for receiving the scholarship and being included in this organization could not be explained in words. Instead, I will show them in the rest of my life that I will be as good a Thai scholar as the founder intended.

